# The Evolution of Long-Period Comets

by

Paul Arnold Wiegert

A Thesis submitted in conformance with the requirements
for the Degree of Doctor of Philosophy
Graduate Department of Astronomy
University of Toronto

ABSTRACT OF THE DISSERTATION

The Evolution of Long-Period Comets

Paul Arnold Wiegert

Doctor of Philosophy in Astronomy

University of Toronto

Toronto, Canada 1996

The observed distribution of long-period ($> 200$ yr) comet orbits has proved difficult to reconcile with theory. Among the discrepancies is the "fading problem": the fraction of comets in the observed sample which are presumed to have made more than one perihelion passage since leaving the Oort cloud is much smaller than that predicted by simple dynamical models of the Solar System. This may indicate that the lifetime of the long-period comets is significantly shorter than expected from purely dynamical considerations. This in turn points to the importance of comet losses through volatile depletion.

We examine the evolution of long-period comets through a direct numerical integration, a more realistic approach than the Monte Carlo methods previously used to study this problem. Our model follows the individual trajectories of thousands of comets from the Oort cloud to their final demise. The comets evolve within a model solar system consisting of the Sun, the four giant planets and the Galactic tide, and to which non-gravitational forces and a solar companion object or circumsolar disk may be added. We also consider the effects of the heliopause, solar wind and radiation pressure, and drag on the nucleus. None of these influences are capable of producing a distribution of long-period comet orbits matching observations. In particular, the comets' dynamical lifetimes are too long.

We also investigate the effects of fading $i.e.$ the reduction of comet brightness over time due to volatile loss, which may lead to a shortening of comets' observable lifetimes. A number of simple fading laws are explored. One in which the fraction of comets remaining observable goes like $m^{-0.6\pm0.1}$, where $m$ is the apparition number, provides a reasonable match with observations, and may imply a differential power-law mass distribution $dN \propto M^{-1.6} dM$. A two-population model in which approximately 95% of comets live for only a short time ($\sim 6$ orbits) and the remainder indefinitely also matches observations reasonably well, and could be explained physically by a division of the Oort cloud population on the basis of their internal cohesiveness into fragile and robust objects.

## ACKNOWLEDGEMENTS

# Contents

# Chapter 1

# Introduction

Hast thou ne'er seen the comet's flaming flight?
The illustrious stranger passing, terror sheds
On gazing nations from his fiery train
Of length enormous; takes his ample round
Through depths of ether; coasts unnumber'd worlds
Of more than solar glory; doubles wide
Heaven's mighty cape; and then revisits earth
From the long travel of a thousand years...

—Edward Young,
*Night Thoughts,*
1741

Comets are sources of much information about the origin of our Solar System. They provide insight into the physical and chemical processes underlying stellar and planetary formation because they are believed to contain the condensed remnants of the solar nebula in relatively unprocessed form. As well, the present distribution of cometary orbital elements may reflect the dynamics of the early stages of planetary formation. Comets also serve as probes of the interplanetary medium and the solar wind.

## 1.1   The nucleus

At the heart of the comet is the **nucleus**, a solid body typically a few kilometers in diameter and with a mass of $10^{13}$ kg $\approx 10^{-12}$ Earth masses. Inferred densities range from 0.1 to 1 g cm$^{-3}$ (Mendis 1988), suggesting a volatile-rich and/or porous makeup. This is reflected in the generally accepted model of the comet nucleus, Whipple's (1950) **dirty snowball**, which depicts the nucleus as a single solid conglomerate of refractory (*e.g.* silicates) and

volatile (*e.g.* $H_2O$, CO, $CO_2$) materials. Interplanetary probes sent to meet comet P/Halley[†] during its 1986 perihelion passage returned pictures of the nucleus which confirmed it was a single solid object, and was releasing both gas and dust (A'Hearn 1988). The released material is influenced by the solar wind, the interplanetary magnetic field and the Sun's gravity to form the coma and tail associated with cometary apparitions.

## 1.2   The gas coma

The nucleus becomes increasingly heated by sunlight if it approaches the Sun. The comet's volatiles begin to sublimate, dragging solid particles along with them. This mixture of gas and dust is called the **coma**, the comet's bright, fuzzy head. A comet typically develops a coma (or becomes **active**) at a comet-Sun distance $r$ between 3 and 5 AU, though significant outgassing from more distant bodies has been observed. For example, the minor planet 2060 Chiron, which never approaches closer to the Sun than 8.5 AU, has been observed both with and without an attendant gas cloud (Meech and Belton 1990). Thus the distinction between comets and asteroids, the latter traditionally characterised by a complete lack of coma and outgassing, may be to some degree artificial.

Solid $H_2O$ sublimates appreciably in interplanetary space at $r \lesssim 4$ AU (Delsemme 1982; Spinrad 1987), in the region where coma production typically begins, and pointing to $H_2O$ as a possible constituent of the nucleus. This hypothesis is supported by spectroscopic evidence, including the detection of water and its photolysis products (*e.g.* OH, H, $H_2O^+$, $H_3O^+$) in the coma. In fact, it is estimated that as much as 85% by mass of the coma's gas phase is derived from $H_2O$ (Festou et al. 1993b). The detection of comae at distances significantly beyond 4 AU may be attributable to pockets of solid CO in the nucleus. This molecule's lower vapour pressure allows it to sublimate up to 60 AU from the Sun (Delsemme 1982). The presence of CO in the nucleus has been inferred from the spectroscopic detection of it in the coma and tail, though photolysis remains a possible source. One of its ions, $CO^+$, dominates the visible emission of the comet's gas tail. Other, less abundant volatiles that are seen directly or inferred to exist from their photolysis products include $NH_3$, CN, $CO_2$, $S_2$, $CH_4$ and $N_2$, among others (Mendis 1988).

---

[†]The prefix "P/" indicates a periodic comet, defined to have an orbital period of less than 200 years or to have confirmed observations at more than one apparition, and "C/" indicates a comet which is not periodic in the above sense (Minor Planet Circulars 23803 & 23804).

The coma can be divided into three concentric, overlapping layers (Whipple and Huebner 1976):

1. The innermost layer is the **molecular** or **inner coma**. Its size is determined by the sublimating molecules' lifetimes $\tau$ against photo-dissociation in the solar radiation field. Jackson (1976) calculated $\tau$ at 1 AU for the more abundant cometary volatiles: water is fairly typical with $\tau \approx 2 \times 10^4$ s. The neutral coma gases expand away from the nucleus at roughly constant velocity $v \approx 0.3$ km s$^{-1}$. The resulting size of the molecular coma $v\tau$ is 6000 km, consistent with observations. A typical gas production rate $Q$ of $10^{29}$ s$^{-1}$ (A'Hearn and Festou 1990) yields a mass flux of 3000 kg s$^{-1}$, and a mean number density of $10^6$ cm$^{-3}$, if we assume that the mean molecular mass of the coma is that of a water molecule.

2. Outside the molecular coma is the **radical coma**, where the composition of the outflowing gas becomes dominated by **radicals**, molecular fragments produced from their parents by photo-dissociation. This region is also called the **visible coma**, and produces prominent fluorescence lines, including those of CN, OH, NH, C$_3$, C$_2$ and NH$_2$ (A'Hearn and Festou 1990; Festou et al. 1993b). The OH radical has a lifetime $\tau \approx 2 \times 10^5$ s at 1 AU (Whipple and Huebner 1976). The theoretical radius of the radical coma is thus roughly $10^5$ km, consistent with the typical observed size of a few times $10^5$ km.

3. The **exosphere** is also called the **hydrogen coma** because it is visible primarily in Lyman-$\alpha$ emission. This region extends out into the interplanetary medium, ending where the coma gases are swept away by the solar wind and radiation pressure.

   A neutral ground-state hydrogen atom of mass $m_H$ has an absorption cross-section $\sigma$ dominated by the Lyman-$\alpha$ transition. The acceleration $\dot{v}$ imparted to the molecule by radiation pressure is thus

   $$\dot{v} \approx \sigma(\mathrm{L}_\alpha)\mathcal{F}_p(\mathrm{L}_\alpha)/m_H, \tag{1.1a}$$

   where $\mathcal{F}_p(\mathrm{L}_\alpha)$ is the momentum flux of the radiation field in the Lyman-$\alpha$ line. The absorption cross-section of hydrogen in L$_\alpha$, $\sigma(L_\alpha)$, is given by $\pi e^2 f_{12}/m_H c$ (*e.g.* Spitzer 1978) where $f_{12} = 0.4162$ is the Lyman-$\alpha$ transition's oscillator strength. The momentum flux is related to the energy flux $\mathcal{F}_E$ through $\mathcal{F}_p = \mathcal{F}_E/c$. Equation 1.1a can

thus be rewritten

$$\dot{v}(r) \quad \approx \quad \frac{\pi e^2 f_{12}}{m_H^2 c^2} \left( \frac{R_\odot}{r} \right)^2 \mathcal{F}_E(\mathrm{L}_\alpha, R_\odot), \tag{1.1b}$$

$$\approx \quad 10^{-3} \left( \frac{r}{1 \ \mathrm{AU}} \right)^{-2} \ \mathrm{m \ s^{-2}}, \tag{1.1c}$$

where $R_\odot$ is the radius of the Sun, and $\mathcal{F}_E(\mathrm{L}_\alpha, R_\odot)$ is the Lyman-$\alpha$ energy flux at its surface, approximately $3 \times 10^5$ erg cm$^{-2}$ s$^{-1}$ (Noyes and Avrett 1987). The distance $D$ from the nucleus at which the radiation-induced change in velocity is comparable to the gases' initial velocity ($D \approx v^2/\dot{v}$) constitutes the outer boundary of the exosphere $D_{exo}$. The hydrogen atoms, having absorbed kinetic energy during the photo-breakup of their parent molecules, are now travelling with typical velocities of 10 km s$^{-1}$ (A'Hearn and Festou 1990), putting the edge of the exosphere at $D_{exo} \sim 10^8$ km from the nucleus. This simple theory is consistent with observations: Lyman-$\alpha$ emission has been detected out to a few tens of millions of kilometers from some comets (Whipple and Huebner 1976).

The molecules' mean free paths are less than their distance from the nucleus inside the **collisional radius** of the coma $D_{coll}$, which defines the boundary between hydrodynamic and collisionless flow. The neutral coma gases are thought to expand freely away from the nucleus, thus their density $n$ goes as $4\pi Q/vD^2$, ignoring dissociation which will add a factor of 2–3. The collisional radius such that $n(D_{coll})D_{coll}\sigma \approx 1$, where $\sigma$ is now the collisional cross-section, implying

$$D_{coll} \approx \frac{1}{\sigma(Q/4\pi D_{coll}^2 v)} = \frac{Q\sigma}{4\pi v}. \tag{1.2}$$

A typical value for $\sigma$ is $10^{-15}$ cm$^2$ (A'Hearn and Festou 1990), from which a collisional radius of a few times $10^4$ km can be deduced, putting the collisional radius inside the visible coma.

The total mass of the gaseous coma $M$ is roughly $QmD_{exo}/v$ where $m$ is the mean molecular mass of the coma constituents, taken to be that of a water molecule. When 1 AU from the Sun, the coma's total mass $M \sim 10^{13}$ g, negligible next to that of the nucleus.

## 1.3 The dust coma

An active comet also produces a **dust coma** consisting of submicron to centimeter-sized solid particles eroded from the nucleus. This "dust" is dragged along by the expanding gases, decoupling from the gaseous coma at about 100 km. The dust's dynamics are then dominated by solar gravity, with radiation pressure and the Poynting-Robertson effect also playing some role for the smaller components. The dust coma may have a radius of $10^5$ km at $r = 1$ AU (Grün and Jessberger 1990).

The dust grains may consist of solid $H_2O$ or other volatiles, which continue to sublimate, or refractory materials, which are modified only slowly (*e.g.* by solar wind and cosmic-ray sputtering). The dust-to-gas mass ratio of comets is difficult to determine, depending critically on the number of large (cm-sized) particles, but is estimated to be of order unity (Grün and Jessberger 1990). Thus, the mass of the dust coma is also small compared to that of the nucleus.

## 1.4 The tail

The flow of gas within the coma is complicated by the solar wind and the interplanetary magnetic field. A bow shock forms ahead of the nucleus, near the point where solar and cometary mass flows $\dot{M}_{sw}$ and $\dot{M}_{comet}$ balance each other (Whipple and Huebner 1976). Given that

$$\dot{M}_{comet} \approx Qm \tag{1.3a}$$

$$\dot{M}_{sw} \approx \pi D^2 n_{sw} m_{sw} v_{sw} \tag{1.3b}$$

where $n_{sw}$, $m_{sw}$ and $v_{sw}$ are the number density, molecular mass and velocity of the solar wind's constituents respectively, then the bow shock is expected near

$$D_{bow} \approx \left( \frac{Qm}{\pi n_{sw} v_{sw} m_{sw}} \right)^{1/2}. \tag{1.4}$$

At the Earth's orbit, $n_{sw} \approx 10$ cm$^{-3}$, $v_{sw} \approx 5 \times 10^7$ cm s$^{-1}$ and $m_{sw} \approx 0.5\, m_{proton} \approx 10^{-25}$ g (Lang 1992), implying that the bow shock is approximately half a million km ahead of the nucleus, in accord with more sophisticated calculations and spacecraft observations (Galeev et al. 1986).

In 1957, Alfvén theorised that interplanetary magnetic field lines would drape themselves over the cometary ionosphere, a prediction which has been confirmed by spacecraft measurements of P/Giacobini-Zinner and P/Halley. This draping arises because the magnetic field lines are "frozen" in the solar plasma. The boundary between the solar and cometary plasmas is called the **discontinuity surface** or **cometopause**. The details of the comet ionosphere are too complex to treat here (see Festou et al. 1993b for a review), but one result of the ionospheric structures and magnetic field is to deflect cometary plasma into a **gas tail** pointing in the anti-sunward direction. This structure, also called a **plasma** or **type I** tail, is visible in the spectral lines of its ions, primarily $CO^+$, with contributions from $H_2O^+$, $N_2^+$, $CO_2^+$, $CH^+$ and $OH^+$. Though not all comets develop detectable gas tails (Antrack et al. 1964), emission from $CO^+$ has been detected over $10^8$ km ($\sim 1$ AU) from the nucleus in the tails of the most spectacular comets (Brandt 1968; Saito 1990). Gas tails may be $10^5$ km wide, with $CO^+$ densities reaching $10^2$ to $10^3$ cm$^{-3}$ (Brandt 1968).

At the surface of the nucleus, the solar gravitational acceleration exceeds the comet's own gravity at heliocentric distances $r \lesssim 3$ AU. Thus dust particles, once decoupled from the gas, orbit the Sun independently of the nucleus, with those particles of small (micron or less) size being strongly influenced by radiation pressure. The dust that comets shed creates the dust coma and the **dust** or **type II tail**. Visible in scattered sunlight, this tail is typically curved and shorter than the gas tail, though dust has been detected up to $10^7$ km from the nucleus (Brandt 1968). Comets generally show both type I and type II tails, though comets which have displayed only one or neither are known.

## 1.5 Jets and streamers

In general, the nucleus will be aspherical and inhomogeneous, and the sublimation of volatiles will be non-uniform. Evidence for asymmetric outgassing includes **dust jets** and **streamers**, fountain-like structures commonly visible in the coma and indicative of strong, localised dust/gas release. Images of P/Halley taken by the Giotto spacecraft (*e.g.* Keller 1990) reveal a highly irregular distribution of active regions across the comet's surface. Sublimation is thus likely to result in a net reaction force, commonly termed the **non-gravitational (NG)** force, which contributes to the comet's dynamical evolution (§ 3.3).

## 1.6 Observing long-period comets

The visual geometric albedo $\alpha_V{}^\dagger$ of a comet nucleus is very low. The ESA Giotto spacecraft measured a value of 0.02 to 0.04 for $\alpha_V$ for P/Halley (Mendis 1988). For comparison, C-type asteroids occasionally have $\alpha_V$ as low as 0.05, though some E-type asteroids have albedos as high as 0.5 (Morrison 1992). The planets have surface-averaged albedos ranging from 0.1 (Mercury, the Moon) to 0.65 (Venus), with their satellites reaching greater extremes: as low as 0.03 to 0.05 for Jupiter V and VI (Amalthea, Himalia) with Saturn III (Tethys) reaching 0.9 (Weast et al. 1989).

The very low albedo of the nucleus makes it difficult to observe comets before they become active. A comet nucleus has an apparent visual magnitude $m_V$ given by

$$m_V = m_\odot + 2.5 \log \left( \mathcal{F}_\odot / \mathcal{F} \right), \tag{1.5}$$

where $m_\odot = -26.7$ is the Sun's apparent visual magnitude and $\mathcal{F}_\odot$ and $\mathcal{F}$ are the visual fluxes received at the Earth from the Sun and the comet respectively. The flux received from the comet is the reflected flux attenuated by the inverse-square law,

$$\mathcal{F} \sim \frac{1}{4\pi D^2} \left[ \alpha_V \pi R_c^2 \mathcal{F}_\odot \left( \frac{r_\oplus}{r} \right)^2 \right] = \frac{\alpha_V R_c^2 \mathcal{F}_\odot}{4 D^2} \left( \frac{r_\oplus}{r} \right)^2, \tag{1.6}$$

where $R_c$ is the radius of the nucleus, and $r$, $r_\oplus$ and $D$ are the Sun-comet, Sun-Earth and the Earth-comet distances respectively. Substituting Equation 1.6 into Equation 1.5, and taking $D \approx r$ yields

$$m_V \approx m_\odot + 2.5 \log \left( \frac{4 r^4}{\alpha_V R_c^2 r_\oplus^2} \right). \tag{1.7}$$

A large, bare comet nucleus ($R_c = 10$ km, $\alpha_V = 0.03$), at Saturn's orbit ($r \approx 10$ AU) thus has a visual magnitude of +24. This value increases to +54 if the comet is moved to $10^4$ AU. The Hubble Space Telescope WFPC2 camera can reach magnitudes of 27.5 to 28 in the V and I bands with long exposures (*e.g.* Groth et al. 1994), and provides the practical observational limit for the near-future. Thus, a comet is almost undetectable with present technology unless it approaches the Sun closely enough to develop a coma. It should be noted however that larger bodies ($\sim 100$ km), possibly cometary in nature but

---

$^\dagger$The geometric albedo is defined as the ratio of the flux received to that expected from a perfectly reflecting, perfectly diffusing disk of the same radius and distance, measured at zero phase angle (Hopkins 1980).

lacking comae, have been detected by the Hubble Space Telescope around 40 AU from the Sun (Cochran et al. 1995).

After coma production has begun, the comet's brightness increases rapidly. The visual magnitude $m_V$ of active comets is traditionally described by the equation

$$m_V = H_0 + 5 \log_{10} D + 2.5 n \log_{10} r, \tag{1.8}$$

where $D$ and $r$ are the Earth-comet and Sun-comet distances in AU. The parameter $n$, which usually ranges between 2 and 6, describes the comet's increase in brightness with $r$. The value of $n$ is generally smaller for long-period comets than short-period ones, the latter tending to have brightness profiles which vary more strongly with $r$. $H_0$ is the comet's **absolute magnitude**, defined to be its apparent magnitude were it to be placed 1 AU from both the Sun and Earth. The observed distribution of $H_0$ peaks at 7. The intrinsic distribution, however, is expected to increase monotonically through values of 12 or more, though the faint end of the luminosity function is poorly known (Everhart 1967b).

## 1.7   Research goals

The goal of this research is to test our current understanding of the dynamical evolution of long-period comets against the observed distribution of their orbits. Limited investigations along these lines have prevously been done (*e.g.* Weissman 1980), revealing significant discrepancies between the expected and observed orbital distributions. But until recently, restrictions in computing speed have prevented the numerical integration of a large ensemble of Oort cloud comets, thus it has been unclear whether the gap between theory and observations is the result of over-simplifications in the models used to predict the comets' distribution, or a real gap in our understanding of the Solar System.

Here, the results of the first large scale numerical integration of long-period comets are presented. In Chapter 2, the observed sample of long-period comets is discussed. The distributions of orbital elements is used to support the hypothesis that the Solar System is likely surrounded by a spherical cloud of comets (the Oort cloud), and that the tidal field of the Galaxy is an important mechanism for perturbing comets in such a cloud onto orbits which pass through the inner Solar System. In Chapter 3, the dynamics of long-period comets are detailed, and the importance of the Galactic tide and the giant planets is demonstrated from theory. In Chapter 4, the algorithm used here to simulate comet

trajectories is described, including testing and error control. In Chapter 5, the results of the simulations are detailed and the gap between theory and observations discussed, along with an examination of possible reasons behind the mismatch. In Chapter 6, conclusions are presented, and an overview of future research possibilities is outlined.

# Chapter 2

# Observations

## 2.1 The catalogue of cometary orbits

Marsden and Williams' Catalogue of Cometary Orbits (1993) lists 1392 apparitions of 855 individual comets, observed between 239 B.C. and 1993 A.D., though with poor completeness at early times. This compilation includes, where possible, the comet's osculating or instantaneous elements with respect to the $FK_5/J2000.0$ system. The orbital elements of comets are traditionally quoted at an osculation epoch at or near perihelion, but if the comet's aphelion distance is large, the elements of the orbit on which the comet approached the planetary system, called the **original** elements, are also of interest. These are likely to be different from those measured at perihelion because of the gauntlet of planetary perturbations the comets must run. In this context, "original" will mean "corrected for planetary perturbations during its most recent passage through the planetary system". The original elements can be calculated from the orbit determined near perihelion by integrating the comet's trajectory backwards until well outside the planetary system, and are traditionally quoted in the centre of mass frame. Marsden and Williams include such a list for those comets with large aphelia for which orbits of sufficient accuracy are known. This list contains a total of 289 objects, observed between 1811 and 1993 A.D.

### 2.1.1 Orbital elements uncertainties

Marsden and Williams do not provide error estimates for elements in their catalogue, but do subdivide the orbits into classes: IA, IB, IIA and IIB in descending order of accuracy. These

10

classes are based on the estimated error in the determination of orbital energy, the time span during which the comet was observed and the number of planets whose perturbations were taken into account. These classes are described in more detail in Marsden et al. (1973). The distribution of the 289 comets among these orbits is 76, 94, 72 and 47 respectively.

## 2.2   Comet families

Comets can be grouped usefully on the basis of their orbital periods $\tau$; the divisions of Carusi and Valsecchi (1992) will be used here, though there are others in the literature. Figure 2.1 plots the values of the semimajor axis $a^\dagger$ versus the cosine of the ecliptic inclination $i$ for all comet apparitions. Note that a statistically uniform distribution of angular momentum vectors upon the celestial sphere, called a **spherically symmetric** or **SS** distribution, will have a flat distribution in $\cos i$. The division of comets into families is based largely on the clustering seen in this plot.

### Short-period comets

The **short-period** (or **SP**) comets are those on orbits with periods less than 200 years. A subset of this class, the **Jupiter family**, is comprised of those comets with $\tau$ less than 20 years. The designation "Jupiter-family" arises from the clustering of their aphelion distances $Q$ around Jupiter's orbit, as shown in Figure 2.2, and the consequent domination of their dynamics by this giant planet. Marsden and Williams' catalogue records 640 perihelion passages by members of the Jupiter family, all on prograde orbits lying near the ecliptic. Largely because of their low inclinations, these objects are believed to have been transferred relatively recently into the planetary system from a ring of material beyond Neptune known as the Kuiper belt (§ 3.10.4).

Also counted among the short-period comets are the **Halley-type** (20 yr $< \tau <$ 200 yr) comets, which have a wider distribution of inclinations (Figure 2.1). Over 41 of the 71 apparitions of Halley family comets listed in Marsden and Williams (1993) have retrograde orbits, though P/Halley ($\tau = 76$ yr, $i = 162°$) itself contributes 34 apparitions, dating back to 239 B.C. The upper boundary of the Halley family corresponds, through Kepler's third

---

$^\dagger$The orbital elements used here, along with some celestial mechanics results important to this project, are outlined in Appendix A.
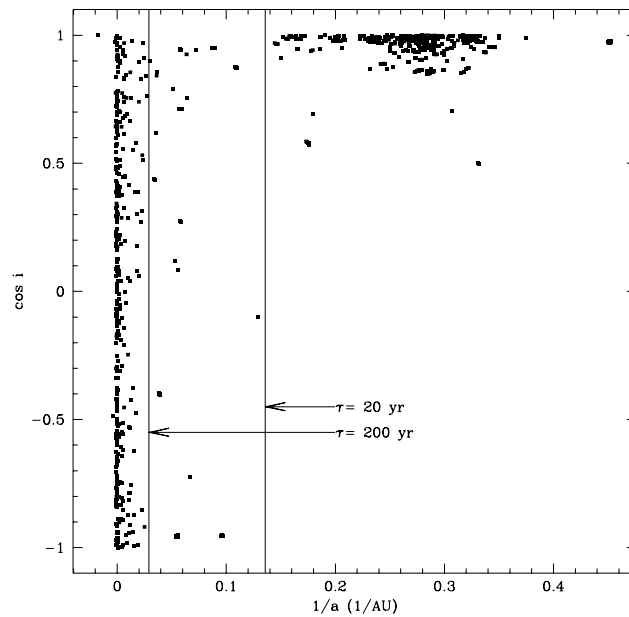
Figure 2.1: The cosine of the ecliptic orbital inclination $i$ plotted against inverse semimajor axis $1/a$ for all observed comet apparitions. The two vertical lines indicate the family boundaries at orbital periods $\tau$ of 20 and 200 years. Data taken from Marsden and Williams (1993).
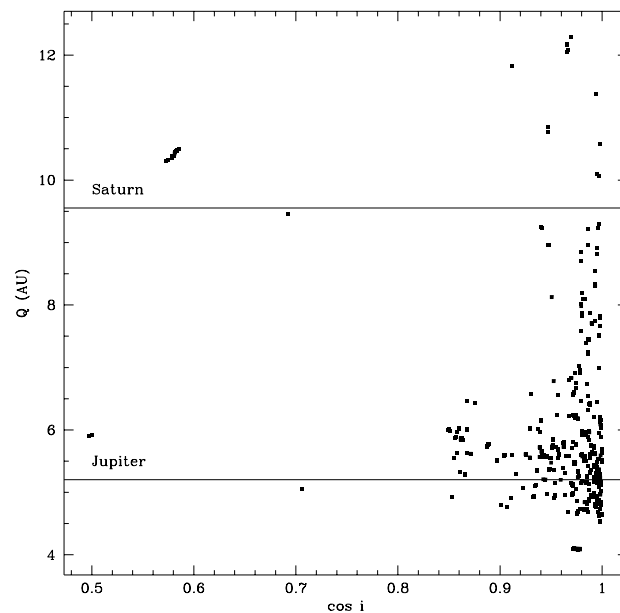


Figure 2.2: Aphelion distance $Q$ versus the cosine of the ecliptic orbital inclination $i$ for the Jupiter family comets. The horizontal lines mark the semimajor axes of Jupiter and Saturn's orbits. Data taken from Marsden and Williams (1993).

law, to a semimajor axis $a \sim 34.2$ AU, and thus the short-period/long-period boundary provides a useful distinction between comets whose aphelia lie within or close to the planetary system, and those that venture significantly beyond.

**Long-period comets**

The **long-period** (or **LP**) comets have periods exceeding 200 years, and their orbits extend outside those of the giant planets. These comets typically have periods of tens of millions of years, and semimajor axes of tens of thousands of astronomical units (AU). Figure 2.1 reveals that LP comets are not confined to the ecliptic plane. These facts suggest that the LP comets are at a different stage of dynamical evolution than the SP comets, or, as is thought more likely, are a dynamically different population from the SP comets. In any case, the LP comets will be the focus of our interest here.

## 2.3 Orbital elements

### 2.3.1 Semimajor axis

The orbital energy $E$ per unit mass of a bound Keplerian orbit is simply $-G(M_1 + M_2)/2a$, where $a$ is measured in the centre of mass frame, and $M_1$ and $M_2$ are the two bodies' masses. For a test particle orbiting the Sun, this expression reduces to $-GM_\odot/2a$. These expressions are not strictly valid in a multi-body system, but nevertheless provide a useful measure of a comet's binding energy. For simplicity, the **inverse semimajor axis** $1/a$ is used here as a measure of the comet's orbital energy, differing from the Keplerian energy only by a simple constant factor (see Appendix A).

The boundary between SP and LP comets is at $1/a = (200 \text{ yr})^{-2/3} \approx 0.029 \text{ AU}^{-1}$. Figure 2.3 displays histograms of $1/a$ for the 289 LP comets with known "original" orbits, at two different magnifications[†].

From Figure 2.3b, it is clear that relatively large numbers of comets travel on orbits with $a \gtrsim 10^4$ AU ($\tau \gtrsim 10^6$ yr). By way of comparison, Pluto's semimajor axis is only 39.5 AU ($\tau \approx 248$ yr). Also notable is a lack of strongly hyperbolic original orbits. Comets entering the Solar System from interstellar space would be expected to have velocities comparable to

---

[†]Unless otherwise stated, the error bars on histograms are $\pm 1$ standard deviation ($\sigma$) assuming Poissonian statistics ($\sigma = \sqrt{N}$).

$(a)$                                                $(b)$
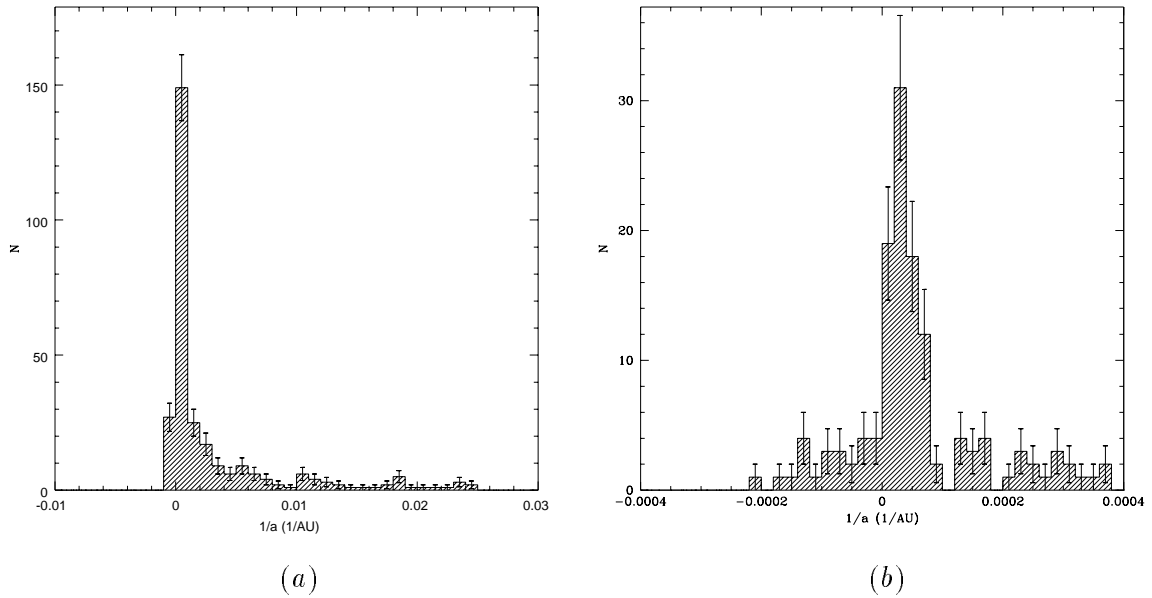
Figure 2.3: Distribution of original inverse semimajor axes of 289 long-period comets at two different magnifications. Data taken from Marsden and Williams (1993).

the velocity dispersion of disk stars, roughly 30 km s$^{-1}$ (Mihalas and Binney 1981). This velocity is equivalent to an inverse semimajor axis of approximately $-1$ AU$^{-1}$, impossible to reconcile with the most hyperbolic original orbit observed, C/Sato (1976 I) which had $1/a \approx -7 \times 10^{-4}$ AU$^{-1}$. The few (27) weakly hyperbolic orbits in Figure 2.3 may be due to observational error or the influence of non-gravitational forces (§ 1.5). The sharp peak in the $1/a$ distribution was interpreted by Oort (1950) as evidence for a population of comets orbiting the Sun at large ($a \gtrsim 10\ 000$ AU) distances, a population which has come to be known as the **Oort cloud**.

It is useful to consider here the distribution of original energies of comets with perihelia inside 3 AU, for the purposes of comparison with later results. These distributions, shown in Figure 2.4, are similar to those in Figure 2.3, but the spike is not as high, due to a tendency for Oort cloud comets to be brighter than other comets, and thus visible at larger distances.

## 2.3.2 Perihelion distance

A histogram of the number $N$ of LP comets versus perihelion distance $q$ is shown in Figure 2.5. There is a strong peak near 1 AU due to observational biases: comets appear brighter when nearer both the Sun and the Earth. Everhart (1967b) concluded that the
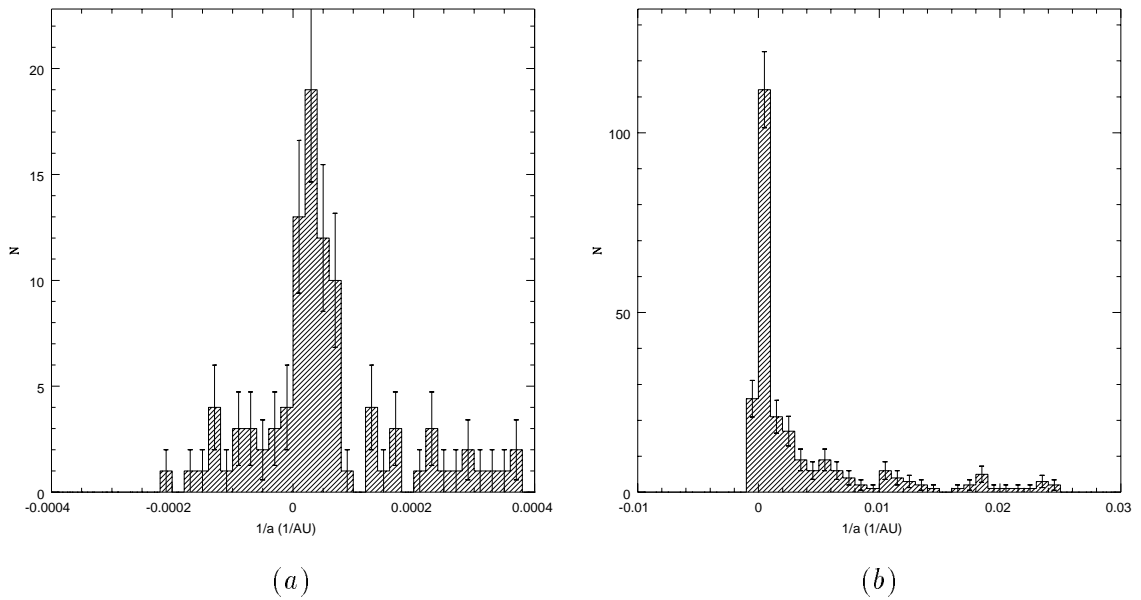
Figure 2.4: Distribution of original inverse semimajor axes of 248 long-period comets with perihelion distances less than 3 AU at two different magnifications. Data taken from Marsden and Williams (1993).

**intrinsic** distribution *i.e.* the distribution which includes all LP comets, observed and un-observed, has a slope $dN/dq \propto 0.4 + 0.6q$ inside the Earth's orbit, but that the distribution at larger distances is poorly constrained, probably lying between a flat profile and one in-
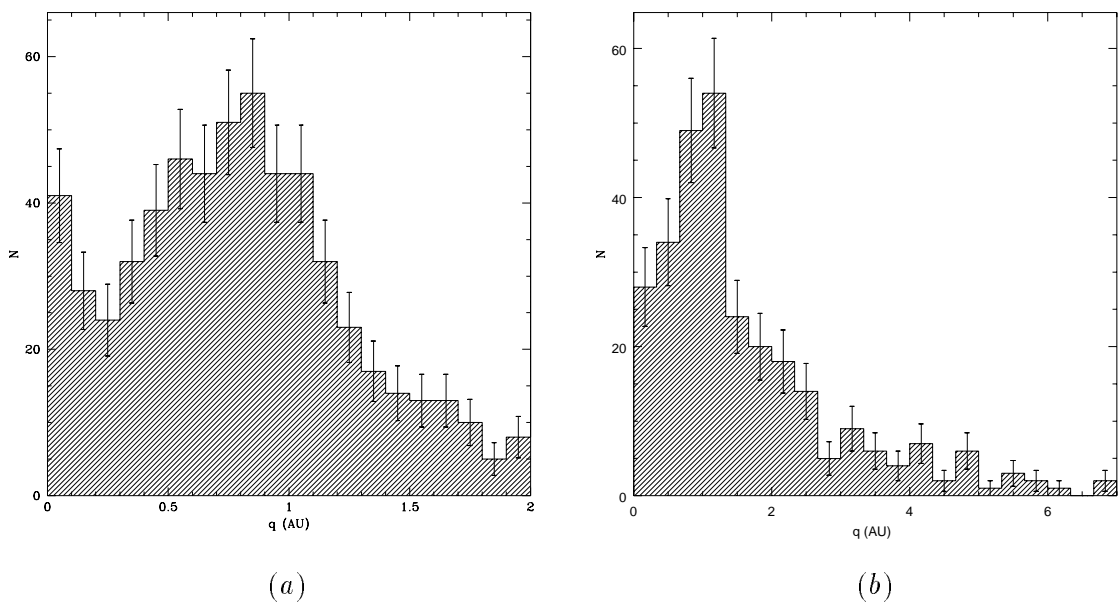


Figure 2.5: Number $N$ versus perihelion distance $q$ for 679 long-period comets. Data taken from Marsden and Williams (1993).

creasing linearly with perihelion distance. Kresák and Pittich (1978) also found the intrinsic distribution of $q$ to be largely indeterminate at $q > 1$ AU, but consistent with $dN/dq \propto q^{1/2}$ over the range $0 < q < 4$ AU.

There are two estimates in the literature of the numbers of comets which pass unobserved through the inner Solar System. Everhart estimates that only 20% of all comets approaching the Sun to within 4 AU are observed. Kresák and Pittich estimate 60% are observed at $q \leq 1$ AU, dropping to only 2% at $q = 4$ AU. Though not directly comparable, these estimates are roughly consistent in that they indicate that a large fraction of comets passing near the Sun likely go unnoticed. It will be assumed here that perihelion distance is not strongly correlated with the comets' semi-major axis or angular elements, and thus that any selection effects acting on $q$ do not affect the observed distributions of the other elements.
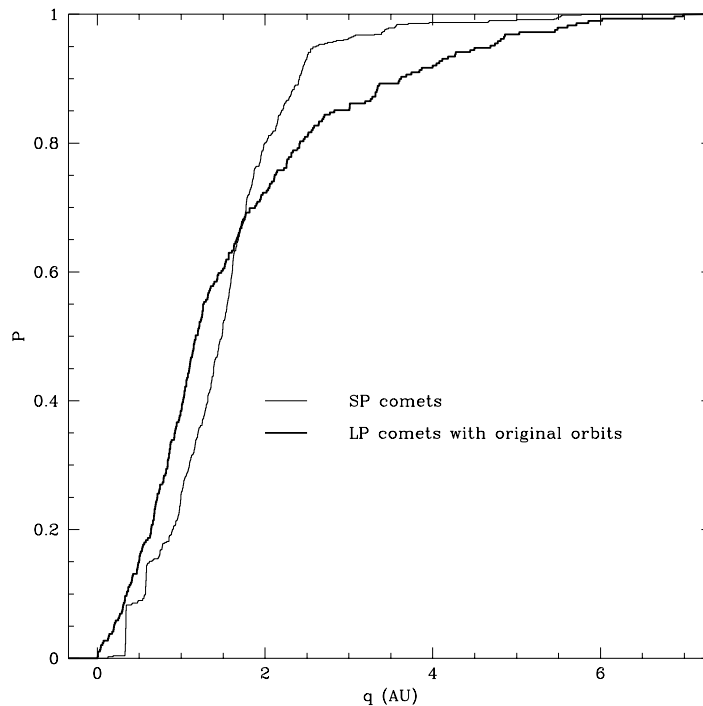


Figure 2.6: The cumulative probability distribution as a function of perihelion distance $q$ for the short-period comets, and for the long-period comets with computed original orbits. Data taken from Marsden and Williams (1993).

It is interesting to compare the cumulative distributions of SP and LP comets as a function of $q$, displayed in Figure 2.6. Comets of all types are rarely observed if their perihelia are beyond 2 AU, but those that are seen are more likely to be LP than SP. This

difference can be explained if the SP comets have typically undergone more apparitions than their long-period counterparts, and hence have smaller volatile inventories and produce fainter comae. The discrepancy becomes even more striking when one considers that there are more chances to discover SP comets due to their more frequent returns. The reduction in cometary brightness with repeated apparitions is important to our understanding of comet dynamics and will be discussed more fully in § 3.10.1.

### 2.3.3   Inclination

Figure 2.7 shows the distribution of the cosine of the LP comet inclinations. For comparison, a spherically symmetric distribution is indicated by the heavy line. Everhart (1967b) showed that selection effects due to inclination should only affect the distribution at the 5% level, well below the statistical noise. The data matches the flat line fairly well by eye: the $\chi^2$ and Kolmogorov-Smirnov (KS) tests return probabilities that the distribution is consistent with spherical symmetry of roughly 0.35 and 0.99 respectively. The $\chi^2$ distribution examines the match at each point and is thus more sensitive to high frequencies in the data set than the KS test, which works with the cumulative distribution. Thus, a high probability of flatness as indicated by the KS test, along with a low probability according to the $\chi^2$ test, is consistent with small-scale clumpiness, but little or no low-frequency signal. Discrepancies between KS and $\chi^2$ tests occur for a number of the distributions to follow, but as their flatness is not central to the discussion, strong interpretations will not be imposed on the $\chi^2$ and KS results.

Long period comets, unlike those with shorter periods, are not confined to the ecliptic, and are equally likely to be on prograde or retrograde orbits. The ratio of prograde to retrograde comets is 144/145. The $\chi^2$ and KS tests conflict, returning probabilities of 0.008 and 0.99 that the ecliptic distributions are flat. The distribution is less flat to the eye in the Galactic frame. There may be a gap near zero inclination, possibly due to the influence of the Galactic tide (§ 3.2), or to selection effects resulting from the confusion of comets with other objects in the Galactic plane.

### 2.3.4   Longitude of the ascending node

The distribution of longitudes of the ascending nodes $\Omega$ is plotted in Figure 2.8. The flat line again indicates a SS distribution. The two curves match fairly well, consistent with

Everhart's (1967a,b) conclusion that there are unlikely to be any selection effects based on $\Omega$ over time scales long compared to one Earth year, assuming the intrinsic distribution is azimuthally symmetric. The $\chi^2$ and KS tests indicate probabilities of 0.35 and 0.999 respectively that the observed longitudes of the ascending nodes are drawn from an intrinsically flat distribution. When applied to the Galactic distribution, the $\chi^2$ and KS tests yield probabilities of 0.05 and 0.99 that the intrinsic distributions are flat; again, the low value determined by the $\chi^2$ test may either be due to noise in the sample, or indicate a real deviation of the distribution from uniformity on small scales.

### 2.3.5 Argument of perihelion

Figure 2.9 shows the distribution of the arguments of perihelion $\omega$ for the LP comets. The $\chi^2$ test reveals a probability less than 0.05 that $\omega$ is drawn from a flat distribution, but the KS test puts it at over 0.99. Comets with $\omega$ less than $\pi$ outnumber those with $\omega$ greater than $\pi$ by a factor of 5/4. This is probably due to an observational selection effect (Everhart 1967a; Kresák 1982): comets with $0 < \omega < \pi$ pass perihelion above the ecliptic, and are more easily visible to observers in the northern hemisphere. The lack of observed apparitions with $\omega > \pi$ is a result of the smaller number of comet searchers in the southern



$(a)$                                                    $(b)$
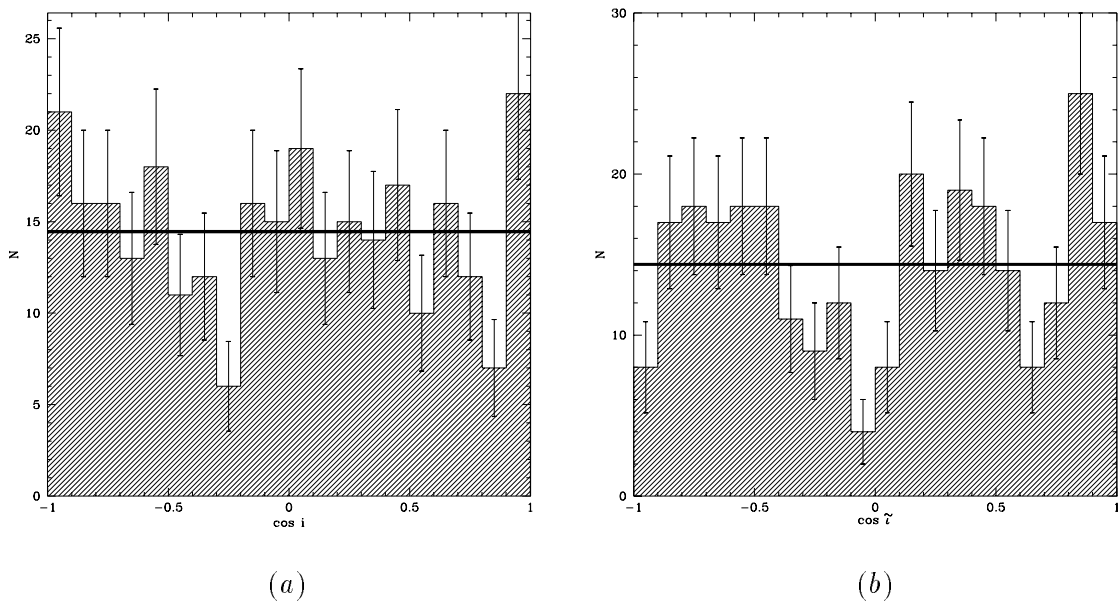
Figure 2.7: The distribution of the cosine of the inclination for the long-period comets in $(a)$ ecliptic coordinates $i$, and $(b)$ Galactic coordinates $\tilde{\imath}$. A spherically symmetric sample is indicated by the flat line. Data taken from Marsden and Williams (1993).
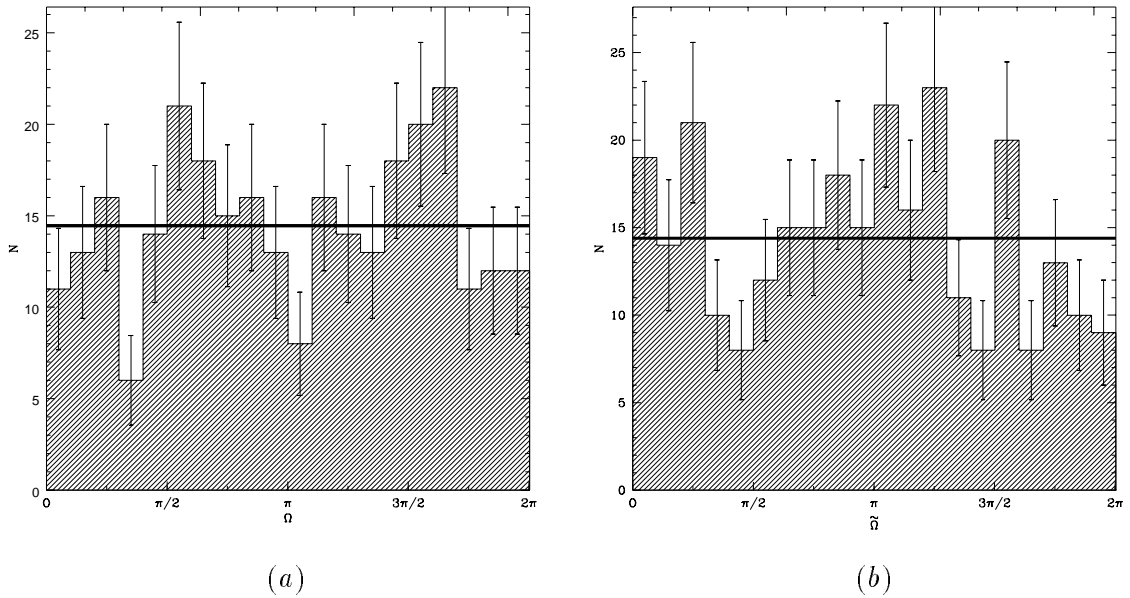
Figure 2.8: The distribution of the longitude of the ascending node of the long-period comets in the (a) ecliptic frame, $\Omega$, and (b) in the Galactic frame, $\tilde{\Omega}$. Data taken from Marsden and Williams (1993).

hemisphere until very recent times. The distribution in the Galactic frame has a slight excess of comets with orbits in the range $\sin 2\tilde{\omega} > 0$ (58% of the total number), and the distribution has a probability of being flat of less than 0.01 and over 0.99 according to the $\chi^2$ and the KS test respectively.

## 2.3.6   Aphelion directions

Figure 2.10 shows the distribution of the aphelion directions of the LP comets in the ecliptic and Galactic references frames. Unfortunately, Marsden and Williams (1993) do not provide the complete set of elements for the "original" orbits, and thus Figure 2.10 was calculated from the orbital elements at perihelion. It will be shown that the angular elements are typically only weakly perturbed during a single passage within the planetary system (§ 3.1), so the errors in the aphelion positions are likely to be small.

Claims have been made for a clustering of aphelion directions around the solar antapex (*e.g.* Tyror 1957; Oja 1975), but newer analyses with improved catalogues (*e.g.* Lüst 1984) have shed doubt on this hypothesis. The presence of complex selection effects, such as the uneven coverage of the sky by comet searchers, render difficult the task of unambiguously determining whether or not clustering is present. Attempts to avoid selection effects end up

$(a)$ $(b)$
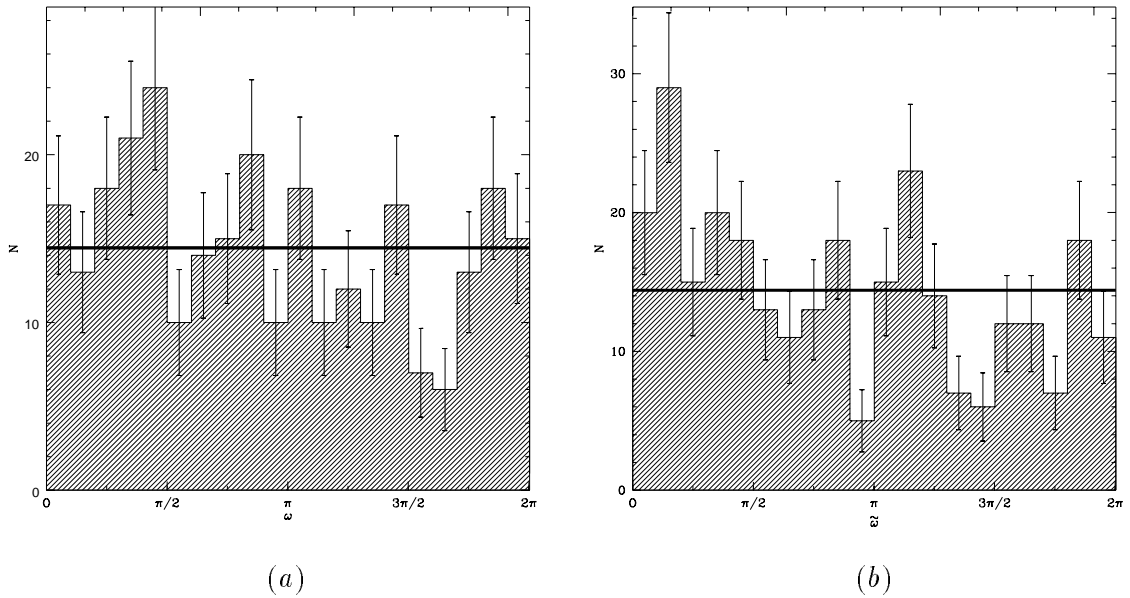
Figure 2.9: The distribution of the argument of perihelion in $(a)$ the ecliptic frame, $\omega$, and $(b)$ in the Galactic frame, $\tilde{\omega}$, for the long-period comets. Data taken from Marsden and Williams (1993).

subdividing the samples into subsamples of such small size as to be of dubious statistical value.

Whipple (1977) has shown that it is unlikely that there are many large comet groups *i.e.* comets related through having split from the same parent body, in the observed sample though the numerous ($\sim 20$) observed comet splittings makes the possibility plausible. A comet group would likely have spread somewhat in semimajor axis: the resulting much larger spread in orbital period ($\tau \propto a^{3/2}$) makes it unlikely that two or more members of such a split group would have passed the Sun in the 200 years for which good observational data exist. The Kreutz group of sun-grazing comets is the only generally-accepted exception.

A feature of the plot of aphelion directions in the Galactic frame, Figure 2.10b, is their concentration at Galactic latitudes $b \sim \pm 45°$. Figures 2.11a and b show histograms of comet number versus the sine of the ecliptic latitude $\beta$ and the Galactic latitude $b$. The ecliptic latitudes deviate only weakly from a SS distribution and this deviation is likely due to the lack of southern hemisphere comet searchers. The Galactic distribution shows two broad peaks, centred roughly on $\sin b \sim \pm 0.5$. It will be shown that this is likely due to the influence of the gravitational tidal field of the Galaxy (§ 3.2), which acts most strongly when the Sun-comet line makes a 45° angle with the Galactic polar axis, though the gap
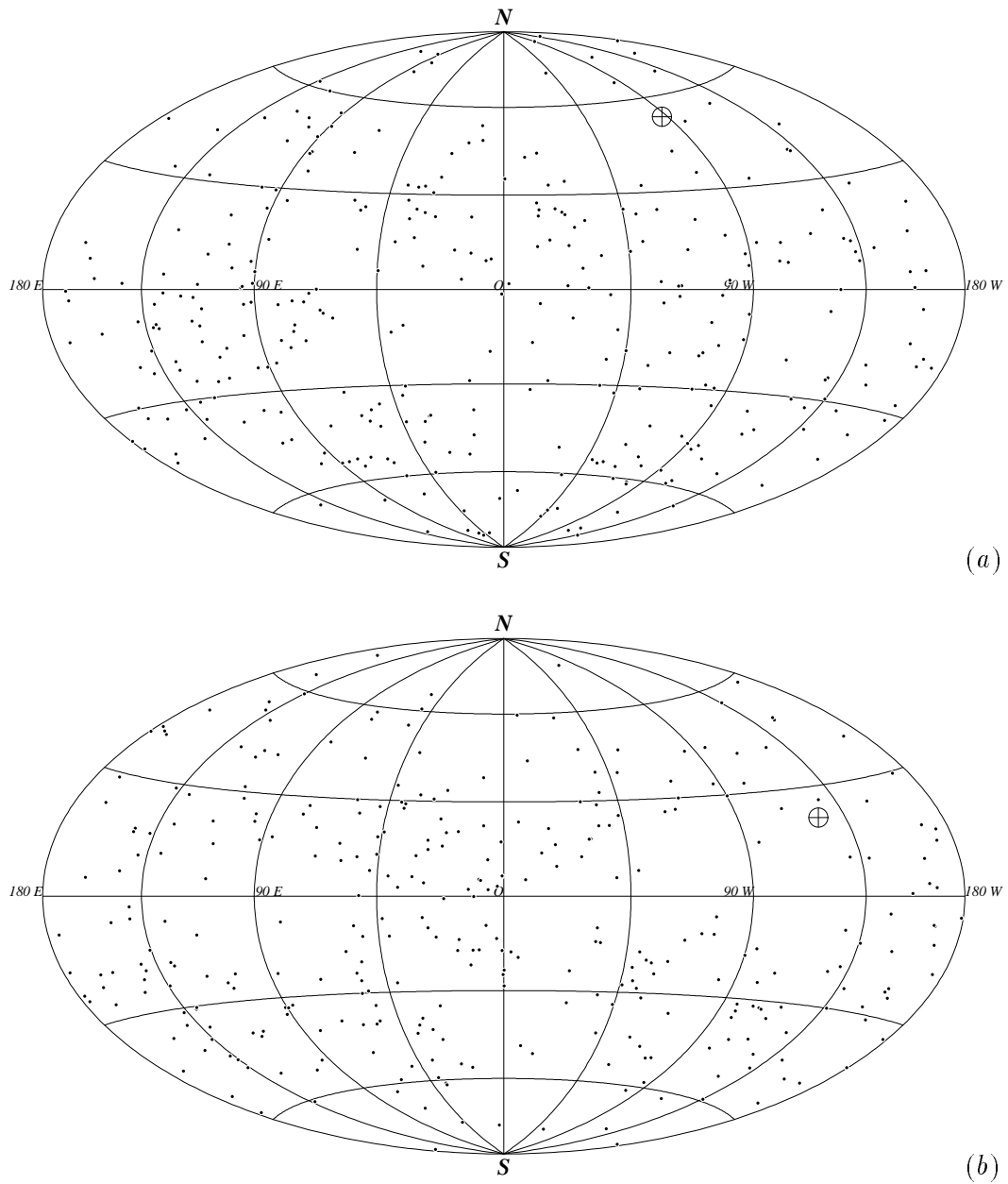
Figure 2.10: Long-period comet aphelion directions on (*a*) ecliptic and (*b*) Galactic equal-area maps. The crossed circle is the solar apex. Data taken from Marsden and Williams (1993).
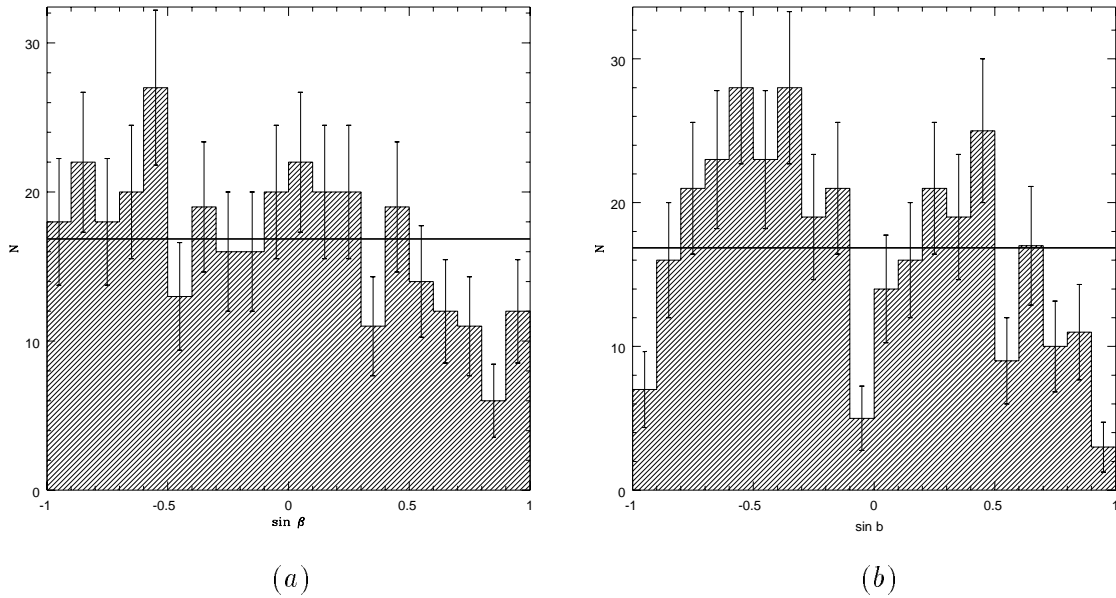
Figure 2.11: The sine of the aphelion latitudes of long-period comets in the ecliptic ($a$) and Galactic ($b$) reference frames. Data taken from Marsden and Williams (1993).

near $b = 0°$ may be a selection effect resulting from the increased difficulty of spotting comets against the more crowded skies of the Galactic plane. The weak selection effects in the ecliptic frame are unlikely to significantly affect the distribution in the Galactic frame, the two frames being tilted at a large angle ($\sim 60°$) to each other.

## 2.4   Summary

The angular orbital elements, in both the ecliptic and Galactic frame, may or may not be consistent with a spherically symmetric distribution. The $\chi^2$ test typically produces a low probability of the distribution being uniform, while the KS test, which examines the cumulative distribution, generally produces a much higher probability. This implies that there is "high frequency" noise in the sample, but no strong "low frequency" signal. However, the distribution of Galactic latitudes does appear to have a doubly-peaked distribution possibly due to the Galaxy's tidal field.

The perihelion distribution is fraught with selection effects and only its gross features are useful for comparison with theory at this point. Fortunately, the orbital energy distribution has a distinctive signature. It will provide the primary diagnostic when comparisons with simulations are performed, though the other distributions also provide useful information.

# Chapter 3

# Dynamics

The equations of motion of the comet can be written as

$$\ddot{\vec{r}} = \vec{F}_\odot + \vec{F}_{planets} + \vec{F}_{tide} + \vec{F}_{stars} + \vec{F}_{clouds} + \vec{F}_{disk} + \vec{F}_{jet} + \vec{F}_{rp} + \vec{F}_{sw} + \vec{F}_{drag}, \qquad (3.1)$$

where the different terms on the right-hand side represent the different accelerations to which the comet is subject. Considering initially the heliocentric frame, $\vec{r}$ is then the vector from the Sun to the comet. The first term of Equation 3.1 represents the Sun's gravitational pull,

$$\vec{F}_\odot = -\frac{GM_\odot}{r^3}\vec{r}, \qquad (3.2)$$

where $G$ is the gravitational constant and $M_\odot$ is the mass of the Sun. The second term of Equation 3.1 represents the gravitational influence of the planets ($\vec{F}_{planets}$), and the remaining terms, the accelerations due to the Galaxy's tidal field ($\vec{F}_{tide}$), individual close encounters with stars ($\vec{F}_{stars}$) and molecular clouds ($\vec{F}_{clouds}$), a hypothetical disk of matter outside the planetary orbits ($\vec{F}_{disk}$), and non-gravitational forces resulting from outgassing ($\vec{F}_{jet}$), solar radiation pressure ($\vec{F}_{rp}$), solar wind pressure ($\vec{F}_{sw}$) and drag ($\vec{F}_{drag}$), respectively. These effects will be considered separately.

## 3.1 The planets

The functional form of $\vec{F}_{planets}$ depends, as do all the terms, on the reference frame in which it is expressed. The frames of interest here are the heliocentric and barycentric frames. In

23

the barycentric frame, $\vec{F}_{planets}$ can be expressed simply as

$$\vec{F}_{planets(bary)} = -\sum_p \frac{GM_p}{r_{pc}^3} \vec{r}_{pc}, \tag{3.3}$$

where $M_p$ is the planetary mass, and $\vec{r}_{pc}$ is the distance vector pointing from the planet to the comet. Complications arise when considering the heliocentric frame because it is non-inertial: the Sun orbits the Solar System's centre of mass. The additional terms needed to account for the solar motion are called the **indirect** terms, and serve as corrections to the **principal** terms (Equation 3.3) when working in the heliocentric frame,

$$\vec{F}_{planets(helio)} = -\sum_p \frac{GM_p}{r_{pc}^3} \vec{r}_{pc} - \sum_p \frac{GM_p}{r_p^3} \vec{r}_p, \tag{3.4}$$

where $\vec{r}_p$ is the Sun-planet radius vector.

The planets may strongly influence a comet's path, but the comet is not massive enough to have a detectable effect on any of the planets: a typical nucleus has a mass only $10^{-9}$ that of Pluto, and only $10^{-14}$ that of Jupiter.

### 3.1.1  Energy

The motion of the comet in the field of even one planet and the Sun has no analytic solution, and may be quite complicated. However, if the comet's aphelion is well outside the planetary system, *i.e.* it is a long-period comet, then the planets' influence is concentrated near perihelion, and can be approximated for some purposes by an instantaneous "kick" in the comet's orbital energy.

The energy kick $\Delta E$ and the corresponding change in the inverse semimajor axis $\Delta(1/a)$ are difficult to calculate analytically (*e.g.* van Woerkom  1948), but have been determined from numerical experiments (Everhart  1968; Fernández  1981). For a single planet, dimensional considerations show that

$$|\Delta E| \quad \sim \quad GM_p/r_p, \tag{3.5a}$$

$$|\Delta(1/a)| \quad \sim \quad M_p/r_p, \tag{3.5b}$$

where in the second equation $M_p$ is in solar masses. The values of $M_p$ and $r_p$ for the planets are listed in Table 3.1.

| Planet | $M_p$ | $r_p$ | $M_p/r_p$ | $M_p r_p^2$ |
|---|---|---|---|---|
| Mercury | $1.7 \times 10^{-7}$ | 0.39 | $4.3 \times 10^{-7}$ | $2.5 \times 10^{-8}$ |
| Venus | $2.5 \times 10^{-6}$ | 0.72 | $3.4 \times 10^{-6}$ | $1.3 \times 10^{-6}$ |
| Earth+Moon | $3.0 \times 10^{-6}$ | 1.00 | $3.0 \times 10^{-6}$ | $3.0 \times 10^{-6}$ |
| Mars | $3.2 \times 10^{-7}$ | 1.52 | $2.1 \times 10^{-7}$ | $7.5 \times 10^{-7}$ |
| Jupiter | $9.6 \times 10^{-4}$ | 5.20 | $1.8 \times 10^{-4}$ | $2.6 \times 10^{-2}$ |
| Saturn | $2.9 \times 10^{-4}$ | 9.54 | $3.0 \times 10^{-5}$ | $2.6 \times 10^{-2}$ |
| Uranus | $4.4 \times 10^{-5}$ | 19.2 | $2.3 \times 10^{-6}$ | $1.6 \times 10^{-2}$ |
| Neptune | $5.2 \times 10^{-5}$ | 30.1 | $1.7 \times 10^{-6}$ | $4.7 \times 10^{-2}$ |
| Pluto | $8 \times 10^{-9}$ | 39.5 | $2 \times 10^{-10}$ | $1.2 \times 10^{-4}$ |

Table 3.1: Quantities related to the mass $M_p$ and semimajor axis $r_p$ of the planets of the Solar System. $M_p/r_p$ is indicative of the size of the energy perturbation a comet receives per perihelion passage (Equation 3.5a), $M_p r_p^2$, of the torque due to the planet's orbital quadrupole (Equation 3.16). Units are $M_\odot$ and AU. Data taken from Lang (1992).

In comparison, given the same conditions as above, simple theory predicts that the angular orbital elements $i$, $\Omega$ and $\omega$ and the perihelion distance $q$ receive perturbations,

$$\Delta i \sim \Delta \Omega \sim \Delta \omega \sim \Delta q/q \sim M_p/M_\odot. \tag{3.6}$$

For a long-period comet with $a = 5000$ AU and $q$ inside Jupiter's orbit, $\Delta(1/a)/(1/a) \sim 1$, while the fractional change in the angular elements and perihelion distance is only of order $10^{-3}$. Thus the energy of LP comets on high eccentricity orbits evolves on a shorter time scale than $i$, $\Omega$, $\omega$ and $q$.

The kicks due to each individual planet are uncorrelated, so the total change in $E$ is given by the square-root of the sum of the squares of the individual kicks

$$|\Delta E| \approx \left[ \sum_p (\Delta E_p)^2 \right]^{1/2} \sim \left[ \sum_p (GM_p/r_p)^2 \right]^{1/2}. \tag{3.7}$$

If the comet's perihelion is inside the orbits of all the giant planets, Jupiter dominates the summation, having $M_p/r_p$ over six times greater than the next largest contributor, Saturn (see Table 3.1, column 4). The contributions of the inner planets and Pluto together constitute less than 5% of Jupiter's contribution. Equation 3.7 is constant (within the constraint $q < r_{Jup}$), and implies a constant

$$|\Delta(1/a)| \sim \frac{2}{r_{Jup}} \left( \frac{M_{Jup}}{M_\odot} \right) \sim 4 \times 10^{-4} \ \text{AU}^{-1} \tag{3.8}$$

per orbit as well. Of course, these values are only rough estimates, the actual changes in the orbital elements being sensitive functions of the initial conditions. Nevertheless,

Equation 3.8 provides a useful simple model, called the **diffusion model**, of the evolution of Oort cloud comets with perihelia within the planetary system.

Under the diffusion model, a near-parabolic comet which makes a series of passages within the planetary system receives an energy kick each time. The kicks are symmetrically distributed about zero, and are uncorrelated and identically distributed as long as the comet's orbital period is long compared to that of the planets. The evolution of such a comet can thus be approximated by a **random walk** in energy space, with step size given by Equation 3.8. The region of energy space LP comets inhabit has two "absorbing" boundaries:

- At $1/a \leq 0$, the comet leaves the Solar System on an unbound orbit.

- As $1/a \to \infty$, the comet's orbit contracts, bringing it into collision with the Sun. In reality, comets do not reach such a state, the diffusion approximation being invalid where $a \lesssim r_p$. Instead, some upper limit $(1/a)_{sp}$ is defined, below which the diffusion model is no longer valid. It is useful to take this cutoff to be the boundary between long and short-period comets *i.e.* where $\tau = 200$ yr, corresponding to $a_{sp} \approx 34.2$ AU, or $(1/a)_{sp} \approx 0.029$ AU$^{-1}$. This boundary is not truly absorbing, as there is nothing to prevent a SP comet from evolving back into an LP comet. However, only a small number of LP comets survive to become SP (Equation 3.10b, and later, Table 5.1), hence the possibility of SP comets returning to the LP domain is small and can be neglected.

### 3.1.2   The Gambler's Ruin problem

The random walk of a LP comet under the diffusion approximation is very similar to the well-known **Gambler's Ruin** problem, with the end-states of ejection and becoming short-period corresponding to bankruptcy and breaking the house, respectively[†].

Consider a comet random-walking on an integer lattice of energies. Let $\eta_{ej}$ be the initial number of steps the comet is from ejection, and let $\eta_{sp}$ be its initial distance in steps from the short-period barrier. For a typical visible Oort cloud comet, $\eta_{ej} \approx 1$ and

$$\eta_{sp} \approx \frac{(1/a)_{sp}}{\Delta(1/a)} \approx 80. \tag{3.9}$$

---

[†]See *e.g.* Kannan (1979) for a more complete description of the Gambler's Ruin problem.

The probabilities $p_{ej}$ and $p_{sp}$ of the comet reaching the ejecting or short-period barriers respectively are simply

$$p_{ej} = \eta_{sp}/(\eta_{ej} + \eta_{sp}) \approx 0.988, \tag{3.10a}$$

$$p_{sp} = \eta_{ej}/(\eta_{ej} + \eta_{sp}) \approx 0.012. \tag{3.10b}$$

If $m$ is the number of orbits a comet survives before crossing one of the absorbing barriers, its expectation value $\bar{m}$ is

$$\bar{m} = \eta_{ej}\,\eta_{sp} \approx 80. \tag{3.11}$$

However, it should be noted that the distribution of lifetimes, being very broad as would be expected for a diffusion process, is not well-characterised by Equation 3.11.

In the case of no short-period barrier $i.e.$ $\eta_{sp} \to \infty$, the number $N$ of LP comets remaining on orbit $m$ is given by (Everhart 1976; Yabushita 1979)

$$N(m) = N_0 m^{-1/2}, \tag{3.12}$$

where $N_0$ is the initial number of comets. This implies a probability $p_{ej}$ of ejection at each orbit of

$$p_{ej}(m) = \frac{1}{2}m^{-3/2}. \tag{3.13}$$

### 3.1.3  Distant planetary encounters

Comets with perihelia outside the planetary system do not have close encounters with the planets, and the resulting perturbations are significantly decreased. Heggie (1975) calculated the change in energy of a binary star system when approached by an interloper on a near-parabolic orbit. His results provide a useful approximation to the situation in question, though he made the assumptions that the three bodies were roughly equal in mass, that the interloper was approaching on a near-parabolic orbit, and that $q \gg r_p$, among others. With the Sun and Jupiter playing the role of the binary, the change in their binding energy is, through conservation of energy, just the energy absorbed by the comet. From Equation (5.43) of Heggie's paper, the energy kick is

$$|\Delta E/E| \sim \exp\left[-\left(\frac{8q^3}{9r_p^3}\right)^{1/2}\right]. \tag{3.14}$$

Though Equation 3.14 was derived based on assumptions not always strictly valid in the case of comets, the conclusion that the energy perturbation drops exponentially as $q \to \infty$ is certainly correct.

### 3.1.4  Angular momentum

In the case of LP comets with perihelia outside the planetary system, changes in the angular momentum $J$ induced by the planets are dominated by the torques resulting from the quadrupole moments of the time-averaged planetary orbits. These torques affect the perihelion distances $q$, related to $J$ through

$$J = [GM_\odot a(1 - e^2)]^{1/2} \approx (2GM_\odot q)^{1/2} \text{ where } e \approx 1. \tag{3.15}$$

Approximating the planet orbits by coplanar circles, the total time-averaged quadrupole moment of the planets $\mathcal{Q}$ is the sum of the planets' individual moments $\mathcal{Q}_p = M_p r_p^2$ (Table 3.1, column 5)

$$\mathcal{Q} = \sum_p \mathcal{Q}_p = \sum_p M_p r_p^2 \approx 0.115 \text{ M}_\odot \text{ AU}^2, \tag{3.16}$$

and the associated torque $\dot{\vec{J}}$ on the comet is

$$\dot{\vec{J}} = -\frac{3G\mathcal{Q}}{2r^3} \sin \beta \cos \beta \; \hat{\phi} \qquad \text{for } q \gg r_p, \tag{3.17}$$

where $\beta$ is comet's ecliptic latitude, given by $\sin \beta = \sin i \sin(\omega + f)$, and $\hat{\phi}$ is the ecliptic azimuthal unit vector. The rate of change of angular momentum $\dot{J}$ is related to the torque through

$$\dot{J} = \frac{\dot{\vec{J}} \cdot \vec{J}}{|\vec{J}|} = -\left|\dot{\vec{J}}\right| \sin i \cos(\omega + f). \tag{3.18}$$

The absolute change in angular momentum per orbit $|\Delta J|$, assuming $|\Delta J| \ll |J|$, is given by

$$|\Delta J| \;=\; \left| \int_0^\tau \dot{J} \, dt \right|, \tag{3.19a}$$

$$\;=\; \frac{3G\mathcal{Q}}{2} \left| \int_0^\tau \frac{\sin \beta \cos \beta \sin i \cos \nu}{r^3} \, dt \right|, \tag{3.19b}$$

$$\;=\; \frac{3k^2 G\mathcal{Q}}{2aJ(1 - e^2)} \left| \int_0^{2\pi} (1 + e \cos f) \sin \nu \cos \nu \sqrt{1 - k^2 \sin^2 \nu} \, d\nu \right|, \tag{3.19c}$$

$$\;=\; 0. \tag{3.19d}$$

where $\nu = \omega + f$ and $k = \sin^2 i$. The planetary quadrupoles produce no net change in the cometary perihelion distance, regardless of their relative orientation. The change in angular momentum is zero because the quadrupole potential, and hence the torque, goes like $r^{-3}$; this is not necessarily the case for potentials with arbitrary dependences on $r$.

### 3.1.5 The loss cylinder

A comet with a semimajor axis greater than 3000 AU that comes close enough to the Sun to become visible is likely to receive an energy kick $|\Delta E|$ comparable to its orbital energy $E$ (Equation 3.8). Such a relatively large kick results in the comet taking on either an unbound or a much more tightly bound orbit, depending on the sign of $\Delta E$. In either case, the comet is no longer a member of the Oort cloud.

The orbit of Saturn is a rough outer limit to the perihelion distance at which an Oort cloud comet typically receives $|\Delta E| \gtrsim |E|$. Thus the region of phase space where $a \gtrsim$ 3000 AU and $q \lesssim 10$ AU is called the **loss cylinder**, because it is swept clear of Oort cloud comets by the giant planets in roughly one comet orbit.

The loss cylinder gets its name from its geometry in a particular three-dimensional velocity space, one axis of which denotes the radial velocity $v_r$, and the others the tangential components $v_{t1}$ and $v_{t2}$, with $v_t = \sqrt{v_{t1}^2 + v_{t2}^2}$. Any fixed orbital angular momentum

$$J = r v_t \tag{3.20}$$

corresponds to a cylindrical surface in this space. As the angular momentum is related to perihelion distance $q$ through Equation 3.15, the loss cylinder can be defined equivalently by a fixed $q$ if $e \approx 1$. The boundary of the loss cylinder is denoted $J_*$ or by the associated perihelion distance $q_*$. A similar surface called the **visibility cylinder** represents the range of perihelia for which comets produce comae; its size will be taken to be 3 AU here.

The existence of the loss cylinder implies that visible comets which approach the planetary system on orbits with $a > 3000$ AU are probably making their first perihelion passage close to the Sun. Such comets are referred to as **dynamically new**. Dynamically new comets in the loss cylinder must have recently had their perihelia displaced inwards from greater distances by some mechanism.

The loss cylinder is emptied on a time scale comparable to the comets' orbital period ($\tau \lesssim 10^7$ yr for $a \lesssim 50\,000$ AU), and must be refilled if a steady-state distribution is to

be maintained. If the Oort cloud is the source of new comets, a mechanism must exist for reducing their perihelia and bringing them into the loss cylinder.

A change in perihelion distance implies a change in angular momentum. If some mechanism produces a change in orbital angular momentum per orbit $\Delta J$ which is much smaller than $J_*$, LP comets make their first perihelion passage inside the loss cylinder close to its boundary, and the loss cylinder is said to be **empty**. In this case, the comets do not become part of the observed sample. They are removed from the loss cylinder before their perihelia can evolve inward sufficiently for coma/tail development. Such comets are sometimes said to encounter the **Jupiter barrier**, because they are typically removed when their perihelia approach Jupiter's orbit.

Oort cloud comets may hurdle the Jupiter barrier and become visible if a mechanism exists to produce

$$\Delta q \gtrsim q_*, \tag{3.21}$$

which could push comets deep into, and possibly even through, the loss cylinder. Under these conditions, the cylinder is said to be **full**.

Due to the lack of net change in angular momentum the giant planets produce in comets with $q \gg r_p$ (Equation 3.19d), some other mechanism is required to draw in the Oort cloud comets which are observed. Though the major planets may produce larger changes in $J$ in comets with perihelia near their orbits, such encounters would strongly affect the comets energies as well. The narrow spike in the observed distribution of comet inverse semi-major axes (Figure 2.3) arges against the giant planets being the dominant injectors of Oort cloud comets.

### 3.1.6 Planet X

There is little evidence for a massive solar companion beyond Pluto, and dynamical considerations set an upper limit to its mass of roughly 30 Jupiter masses, and probably much less (Tremaine 1990; Hogg et al. 1991). Nevertheless, the presence of such a companion could strongly affect the evolution of long-period comets, which may be useful probes of the existence of such an object, and will be discussed further in § 5.4.2.

## 3.2 The Galactic tidal field

The Solar System resides within an extended mass distribution, namely the Galaxy. This distribution produces a tidal field in our vicinity, which is referred to as the Galactic tidal field or the **Galactic tide** (Morris and Muller 1986; Torbett 1986; Heisler and Tremaine 1986; Matese and Whitman 1989).

The effect of the Galactic tide is distinct from that of individual close stellar encounters. They constitute two different parts of the Galaxy's gravitational field: the overall "smooth" field, and the "clumpy" field due to the concentration of mass into stars. Heisler and Tremaine (1986) have shown that individual stellar encounters are the source of the variance of the changes in comet velocity, while the Galactic tide is the source of the mean change.

### 3.2.1 The Galactic reference frame

Consider a set of mutually perpendicular unit vectors $\{\hat{e}_{\tilde{x}}, \hat{e}_{\tilde{y}}, \hat{e}_{\tilde{z}}\}$ with their origin at the Sun and rotating with it about the Galactic centre. Let $\hat{e}_{\tilde{x}}$ be directed radially outward from the Galactic centre, let $\hat{e}_{\tilde{y}}$ be directed tangentially to the Galaxy, in the direction of its rotation, and let $\hat{e}_{\tilde{z}}$ be directed towards the North Galactic Pole. These vectors form the **Galactic reference frame** (see also Appendix A).

The acceleration term due to the Galactic tide in Equation 3.1 has the form (Heisler and Tremaine 1986)

$$\vec{F}_{tide} = (A - B)(3A + B)\tilde{x}\hat{e}_{\tilde{x}} - (A - B)^2\tilde{y}\hat{e}_{\tilde{y}} - [4\pi G\rho_0 - 2(B^2 - A^2)]\tilde{z}\hat{e}_{\tilde{z}}, \qquad (3.22)$$

where $\rho_0$ is the mass density in the solar neighbourhood; and $A$ and $B$ are the usual Oort constants. The numerical values of the Oort constants are $A = 14.4 \pm 1.2$ km s$^{-1}$ kpc$^{-1}$ and $B = -12.0 \pm 2.8$ km s$^{-1}$ kpc$^{-1}$ (Kerr and Lynden-Bell 1986). The local mass density is less well-known. Observable matter (stars and gas) contributes about 0.1 M$_\odot$ pc$^{-3}$, but the amount of dark matter present in the solar neighbourhood, if any, is controversial. Recent calculations based on dynamical arguments allow the total/observed mass ratio $P$ to be between 1 and 2 (Bahcall 1984; Kuijken and Gilmore 1989; Kuijken 1991). A recent determination by Bahcall et al. (1992) finds $P = 1.53$, and a constant value for $\rho_0$ of 0.15 M$_\odot$ pc$^{-3}$ will be adopted here. It should be noted that $\rho_0$ is probably not constant, but modulated somewhat by the Sun's excursions above and below the Galactic plane during its orbit around the Galaxy (Matese et al. 1995).

| Coordinate | Momentum |
|:---:|:---:|
| $f$ | $L = (GM_\odot a)^{1/2}$ |
| $\tilde{\omega}$ | $J = [GM_\odot a(1 - e^2)]^{1/2}$ |
| $\tilde{\Omega}$ | $J_{\tilde{z}} = J\cos\tilde{\imath}$ |

Table 3.2: A set $\mathcal{T}$ of canonical coordinate-momentum pairs, useful for the orbit-averaged Hamiltonian of a comet orbiting the Sun in the presence of the Galactic tide.

Given the above values of $A$, $B$ and $\rho_0$, the $4\pi G\rho_0$ term of Equation 3.22 exceeds the others by an order of magnitude. This dominant component of the tidal acceleration can be expressed as

$$\vec{F}_{tide} \approx -4\pi G\rho_0\,\tilde{z}\hat{e}_{\tilde{z}} = -4\pi G\rho_0\,r\sin b\,\hat{e}_{\tilde{z}}, \qquad (3.23)$$

where $b$ is the comet's Galactic latitude $\sin b = \sin\tilde{\imath}\,\sin(\tilde{\omega} + f)$. This dominant component is along the Galactic polar axis, and corresponds to a gravitational potential of the form

$$V_{tide} = 2\pi G\rho_0\tilde{z}^2. \qquad (3.24)$$

The Hamiltonian $H$ of a body orbiting the Sun under the influence of the Galactic tide provides a complete description of the body's motion. However, this description is more comprehensive than is required for some investigations. If the changes in the orbit due to the tidal perturbation are small, it is reasonable to average $H$ over a full orbit $\tau$ and consider the resulting simpler Hamiltonian $H_{av}$. The orbit-averaged Hamiltonian provides a useful description of the evolution of the comet's orbital elements under the tide, though at a loss of short time scale ($t \lesssim \tau$) information.

Following the example of Heisler and Tremaine (1986), the set $\mathcal{T}$ of canonical coordinate-momentum pairs listed in Table 3.2 will prove useful in the discussion of the orbit-averaged Hamiltonian. The symbols $\tilde{\imath}$, $\tilde{\Omega}$ and $\tilde{\omega}$ represent the inclination, longitude of the ascending node and argument of perihelion measured in the Galactic frame; $f$ is the true anomaly, which is independent of the reference frame. The momentum $J$ is the usual orbital angular momentum per unit mass of the comet, and $J_{\tilde{z}}$ is its component along the $\tilde{z}$-axis. $L$ is a measure of the two-body orbital energy through the semimajor axis $a$.

Expressed in these canonical variables, the orbit-averaged Hamiltonian $H_{av}$ has the form (Heisler and Tremaine  1986)

$$H_{av} = -\frac{(GM_\odot)^2}{2L^2} + \frac{\pi\rho_0}{GM_\odot^2}\frac{L^2}{J^2}(J^2 - J_{\tilde{z}}^2)\left[J^2 + 5(L^2 - J^2)\sin^2\tilde{\omega}\right], \qquad (3.25\text{a})$$

which can be expressed in terms of the standard orbital elements as

$$H_{av} = -\frac{GM_\odot}{2a} + \pi G\rho_0\, a^2 \sin^2\tilde{\imath}\,(1 - e^2 + 5e^2 \sin^2\tilde{\omega}). \tag{3.25b}$$

The canonical variables $f$ and $\tilde{\Omega}$ are absent from Equation 3.25a, so the corresponding momenta $L$ and $J_{\tilde{z}}$ are conserved. The conservation of $L$ implies that of $a$ as well, hence the semimajor axis and the orbital energy are conserved under $H_{av}$. However, $\tilde{\omega}$ does appear in Equation 3.25a, implying that the angular momentum $J$, and hence the perihelion distance $q$ are not constants of the motion.[†]

The comet's angular momentum oscillates with time, with the eccentricity reaching minimum and maximum values $e_\pm$. If $C = 1 - e^2 + 5e^2 \sin^2\tilde{\imath}\sin^2\tilde{\omega}$ is greater than 1, then

$$e_\pm = \sqrt{1 + \frac{1}{8}\left[C - 5(1 + K_{\tilde{z}}^2) \pm \sqrt{(5 + 5K_{\tilde{z}}^2 - C)^2 - 80K_{\tilde{z}}^2}\right]}, \tag{3.26}$$

where $K_{\tilde{z}} = (1 - e^2)^{1/2}|\cos\tilde{\imath}|$. If $C \leq 1$ then the limiting eccentricities are given by

$$e_- = \sqrt{1 - C}, \tag{3.27a}$$

$$e_+ = \sqrt{1 + \frac{1}{8}\left[C - 5(1 + K_{\tilde{z}}^2) + \sqrt{(5 + 5K_{\tilde{z}}^2 - C)^2 - 80K_{\tilde{z}}^2}\right]}. \tag{3.27b}$$

Equations 3.26 and 3.27a,b can be used in conjunction with the conservation of the semimajor axis to compute the minimum and maximum perihelion distances a comet will oscillate between under the tide's influence.

To determine whether or not the tide can fill the loss cylinder, consider the orbit-averaged rate of change of angular momentum $\dot{J}$, which can be obtained from $H_{av}$ through Hamilton's canonical equations

$$\dot{J} = -\frac{\partial H_{av}}{\partial\tilde{\omega}}, \tag{3.28a}$$

$$= -\frac{5\pi\rho_0}{GM_\odot^2}\frac{L^2}{J^2}(J^2 - J_{\tilde{z}}^2)(L^2 - J^2)\sin 2\tilde{\omega}, \tag{3.28b}$$

$$= -\frac{5\pi\rho_0}{GM_\odot^2}e^2 L^4 \sin^2\tilde{\imath}\sin 2\tilde{\omega}, \tag{3.28c}$$

from which it can be deduced that

$$|\dot{J}| \leq \frac{5\pi\rho_0}{GM_\odot^2}e^2 L^4. \tag{3.29}$$

---

[†]Though no notational distinction is made here, the orbit-averaged coordinates and momenta in $H_{av}$, i.e. $L$, $J$, $J_{\tilde{z}}$ and $\tilde{\omega}$, are not, in general, equal to their instantaneous values in the unaveraged system, except in the limit $\rho_0 \to 0$.

The change in angular momentum over a single orbit $|\Delta J| = |\int_0^\tau \dot{J} dt| \sim |\dot{J}\tau|$ is given by

$$|\Delta J| \sim \frac{5\pi\rho_0}{GM_\odot^2} e^2 L^4 \left(\frac{4\pi^2 a^3}{GM_\odot}\right)^{1/2} = \frac{10\pi^2\rho_0}{G^3 M_\odot^4} e^2 L^7. \qquad (3.30)$$

Equation 3.30 can be solved to determine the conditions under which the tide can fill the loss cylinder, *i.e.* produce $\Delta J \geq J_*$. These conditions are, assuming $e \approx 1$, that

$$a \quad \gtrsim \quad \left(\frac{\sqrt{2q_*}M_\odot}{10\pi^2\rho_0}\right)^{2/7}, \qquad (3.31a)$$

$$\gtrsim \quad 25\,000 \left(\frac{q_*}{10\ \text{AU}}\right)^{1/7} \left(\frac{\rho_0}{0.15\ \text{M}_\odot\ \text{pc}^{-3}}\right)^{-2/7} \quad \text{AU}. \qquad (3.31b)$$

The Galactic tide thus provides a mechanism by which Oort cloud comets may become observable, but only if the comets' semimajor axes exceed 25 000 AU.

## 3.3  Non-gravitational forces

The asymmetric sublimation of cometary volatiles results in a net acceleration of the nucleus. These **non-gravitational**[†] **(NG)** forces are limited to times of significant outgassing (*i.e.* coma production), and remain small even then. For example, as P/Halley passed perihelion in 1986, the nucleus was subjected to a radial NG acceleration only $10^{-5}$ times that of the Sun's gravity. The transverse and normal components were over 10 times weaker still (Rickman 1986). NG forces are small but not negligible: acting in the same direction over many perihelion passages, they may produce significant changes in a comet's orbit. In fact, the need for NG correction terms in comet orbit calculations has long been known. As early as 1823, Encke noted that some comets' orbits deviated from purely gravitational ones, which he attributed to a resisting medium through which the comets passed.

Non-gravitational forces are difficult to model. Their strength depends on the comet's distance from the Sun, but displays less regular variability as well: Gas production may vary by a factor of 2 or more between the pre- and post-perihelion legs of the orbit (Sekanina 1964; Festou 1986); and jets and streamers are observed to evolve on time scales of less than a day (Festou et al. 1993b), suggesting that NG forces change on similar time scales.

---

[†]Traditionally, the term "non-gravitational forces" has been reserved for the reaction forces resulting from the uneven sublimation of cometary volatiles, and it will be used here in that manner. It will be shown in § 3.7 that the other forces of a non-gravitational nature *e.g.* radiation pressure, are negligible in comparison to the outgassing forces.

Further complications arise from the rotation of the nucleus, which is difficult to measure through the coma, and which may be quite complicated due to precession (Wilhelm 1987). Our inability to measure or predict the effects of outgassing with confidence makes a precise treatment of these accelerations difficult.

A simple and naive model of NG accelerations, which is all the data allows, assumes that the short time scale components of the NG forces are uncorrelated and cancel out, leaving only fairly regular, longer time scale components as dynamically important. A simple and widely-used model called **Style II parameters** was devised by Marsden et al. (1973). The NG acceleration term $\vec{F}_{jet}$[†] in Equation 3.1 is written as

$$\vec{F}_{jet} = F_1 \hat{e}_1 + F_2 \hat{e}_2 + F_3 \hat{e}_3, \tag{3.32}$$

where the three orthogonal components are: radial $F_1$ (positive outward from the Sun), transverse $F_2$ (in the orbital plane, positive along the direction 90° ahead of the Sun-comet line), and normal $F_3$ (perpendicular to the orbital plane, parallel to $\hat{e}_1 \times \hat{e}_2$). The Style II model assumes that the accelerations are symmetric about perihelion, and can be represented by

$$F_1(r) = A_1 g(r), \qquad F_2(r) = A_2 g(r), \qquad F_3(r) = A_3 g(r), \tag{3.33}$$

where $\{A_1, A_2, A_3\}$ are independent constants, and $g(r)$ is a non-negative function describing the increase in activity with decreasing comet-Sun distance $r$. The form of $g(r)$ is based on an empirical water sublimation curve by Delsemme and Miller (1971),

$$g(r) = \alpha \left( \frac{r}{r_o} \right)^{-m} \left[ 1 + \left( \frac{r}{r_o} \right)^n \right]^{-k}, \tag{3.34}$$

where $m = 2.15$, $k = 4.6142$, $n = 5.093$, $r_o = 2.808$ AU and $\alpha$, the normalisation parameter, is chosen to be 0.1113 so that $g(1 \text{ AU}) = 1$. Note that $g(r)$ is roughly proportional to $r^{-m} \approx r^{-2}$ for $r \ll r_o$. At $r \gg r_o$, $g(r)$ drops much faster than the simple inverse square that describes the incident solar flux (Figure 3.1).

The constants $A_1, A_2$ and $A_3$ are calculated by Marsden et al. (1973) for each comet by a fitting process: the constants are assigned the values which minimise the difference between the observed and modelled positions of the comet. If the residuals calculated from a model including NG forces are significantly smaller than those predicted from a purely

---

[†]The symbol $\vec{F}$ is again used here to represent the acceleration and not the force, to maintain consistency with the literature.
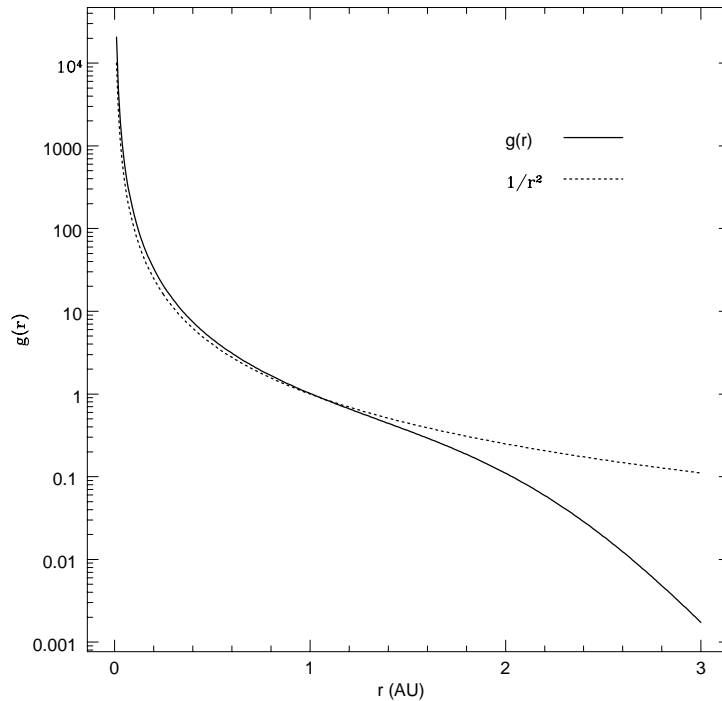
Figure 3.1: The Style II non-gravitational acceleration function $g(r)$, and a $1/r^2$ curve.

gravitational description of the comet's motion, then NG forces may play a significant role. Note that determinations of $\{A_1, A_2, A_3\}$ sometimes assume that their values are constant over one or more apparitions, despite the fact that some comets show changes in these values, in both sign and amplitude, from apparition to apparition (Marsden 1976). As the peak outgassing occurs on the sunward side of the cometary nucleus, the sign of $A_1$ is always positive. The signs of $A_2$ and $A_3$ are determined by the rotation of the nucleus and the non-symmetrical nature of the gas release, which cause the acceleration to deviate from the precisely sunward direction.

Despite the uncertainties involved, the calculated values of the NG constants give us an idea of the order of magnitude of the forces involved. The value of $A_1$ is typically $10^{-9}$ to $10^{-7}$ AU day$^{-2}$ ($\sim 10^{-3}$ to $10^{-1}$ m s$^{-1}$ day$^{-1}$) with error estimates variable, but in the 10-50% range (Marsden et al. 1973). Comets with shorter periods tend to have smaller values of $A_1$, which does suggest that their volatile supplies have been depleted by their more frequent passages near the Sun. The values of $|A_2|$ are typically only 10% of $|A_1|$, with similar errors. The tangential component is presumed to be due to the displacement of the

most active outgassing region away from the subsolar point due to rotation of the nucleus. If this is the case, a ratio of $A_1/A_2 \sim 10$ implies a lag angle of roughly $\sin^{-1} 0.1 \approx 6°$. The inclusion of a normal component in the models does not reduce the residuals significantly, and so $A_3$ is generally taken to be zero (Marsden et al. 1973; Marsden 1976).

The effect of the NG forces can be deduced from Gauss's planetary equations (described in Appendix A). Note that the absence of a normal component $F_3$ would mean that Equations A.19c and A.19d are identically zero, and that the comet's orbital plane is constant.

Gauss's equations allow us to estimate the impact of NG forces on cometary dynamics. Assuming the accelerations imparted are given by the Style II function $g(r)$ (Equation 3.34), Equations A.19a–f yield expected changes in inverse semimajor axis and perihelion of

$$\Delta(1/a) = -\frac{4q}{GM_{\odot}} A_2 \int_{-\pi}^{\pi} \frac{g(r)}{1 + e \cos f} \, df, \tag{3.35a}$$

$$\Delta q = \frac{4q^3}{GM_{\odot}} A_2 \int_{-\pi}^{\pi} g(r) \frac{(1 - 2\cos f)}{(1 + e \cos f)^3} \, df, \tag{3.35b}$$

where $e \approx 1$ has been assumed, and $df = J dt/r^2$ (which can be deduced from Kepler's second law) has been used. The median value of the semimajor axis in these simulations will be shown to be around 100 AU (§ 5.2). Taking a typical visible long-period comet to have $q = 1.5$ AU, and $a = 100$ AU (though the result is insensitive to the exact value of $a$ as long as $e \lesssim 1$), the integrands in Equations 3.35a and 3.35b can be numerically integrated, using the expression $r = a(1 - e^2)/(1 + e \cos f)$ to transform $g(r)$ to a function of the true anomaly. We find

$$\Delta(1/a) \approx -6.8 \times 10^{-6} \left( \frac{A_2}{10^{-9} \text{ AU day}^{-2}} \right) \text{ AU}^{-1}, \tag{3.36a}$$

$$\Delta q \approx -2.5 \times 10^{-6} \left( \frac{A_2}{10^{-9} \text{ AU day}^{-2}} \right) \text{ AU}, \tag{3.36b}$$

Typical values of $A_2$ are $10^{-9}$ AU day$^{-2}$ (Marsden et al. 1973) and thus, acting alone, NG forces could move a comet out of the visibility cylinder only on a time scale of hundreds of thousands of orbits. However, the energy change imparted is only about a factor of sixty less than that due to the planets (Equation 3.8), thus a comet could conceivably be moved from an orbit with a semimajor axis of 100 AU to an unbound one in a thousand orbits.

Equation 3.36a and 3.36b do not depend on $A_1$ because the radial NG forces' effect on the energy and perihelion distance averages to zero over a full orbit. However, the radial

acceleration may produce variations in the elements on shorter time scales *e.g.* from aphelion to perihelion. These short-term variations might be important if, say, the NG forces were strong enough to push comets into unbound orbits during the outbound leg of the orbit. The "typical" kick during the perihelion-aphelion leg is

$$\Delta(1/a) \approx -\frac{4q}{GM_\odot}A_1 \int_0^\pi \frac{g(r)\sin f}{(1+e\cos f)^2}df, \tag{3.37a}$$

$$\approx -9.6 \times 10^{-6}\left(\frac{A_1}{10^{-8} \text{ AU day}^{-2}}\right), \tag{3.37b}$$

which is too small to unbind orbits with semimajor axes less than 100 000 AU. Larger values of $A_1$ impart larger kicks, and an order of magnitude increase would provide an energy change of order that of the planets; thus radial non-gravitational forces may have some role to play in certain highly active comets.

When a comet's nodes cross the orbit of a planet, a close encounter becomes much more likely. The nodal distances $r_n$ are given by

$$r_n = \frac{a(1-e^2)}{1 \pm e\cos\omega} \tag{3.38}$$

where the plus in the denominator refers to the ascending node, the minus to the descending node. The rate of change of the nodal distances under NG forces is

$$\Delta r_n \approx \frac{2\Delta q}{1 \pm \cos\omega} \pm \frac{2q\sin\omega\Delta\omega}{(1 \pm \cos\omega)^2}, \tag{3.39}$$

where $e \approx 1$ has been used. Using Gauss's equations, the change in $\omega$ is found to be

$$\Delta\omega = -\frac{4q^2}{GM_\odot}A_1 \int_{-\pi}^\pi \frac{g(r)\cos f}{(1+e\cos f)^2}df, \tag{3.40}$$

and the change in $r_n$ per orbit can then be deduced to be

$$\Delta r_n \sim -\frac{5\times10^{-6}}{1 \pm \cos\omega}\left(\frac{A_2}{10^{-9} \text{ AU d}^{-2}}\right) \pm \frac{1.3\times10^{-4}\sin\omega}{(1+\cos\omega)^2}\left(\frac{A_1}{10^{-8} \text{ AU d}^{-2}}\right) \text{ AU}, \tag{3.41}$$

where again $a = 100$ AU and $q = 1.5$ AU have been used.

If $\Delta r_n/r_p \ll 1$, a close encounter is very likely if one of the nodes crosses a planet's orbit. The number of orbits $m$ required for a node to migrate near to a planet's orbit is of order $r_p/\Delta r_n$ or, for Jupiter's orbit and the values used above, $m \sim 10^6$ orbits. Thus, the motion of the nodes is too slow to appreciably shorten the lives of LP comets.

## 3.4   Passing stars

A long-period comet, passing aphelion far from the Sun, may have its orbit perturbed by stars travelling through the solar neighbourhood. The comet's velocity at aphelion is of order 100 m s$^{-1}$, much less than the velocity dispersion of stars in the Galactic disk, which is 30 km s$^{-1}$ (Mihalas and Binney 1981). Thus, to a first approximation, the comet can be considered stationary during a stellar encounter, and the **impulse approximation** used. The net impulse $\Delta\vec{v}$ due to a passing star of mass $M_\star$ and velocity $v_\star$ is the difference between the impulses imparted to the Sun $\Delta\vec{v}_\odot$ and the comet $\Delta\vec{v}_c$,

$$\Delta\vec{v} = \Delta\vec{v}_c - \Delta\vec{v}_\odot \approx \frac{2GM_\star}{v_\star D_c^2}\vec{D}_c - \frac{2GM_\star}{v_\star D_\odot^2}\vec{D}_\odot, \tag{3.42}$$

where $\vec{D}_c$ and $\vec{D}_\odot$ are the vectors directed to the point of closest approach from the comet and the Sun respectively. In the case of a star passing very close to the Sun, $D_\odot \ll D_c$, and Equation 3.42 can be approximated by

$$|\Delta v| \approx \frac{2GM_\star}{v_\star D_\odot}. \tag{3.43a}$$

If the encounter is a distant one, $\vec{D}_c$ and $\vec{D}_\odot$ are nearly parallel, and the impulse reduces to

$$|\Delta v| \approx \frac{2GM_\star r \cos\theta}{v_\star D_\odot^2}, \tag{3.43b}$$

where $\theta$ is the angle between $\vec{D}_\odot$ and the Sun-comet vector $\vec{r}$.

Consider the case of the Sun and its attendant comet cloud moving with velocity $v_\odot$ through a homogeneous and isotropic distribution of static stars of mass $M_\star$ and number density $n_\star$. The stars transfer kinetic energy to the comet cloud; the average rate of change in the square of a comet's velocity $\langle \dot{v}^2 \rangle$ is given by (*cf.* Bailey 1983, Equation 45)

$$\langle \dot{v}^2 \rangle \sim \frac{8\pi G^2 M_\star^2 n_\star}{v_\odot}\left[\ln\left(\frac{r^2}{d_{min}\, b_{min}}\right) - 2(1 - \ln 2)\right], \tag{3.44}$$

thus the change per orbit $\Delta v^2$ is

$$\langle \Delta v^2 \rangle \quad\sim\quad \tau\,\frac{8\pi G^2 M_\star^2 n_\star}{v_\odot}\left[\ln\left(\frac{r^2}{d_{min}\, b_{min}}\right) - 2(1 - \ln 2)\right], \tag{3.45a}$$

$$\sim\quad \frac{16\pi^2 G^{3/2} M_\star^2 n_\star a^{3/2}}{v_\odot M_\odot^{1/2}}\left[\ln\left(\frac{r^2}{d_{min}\, b_{min}}\right) - 0.614\right], \tag{3.45b}$$

$$\sim\quad \frac{8\pi^2 G^{3/2} M_\star^2 n_\star a^{3/2}}{v_\odot M_\odot^{1/2}}\left[\ln\left(\frac{\pi n_\star a^3 v_\odot^3 M_\odot t_{SS}}{2GM_\star^2}\right) - 1.23\right], \tag{3.45c}$$

where $b_{min} \approx (2\pi n_\star v_\odot t_{SS})^{-1/2}$ is the minimum impact parameter expected during the Solar System's lifetime $t_{SS}$, $d_{min} \approx 2M_\star(GM_\odot r)^{1/2}/M_\odot v_\odot$ is the distance within which a single encounter would result in the comet escaping from the Solar System, and $r^{3/2} \sim \langle r^{3/2} \rangle \sim a^{3/2}$ has been used.

### 3.4.1 Energy

The change in a comet's inverse semimajor axis $\Delta(1/a) \approx -\Delta v^2/GM_\odot$ caused by passing stars can be obtained from Equation 3.45c. Taking $v_\odot = 30$ km s$^{-1}$, the local stellar velocity dispersion, $n_\star = 0.15$ pc$^{-3}$ and $M_\star = 0.3$ M$_\odot$ (Bahcall and Soneira 1980), the change in $1/a$ is

$$\Delta\left(1/a\right) \sim 10^{-8} \left(\frac{n_\star}{0.15 \text{ pc}^{-3}}\right) \left(\frac{30 \text{ km s}^{-1}}{v_\odot}\right) \left(\frac{M_\star}{0.3 \text{ M}_\odot}\right)^2 \left(\frac{a}{25\ 000 \text{ AU}}\right)^{3/2} \text{AU}^{-1} \qquad (3.46)$$

per orbit, where the logarithmic term has been taken to be constant. This result is consistent with other derivations (*cf.* Fernández 1980; Fernández and Ip 1991), and from it one deduces that stellar perturbations have only a very small effect on comet orbital energies over a single orbit. Over time, however, the net transfer of energy to the cloud unbinds its members, and may significantly deplete its numbers over the age of the Solar System (Bailey 1986).

### 3.4.2 Angular momentum

The analytic determination of the change in cometary angular momentum due to passing stars is complex, and beyond the scope of this project. The subject was treated thoroughly by Heisler and Tremaine (1986). A result of interest is that the loss cylinder is only filled at semimajor axes

$$a \gtrsim 36\ 000 \text{ AU} \qquad (3.47)$$

(*l. c.* Equation 39), well outside the Galactic tide's value of $a \gtrsim 25\ 000$ AU (Equation 3.31b).

We will see that the number density of comets in the Oort cloud drops sharply with distance (§ 4.2.2), with the result that the tide dominates the overall flux into the loss cylinder. This result allows the injection of comets into the loss cylinder by passing stars to be neglected when constructing a theoretical model of LP comet evolution.

### 3.4.3  Comet showers

Every $10^8$ yr on average, a very close stellar encounter ($D_\odot \lesssim 10\,000$ AU) may cause a **comet shower**, enhancing the comet influx rate by up to a factor of twenty (Hills 1981; Heisler et al. 1987; Duncan et al. 1987). Because the loss cylinder is cleared on time scales of order $10^7$ yr, the odds are against a shower currently being in progress. Heisler (1990) estimates that the comet flux significantly exceeds its background rate only 2% of the time. The correlation of comet aphelion directions with the Galactic plane, along with the lack of strong clustering associated with any other points in the sky (Figure 2.10), also suggest that the present comet flux is at its quiescent level, though the possibility of a weak shower being in progress has been advanced (Heisler 1990). The possibility of comet showers will be ignored here.

## 3.5  Molecular clouds

A penetrating encounter between the Solar System and an interstellar molecular cloud with velocity $v_{cl}$ and impact parameter $D$ applies an impulse of

$$|\Delta v| \approx \frac{2rGM_{cl}}{v_{cl}D^2} \left[ 1 - \left(1 - \frac{D^2}{R_{cl}^2}\right)^{3/2} \right] |\cos\theta|, \tag{3.48}$$

to a comet, where $\theta$ is the angle between $\vec{r}$ and $\vec{D}$, and the cloud is assumed to be spherical and of uniform density with mass $M_{cl}$ and radius $R_{cl}$ (Biermann 1978; Fernández and Ip 1991). Assuming for simplicity that $D \sim R_{cl}$, $e \approx 1$, and that the comet is at aphelion during the encounter, the corresponding change in angular momentum $\Delta J$ is

$$\Delta J = r\Delta v \sin\theta \approx \frac{4GM_{cl}\,a^2 \sin 2\theta}{v_{cl}D^2}. \tag{3.49}$$

The semimajor axis above which the molecular cloud fills the loss cylinder is

$$a \gtrsim \left(\frac{q_* v_{cl}^2 M_\odot D^4}{8GM_{cl}^2 \sin^2 2\theta}\right)^{1/4} \tag{3.50}$$

$$\gtrsim 8000 \left(\frac{D}{20\text{ pc}}\right) \left(\frac{M_{cl}}{10^5\text{ M}_\odot}\right)^{-1/2} \left(\frac{v_{cl}}{10\text{ km s}^{-1}}\right)^{1/2} \left(\frac{q_*}{10\text{ AU}}\right)^{1/4}\text{ AU}. \tag{3.51}$$

Such encounters stir the Oort cloud to great depths and result in large increases in the cometary influx, but their frequency is unknown: giant molecular clouds ($M_{cl} \gtrsim 10^5$ M$_\odot$, $R_{cl} \sim 20$ pc) may be encountered as rarely as every $5 \times 10^8$ yr (Bailey 1983; Torbett 1986),

but smaller clouds ($M_{cl} \sim 10^3$ to $10^4$ $M_\odot$) could be 100 times more common (Drapatz and Zinnecker  1984). It will be assumed here that the current flux of comets is unaffected by a recent encounter with a molecular cloud, because of the rarity of such encounters and the Galactic tide's strong signature in the distribution of cometary aphelion directions (Figure 2.11b).

## 3.6   A massive circumsolar disk

If the Sun were to have a matter disk, a possibility suggested by the presence of disks around $\beta$ Pictoris and other stars, the dynamics of long-period comets would be affected. A disk potential can be approximated by a Miyamoto-Nagai potential, expressed mathematically as (*e.g.* Binney and Tremaine  1987),

$$V_{disk} = \frac{-GM_d}{\left[ x_{cm}^2 + y_{cm}^2 + \left( a_d + \sqrt{z^2 + b_d^2} \right)^2 \right]^{1/2}} \tag{3.52}$$

where $M_d$ is the disk mass, $r_{cm}^2 = x_{cm}^2 + y_{cm}^2 + z^2$ is the distance to the Solar System's barycentre[†], and $a_d$ and $b_d$ are parameters describing the disk's characteristic radius and thickness respectively. This disk will be taken here to be centred on the Solar System's barycentre, with the disk plane coinciding with the ecliptic.

The resulting acceleration $\vec{F} = -\nabla V$ is

$$\vec{F}_{disk} = \frac{-GM_d}{\left[ x_{cm}^2 + y_{cm}^2 + \left( a_d + \sqrt{z^2 + b_d^2} \right)^2 \right]^{3/2}} \left( \vec{r}_{cm} + \frac{a_d \vec{z}}{\sqrt{z^2 + b_d^2}} \right). \tag{3.53}$$

The disk potential is conservative and axisymmetric, and thus conserves the $z$ component of the angular momentum.

The disk around $\beta$ Pic is observed in the infrared out to a least 1100 AU (Smith and Terrile  1987). It is seen nearly edge-on, allowing its axis ratio $a_d/b_d$ to be estimated at five a few hundred AU from the central star (Smith and Terrile  1984; Paresce and Burrows 1987). The mass of the $\beta$ Pic disk is poorly known: estimates of H column density based on observations of CO predict values between $10^{14}$ $r_{disk}^2$ kg and $10^{20}$ $r_{disk}^2$ kg, where $r_{disk}$ is the gas' distance from the central star in AU. For values of $r_{disk}$ of 500 AU, this yields values of $10^{-8}$ to $10^{-2}$ Jupiter masses. Early estimates of the mass in dust yield results of $10^{-5}$ to one Jupiter mass (Smith and Terrile  1984).

---

[†]As the planets have been assumed to be coplanar and in the ecliptic, $z_{cm} = z$.

There is little or no evidence for a substantial disk in our own Solar System. A study of planetary residuals limits the mass in a 100 to 1000 AU disk to less than a few Jupiter masses. A study of P/Halley sets much more stringent limits, around $10^{-2}$ Jupiter masses, though the inclusion of non-gravitational corrections could be masking the effects of a disk (Tremaine 1990; Hogg et al. 1991).

Observational evidence also puts relatively strong limits on the mass of such a disk. Imaging with the Hubble Space Telescope puts a preliminary limit of less than $10^{-3}$ Jupiter masses in 5–10 km sized objects within 40 AU of the Sun (Cochran et al. 1995). Models of the infrared emission expected from dust generated by collisions in a belt of comets distributed over 30–100 AU from the Sun puts a similar limit (Backman et al. 1995). A more distant (500–1000 AU) belt could have an upper mass of roughly one Jupiter mass (Backman 1995).

Thus, it is unlikely that a significant amount of mass resides in an unseen disk within 100 AU of the Sun, but that at larger distances ($\sim$ 1000 AU) much larger masses ($\sim M_{Jup}$) could be present.

## 3.7 Miscellaneous perturbations

### 3.7.1 Radiation pressure and the solar wind

The acceleration $F$ imparted to the nucleus by the solar wind or radiation pressure is given by

$$F = \eta \pi R_c^2 \mathcal{F}_p / M_c, \tag{3.54}$$

where $M_c$ and $R_c$ are the comet's mass and radius, $\mathcal{F}_p$ is the momentum flux to which the comet is subjected, and $\eta$ is a coefficient describing the efficiency of the momentum transfer. For a radiation field, $\mathcal{F}_p$ is related to the energy flux $\mathcal{F}_E$ through $\mathcal{F}_p = \mathcal{F}_E/c$. For the solar wind, whose parameters are given in § 1.4, the momentum flux is $n_{sw} m_{sw} v_{sw}^2$.

These accelerations are small, and since they are always directed radially outward, the perturbations arising during the inward and outward legs tend to cancel. However, the acceleration during the outbound leg could potentially serve to eject comets. Using Gauss's equations for the $e \approx 1$ case (Equation A.21a), one finds the perturbation incurred during

the outbound leg to be

$$\Delta(1/a) = -\frac{1}{a^2} \int_0^{\tau/2} \dot{a}\, dt, \tag{3.55a}$$

$$= -\frac{2\eta\pi r_\oplus^2 R_c^2 \mathcal{F}_p(r_\oplus)}{GM_\odot M_c q}, \tag{3.55b}$$

where $r_\oplus$ is the radius of the Earth's orbit. The numerical values of these perturbations, for a small nucleus ($R_c = 1$ km, $M_c = 10^{12}$ kg) with perihelion $q = 1.5$ AU, are

$$\Delta(1/a)_{rp} \sim -3 \times 10^{-9} \left(\frac{q}{1.5\ \text{AU}}\right)^{-1} \left(\frac{R_c}{1\ \text{km}}\right)^2 \left(\frac{M_c}{10^{12}\ \text{kg}}\right)^{-1} \text{AU}^{-1}, \tag{3.56a}$$

$$\Delta(1/a)_{sw} \sim -10^{-13} \left(\frac{q}{1.5\ \text{AU}}\right)^{-1} \left(\frac{R_c}{1\ \text{km}}\right)^2 \left(\frac{M_c}{10^{12}\ \text{kg}}\right)^{-1} \text{AU}^{-1}. \tag{3.56b}$$

where the solar constant $\mathcal{F}_E(r_\oplus)$ is taken to be 1400 W m$^{-2}$, and inelastic collisions ($\eta = 1$) are assumed.

During times of close approach to the Sun, the effective solar wind cross-section of the nucleus is increased by the draping of solar magnetic field lines over the coma. However, the nucleus itself has no substantial magnetic field; any back reaction can only be transmitted back to the nucleus through the coma's gases. Thus, instead of the solar wind impacting the nucleus directly, a pressure gradient is set up across the coma. This pressure will be of order the solar wind pressure, and thus will not result in perturbations significantly larger than those calculated above.

The single-leg solar wind and radiation pressure perturbation are small, and unlike outgassing accelerations, the contributions on the inward and outward bound legs tend to cancel. These perturbations will thus be assumed to be negligible.

Under a radial acceleration, there is no change in a comet's angular momentum, a fact which is implicit in the calculation of Equations 3.56a and 3.56b. But the flow direction of the solar wind is not precisely radial, and the resulting transverse component of the acceleration does not have opposite signs on the inward and outward legs. However, the angle $\theta$ by which the solar wind deviates from radial is less than 1° (Foukal 1990). The resulting one-orbit perturbations are, for the orbital energy,

$$|\Delta(1/a)_{sw}| = \left| \frac{1}{a^2} \int_0^{\tau} \dot{a}\, dt \right|, \tag{3.57a}$$

$$\approx \quad \frac{2\pi^2 \eta r_\oplus^2 R_c^2 \mathcal{F}_p(r_\oplus)|\sin\theta|}{GM_\odot M_c q}, \tag{3.57b}$$

$$|\Delta(1/a)_{sw}| \quad \sim \quad 5 \times 10^{-14} \left(\frac{q}{1.5 \text{ AU}}\right)^{-1} \left(\frac{R_c}{1 \text{ km}}\right)^2 \left(\frac{M_c}{10^{12} \text{ kg}}\right)^{-1} \left(\frac{|\sin\theta|}{0.017}\right) \text{AU}^{-1} \tag{3.57c}$$

and for the perihelion distance,

$$|\Delta q_{sw}| \quad = \quad \left| \int_0^\tau [\dot{a}(1-e) - a\dot{e}] \, dt \right|, \tag{3.58a}$$

$$\approx \quad \frac{\pi \eta q r_\oplus^2 R_c^2 \mathcal{F}_p(r_\oplus)}{GM_\odot M_c} \left| \sin\theta \int_{-\pi}^{\pi} \frac{1 - 2\cos f - e\cos^2 f}{1 + e\cos f} \, df \right|, \tag{3.58b}$$

$$|\Delta q_{sw}| \quad \sim \quad 3 \times 10^{-13} \left(\frac{q}{1.5 \text{ AU}}\right) \left(\frac{R_c}{1 \text{ km}}\right)^2 \left(\frac{M_c}{10^{12} \text{ kg}}\right)^{-1} \left(\frac{|\sin\theta|}{0.017}\right) \text{ AU}. \tag{3.58c}$$

These perturbations are also small compared to those resulting from outgassing. Thus, the solar wind and radiation pressure have negligible effects on cometary orbital dynamics.

### 3.7.2  Drag

The solar wind, unlike solar radiation, does not reach distances arbitrarily far from the Sun, but is halted by the pressure of the interstellar medium at the **heliopause**. This boundary lies between 75 and 105 AU from the Sun in the direction of the solar apex, and further in other directions (Hall et al.  1993). When outside this boundary, comets are subjected to drag from the interstellar medium (ISM). Long-period comets spend most of their orbital periods outside the heliopause, and for the purposes of computing the drag from the ISM on comet nuclei, it will be assumed they spend all their time there.

The drag acceleration exerted on the nucleus is

$$F_{drag} = \frac{\pi R_c^2 C_D n_{ism} m_{ism} v^2}{2 M_c} \tag{3.59}$$

where $n_{ism}$ and $m_{ism}$ are the number density and mass of the interstellar medium particles, and $C_D$ is the drag coefficient of the nucleus, of order unity for spheres in high Reynolds number *i.e.* low viscosity, fluids (Streeter and Wylie  1985). The local interstellar medium has $n_{ism} \sim 0.2$ cm$^{-3}$ and $m_{ism} \sim 10^{-28}$ kg (Baranov  1986).

The drag force is always opposite to the comet's direction of motion, and thus the use of Gauss's equations becomes quite complicated. Nonetheless, the effect of drag on Keplerian

orbit is well-understood (*e.g.* Roy 1978), and the resulting change in $1/a$ per orbit is

$$\Delta(1/a) \quad = \quad \frac{\pi R_c^2 C_D n_{ism} m_{ism}}{M_c} \int_{-\pi}^{\pi} \frac{(1 + e \cos u)^{3/2}}{(1 - e \cos u)^{1/2}} \, du, \tag{3.60a}$$

$$\sim \quad 4 \times 10^{-16} \left( \frac{R_c}{1 \text{ km}} \right)^2 \left( \frac{M_c}{10^{12} \text{ kg}} \right)^{-1} \left( \frac{n_{ism}}{0.2 \text{ cm}^{-3}} \right) \text{ AU}^{-1}, \tag{3.60b}$$

where $u$ is the eccentric anomaly, and $e = 0.99997$ has been assumed *e.g.* $a = 50\ 000$ AU and $q = 1.5$ AU. This result is independent of the semimajor axis, but small in any case. The change in perihelion distance for this same comet is

$$\Delta q \quad \approx \quad -\frac{\pi R_c^2 C_D n_{ism} m_{ism} a q}{M_c} \int_{-\pi}^{\pi} (1 + \cos u) \left( \frac{1 + e \cos u}{1 - e \cos u} \right)^{1/2} \, du, \tag{3.61a}$$

$$\sim \quad -2 \times 10^{-11} \left( \frac{R_c}{1 \text{ km}} \right)^2 \left( \frac{M_c}{10^{12} \text{ kg}} \right)^{-1} \left( \frac{n_{ism}}{0.2 \text{ cm}^{-3}} \right) \text{ AU}. \tag{3.61b}$$

Both the change in energy and angular momentum due to drag by the ISM are negligible, and will be ignored.

## 3.8 Comet lifetimes

Continued loss of volatiles ultimately transforms comet nuclei into inert bodies, containing only the leftover refractory elements of their initial inventories. Given a perihelion distance of 1 AU, a typical comet's volatiles might be depleted after a thousand orbits (Weissman 1980).

There is evidence that spent comets may either remain a single solid body, or break into a collection of fragments:

- Some regular meteor showers have been associated with the orbits of comets *e.g.* the $\eta$-Aquarids and Orionids with P/Halley.

- A few asteroids have elliptical orbits strongly resembling those of Jupiter-family comets *e.g.* 1992 XA which has a perihelion distance of 1.8 AU and an aphelion distance of 5.1 AU (Kresák 1977; Marsden and Williams 1994).

Whether or not a dead comet breaks up probably depends on various factors, including its internal cohesiveness and the patterns of thermal/gravitational stress to which it is subject.

Comets may also be destroyed or become unbound from the Sun before their volatiles are exhausted. Approximately 50% of comets entering the planetary system on near-parabolic orbits will be transferred to hyperbolic orbits by perturbations from the giant planets (especially Jupiter) after their first perihelion passage; a further fraction will be lost on each subsequent perihelion passage, as the comets diffuse through the available energy space (Gambler's Ruin, § 3.1.2).

The nucleus may also break into one or more large pieces before complete loss of volatiles occurs. After such a **splitting event**, a comet is often not observed at its next expected return. A comet stands a roughly 10% chance of being disrupted on its first close perihelion passage; the probability drops to less than 1% per perihelion passage for short-period comets (Weissman  1980; Kresák  1985).

A splitting probability $p \approx 0.1$ per revolution yields a half-life $m_{1/2}$ against splitting of

$$m_{1/2} = -\ln 2 / \ln(1 - p) \approx 7. \tag{3.62}$$

Thus, splitting may significantly reduce a comet's lifetime.

Comets may be destroyed by collision with the Sun or a planet, but this is unlikely. If the collision probability is simply taken to be the ratio of the planet's cross-section to the area of a sphere of the same radius as its orbit, then the probability of a comet passing within the Roche limit of the Sun or a planet is only of order $10^{-7}$ per perihelion passage (Weissman  1980).

## 3.9   The Oort cloud

The existence of the Oort cloud is now generally accepted (see Lyttleton 1974 for a dissenting viewpoint) based primarily on the observed distribution of $1/a$ (Figure 2.3), but the mechanism of its formation, as well as its present characteristics, remain the subject of debate.

The Oort cloud may either be primordial *i.e.* formed from the solar nebula, or have been captured or produced by the Solar System at a later time. In the latter case, the Oort cloud may have a survival time short compared with the age of the Solar System. However, the production of cometary bodies within the Solar System after the dissipation of the solar nebula almost certainly can be ruled out for lack of a viable mechanism, though the origin of comets from the breakup of a planet in the present-day asteroid belt has been postulated

(van Flandern 1978). It has also been postulated that a non-primordial Oort cloud could be captured from a passing molecular cloud (Clube and Napier 1984; Yabushita and Hasegawa 1978), but it remains unclear whether comet nuclei exist in such clouds. In addition, the Solar System has a very low capture cross-section for interstellar comets, owing to the high encounter velocities involved.

If the Oort cloud is primordial, its formation through *in situ* accretion seems unlikely: the condensation of cometary bodies from the solar nebula at Oort cloud distances is difficult to explain due to the low density of matter expected there (Öpik 1973), though radiation pressure (Hills 1982) or wind-powered shells (Bailey 1987) have been proposed as mechanisms by which the required density enhancements could be produced. The most widely accepted model of the origin of the Oort cloud holds that comet nuclei are planetesimals that accreted in or near the planetary region ($r < 50$ AU) at the same time as the planets. The growing planets, especially Uranus and Neptune, would have scattered some planetesimals from their initial near-circular orbits onto highly elliptical ones (Safronov 1972; Tremaine 1993). Those proto-comets finding themselves on orbits with large semimajor axes ($a \gtrsim 3000$ AU) could have their perihelia rapidly increased by the Galactic tide. The removal of their perihelia from the planetary system effectively decouples the planetesimals from the planets, and at this point the comets are said to have reached the Oort cloud.

As cometary isotope abundances are consistent with solar values (Krankowsky et al. 1986; Eberhardt et al. 1986), the current understanding of the Solar System and its formation is consistent with a primordial origin for the Oort cloud (Fernández 1985 offers a more complete review of the primordial vs. captured question). The question of the origin of the Oort cloud is only of secondary interest here except insofar as it affects the steady-state nature of the Oort cloud; on the basis of the cloud's likely primordial origin, it will be assumed that the Oort cloud is in a quasi-steady state *i.e.* the cloud's dynamical evolution time scale is comparable to the age of the Solar System.

The present distribution of comets in the Oort cloud cannot be observed directly, but Duncan et al. (1987) have derived a theoretical distribution based on the assumption that these comets formed in the outer planetary region and were scattered out into the Oort cloud through the combined perturbations of the tide and planets. They found the cloud's inner edge to be near 3000 AU, with a space number density of comets roughly proportional to

$r^{-3.5}$ from 3000 to 50 000 AU. This power law is consistent with Bailey's (1986) analytical treatment of the Oort cloud (*l.c.* Equation 103). Hills (1980) first pointed out that the cloud might extend further inwards than indicated by the minimum semi-major axis in the spike; thus the inner region ($a < 2 \times 10^4$ AU) is often referred to as the **Hills' cloud**.

Though the orbits of the comets would have initially been near the ecliptic, the inclinations of orbits with semimajor axes greater than about 2000 AU are randomised by passing stars on a time scale of $10^9$ yr. This mixing results in the Oort cloud comets occupying a spherical rather than a flattened distribution.

External influences strip comets with large orbits from the Solar System, thus truncating the Oort cloud at some distance from the Sun. The last closed **Hill's surface** provides a useful measure of the maximum possible size of the Oort cloud. Antonov and Latyshev (1972) calculated the Hill's or **zero-velocity surface** for a comet moving in the field of the Sun and the Galaxy. On such a surface, the Jacobi integral $\tilde{W}$ (§ 4.4.3) is constant. Expressed in the Galactic frame, $\tilde{W}$ is

$$\tilde{W} = 2A(A - B)\tilde{x}^2 + (B^2 - A^2 - 2\pi G\rho_0)\tilde{z}^2 + \frac{GM_\odot}{r}, \tag{3.63}$$

where $A$ and $B$ are the Oort constants. A particle having zero velocity relative to the Sun inside a closed Hill's surface cannot leave the enclosed volume, in the absence of other perturbations. The last closed surface is at $\tilde{W} = \frac{3}{2}(GM_\odot)^{2/3}[4A(A - B)]^{1/3}$. Substituting this value into Equation 3.63 and solving yields semiaxes for the Hill's surface

$$\tilde{x} \approx 1.41 \text{ pc} \approx 290\,000 \text{ AU}, \tag{3.64a}$$

$$\tilde{y} \approx 0.94 \text{ pc} \approx 190\,000 \text{ AU}, \tag{3.64b}$$

$$\tilde{z} \approx 0.63 \text{ pc} \approx 130\,000 \text{ AU}. \tag{3.64c}$$

The last closed Hill's surface is triaxial and resembles a prolate ellipsoid. In this work, the outer boundary of the Oort cloud is taken to be simply spherical, and at an aphelion distance of 100 000 AU ($a = 50\,000$ AU for comets with $e \approx 1$) rather than 130 000 AU. The prolate nature of the cloud and the exact location of the boundary is unlikely to be relevant here, due to the rapid drop off in comet number density with $r$.

The steep $r^{-3.5}$ radial density profile deduced by Duncan et al. (1987) provides an answer to the question of why the aphelion directions of Oort cloud comets are crowded at mid-Galactic latitudes. The ability of the tide to fill the loss cylinder at smaller distances

than passing stars (*cf.* Equation 3.31b to 3.47) allows it to reach into regions of higher comet density, and makes the tide the dominant injector of Oort cloud comets. Heisler and Tremaine (1986) have shown that the flux due to the tide exceeds that due to passing stars by a factor of 1.5 to 2. The tide's maximum injection efficiency is at mid-Galactic latitudes, a signature which can be seen in Figure 2.11b.

In the absence of a recent close encounter with a star or a molecular cloud, the loss cylinder is filled only at distances beyond 25 000 AU, yet the inner edge of the Oort cloud may be as close to the planetary system as 3000 AU. Comets in this inner region never become visible even if their perihelia are evolving inwards under the tide, because they hit the Jupiter barrier. These comets may, however, provide a source from which the outer Oort cloud is replenished. Encounters with stars and molecular clouds may scatter some of the comets in this inner Oort cloud into more loosely bound orbits, "pumping" them up into the outer Oort cloud, and may also give rise to occasional rare comet showers.

The population of the Oort cloud is expected to be eroded over time scales comparable to the age of the Solar System, as comets are ejected into interstellar space or captured into smaller orbits. Between 40% (Duncan et al. 1987) and 80% (Weissman 1985) of the original Oort cloud may have been lost over the lifetime of the Solar System, leaving $10^{12}$ comets totalling $10M_\oplus$ in the present-day comet cloud (Weissman 1991). These numbers are poorly known, and estimates of the current Oort cloud population range from $10^{11}$ (Öpik 1973) to $10^{15}$ (Marsden 1977) objects.

## 3.10   Problems in long-period comet dynamics

### 3.10.1   The fading problem

The energy kick received by a visible comet ($4 \times 10^{-4}$ AU$^{-1}$, Equation 3.8) is larger than the width of the main spike in the $1/a$ distribution of long-period comets (Figure 2.3). From this, it has been concluded that the spike consists of dynamically new comets, and that older comets, diffusing in energy space over many perihelion passages, populate the tail.

The spike will be taken here to be the region where the original inverse semimajor axis of the comets is less than $10^{-4}$ AU$^{-1}$. This value is chosen because of the width of the spike in the observed distribution (Figure 2.3b). All remaining LP comets are considered to be part of the tail.

Define $\Psi_1$ to be the ratio of the number of long-period comets in the spike to the total number,

$$\Psi_1 = \frac{N(a > 10\ 000\ \text{AU})}{N}. \tag{3.65}$$

Then $1/\Psi_1$ is an estimate of a comet's life expectancy in perihelion passages. A more precise measure of comet life expectancy is $1/\Upsilon_1$, where $\Upsilon_1$ is the ratio of dynamically new to the total number of LP comets,

$$\Upsilon_1 = \frac{N(m = 1)}{N}, \tag{3.66}$$

where $m$ is the number of apparitions a comet has made. Theory and observations can be compared through these quantities: let the prime $'$ symbol denote the relevant quantity derived from observations $e.g.$ $\Psi_1'$ is the ratio of the number in the spike to the total number for the observed sample, and let $\Xi_1 = \Psi_1/\Psi_1'$. If $\Xi_1 = 1$, then observations and theory match on this point.

The value of $\Psi_1'$ computed from the observed sample is $81/246 = 0.33 \pm 0.04$, where comets with perihelion beyond 3 AU have been excluded, and the quoted error is based on Poissonian ($\sqrt{n}$) noise. Note that the definition of the spike includes the seventeen comets with original $1/a < 0$ in Figure 2.3, on the assumption that they are coming from the Oort cloud, rather than interstellar space. The outright exclusion of the comets on hyperbolic original orbits yields a value of $\Psi_1' = 64/229 = 0.28 \pm 0.04$.

The observations provide a value of $\Psi_1' \approx 0.33$; the Gambler's Ruin problem predicts $\Psi_1 \sim 1/\bar{m} \sim 1/80 = 0.0125$ (Equation 3.11); that is $\Xi_1 \approx 0.038$. Thus, the Gambler's Ruin implies that only 1 in 25 of the perihelion passages expected to be made by older LP comets are observed. Why this large discrepancy?

Observations and theory have proved difficult to reconcile on this point. Though more sophisticated analytical treatments than the Gambler's Ruin narrow the gap significantly, the problem persists ($e.g.$ Kendall 1961). Experimental results show the same discrepancy: for example, Everhart (1979) found $\Xi_1 \sim 0.2$, using a straightforward Monte Carlo simulation that included Jupiter, Saturn and passing stars.

The gap between theory and observation is known as the **fading problem**, since it can be resolved if dynamically new comets fade drastically in brightness after their first perihelion passage near the Sun. This fading makes them less likely to be observed at subsequent perihelion passages, thus reducing their apparent lifetimes $1/\Psi_1$, and thus increasing $\Xi_1$.

Weissman (1980), using a Monte Carlo scheme similar to Everhart's (1979), was able to increase $\Xi_1$ to unity, but not without adding such a fading law.

The standard explanation proposed for such fading goes along the following lines: comets in the Oort cloud may never have approached the Sun to within more than a few tens of astronomical units since their condensation from the solar nebula, and thus may contain particularly volatile ices (*e.g.* CO, $CO_2$) that cannot survive the comet's first perihelion passage close to the Sun. These volatiles create a large bright coma for the new comet, but are substantially or completely depleted in the process. When the comet subsequently returns (assuming it has avoided ejection and the other loss mechanisms), it will be much fainter and may escape detection. The decrease in brightness is required to be largest over the comet's first few perihelion passages, levelling off as the most volatile components of the comet's inventory are lost. Thus, the fading problem may "simply" be caused by selection effects.

However, a comet's failure to reappear at its next perihelion passage could be the result of other, possibly unsuspected, loss mechanisms. Any phenomena which results in a decrease in the life span of LP comets would tend to increase $\Xi_1$. The reduction in brightness of the comet due to a depletion of readily vapourised volatiles will be referred to as **standard fading**. Determining whether or not standard fading is required to solve the fading problem, or if some other dynamical mechanism is involved is a central goal of this research. Some key points pertaining to the fading problem are listed below.

**Pre- and post-perihelion brightnesses** The evidence against the fading hypothesis includes the lack of observed large decreases in brightness as LP comets pass perihelion, decreases which might be expected if their volatile inventory is being exhausted (Festou 1986). Though no collection of Oort cloud comet light curves seems available in the literature, those few published show brightness variations typically no larger than those of dynamically older comets (Whipple 1978; Roettger et al. 1990).

**Short-period comet fading** The reduction in brightness of comets over many perihelion passages remains controversial, even for SP comets. Sekanina (1969) claims P/Encke has faded by 0.03 magnitudes per orbit over the last century, but Kresák (1974, 1977) has argued that this is an artifact of instrumental and selection effects, and that random variations in a comet's brightness dominate any secular trend. In either

case, the brightnesses of SP comets have not been observed to change drastically and permanently over a few orbits, except for occasional splittings.

**Splitting** The physical break-up of the nucleus may provide a comet sink, but a half-life of $m_{1/2} \approx 1/\Psi_1 \sim 2$ or a splitting probability $p \sim 0.3$ would be required to produce the required tail-spike ratio (see Equation 3.62). Such a high rate of splitting would not allow comets to survive long enough to diffuse in $1/a$ up to the large values seen in the tail of Figure 2.3. However, dynamically young comets have higher splitting rates than older ones. Weissman (1980) showed that, over the period 1846 to 1980, long-period comets had a 0.045 chance per perihelion passage of splitting, the short-period comets only 0.008. In addition, the probability was higher for new comets (0.1) than older LP comets (0.02).

The cause of splitting is not well understood: though some are caused by passages near the giant planets, many are not associated with such encounters. Studies of cometary **outbursts**, during which the comet may brighten by up to a factor of 100 for of order a week, show that impacts by "interplanetary boulders" and chemical and/or phase changes in the nucleus are not capable of fully explaining the distribution of events (Hughes 1975). The splitting events appear not or only weakly correlated with the ecliptic plane, asteroid belt and cometary perihelion points (Pittich 1971) but rather are randomly distributed. Splitting events are, however, more likely to occur post-perihelion by a factor of 2 or so, though better observational coverage at this time may be a factor (Smoluchowski 1986).

**Cratering rates** If comets do fade drastically rather than being ejected or otherwise destroyed, then their cores may still be present in the Solar System, but be too faint to be observed. These **dead comets** should, however, contribute to the cratering rate. Shoemaker (1983) compared the cratering rate determined from number counts of impact basins on the Earth's surface to that expected from the observed flux of potential impactors, and found them to be consistent within a factor of two. Both rates are difficult to compute and are based on the extrapolation of relatively poorly determined data, but there is no evidence from cratering rate studies for an additional source of Earth-impacting objects.

### 3.10.2   The ratio of prograde to retrograde comets

In the Gambler's Ruin problem, the lifetime $\bar{m}$ is proportional to the initial distance to the short-period barrier $\eta_{sp}$ (see Equation 3.11). A more careful determination of the energy kicks imparted by the planets reveals that retrograde comets receive smaller $\Delta(1/a)$ on average, and hence should have lifetimes three times longer on average.

If the lifetime of retrograde comets is three times that of prograde comets, the observations should reflect this fact through a ratio of retrograde to prograde of three to one in the absence of other important comet loss mechanisms. But the observations, plotted in Figure 2.7, show no such bias. Why is this the case?

### 3.10.3   The clustering of aphelion directions

A number of researchers (Tyror 1957; Oja 1975; Lüst 1984), have reported that the aphelion directions of LP comets are clustered in specific directions on the sky. However, due to the presence of strong selection effects the results are not compelling. There is a clear concentration towards mid-Galactic latitudes (Figure 2.11b), an effect which is expected since the Galactic tide is most efficient when the Sun-comet line is at 45° to the plane of the Galaxy.

However, even comets with semimajor axes greater than 36 000 AU show concentrations at mid-Galactic latitudes (Fernández and Ip 1991), shown in Figure 3.2. At these distances, stellar perturbations should also be able to fill the loss cylinder (Equation 3.47), so the distribution of aphelion directions should be isotropic. The $\chi^2$ test indicates only a $10^{-7}$ chance of the Galactic latitudes being drawn from a spherically symmetric distribution. However, the sample size is small, and thus the concentration at mid-latitudes may be a result of sampling noise.

### 3.10.4   The source of short-period comets

Some LP comets may survive long enough to diffuse into short-period orbits. The inclinations of Halley-type orbits are, at first glance, consistent with a spherically symmetric source (see Figure 2.1): is this source the Oort cloud?

The Jupiter family of comets have inclinations which are clearly not uniformly distributed, but rather concentrated in the ecliptic. Though Everhart (1972) showed that
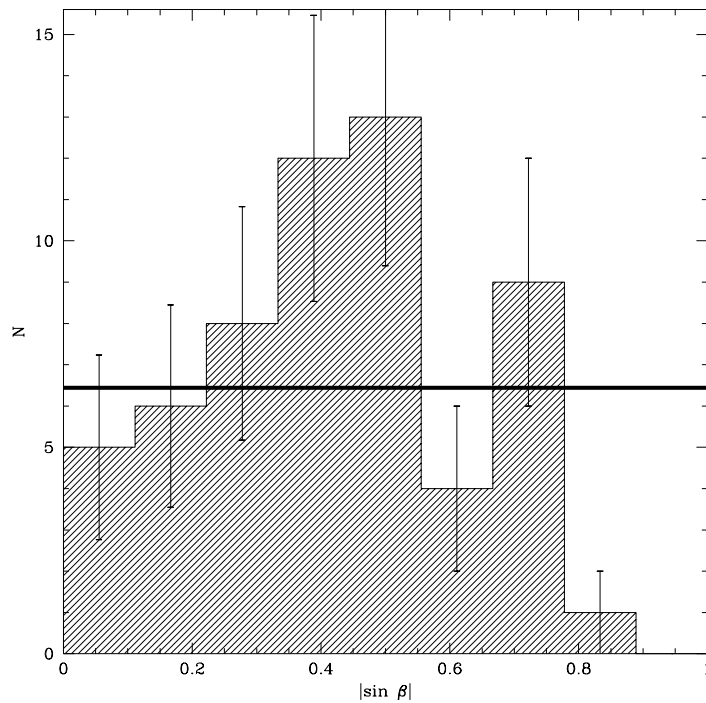
Figure 3.2: The distribution of Galactic latitudes of the aphelion directions of the 58 long-period comets in Marsden and Williams (1993) with original semimajor axes greater than 36 000 AU. The heavy line indicates the distribution expected for a spherically symmetric distribution of aphelion directions.

Jupiter is most efficient at capturing the lowest inclination comets from a spherical source, the capture rate is still too low by a factor of $10^3$ to account for the number of Jupiter-family comets seen today (Joss 1973). The orbital elements of the Jupiter-family comets are most consistent with capture from a low-inclination belt of material at 30 to 50 AU (Whipple 1972; Fernández and Ip 1983; Quinn et al. 1990). Kuiper proposed in 1951 that material might remain in this region as leftovers from the formation of the planets, so this ring is commonly known as the **Kuiper belt**. Though the existence of the Kuiper belt has been confirmed observationally *e.g.* Jewitt and Luu (1995), some fraction of the SP comets are almost certainly dynamically very old Oort cloud comets. Is the Oort cloud's contribution to the population of short-period comets important?

### 3.10.5   Hyperbolic comets

Some comets appear to be approaching the Solar System on weakly hyperbolic orbits (Figure 2.3) and treatments of non-gravitational forces are unable to fully explain this phenomena. Are there perhaps unexplored dynamical mechanisms which might explain such orbits?

## 3.11   The present state of the field

Most research on comet dynamics to date has been limited to analytical approximations and Monte Carlo simulations, which may not capture all the dynamically important physics.

Analytical investigations of cometary behaviour can be performed through perturbational and averaging techniques. These methods treat a simple two-body problem with an additional, necessarily weak, perturbation. For example, the effects of the Galactic tide (Heisler and Tremaine 1986; Torbett 1986; Matese and Whitman 1989) and of a single planet (Quinn et al. 1990) on a comet's evolution have been examined over restricted regions of phase space. These methods usually examine only a single facet of comet evolution, and break down if the interactions are too strong.

Monte Carlo methods allow long time scale investigations to be made relatively cheaply, by evolving comets within a phase space with fewer dimensions than the full problem. The simulation advances in fixed discrete time steps: at each one, the comets are redistributed throughout the phase space based on pre-computed **transition probabilities** determined by averaging over the omitted dimensions. However, Monte Carlo methods require significant simplifications of the problem and may prove too coarse-grained to reveal all the dynamics of interest (see Froeschlé and Rickman 1988 for a review).

Weissman (1978; 1979; 1980) has completed the most extensive Monte Carlo investigation of long-period comets dynamics to date. His model included the planets, nongravitational forces, the effects of passing stars, fading and splitting. However, his simulations had some restrictions: they did not include the tide, the initial semimajor axis was always 25 000 AU, the effects of the planets were represented by a Gaussian distribution of energy kicks and comets were run for only 1000 returns.

His model can produce $\Xi_1 \sim 0.66$ to 1, with reasonable agreement between the inclination and intrinsic perihelion distributions. His models include *ad hoc* assumptions *e.g.*

some fraction of indestructible comets, increased fading for comets with small perihelia, and a fixed disruption probability for new and old comets, but none that contradict cometary physics as now understood.

Weissman had to add very strong fading (28% of his sample of comets fade) to his simulations in order to match observations. Because his Monte Carlo simulations were fairly coarse-grained and there is little or no other evidence for strong fading, the possibility that the "fading" required is simply an unmodelled facet of the dynamics remains strong.

The most direct approach to the study of cometary dynamics is the numerical integration of the comets' equations of motion, including all significant perturbations. Until recently, computational restrictions have placed severe limitations on the sophistication and time scale of possible investigations. For example, Dvorak and Kribbel (1990) numerically integrated the trajectories of five Halley-type comets in the presence of the Sun, Jupiter and Saturn for $10^6$ years ($\sim$ 10 000 orbits). Manara and Valsecchi (1991) used similar methods to follow 100 short-period comets for 1000 revolutions in low inclination orbits in the outer Solar System.

As technological development has eased computational restrictions, direct integrations of cometary dynamics have increased in complexity and length. Levison and Duncan (1994) numerically integrated the known SP comets under the influence of all the planets except Mercury and Pluto for $10^7$ years. However, the research presented here represents the most sophisticated direct integration of the long-period comets yet published.

# Chapter 4

# Algorithm

The purpose of this research is to examine the dynamical processes important in the evolution of long-period comets, and to investigate the discrepancies between the observed distribution of orbital elements and simple theoretical models. To accomplish this, a model has been created to simulate the important dynamical effects influencing a long-period comet's trajectory as it travels from the Oort cloud to its destruction or departure from the Solar System.

The model is embodied by a computer code called LOCI which has the following basic framework:

- Each comet is represented by a massless test particle. The test particles are followed independently, one at a time; thus interactions between comets are neglected. Each comet is started in the Oort cloud, and its evolution is followed analytically until it approaches the Sun close enough for planetary perturbations to become important. The comet is subsequently followed by numerically integrating its equations of motion, expressed in regularised coordinates (§ 4.1.2), until lost from the Solar System.

- The model Solar System in which the test particles evolve consists of the Sun, and four planets representing Jupiter, Saturn, Uranus and Neptune. Their physical characteristics are listed in Table 4.1. The terrestrial planets and Pluto are omitted for the following reasons:

    1. The orbit-averaged quadrupole moments of their orbits $\mathcal{Q} \propto M_p R_p^2$, are each at least two orders of magnitude less than that of any giant planet (Equation 3.16

| Name | $M_\odot/M_p$ | $r_p$ ( AU) | $R_p$ (km) |
|---|---|---|---|
| Jupiter | 1047.355 | 5.202803 | 71492 |
| Saturn | 3498.5 | 9.53884 | 60268 |
| Uranus | 22869 | 19.1819 | 25559 |
| Neptune | 19314 | 30.0578 | 25269 |

Table 4.1: The values of the reciprocal masses ($M_\odot/M_p$), orbital ($r_p$) and physical ($R_p$) radii used for the giant planets (Newhall et al.  1983; Lindal  1992; U.S. Naval Observatory 1992).

and column 5 of Table 3.1), and thus the smallest planets' influence on cometary perihelia is negligible compared to that of the giant planets.

2. The energy perturbations imparted by the smallest planets are unimportant: if the comet's perihelion distance is within the planets' orbit, $\Delta(1/a) \propto M_p/R_p$ (Equation 3.5b) and the perturbation is dominated by Jupiter and Saturn (column 4 of Table 3.1).

- The planets' orbits are modelled as circular and coplanar.  There is no reason to expect that the small eccentricities and inclinations of the planets play significant roles in long-period comet dynamics. Mutual planetary perturbations are ignored. It should be noted that the planets are represented consistently throughout the numerical integration. No further approximations (*e.g.*  putting the planets' mass into the Sun when the comets are far outside the planetary system) are made.

- The model includes the dominant component of the Galactic tidal field, as described by Equation 3.23. The Solar System's orbit about the Galactic centre is taken to be circular, and in the Galactic plane. Deviations from this idealised orbit are ignored, though they may result in some temporal variation in the tidally-induced cometary flux, if there is a large amount of dark matter with small ($\lesssim$ 50 pc) scale height in our Galaxy (Matese et al.  1995). The Galactic centre and poles are oriented so as to match their current positions relative to the ecliptic.

- The model does not account for encounters with passing stars. In the absence of close stellar encounters, the transfer of comets from the Oort cloud to the loss cylinder is dominated by the Galactic tide, because the tide fills the loss cylinder at smaller semimajor axis than passing stars (page 50). The omission of stellar encounters has the

considerable benefit of yielding a deterministic model, in which the comet's evolution is completely determined by the system's initial conditions.

- The model includes the effects of non-gravitational forces of arbitrary magnitude and direction. These parameters can be varied to observe their effects on the simulation output.

- The model also contains provisions for investigating hypothetical phenomena, such as a circumsolar disk or a solar companion.

### 4.0.1 Comparison with observations

The sample of known comets includes objects of varied and unknown dynamical ages, observed to varying degrees of completeness over a relatively indefinite period. This is in sharp contrast to the data available from simulations, where dynamical ages are known and selection effects are non-existent. Thus, a basis for comparing the two sets must first be constructed.

Let $\mathcal{O}$ be the set of comets for which Marsden and Williams (1993) calculated original orbital elements, and which have perihelion distances less than 3 AU. It will be assumed that the distributions of orbital elements of $\mathcal{O}$ are free of selection effects, except in the perihelion distance $q$. With this exception, $\mathcal{O}$ is representative of a complete sample of long-period comets passing within 3 AU of the Sun over some fixed, though unknown, interval of time. This assertion assumes that the flux of LP comets has not varied significantly in rate or functional form over the observation interval ($\lesssim 200$ yr), and is based on the fact that no LP comet has a period short enough to have made more than one appearance in the observed sample.

Consider the expected flux of LP comets into the loss cylinder. This flux can be derived (§ 4.2.2), and constitutes the probability distribution from which the simulations' initial conditions are chosen. Any sample of such initial conditions represents the LP comets injected into the entrance surface over some fixed period of time. Let $\mathcal{S}$ be the sample of *all* apparitions *i.e.* visible perihelion passages, performed by the comets represented by such a set of initial conditions. Then comparisons between the model and observations can be made by *directly* contrasting $\mathcal{S}$ and $\mathcal{O}$.

That $\mathcal{O}$ and $\mathcal{S}$ are directly comparable is due to our choice of the *flux* into the entrance

surface as the initial conditions for the simulations, as well as the steady-state distribution of LP comets. In the Solar System there are comets of all ages, but given a steady-state, one comet "dies" *e.g.* is ejected, destroyed, *etc.*, for every one that arrives from the Oort cloud. This continuous distribution of ages is reproduced by the simulations by following individual objects throughout their entire lifetimes. As the life-long evolution of the ensemble of simulated comets is statistically equivalent to a snap-shot of the steady-state distribution, $\mathcal{S}$ and $\mathcal{O}$ are directly comparable with each other.

## 4.1 Numerics

### 4.1.1 The integration algorithm

LOCI's primary integration algorithm is the **Bulirsch-Stoer** method. The implementation used is *bsstep()* from Press et al. (1986). The routine *bsstep()* has automatic step-size control, achieved by monitoring the local truncation error *i.e.* the error due to the omission of higher order terms by the integrator. A fourth-order Runge-Kutta-Fehlberg algorithm, a Runge-Kutta variant designed for efficient step-size control (Burden and Faires 1989), was used for testing the Bulirsch-Stoer routine.

### 4.1.2 Regularisation

Integrating the equations of motion of a comet on a highly elliptical orbit is difficult in Cartesian coordinates, due to the very small step sizes required to maintain accuracy near perihelion. The **Kustaanheimo–Stiefel** or **K–S**[†] transformation replaces the six Cartesian coordinates of position $\vec{r} = \{x, y, z\}$ and velocity $\vec{v} = \{\dot{x}, \dot{y}, \dot{z}\}$, with ten regularised coordinates. It also replaces the independent variable, the physical time $t$, with the **fictitious time** $s$, where $dt = r\,ds$. The advantage of the regularised coordinates is that the unperturbed (two-body) equations of motion become those of a harmonic oscillator: thus the acceleration does not blow up as $r$ goes to zero, and the ensuing small step-sizes and numerical difficulties are avoided. Regularised coordinates are used in all the simulations discussed here.

---

[†]The distinction between the Kustaanheimo-Stiefel transformation and the Kolmogorov-Smirnov test, though usually clear from the context, will be made by using the abbreviations K–S and KS respectively.

Eight of the regularised coordinates represent the particle's phase space position $\vec{u} = \{u_1, u_2, u_3, u_4\}$ and velocity $\vec{u}' = \{u_1', u_2', u_3', u_4'\}^\dagger$. The ninth regularised coordinate is the negative of the orbital energy $h$ of the particle, given by

$$h = \frac{GM_\odot}{r} - \frac{1}{2}|\vec{v}|^2 - V = \frac{GM_\odot - 2|\vec{u}'|^2}{|\vec{u}|^2} - V, \tag{4.1}$$

where $V$ represents any potentials besides the Sun's. The tenth coordinate is the physical time $t$. Both $h$ and $t$ are dependent variables and must be integrated along the particle's trajectory in the same manner as the eight position and velocity coordinates.

The regularised position and velocity are obtained from the Cartesian coordinates by means of the K–S transformation (see Stiefel and Scheifele 1971 for a fuller exposition of the K–S formalism). Because the regularised space has two more dimensions than Cartesian space, the K–S transformation is not one-to-one; each position in physical space corresponds to a one-dimensional manifold in K–S space, as do the velocities.

A requirement of K–S regularisation is that the frame origin must coincide with the primary force centre. This fact dictates the reference frame in which the comet integration can best be performed.

**Reference frames**

The equations of motion differ depending on the reference frame in which they are expressed. Two frames prove useful:

1. The **barycentric** frame is an inertial frame. However, the barycentre does not coincide with the primary force centre, the Sun. Regularisation requires the force centre and frame origin to coincide if its superiority in handling highly eccentric orbits near perihelion is to be effective.

2. The **heliocentric** frame is non-rotating and centred on the Sun. Its advantage is that the origin and central force coincide, thus allowing regularisation's benefits to be fully exploited during cometary passages close to the Sun. Its primary disadvantage is that it is a non-inertial frame: it suffers accelerations as the Sun orbits the Solar System's barycentre, and thus the indirect terms (Equation 3.4) are not identically zero. These terms do not go to zero as $r$ becomes large, and result in extremely small

---

$\dagger$The prime symbol $'$ here represents a derivative with respect to $s$, *i.e.* $u_1' = du_1/ds$, *etc.*

step-sizes at large distances.  To understand why, consider a comet far outside the planetary system, whose period $\tau$ is large compared to those of the planets.  On time scales much less than $\tau$, the comet is effectively travelling in a straight line relative to the Solar System's barycentre.  But the Sun continues its orbit around the centre of mass, a complicated motion which is reflected in the heliocentric frame by the comet taking on a tortuous looping trajectory, like a telephone cord.  This complicated path results in very small step sizes in the integration algorithm, with corresponding slow progress and numerical difficulties.

The two frames complement each other: the benefits of both can be obtained by performing the integration in the heliocentric frame near perihelion, and switching to the barycentric frame at large radii.  Regularised coordinates are used in both frames; regularisation provides little benefit and some increase in complexity over Cartesian coordinates in the barycentric frame, but its use eliminates the need for duplicate Cartesian and regularised coordinate subroutines.  The switch between the two frames is accomplished by the model at a constant distance from the Sun, normally taken to be at 10 AU.

### 4.1.3   Error tolerances

The error in a single integration step is dictated by a set $\mathcal{E}$ of ten error limits

$$\mathcal{E} = \{\mathcal{E}_{u_1}, \ldots, \mathcal{E}_{u_4}, \mathcal{E}_{u'_1}, \ldots, \mathcal{E}_{u'_4}, \mathcal{E}_h, \mathcal{E}_t\}, \tag{4.2}$$

one for each of the regularised coordinates.  The Bulirsch-Stoer routine compares its own estimate of the local truncation error against $\mathcal{E}$ in order to adjust the step-size, and to keep the single-step error below those limits.

The value of the error limits is controlled by means of a single parameter $\zeta$ called the **tolerance**, which is translated into an error limit through a process described in Appendix B. The tolerance is typically chosen to be $10^{-9}$ for reasons described in § 4.4, with an upper limit set by the machine precision of roughly $10^{-14}$.

### 4.1.4   Random numbers

A sequence of random numbers is required to initialise the simulations.  In this research, approximately $10^6$ random numbers are required, ten for each simulated comet.  Six are

required for the six initial orbital elements, and four for the initial phases of the planets. The model uses *ran2()* from Press et al. (1992), modified for use with double precision (64-bit) numbers, to produce the required values. This routine uses Bays-Durham shuffling to avoid serial correlations and has a period of over $10^{18}$ calls.

### 4.1.5 Chaos

The motion of Halley's comet has been shown to be chaotic (Chirikov and Vecheslavov 1986), as has that of comets on near-parabolic orbits with perihelia near the giant planets (Petrosky 1986; Sagdeev and Zaslavsky 1987). It is likely that the motions of most comets in these simulations will be chaotic as well. Thus, the numerically integrated trajectory provided by LOCI is expected to diverge exponentially from the true one as a result of truncation and roundoff errors (*e.g.* Miller 1964).

This problem is inherent in all N-body simulations: arbitrary precision mathematical routines are becoming available, but remain much too slow. However, it is reasonable to suppose that the simulated results still provide an accurate reflection of reality. The errors introduced by finite precision arithmetic (roughly 1 in $10^{15}$ per step) are likely similar in order of magnitude to those introduced into the real Solar System by such weak and neglected effects as the non-uniform distribution of matter in the solar neighbourhood. Thus, one may hope that, statistically, the simulations continue to reflect reality.

### 4.1.6 Time requirements

The question of where most of the CPU time is likely to be spent can be addressed as follows: The probability of a comet being ejected from a simple Sun-planet system on the $m^{th}$ orbit is given by a power law (Equation 3.13). If the probability of a comet reaching an end-state remains a power law under the addition of the tide and the other relevant physics, and this power law has the form

$$p(m) \propto m^\gamma, \tag{4.3}$$

where $\gamma$ is some constant, then the expectation value $\overline{m}$ of $m$ is just

$$\overline{m} = \sum_{m=1}^{\infty} m \cdot p(m) \propto \sum_{m=1}^{\infty} m^{\gamma+1}. \tag{4.4}$$

Equation 4.4 diverges if $\gamma \geq -2$. A Sun-planet system has $\gamma = -3/2$ (Equation 3.13), and though the extra physics in the model is expected to increase the rate at which comets evolve

and hence lower $\gamma$, it seems likely that $\bar{m}$ will ultimately prove to diverge, *i.e.* that most of the time will be spent following a few very long-lived comets. This problem is handled by putting "on hold" any comets which prove to have very long lifetimes, and re-examining them at a later date. However, such cases are relatively rare, and only a few dozen of the hundreds of thousands of comets simulated here are not eventually integrated throughout their full lifetimes.

### 4.1.7   Planetary encounters

Close encounters between comets and planets, including collisions, are of interest for determining both current and past cratering rates. These simulations track such events. A close encounter with a planet is defined here to be a passage through a planet's **sphere of influence** $R_I$. The sphere of influence is defined to be surface around a planet at which the perturbation of the planet on the two-body heliocentric orbit is equal to that of the Sun on the two-body planetocentric orbit. If the planet's mass is much less that that of the Sun, this surface is roughly spherical and is given by

$$R_I = \left( \frac{M_p}{M_\odot} \right)^{2/5} r_p, \tag{4.5}$$

where $r_p$ is the planet's orbital radius. The Sun has no sphere of influence in this sense, so a close encounter with the Sun is instead defined to be passage within 10 solar radii.

Each crossing from outside the sphere of influence to within is counted as one encounter: the simulation does not check for multiple close approaches while the comet is within the sphere of influence. However, it will be seen that **captures**, defined here to be a close encounter with a planet during which the eccentricity relative to the planet at closest approach is less than unity, are extremely rare events.

## 4.2   Initial conditions

In the absence of recent ($t \lesssim 10^7$ yr) stellar encounters, the injection of new long-period comets from the Oort cloud is dominated by the Galactic tide. Equation 3.28c reveals that a comet's perihelion decreases under the tide's influence when $\sin 2\tilde{\omega} > 0$, that is when

$$0 < \tilde{\omega} < \pi/2 \qquad \text{or} \qquad \pi < \tilde{\omega} < 3\pi/2. \tag{4.6}$$

Comets with $\tilde{\omega}$ outside this region have increasing perihelia, and therefore are not of immediate interest.

LOCI randomly selects the comets' initial conditions from the flux of comets with decreasing perihelia. The flux is measured at a phase space boundary called the **entrance surface**.

## 4.2.1  The entrance surface

The entrance surface defines the angular momentum at which LOCI begins the simulation of a comet. Taking the entrance surface $J_E$ to be a cylinder *i.e.* a fixed perihelion distance, proves too restrictive for our purposes, and thus $J_E$ is permitted to be a function of comet's initial orbital elements.

There are two main criteria for the selection of an appropriate entrance surface. Firstly, the corresponding perihelion distance $q_E$ should be far enough outside the planetary system that the orbit-averaged approximation for the tide is valid for $q \geq q_E$. Secondly, $q_E$ should be close enough to the planetary system that CPU cycles are not wasted by numerically integrating the comets' trajectories in the regions where they can be handled well analytically.

To calculate $J_E$, consider the change in angular momentum per orbit $\Delta J$, given by Equation 3.30. If $J_E$ is taken to be a constant $\mathcal{Z}$ times $\Delta J$, then the orbit-averaged approximation is correct outside $J_E$, as long as $\mathcal{Z} \gtrsim 1$. A value of 3 for $\mathcal{Z}$ will be used here. The expression for $J_E$ thus becomes, through Equation 3.30

$$J_E(L) = \mathcal{Z}\frac{10\pi^2\rho_0}{G^3 M_\odot^4}e^2 L^7,  \tag{4.7}$$

or, in terms of the entrance perihelion distance $q_E$,

$$q_E(a)  =  a\left[1 - \left(1 - \mathcal{Z}^2\frac{100\pi^4\rho_0^2 e^4 a^6}{M_\odot^2}\right)^{1/2}\right],  \tag{4.8a}$$

$$\approx  \mathcal{Z}^2\frac{50\pi^4\rho_0^2}{M_\odot^2}a^7  \qquad \text{where } e \approx 1.  \tag{4.8b}$$

There are three restrictions on this expression:

1. The initial perihelion distance $q_E$, must be sufficiently far outside the planetary system that the typical energy perturbation per orbit is small. Equation 4.8b has no minimum
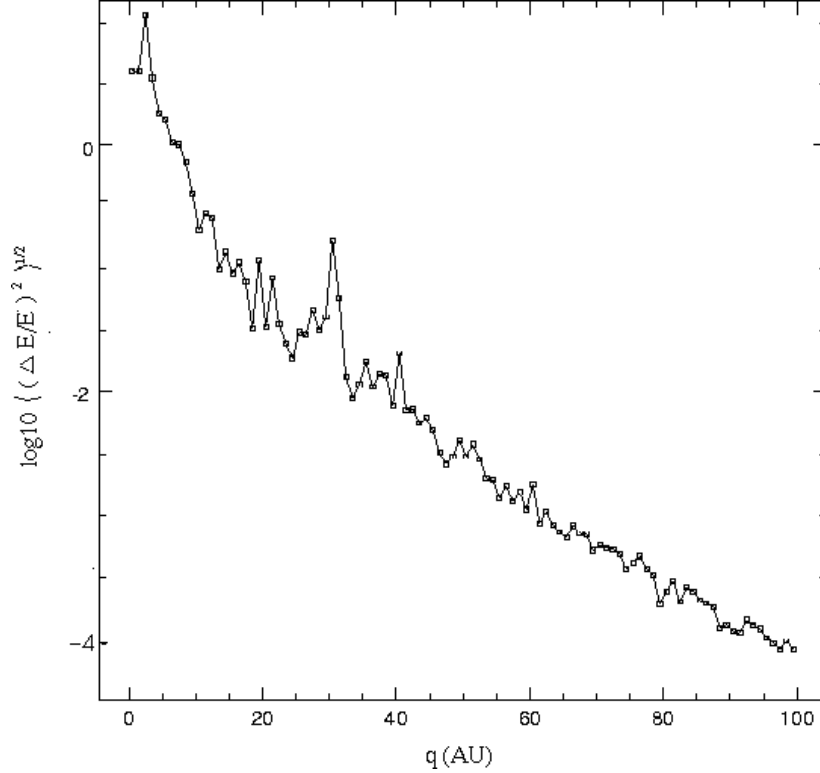
Figure 4.1: The base 10 logarithm of the fractional root-mean-square change in energy, $\langle(\Delta E/E)^2\rangle^{1/2}$, per perihelion passage caused by the four giant planets, as a function of perihelion distance $q$.

perihelion distance, so a lower limit $q_{E_-}$ on the perihelion distance must be imposed. The exponential decrease of $\Delta E$ with $r$ (see Equation 3.14) suggests that $q_{E_-}$ need not be much greater than the size of the planetary system. The value of $q_{E_-}$ was chosen so that the root-mean-square of the fractional change in energy $\langle(\Delta E/E)^2\rangle^{1/2}$ after one orbit (aphelion to aphelion) in a model Solar System containing only the Sun and the four giant planets, would be less than 0.1% for typical Oort cloud comets. Figure 4.1 shows the distribution of $\Delta(1/a)$ in such a system as a function of $q$: all orbits have an initial semimajor axis of 25 000 AU, and the values of $\cos i$, $\omega$ and $\Omega$ were selected from uniform probability distributions. The energy change drops below 0.1% per orbit at about 60 AU; this distance is taken to be $q_{E_-}$.

The semimajor axis $a_=$ where Equation 4.8b is equal to $q_{E_-}$ is easily shown to be

$$a_= \quad \approx \quad \left(\frac{M_\odot^2 \, q_{E_-}}{50\pi^4 \mathcal{Z}^2 \rho_0^2}\right)^{1/7}, \tag{4.9a}$$

$$\approx \ 24\ 000 \left(\frac{\mathcal{Z}}{3}\right)^{-2/7} \left(\frac{q_{E-}}{60\ \text{AU}}\right)^{1/7} \left(\frac{\rho_0}{0.15\ \text{M}_\odot\ \text{pc}^{-3}}\right)^{-2/7} \ \text{AU}. \qquad (4.9\text{b})$$

2. It is clear from Table 3.2 that $J$ is always less than $L$, which reflects the requirement $q \leq a$. Equations 4.7 and 4.8a, b violate this condition at large $L$, as the analytical treatment of the tide breaks down where $\Delta J \sim J$. The condition $J_E \leq L$ is violated where

$$a \ > \ \left(\frac{M_\odot}{10\pi^2 \mathcal{Z} \rho_0}\right)^{1/3}, \qquad (4.10\text{a})$$

$$\gtrsim \ 58\ 000 \left(\frac{\mathcal{Z}}{3}\right)^{-1/3} \left(\frac{\rho_0}{0.15\ \text{M}_\odot\ \text{pc}^{-3}}\right)^{-1/3} \ \text{AU}. \qquad (4.10\text{b})$$

This is outside but near the Oort cloud outer boundary chosen here, and which is given by the maximum initial semimajor axis $a_+ = 50\ 000$ AU. Equation 4.10a provides a restriction on our choice of $\mathcal{Z}$, confining it to values of $\mathcal{Z} \lesssim 4.75$ for our chosen value of $a_+$.

As the entrance surface expands towards larger semimajor axes, $q_E \rightarrow a$, and the fraction of comets which evolve entirely within the entrance surface becomes important. In fact, at $q_E = a$, all comets are already inside (or just on) the entrance surface. The assumed uniform distribution in angular momentum assumed implies that at any given semimajor axis, the fraction $\vartheta$ of comets already inside the entrance cylinder and which can cross the Jupiter barrier is $J_E/L$ or, from Equation 4.7

$$\vartheta = \mathcal{Z} \frac{10\pi^2 \rho_0}{G^3 M_\odot^4} L^6 \approx 0.6 \left(\frac{\mathcal{Z}}{3}\right) \left(\frac{a}{50\ 000\ \text{AU}}\right)^3 \left(\frac{\rho_0}{0.15\ \text{M}_\odot\ \text{pc}^{-3}}\right). \qquad (4.11)$$

Thus a substantial fraction of comets at the outer edge of the Oort cloud are missed, but this fraction decreases rapidly with decreasing $L$. Integrating the phase-space density (described later in § 4.2.2) of comets both inside and outside the entrance surface shows that, for the afore-mentioned values, approximately 90% of comets reside outside the entrance surface. Thus only a small fraction of comets are missed through our choice of the entrance surface.

In a similar vein, the approximation $e \approx 1$ becomes invalid as $q_E \rightarrow a$. Equation 4.8a yields a value for $q_E$ at the outer Oort cloud edge of approximately 10 000 AU,

implying $e \approx 0.8$. Thus, the large eccentricity approximation remains accurate in this limit under $\mathcal{Z} = 3$.

3. Equations 3.26 and 3.27a,b reveal that not all cometary perihelia are eventually drawn into the planetary system by the tide. Many comets reach a minimum perihelion distance far outside the planetary system, and thus do not become subject to significant planetary perturbations. In the absence of stellar perturbations, such comets remain in the Oort cloud, and never become visible. To avoid wasting CPU cycles on such comets, the trajectories of comets whose initial conditions would result in a tidally-induced minimum $q$ greater than 40 AU are not numerically integrated, but terminated immediately. From numerical experiment it is found that approximately five of every six comets entering our entrance surface have perihelia which will not cross the $q = 40$ AU boundary; thus the exclusion of such orbits nets a significant savings in processor time.

The entrance surface as detailed above can be summarised as

$$
q_E = \begin{cases} q_{E-} & \text{where } a_- \leq a \leq a_= \\ \mathcal{Z}^2 \dfrac{50\pi^4 \rho_0^2}{M_\odot^2} a^7 & \text{where } a_= \leq a \leq a_+ \end{cases}
\tag{4.12}
$$

subject to the condition $\mathcal{Z} \leq \mathcal{Z}_+$ where

$$
\mathcal{Z}_+ = \frac{M_\odot}{10\pi^2 \rho_0 a_+^3},
\tag{4.13}
$$

and where $a_+$ and $a_-$ are the outer and inner limits of the Oort cloud respectively. Plugging in the previously discussed numerical values, Equation 4.12 becomes

$$
q_E \approx \begin{cases} 60 \text{ AU} & \text{where } 10\,000 \text{ AU} \leq a \leq 24\,000 \text{ AU} \\ 60 \left( \dfrac{a}{24\,000 \text{ AU}} \right)^7 \text{ AU} & \text{where } 24\,000 \text{ AU} \leq a \leq 50\,000 \text{ AU} \end{cases}
\tag{4.14}
$$

noting that our choices of $\mathcal{Z} = 3$ and $a_+ = 50\,000$ AU satisfy $\mathcal{Z} \leq \mathcal{Z}_+$ (Equation 4.13).

## 4.2.2 The flux of comets into the entrance surface

Let the phase space density of comets, expressed in the canonical system $\mathcal{T}$ of Table 3.2, be given by $g(L, J, J_{\tilde{z}}, \tilde{\Omega}, \tilde{\omega}, f)$. The phase space density may in principle be a function of all the coordinates and momenta. However, if the Oort cloud is collisionless, and in a quasi-steady state, Jeans theorem states that $g$ is a function only of the integrals of motion. If no

perturbations are present, the integrals of motion include the energy and the components of the angular momentum.

The Oort cloud is certainly collisionless, with a two-body relaxation time of over $10^{26}$ years (Binney and Tremaine 1987, Equation 4–9). For a quasi-steady state in which $L$, $J$ and $J_{\tilde{z}}$ are integrals requires firstly that any perturbing forces be weak, and secondly that the loss cylinder be small.

1. The requirement that the perturbing forces be weak is fulfilled if the tidal forces are weak, as the tide is the dominant perturber of the Oort cloud. The ratio of the tidal to the solar force (*cf.* Equations 3.2 and 3.23), given by

$$\left| \frac{\vec{F}_{tide}}{\vec{F}_{M_\odot}} \right| = \frac{4\pi \rho_0 |z| r^2}{M_\odot} \leq \frac{4\pi \rho_0 r^3}{M_\odot}. \tag{4.15}$$

   is less than unity where

$$r < \left( \frac{M_\odot}{4\pi \rho_0} \right)^{1/3} \approx 0.8 \text{ pc} \approx 1.7 \times 10^5 \text{ AU}. \tag{4.16}$$

   Thus, for comets with $a \lesssim 85\ 000$ AU, the assumption of weak tidal forces is valid. The next strongest perturbing forces are those of the planets, but they are important only near the loss cylinder. As the entrance surface $q_E$ is chosen to be everywhere well outside the loss cylinder and the planetary system, the assumption of weak planetary perturbations is valid outside $q_E$.

2. The loss cylinder must be small because losses are irreversible and detract from the steady-state. The cross-sectional area $\Theta_*$ of the loss cylinder $J_* = r v_{t*}$ (Equation 3.20) is

$$\Theta_* = \pi v_{t*}^2 = \pi \left( \frac{J_*}{r} \right)^2 \approx \frac{2\pi G M_\odot q_*}{r^2}. \tag{4.17}$$

   An upper limit to the bound transverse velocity $v_{t\infty}$ possible at any radius is the parabolic velocity $v_{t\infty} = 2GM_\odot/r$, yielding a total cross-sectional area $\Theta_\infty = \pi v_{t\infty}^2 = 2\pi GM_\odot/r$. The ratio of the loss cylinder area to the total phase space area is

$$\frac{\Theta_*}{\Theta_\infty} \approx \frac{q_*}{r} \approx 10^{-3} \left( \frac{q_*}{10 \text{ AU}} \right) \left( \frac{r}{10\ 000 \text{ AU}} \right)^{-1}, \tag{4.18}$$

   indicating that the loss cylinder is indeed small.

Having ascertained that the distribution of Oort cloud orbits outside and near the entrance surface is collisionless and in a quasi-steady state, Jeans theorem now assures us that the distribution function $g$ can be a function only of $L, J$, and $J_{\tilde{z}}$. The Oort cloud phase space density $g$ used in these simulations is based on the results of Duncan et al. (1987), who determined the Oort cloud's number density $n$ to be a function only of radius $r$, and to be of the form

$$n(r) \propto r^{\alpha} \tag{4.19}$$

where $\alpha = -3.5 \pm 0.5$, within a range of $r$ from 3000 to 50 000 AU. Integrating Equation 4.19 over $r$ yields the number of comets $N(r)$ within a given shell with its inner edge located 3000 AU from the Sun,

$$N(r) = \int\limits_{3000 \text{ AU}}^{r} 4\pi r^2 r^{\alpha} \, dr \propto r^{\alpha+3}. \tag{4.20}$$

The Oort cloud being in a quasi-steady state, $r$ can be replaced by its time-average $\langle r \rangle = a(2 + e^2)/2$, yielding

$$N(a) \quad \propto \quad a^{\alpha+3} \qquad \text{where 4500 AU} \leq a \leq 75\,000 \text{ AU.} \tag{4.21a}$$

$$N(L) \quad \propto \quad L^{2\alpha+6} \tag{4.21b}$$

Duncan et al. (1987) also found cometary inclinations to be randomised for $a > 5000$ AU, indicating that $g$ is not a function of the inclination $i$, and hence $J_{\tilde{z}}$, at large radii. It will be assumed here that the angular momenta are randomised, and hence that $g$ is not a function of $J$. This last assumption rests on the mixing of the Oort cloud by passing stars, which is also presumed to replenish any regions of phase space depleted by the actions of the tide and the loss cylinder.

Taking $g(L) \propto L^{\beta}$ where $\beta$ is some constant, the total number of comets can be expressed in terms of $L$ as

$$N(L) = \int\limits_{0}^{2\pi} df \int\limits_{0}^{2\pi} d\tilde{\Omega} \int\limits_{0}^{2\pi} d\tilde{\omega} \int\limits_{0}^{L} dL \int\limits_{0}^{L} dJ \int\limits_{-J}^{J} g \, dJ_{\tilde{z}} = 8\pi^3 \int\limits_{0}^{L} g(L) L^2 dL \propto L^{\beta+3}. \tag{4.22}$$

Comparison of Equations 4.21b and 4.22 shows that $\beta + 3 = 2\alpha + 6$, and hence that $g \propto L^{2\alpha+3}$. The final form chosen for the phase space density is

$$g(L) = g_0 L^{2\alpha+3} \qquad\qquad (\alpha = -3.5, \; 10\,000 \text{ AU} \leq a \leq 50\,000 \text{ AU}), \tag{4.23}$$

where $g_0$ is a constant factor related to the total number of comets in the cloud. The inner edge of the Oort cloud was chosen to be $a_- = 10\ 000$ AU instead of 3000 to 5000 AU to conserve CPU time by neglecting comets which cannot pass the Jupiter barrier, as our interest here is restricted to comets that can become visible. The outer edge of the Oort cloud is taken to be at $a_+ = 50\ 000$ AU.

Let $\Phi(L, J_E, J_{\tilde{z}}, \tilde{\Omega}, \tilde{\omega}, f)\,dL\,dJ_{\tilde{z}}\,d\tilde{\Omega}\,d\tilde{\omega}\,df$ be the average flux per unit time of comets crossing into the entrance surface $J_E$ at a given point, then

$$\Phi(L, J_E, J_{\tilde{z}}, \tilde{\Omega}, \tilde{\omega}, f) = \frac{1}{\tau} \int_{J_E}^{J_E - J\tau} g(L, J, J_{\tilde{z}}, \tilde{\Omega}, \tilde{\omega}, f)\,dJ, \tag{4.24}$$

where $\tau$ is the comet orbital period and $\dot{J}$ is the usual time derivative of the angular momentum and here represents the phase-space velocity normal to the entrance surface, positive outwards. Note that Equation 4.24 holds whether or not the entrance surface is "filled", *i.e.* whether or not $\dot{J}\tau \sim J_E$.

Substituting Equation 3.28b and Equation 4.23 into Equation 4.24 yields the flux $\Phi$ into the entrance surface

$$\Phi(L, J_E, J_{\tilde{z}}, \tilde{\omega}) = -\frac{5\pi\rho_0 g_0}{GM_\odot^2} \frac{L^{2\alpha+5}}{J_E^2} (J_E^2 - J_{\tilde{z}}^2)(L^2 - J_E^2) \sin 2\tilde{\omega}. \tag{4.25}$$

The sign of Equation 4.25 is determined by $\sin 2\tilde{\omega}$. Since only the flux *into* the surface is of interest, the quantity $\Phi_E$ is defined to be

$$\Phi_E = \begin{cases} \Phi & \text{where } \Phi < 0, \text{ that is where } 0 < \tilde{\omega} < \pi/2 \text{ or } \pi < \tilde{\omega} < 3\pi/2 \\ 0 & \text{otherwise} \end{cases} \tag{4.26}$$

such that $\Phi_E$ is non-zero only where the tide is moving cometary perihelia inwards.

In these simulations, the comets' initial elements are drawn at random from $\Phi_E$. A practical implementation of this selection process requires the cumulative probability distribution $P(w)$ of comets drawn into the entrance surface by the tide, as a function of each relevant variable $w$. If $P(w)$ is known, one can generate an appropriately distributed set of $w$'s by solving the equation $w = P^{-1}(\xi)$, where $\xi \in [0, 1]$ is a uniform random deviate and $P^{-1}$ is the inverse transform of $P$, mapping $[0, 1] \to w$. $P(w)$ is related to $\Phi_E$ through

$$P(w) = \int_{-\infty}^{w} dw \int_{-\infty}^{\infty} \int_{-\infty}^{\infty} \int_{-\infty}^{\infty} \Phi_E(w, x, y, z)\,dx\,dy\,dz \tag{4.27}$$

where $w, x, y$ and $z$ are the canonical variables, and it has been assumed that $\Phi_E$ is separable.

Combining Equations 4.26 and 4.27 and converting to orbital elements, the expressions for the cumulative probabilities are found to be

$$P(\tilde{\Omega}) = \frac{\tilde{\Omega}}{2\pi} \qquad\qquad (0 \le \tilde{\Omega} < 2\pi) \qquad (4.28\mathrm{a})$$

$$P(\tilde{\omega}) = \begin{cases} \frac{1}{4}(1 - \cos 2\tilde{\omega}) & (0 \le \tilde{\omega} < \frac{\pi}{2}) \\ \frac{1}{2} & (\frac{\pi}{2} \le \tilde{\omega} < \pi) \\ \frac{1}{2} + \frac{1}{4}(1 - \cos 2\tilde{\omega}) & (\pi \le \tilde{\omega} < \frac{3\pi}{2}) \\ 1 & (\frac{3\pi}{2} \le \tilde{\omega} < 2\pi) \end{cases} \qquad (4.28\mathrm{b})$$

$$P(\tilde{\imath}) = \frac{1}{\pi}\left(\tilde{\imath} - \frac{1}{2}\sin 2\tilde{\imath}\right) \qquad\qquad (0 \le \tilde{\imath} < \pi) \qquad (4.28\mathrm{c})$$

$$P(\mu) = \frac{\mu}{2\pi} \qquad\qquad (0 \le \mu < 2\pi) \qquad (4.28\mathrm{d})$$

Note that the mean anomaly $\mu$ is chosen from a uniform random distribution. The orbit-averaged approximation, by its very nature, tells us nothing about the role of $\mu$ or the true anomaly $f$ in the dynamics. The flux into the entrance cylinder could in principle be a function of $f$, but our choice of initial conditions should be insensitive to this fact unless the comet can cross the entrance cylinder in less than one orbit $i.e.$ $\Delta J \sim J_E$. Our definition of $J_E = \mathcal{Z}\Delta J$ with $\mathcal{Z} > 1$ specifically precludes this possibility, so $\mu$ may be chosen at random.

The cumulative probability function of the semimajor axis is more complicated, its calculation being left to Appendix C. Between the inner edge of the Oort cloud $a_-$ and $a_=$,

$$P(a) = \frac{(2q_{E-})^{1/2}}{3\mathcal{P}_a}\left[a^{1/2} - a_-^{1/2} + 2q_{E-}\left(a^{-1/2} - a_-^{-1/2}\right)\right], \qquad (4.28\mathrm{e})$$

and where $a_= < a \le a_+$

$$P(a) = P(a_=) + \frac{5\pi^2\rho_0}{2M_\odot\mathcal{P}_a}\left[\frac{a^4 - a_=^4}{2} - \left(\frac{10\pi^2\rho_0\mathcal{Z}}{M_\odot}\right)^2\frac{a^{10} - a_=^{10}}{5}\right], \qquad (4.28\mathrm{f})$$

where $\mathcal{P}_a$ is a constant such that $P(a_+) = 1$. The eccentricity $e$ is determined by our choice of $q_E$ and $a$,

$$e = 1 - \frac{q_E}{a}. \qquad (4.28\mathrm{g})$$

These seven equations (4.28a through g) are used by LOCI to choose the comet's initial orbital elements.

## 4.3 The end-states of comets

A comet's dynamical lifetime is finite: any of a number of processes may transfer it to an unbound orbit or destroy it outright. A comet is said to have reached an **end-state** if its orbital parameters allow it to be classified into one of nine categories, listed below. Entering an end-state may indicate the loss or destruction of a comet or simply an intermediate stopping point, from which the simulation can subsequently be restarted. The nine end-states are:

**Collision** : The distance between the comet and a Solar System member *i.e.* the Sun or one of the giant planets, is less than that object's physical radius. Simply comparing the planet-comet distance to the planets' radii at each time step is insufficient to detect all collisions: the integrator's finite step-size could result in the integration "stepping over" the planet, and failing to record a collision. Collision detection is ensured by calculating the Keplerian *i.e.* two-body, orbit of the comet around the nearest planet, and using the pericentric distance of this orbit as the minimum planet-comet separation.

**Ejection** : The comet is leaving the Solar System on an orbit which is unbound *i.e.* parabolic or hyperbolic with respect to the Solar System's barycentre. The simulation is not terminated until the comet is at least $10^5$ AU from the Sun, to allow for the possibility that subsequent perturbations will result in the comet losing energy and returning to a "bound" state.

**Escape** : Though still bound to the barycentre in the two-body sense *i.e.* $e \leq 1$, the comet has ventured beyond the last closed Hill's surface (Equations 3.64a, b and c), and is considered stripped from the Solar System by the action of passing stars, molecular clouds, *etc.* The distinction between ESCAPE and EJECTION is somewhat arbitrary.

**Exceeded age of Solar System** : The comet lifespan has exceeded the present age of the Solar System, taken to be $5 \times 10^9$ yr. Such a comet would, given time, reach one of the other end-states, but has not yet had time to become part of the observed sample.

**Exceeded time limit** : The comet has completed more than 5000 orbits without entering one of the other end-states. The simulation is terminated and saved, and will be re-

examined at a later date. This is merely a safeguard that prevents extremely long-lived comets from consuming large amounts of CPU time, as discussed in § 4.1.6.

**Faded** The comet is considered to have faded through loss of volatiles, splitting or other mechanisms, and is no longer bright enough to be observed, even if its orbit should carry it close to the Sun. The probability of a comet fading is largely unknown, and the determination of this **fading function** is a primary goal of this research. The fading end-state is not allowed as an end-state in any simulations unless explicitly mentioned in the accompanying text.

**Perihelion too large** : The comet's perihelion $q$ has evolved beyond some limit, usually taken to be 40 AU, and is moving outwards under the influence of the tide *i.e.* $\sin 2\tilde{\omega} < 0$. Such a comet is unlikely to become visible in the near-future. Though the comet's perihelion may begin to decrease once again, these "new" orbital parameters should already be represented within the flux of comets into the entrance surface, and thus need not be considered further.

**Short-Period** The comet's orbital period has decreased below 200 yr: it has become a short-period comet. The possibility exists that such a comet will diffuse back out to the LP regime, but the small number of comets which reach this end-state (see Tables 5.1 and 5.3 later) make the consideration of a return from this end-state unnecessary.

**Visible** The comet has passed within 3 AU of the Sun. Such comets continue to evolve after their first apparition, however, it will be seen in § 5.1 that the first apparition provides a useful intermediate stopping point for the simulations. Though some comets do become visible with perihelia greater than 3 AU, the observed sample is almost certainly not complete beyond this point.

## 4.4 Model implementation and testing

The model was implemented as a computer code written in ANSI C, with all floating-point values in double (64 bits $\approx$ 15 digits) precision. The primary testing platform was a Silicon Graphics IRIS 4D/25S; the primary simulation platforms were two DEC Alpha AXP 2100 4/200's.

### 4.4.1 Integration tolerance

Testing was accomplished by examining each segment of included physics *e.g.* planets, non-gravitational forces, *etc.* in isolation, and comparing these restricted simulations with known analytical results. First, however, a set of criteria is needed to choose the tolerance $\zeta$, while balancing speed and accuracy. The full simulation has no conserved quantities suitable for determining the tolerance, so $\zeta$ was chosen such that the typical fractional error per orbit is less than $10^{-7}$ for the relevant conserved quantities in each of the restricted simulations, described below. After experimentation, the value of the tolerance $\zeta$ was chosen to be $10^{-9}$. The typical errors, described in the sections below, are summarised in Table 4.2. The fractional energy change per orbit for a typical LP comet in the complete model is of order unity, so an integration tolerance of one part in $10^7$ is more than sufficient for this problem.

### 4.4.2 The two-body problem

Consider the Sun and a single test particle. This simple system tests the implementation and benefits of regularising the coordinates. A hundred particles were run on orbits with $a = 10^5$ AU and $q = 0.01$ AU ($e = 0.9999999$). The other elements were chosen randomly from a spherically symmetric distribution and the particle trajectories were integrated for $10^6$ orbits ($\sim 10^{13}$ yr).

The angular elements ($i$, $\Omega$, $\omega$) and the angular momentum both showed a roughly linear secular trend in error growth with orbit number, with a fractional change of roughly $10^{-9}$ orbit$^{-1}$. A certain amount of scatter was also present, with a fractional root-mean-square (RMS) value per orbit of $10^{-8}$.

The errors in orbital energy showed no net growth, but did show a fractional scatter of about 1% about the correct value. However, this scatter was not due to error in the regularised energy coordinate $h$ (§ 4.1.2), which was perfectly conserved, but to slight roundoff errors in the transformation from the regularised coordinates to Cartesian coordinates to orbital elements. Also, $|E|$ is small to begin with, only $10^{-5}$ AU$^{-1}$, so this "large" error is not a concern.

When the particles' equations of motion are expressed in Cartesian coordinates, a much lower integration accuracy is achieved. Given the same initial conditions, the angular elements are typically conserved to only 1 in $10^5$ over 1000 orbits, both the energy and angular

| Test | $a$ ( AU) | $q$ ( AU) | $\Delta E/E$ | $\Delta J/J$ | $\Delta W/W$ |
|------|-----------|-----------|--------------|--------------|--------------|
| Two-body | 100 000 | 0.01 | $10^{-8}$ | $10^{-8}$ | — |
| Jupiter | $\infty$ | 0–5.2 | — | — | $10^{-5}$ |
| Tide | 47 000 | $\sim 10\ 000$ | — | $10^{-12}$ | — |
| NG | 10 000 | 0.1 | $10^{-8}$ | $10^{-11}$ | — |
| Disk | 10 000 | 0.1 | $10^{-7}$ | $10^{-10}$ | — |

Table 4.2: Typical per-orbit errors for different test scenarios. Initial semimajor axes $a$ and perihelion distances $q$ are shown on the left. The errors are in the orbital energy ($\Delta E/E$), angular momentum ($\Delta J/J$) and Jacobi constant ($\Delta W/W$).

momentum drift by factors of ten or more, and particles frequently reach unbound orbits. The regularised coordinates are thus to be preferred for the integration of high-eccentricity orbits.

### 4.4.3 The planets

In this section, the gravitational influences of the Sun and Jupiter alone on a test particle will be considered. Collisions are ignored, Jupiter's orbit is taken to be circular, and the only allowed end-state is ejection. This simplified system will be termed the **Sun-Jupiter** model or a **Sun-planet** model if an arbitrary planet is to be considered.

### Precession

The planets perturb comets in ways other than a simple energy kick. Quinn et al. (1990) showed that the planets produce a precession of the comets' orbits, which can be pictured as a trajectory in $q$–$\omega$ space. This precession is due to the quadrupole moment of the planet's time-averaged orbit. A comparison of the results obtained with LOCI with those of Quinn et al. under the same initial conditions is shown in Figure 4.2.

The phase-space trajectories show the same general behaviour, and the differences observed are expected. Quinn et al. orbit-averaged the system's Hamiltonian, and thus their results lack the realistic stochasticity present in our integration. As well, quantities which are integrals of the motion of the averaged Hamiltonian are not strictly conserved under the unaveraged Hamiltonian. Figure 4.2a reflects this fact through the slow wandering of trajectories away from their averaged ideals $e.g.$ two of the trajectories in Figure 4.2a cross the $q = 0.4$ line due to drift in the $z$-component of the angular momentum. Though the existence of the above-mentioned differences between LOCI's and the orbit-averaged results

(a)                                                    (b)
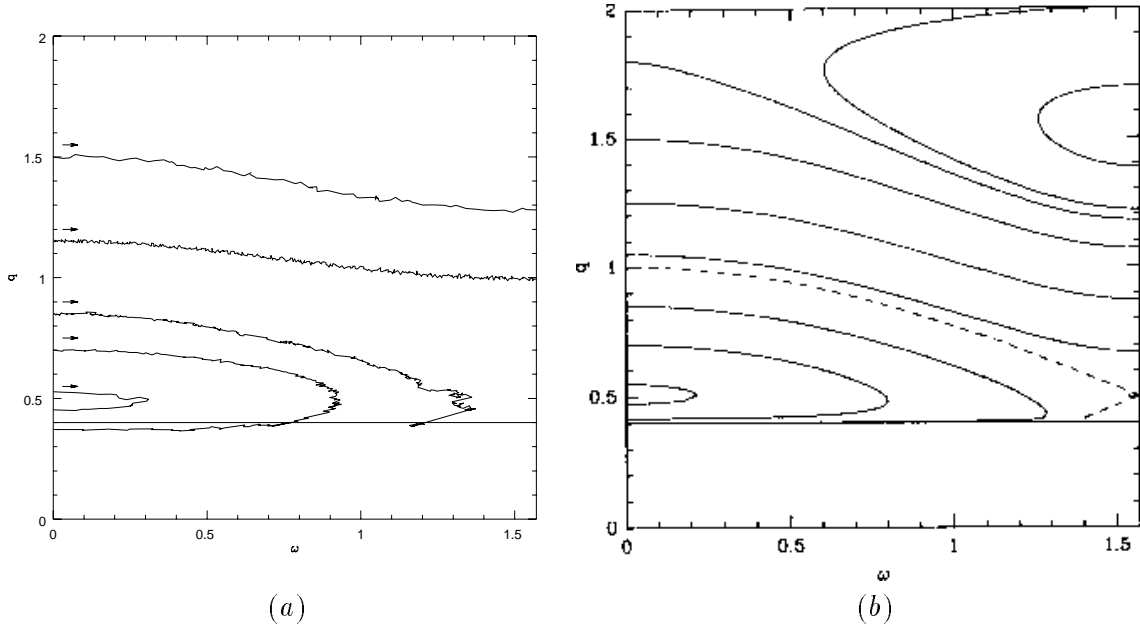
Figure 4.2: Evolution in $q$–$\omega$ space of a test particle in a Sun-Jupiter system: ($a$) LOCI's integration and ($b$) orbit-averaged results from Quinn et al. (1990). The arrows in ($a$) indicate the direction of evolution with time.

are due to the more realistic treatment used, the quantitative correctness of these deviations remains unverified by this test.

### Lifetime against ejection

The Gambler's Ruin problem (§ 3.1.2) predicts that, of an initial sample of parabolic orbits, the probability of a particle remaining bound to a Sun-planet system at the $m^{th}$ perihelion passage is proportional to $m^{-1/2}$ (Equation 3.12). LOCI's duplication of this result appears in Figure 4.3: the straight line indicates the least-squares best fit, the slope of which matches the expected result to within 0.5%. The initial cometary perihelia are uniformly distributed inside Jupiter's orbit.

### Jacobi's integral

The **circular restricted three-body problem** deals with a massless particle in a Sun-planet system. The only known integral of motion of this system is Jacobi's integral $W$. Expressed in a non-rotating barycentric coordinate system with the $x$-axis increasing along the Sun-Jupiter line, and the $y$-axis perpendicular to $x$ and in the orbital plane, Jacobi's
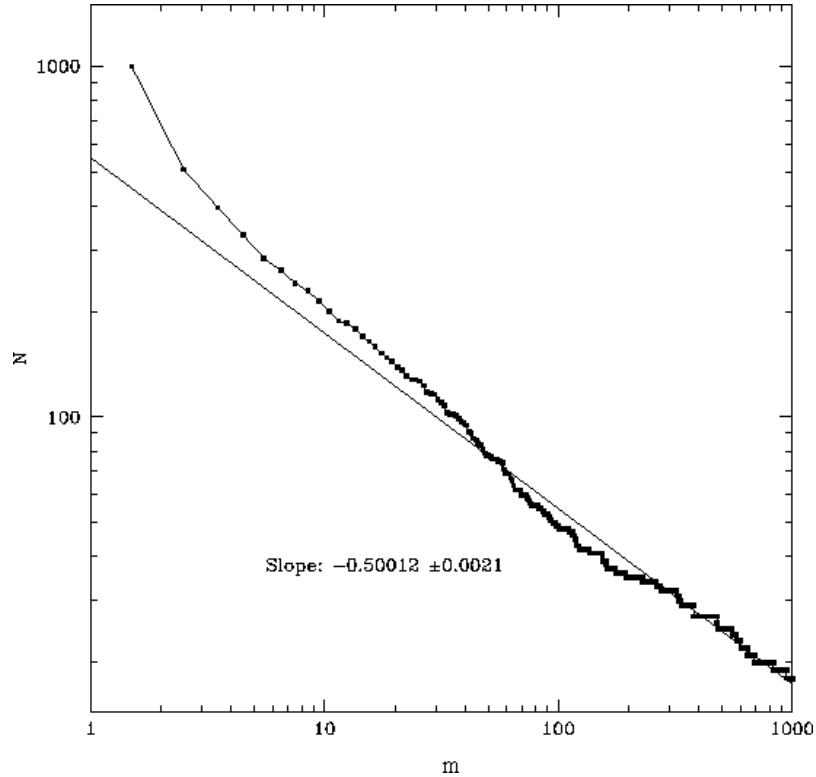
Figure 4.3: Number $N$ of test particles remaining in the Sun-Jupiter system as a function of orbit number $m$ for a set of 1000 initially parabolic comets. The particles' initial perihelia were distributed linearly in $q$ inside Jupiter's orbit. The straight line is a least-squares fit to the points.

integral can be expressed as

$$W = v^2 + 4\pi(y\dot{x} - x\dot{y})/\tau_{Jup} - 2G\left(\frac{M_\odot}{r} + \frac{M_{Jup}}{r_{Jup}}\right), \tag{4.29}$$

where $\tau_{Jup}$ is Jupiter's orbital period, and $v^2 = \dot{x}^2 + \dot{y}^2 + \dot{z}^2$ is the test particle's velocity.

Consider the 1000 test particles in the random walk described in the previous section. Most particles are ejected by the one thousandth orbit, but twenty remain. These survivors displays errors of $\langle(\Delta W/W)^2\rangle^{1/2} \sim 10^{-2}$, or $10^{-5}$ per orbit.

The error in the Jacobi integral is large compared to, say, the energy error in the two-body problem (§ 4.4.2). The difficulty arises from close planetary encounters: the coordinates are regularised about the Sun, not the planet, and the large accelerations which occur during encounters degrade the simulation's accuracy, despite the reductions in step-size. Though one could switch to a coordinate system regularised about the planet in question during close approaches, the added complexity has been judged excessive for our purposes. The Jacobi error is the exception to the rule that the integrals of motion should

be constant within $10^{-7}$ per orbit (§ 4.4.1).

**The distribution of energy perturbations**

The energy perturbations imparted to parabolic comets making a single perihelion passage through a Sun-planet system were examined numerically by Everhart (1968). Figure 4.4 shows a comparison of our results for a Sun-Jupiter system with Everhart's functional fit. The points are LOCI's results with $\sqrt{n}$ error bars, the solid curve is Everhart's result. The initial conditions for the $10^4$ comets used in our simulation were

- Parabolic orbits, started $10^5$ AU from the Sun,

- Perihelion distances distributed uniformly between 0.9 and 1.1 times Jupiter's orbital radius,

- Angular elements $(i, \Omega, \omega)$ chosen from a spherically symmetric distribution.

The initial conditions for Everhart's result were: spherically symmetric angular elements and perihelia at Jupiter's orbit. The distributions show some slight differences, but these are to be expected. Everhart's function is chosen empirically to match the observed distribution's shape, rather than from any consideration of the physics, and because the shape of the distribution depends strongly on inclination, it would be surprising if an empirical function could accurately represent all the phase space in question.

In fact, the function shown in Figure 4.4 is not the function Everhart claims as representative of the distribution averaged over all inclinations, but rather the sum of the 14 separate fits he produced, each for a small range of inclinations between 0 and $\pi$. Everhart's all-inclinations function differs markedly from our results and from the sum of his separate determinations, especially for small perturbations ($|\Delta(1/a)| < 0.0002$ AU$^{-1}$). The cause of this discrepancy seems to be that the empirical function Everhart chose, though providing a reasonable match when fitted to the distribution associated with a small inclination range, it is rather poorly designed to match the sum of these distributions.

### 4.4.4 The Galactic tide

Heisler and Tremaine (1986) analytically derived the orbit-averaged evolution of a comet moving under the Galactic tide. The comet moves along a trajectory in $K$–$\tilde{\omega}$ space, where $K = J/L = \sqrt{1 - e^2}$ and $\tilde{\omega}$ is the usual argument of perihelion relative to the Galactic

(a)                                              (b)
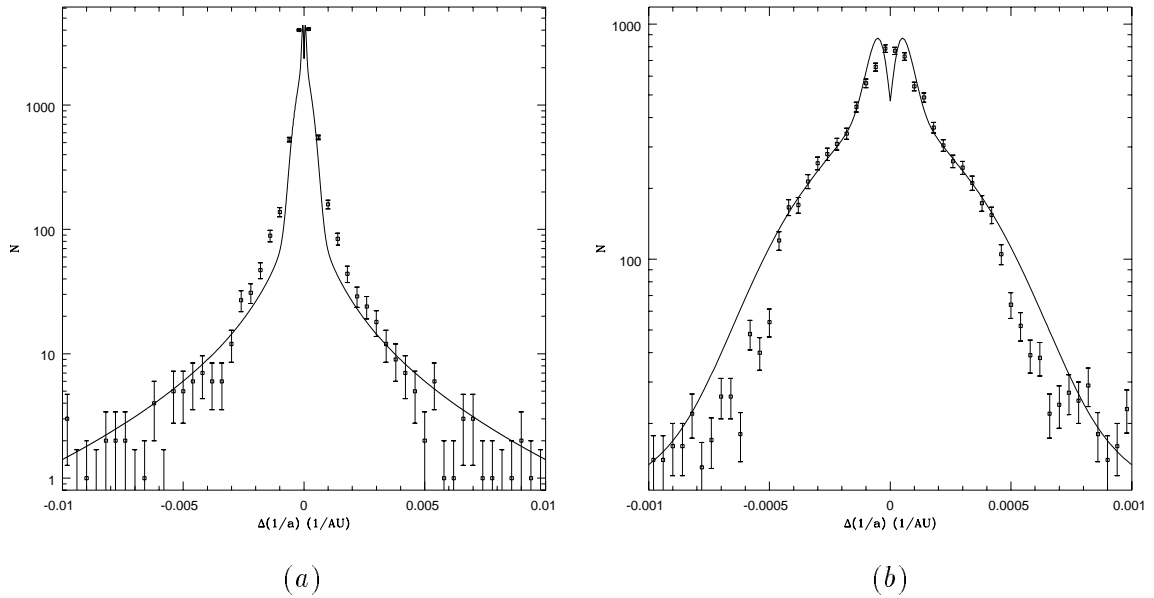
Figure 4.4: The $\Delta(1/a)$ distribution for parabolic comets making a single orbit with peri-helion near Jupiter's orbit, at two different magnifications. The heavy line is a composite of Everhart's (1968) empirical fits.

frame. The allowed curves are parametrised by $K_{\tilde{z}} = K \cos \tilde{\imath}$, the component of $K$ along the Galactic $\tilde{z}$-axis. Figure 4.5a displays LOCI's results for $K_{\tilde{z}} = 0.585$; Figure 4.5b those of Heisler and Tremaine (1986). The data in Figure 4.5a, which is sampled about once per orbit, shows some scatter around the analytical trajectory, because our model does not ignore the high-frequency components that have been averaged out of Heisler and Tremaine's result.

The quantities $J_{\tilde{z}}$, $K_{\tilde{z}}$ and $L$ are all conserved in the orbit-averaged approximation, but only $J_{\tilde{z}}$ is an integral of the unaveraged motion. Our results display a net error in $J_{\tilde{z}}$ of less than 1 part in $10^{12}$ per orbit over the 500 to 5000 orbits required to travel from $\tilde{\omega} = \pi/2$ and back again along the curves plotted in Figure 4.5. The RMS error per orbit was roughly 1 in $10^6$, the source of this error again being the accumulated error in the transformation of coordinates from regularised to Cartesian to orbital elements to $J_{\tilde{z}}$, and is thus not of concern.

### 4.4.5   Non-gravitational forces

Non-gravitational forces can be handled by K–S regularisation despite the fact that they are not conservative and thus cannot be represented by a potential. The accuracy of the

$(a)$                                   $(b)$
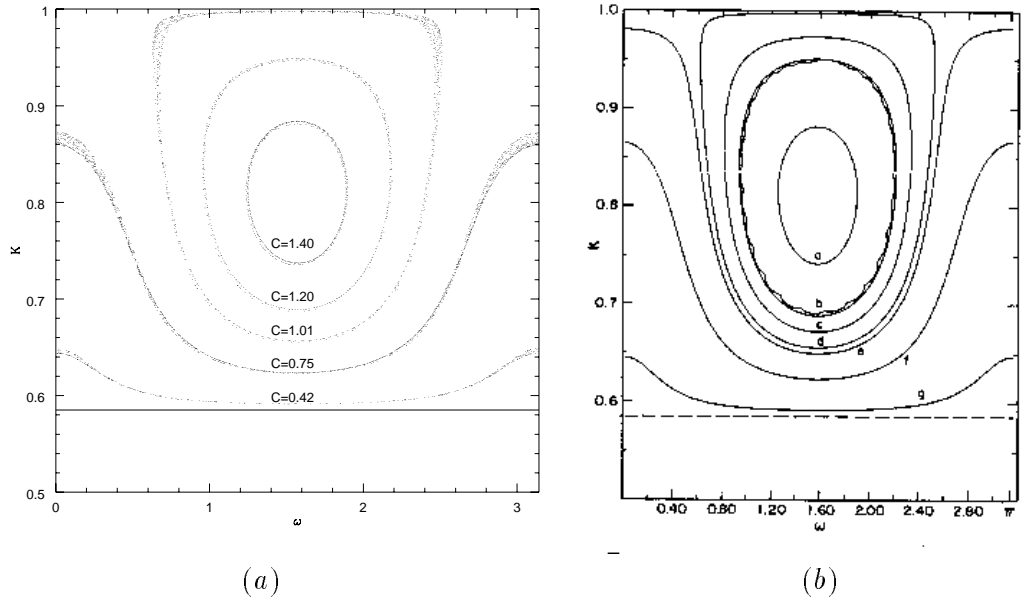
Figure 4.5: Orbital evolution in $K$–$\tilde{\omega}$ space under the dominant component of the Galactic tide: ($a$) LOCI's results, and ($b$) analytical treatment by Heisler and Tremaine (1986). The curves labelled $a, b, d, f$ and $g$ in ($b$) correspond to the curves with $C = 1.4, 1.2, 1.01, 0.75$ and 0.42 in ($a$) respectively.

NG module of the simulation was evaluated by comparing its results with a parallel but independent[†] integration of Gauss's equations (Equations A.19a-f).

The test orbits had semimajor axes of 10 000 AU, perihelion distances of 0.1 AU and random, spherically symmetric angular elements. The test duration was 1000 orbits. Each of the three NG parameters, radial, tangential and normal, was tested individually, with values of $\pm 10^{-9}$ AU day$^{-2}$.

The two methods showed differences less than 1 in $10^{12}$ on all elements on which the NG forces in question should have no effect $e.g.$ semimajor axis in the case $A_1 = A_2 = 0$. Otherwise, the methods typically differed by $10^{-8}$ rad orbit$^{-1}$ in the angular coordinates. The fractional differences in the energy and angular momentum were typically 1 in $10^5$ and 1 in $10^8$, or $10^{-8}$ and $10^{-11}$ per orbit, respectively.

---

[†]"Independent" here means that, though all differential equations are integrated by the same routines, the simulation and the parallel integration cannot see each others coordinate values.

### 4.4.6 Massive circumsolar disk

The effects of a hypothetical disk of material orbiting the Sun at distances of 100 to 1000 AU were modelled through the addition of a Miyamoto-Nagai disk potential, described in § 3.6. The test case had $a_d = 1000$ AU, $b_d = 100$ AU and $M_d = 10^{-3}M_\odot$, with the test particle orbits having $a = 10\,000$ AU, $q = 0.1$ AU and spherically symmetric angular elements. The test particles were followed for 1000 orbits. The $z$-component of the angular momentum $J_z$ is an integral of the motion, and was conserved to better than 1 in $10^{10}$ per orbit. The Keplerian orbital energy ($\propto 1/a$) is not conserved in the presence of the disk potential, but the total energy (Keplerian + disk potential) is: in the simulations it varied by only 1 in $10^{10}$ per orbit as well.

A more comprehensive test involved the co-integration of Gauss's equations, as was done for the NG forces. In this case, the two schemes typically differed by $10^{-8}$ rad orbit$^{-1}$ in the angular coordinates. The fractional differences in the angular momentum and the Keplerian energy were 1 in $10^7$ and 1 in $10^{10}$ per orbit respectively.

# Chapter 5

# Results

The dynamical evolution of an Oort cloud comet can be conveniently divided into two separate stages for our purposes. The first is the comet's sojourn in the outer reaches of the Solar System before first becoming visible, visibility taken here to mean passage within 3 AU of the Sun. The second stage encompasses the remaining evolution up to the point where the comet is ejected or otherwise permanently excluded from the sample of observable comets.

Let the set of those LP comets which are making their first visible perihelion passage be called the $V_1$ comets, and those making their $m^{th}$ visible apparition, the $V_m$ comets. The union of all visible LP comets will be called the dynamically evolved visible LP comets. The lifetime of a comet $m_x$ can be measured by the number of perihelion passages since (and including) its first apparition. The number of visible perihelion passages a comet makes in its lifetime is denoted $m_v$. The comet's lifetime in terms of physical time $t_x$ is also useful, but is not clearly defined in all cases *e.g.* the exact moment of ejection may be difficult to determine.

### 5.0.1 Original elements

The original elements of observed comets are computed by integrating their orbits backwards from perihelion, and are typically quoted at distances of 60 to 100 AU from the Sun. However, hypothetical structures with radii of 100 to 1000 AU are introduced into some of our simulations, and complicated artifacts might be introduced into the elements if they are calculated near a massive perturber. To avoid this possibility, the original elements

of our simulations are measured at aphelion instead. Adjustments must thus be made to the simulated distributions of orbital elements in order to compare them with the observed distributions, but these adjustments are usually small. The original inverse semimajor axis is affected somewhat by the comet's climb out of the Galactic potential well (Equation 3.24), but the resulting change in $1/a$ is only of order

$$\Delta(1/a) \sim \frac{4\pi\rho_0\tilde{z}^2}{M_\odot} \approx 5 \times 10^{-7} \left(\frac{\tilde{z}}{50\ 000\ \text{AU}}\right)^2\ \text{AU}^{-1}, \tag{5.1}$$

which is small and can be ignored. However, the shift in energy produced by a disk or Planet X may be more pronounced, of order

$$\Delta(1/a) \sim \begin{cases} \dfrac{2M_X}{r_X M_\odot} \approx 2 \times 10^{-4} \left(\dfrac{M_X}{0.01 M_\odot}\right) \left(\dfrac{r_X}{100\ \text{AU}}\right)^{-1}\ \text{AU}^{-1}, \\ \dfrac{2M_d}{a_d M_\odot} \approx 2 \times 10^{-4} \left(\dfrac{M_d}{0.01 M_\odot}\right) \left(\dfrac{a_d}{100\ \text{AU}}\right)^{-1}\ \text{AU}^{-1}, \end{cases} \tag{5.2}$$

where the companion has mass $M_X$ and orbital radius $r_X$, and the disk has a potential described by Equation 3.52. The numerical values in Equation 5.2 correspond to the maximum change in $1/a$ among the simulations to be described here. In most cases, the effect is smaller and will be neglected.

It is interesting to note that that the mean excess velocity of observed hyperbolic comets, roughly equivalent to $1/a \sim 10^{-4}$ AU$^{-1}$, is not well explained by the presence of such "dark matter". A shift of $10^{-4}$ AU$^{-1}$ in inverse semimajor axis would pull the outer edge of the Oort cloud inside $10^4$ AU, and thus preclude the filling of the loss cylinder, either by the tide or passing stars (Equations 3.47 and 3.31b). Nevertheless, a few "high dark-matter" simulations will be performed for completeness.

## 5.1 The newly visible comets

The newly visible or $V_1$ comets constitute the injection spectrum from which the observed LP distribution has evolved. The $V_1$ set can be used as a starting point for any investigation of phenomena that only affect the comet after its first apparition *e.g.* non-gravitational forces, fading. The elements of the $V_1$ comets are here measured in the barycentric frame at the aphelion immediately preceding their first apparition.

The set of $V_1$ comets produced in the course of this research has 1368 members, and was obtained from a set of 125 495 initial conditions within the Oort cloud. Of these 1368 new comets, 1340 first became visible while still Oort cloud members *i.e.* when $a > 10\ 000$ AU.

| End-state | Ejection | Escape | Exc. Limit | Large $q$ | Short pd. | Visible | Total |
|---|---|---|---|---|---|---|---|
| Number | 3803 | 4 | 57 | 15023 | 31 | 1368 | 20286 |
| Fraction | 0.1875 | 0.0002 | 0.0028 | 0.7406 | 0.0015 | 0.0674 | 1.0000 |
| Minimum $t_x$ | 6.80 | 34.4 | 17.2 | 7.46 | 11.7 | 7.14 | 6.8 |
| Median $t_x$ | 28.7 | 56.7 | 152 | 35.2 | 29.3 | 26.8 | 33.3 |
| Maximum $t_x$ | 342 | 108 | 480 | 1182 | 72.4 | 147 | 1182 |
| Minimum $m_x$ | 1 | 13 | 5000 | 1 | 6 | 1 | 1 |
| Median $m_x$ | 8 | 14 | 5000 | 5 | 387 | 5 | 6 |
| Maximum $m_x$ | 4799 | 28 | 5000 | 4872 | 3432 | 2937 | 5000 |

Table 5.1: The distribution of end-states of the 20 286 Oort cloud comets with minimum perihelia under the tide of less than 40 AU. The minimum, median and maximum lifetimes $m_x$ and $t_x$ are shown in in orbital periods and millions of years, respectively. No comets suffered collisions or survived for the lifetime of the Solar System.

The $V_1$ comets were produced over twenty-seven separate runs on a DEC Alpha, requiring over thirteen weeks of real time and roughly eight weeks of CPU time at a tolerance $\zeta = 10^{-9}$. On average, a new Oort cloud comet was started every 40 seconds, and a visible comet produced every 3800 seconds.

Of the 125 495 Oort cloud comets simulated, 105 209 were determined to have minimum perihelion distances under the Galactic tide (Equations 3.26 and 3.27a,b) greater than 40 AU, too far outside the planetary system to suffer appreciable planetary perturbations (Figure 4.1). These simulations were terminated immediately, and counted as part of the PERIHELION TOO LARGE end-state. The remaining 20 286 were integrated numerically, and of these only 1 in 15 became visible. Table 5.1 shows the distribution of these 20 286 comets among the various end-states.

During this pre-visibility stage of LP comet dynamical evolution, there were 694 close encounters with the giant planets by 341 individual comets, distributed as shown in Table 5.2. There were no captures or collisions, though some comets did pass within the planets' satellite families.

Only 57 of the 20 286 comets which were numerically integrated triggered the EXCEEDED TIME LIMIT flag (see § 4.3), set at 5000 revolutions. These comets constitute only 0.05% of all initial conditions and are not included in the discussions to follow, but will be addressed again in § 5.1.1.

| Planet | Jupiter | Saturn | Uranus | Neptune | Total |
|---|---|---|---|---|---|
| Number of comets | 60 | 145 | 71 | 67 | 341 |
| Number of encounters | 210 | 317 | 109 | 93 | 694 |
| Encounters/comet | 3.5 | 2.19 | 1.53 | 1.39 | 2.04 |
| Collisions | 0 | 0 | 0 | 0 | 0 |
| Captures | 0 | 0 | 0 | 0 | 0 |
| $R_I (R_p)$ | 674 | 907 | 2030 | 3510 | — |
| Min. distance $(R_I)$ | 0.023 | 0.043 | 0.074 | 0.049 | 0.023 |
| Min. distance $(R_p)$ | 16.0 | 38.7 | 150 | 167 | 16.0 |
| Outer satellite $(R_p)$ | 326 | 216 | 23 | 222 | — |

Table 5.2: Planetary close encounter data for the 20 286 initial conditions which had initial perihelia within 40 AU of the Sun. Encounters for the 57 comets in the EXCEEDED TIME LIMIT end-state are included only up to their $5000^{th}$ orbit. The size of planet's sphere of influence $R_I$ (Equation 4.5) and that of the orbit of the planet's outermost satellite are also given.

**Perihelion distance**

The distribution of perihelion distances of the $V_1$ comets is shown in Figure 5.1a. The distribution is sloped slightly upwards towards larger $q$. This is to be expected: a full loss cylinder should have a flat distribution in $q$, but empty or partially full loss cylinders will have a preponderance of orbits at larger perihelia. This conclusion is strengthened by an analysis of Figure 5.1b, which plots first apparition perihelion distance versus original



$(a)$ $(b)$
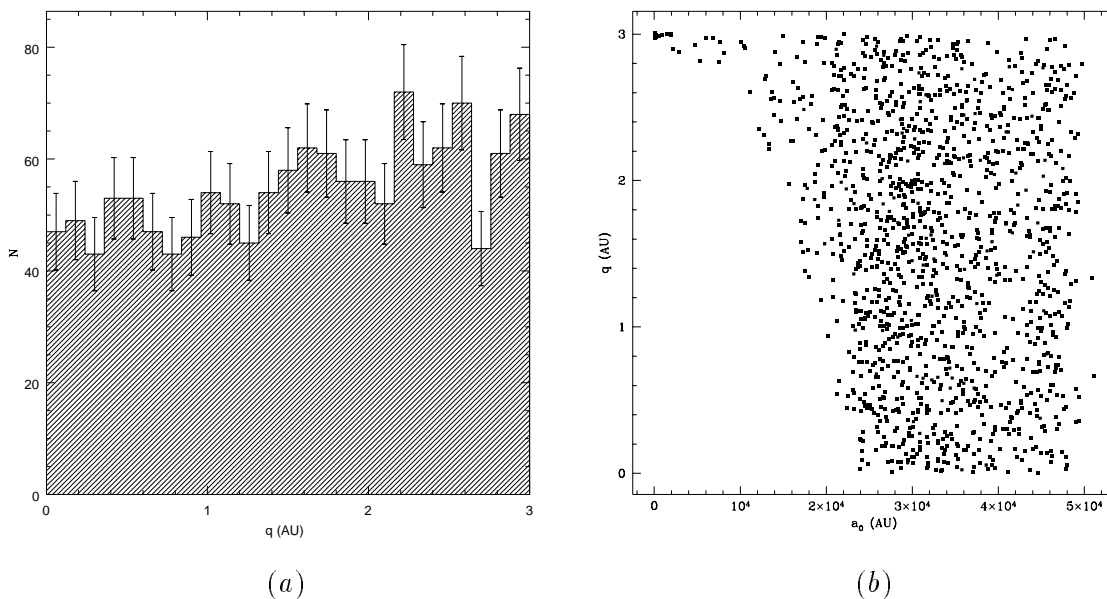
Figure 5.1: The $V_1$ comets: $(a)$ their number distribution versus perihelion distance $q$, and $(b)$ their first apparition perihelion distance $q$ versus original semimajor axis $a_0$.

semimajor axis, and which confirms the filling of the loss cylinder at $a \gtrsim 25\ 000$ AU (Equation 3.31b).



$$(a) \qquad\qquad\qquad\qquad (b)$$
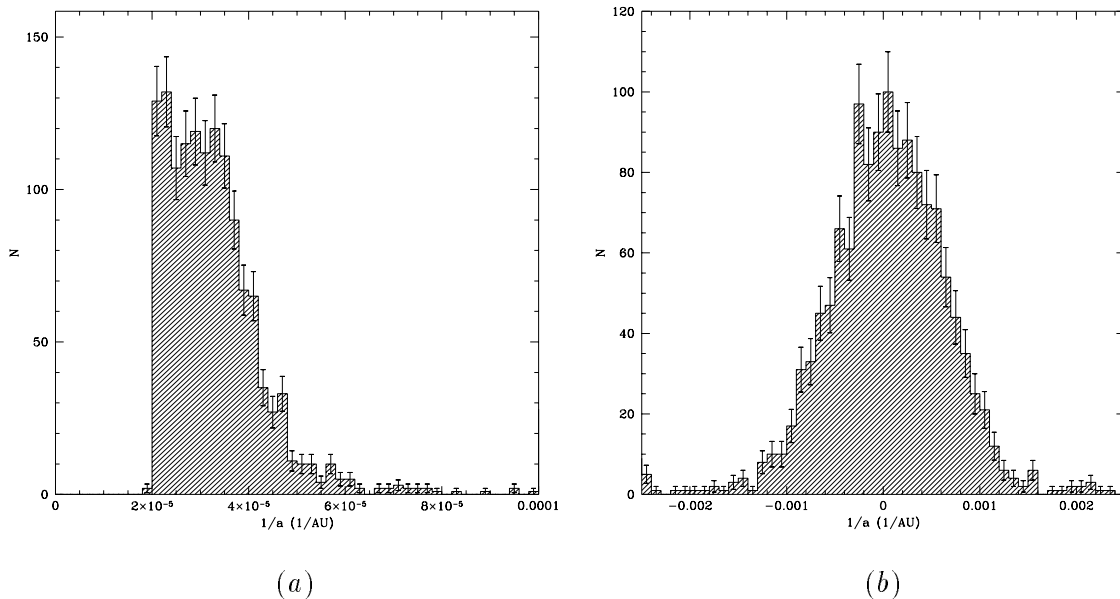
Figure 5.2: Distribution of orbital energies for the $V_1$ comets: $(a)$ at the aphelion before their first apparition *i.e.* original energies and $(b)$ at the aphelion immediately following first apparition. The energies of unbound orbits are measured at $r = 10^5$ AU.

### Orbital energy

The distribution of $V_1$ orbital energies is shown in Figure 5.2, both at the aphelion before the comets become visible and at the aphelion immediately after their first apparition. The cutoff at $2 \times 10^{-5}$ AU$^{-1}$ in Figure 5.2 is artificial, a result of our choice of the Oort cloud's outer edge at 50 000 AU. Note the concentration of original orbits at very small but positive energies. In fact, all but 28 ($\sim 2$ %) are in the region of the spike ($1/a < 10^{-4}$ AU$^{-1}$). The orbits within the spike have a mean $1/a \approx 3.3\pm1\times10^{-5}$ AU$^{-1}$. This result is in good accord with Heisler's (1990) Monte Carlo simulations, which indicated that, outside of showers, the energy distribution of new comets is expected to peak at $3.55 \times 10^{-5}$ AU$^{-1}$. Heisler's simulations also included passing stars, indicating that our omission of these perturbers does not strongly affect the distribution of original semimajor axes.

The post-perihelion energy distribution (Figure 5.2b) is much broader, due to the planetary perturbations discussed in § 3.1. The distribution is highly symmetric about zero, with a median $1/a$ of $5.0\pm0.3\times10^{-5}$ AU$^{-1}$; its full width at half maximum is $6.2\pm0.3\times10^{-4}$ AU$^{-1}$,

in reasonable agreement with the expected size of planetary perturbations (Equation 3.8).
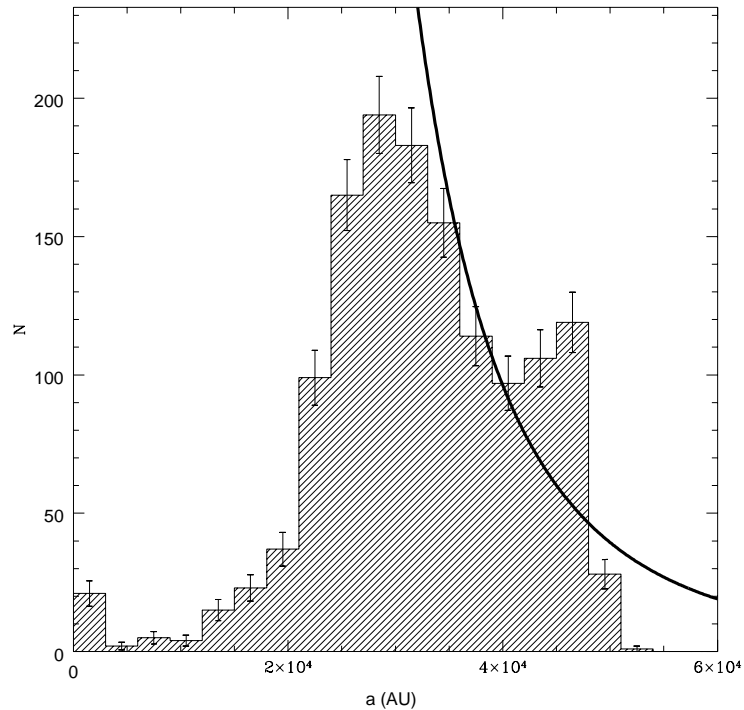


Figure 5.3: Distribution of original semimajor axes $a$ of the 1368 $V_1$ comets. The curve is an analytical approximation to the expected distribution, derived in Appendix C.

Despite the decrease in comet number density with radius in the Oort cloud, comets are injected primarily from its outer portion. The distribution of original semimajor axes is shown in Figure 5.3. The median original semimajor axis is roughly 32 000 AU, and the distribution displays a double-peaked shape, with one peak near 27 500 and a smaller one at 45 000 AU. An analytical approximation to the expected flux is shown by the curve; it is valid only where the loss cylinder is full, and is derived in Appendix C.

Our choice of the edge of the Oort cloud at 50 000 AU is the cause of the sharp decrease in simulated comets beyond this point in Figure 5.3. The sharp drop-off at semimajor axes smaller than about 27 500 AU is a result of the emptying of the loss cylinder as semimajor axis decreases (§ 3.2.1). The position and steepness of this drop-off supports our choice of the inner boundary of the Oort cloud at 10 000 AU, rather than closer in: Oort cloud comets on orbits smaller than about 20 000 AU are unable to enter the visibility cylinder in appreciable quantities, and thus their exclusion from our simulated Oort cloud should not bias the results.

The nature of the smaller peak at 45 000 AU is unclear: if the sample is split into two parts, it appears only in one half, and thus may be a statistical fluke despite its relatively large size. It will assumed to be unimportant for two reasons. Firstly, only a few percent of the $V_1$ comets are involved; and secondly, the subsequent planet-dominated evolution of the $V_1$ comets is relatively insensitive to the comets' original semimajor axis, as all Oort cloud comets approach the Sun on essentially parabolic orbits.

**Angular elements**

The aphelion directions of the $V_1$ comets, measured at the aphelion passage immediately preceding their first apparition, are shown in Figure 5.4. The most striking feature is the concentration towards mid-Galactic latitudes, a result of the Galactic tide. However, the real distribution is expected to be much clumpier, due to the injection of comets by passing stars.

The inclinations, longitudes of the ascending nodes, and arguments of perihelion in the ecliptic and Galactic frames are shown in Figures 5.5, 5.6 and 5.7. The peak in the $\cos\tilde{\imath}$ distribution near zero is expected: the flux $\Phi$ is proportional to $(J_E^2 - J_{\tilde{z}}^2)/J_E^2 = \sin^2\tilde{\imath}$ (Equation 4.25). Thus the flux is expected to increase towards high Galactic inclination $i.e.$ $\tilde{\imath} \sim \pi/2$. The peaks in Figure 5.7b are also expected: the regions where $\sin 2\tilde{\omega} > 0$ are the regions where the perihelia are moving inwards under the tide. The distributions of $\cos i$, $\Omega$, $\tilde{\Omega}$ and $\omega$ are relatively uniform, expected because the Galactic tide is independent of these quantities.

## 5.1.1   The longest-lived comets

Only a small fraction of comets survive for more than 500 orbits after their initial apparition, but this remnant's extremely long lifetimes make it difficult to follow their evolution to completion, as noted in § 4.1.6.

The number of comets remaining in the simulations as a function of orbit number is shown in Figure 5.8a. The amount of CPU time needed to follow all remaining comets for the previous 500 orbits is shown in Figure 5.8b. As the number of orbits increases, neither the number of comets remaining nor the CPU time approach zero rapidly, if at all. Thus, for all practical simulation lengths, some number of comets will always remain. These long-lived comets are not necessarily the oldest in terms of physical time, though they tend to
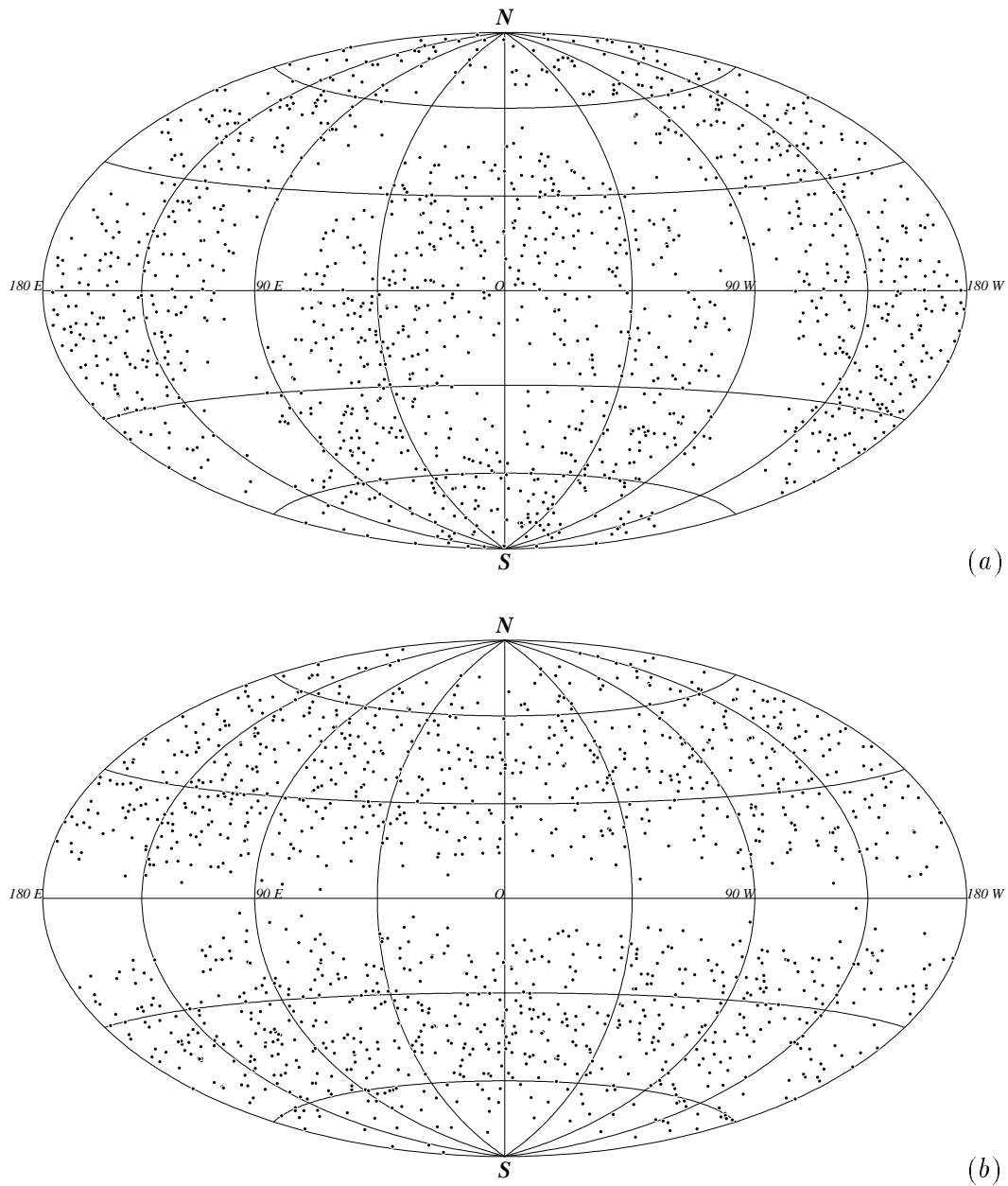
Figure 5.4: Equal area plots of the aphelion directions of the $V_1$ comets, in the ($a$) ecliptic and ($b$) Galactic frames, measured at the aphelion immediately preceding their first apparition.
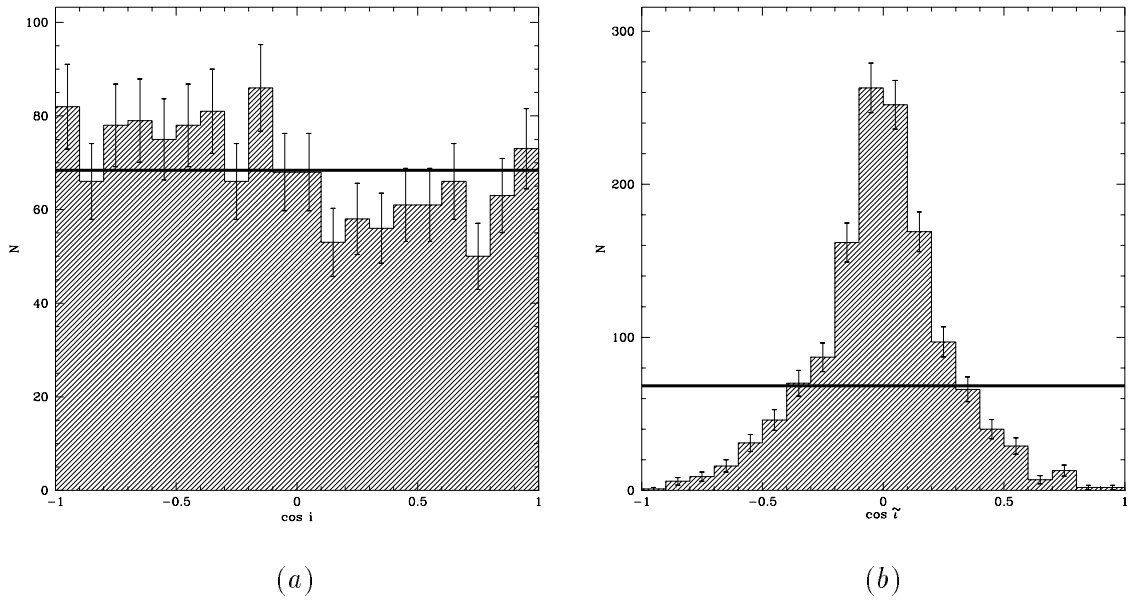
Figure 5.5: Distribution of the cosine of the orbital inclinations for the $V_1$ comets: $(a)$ at perihelion in the ecliptic frame, and $(b)$ at the previous aphelion in the Galactic frame.
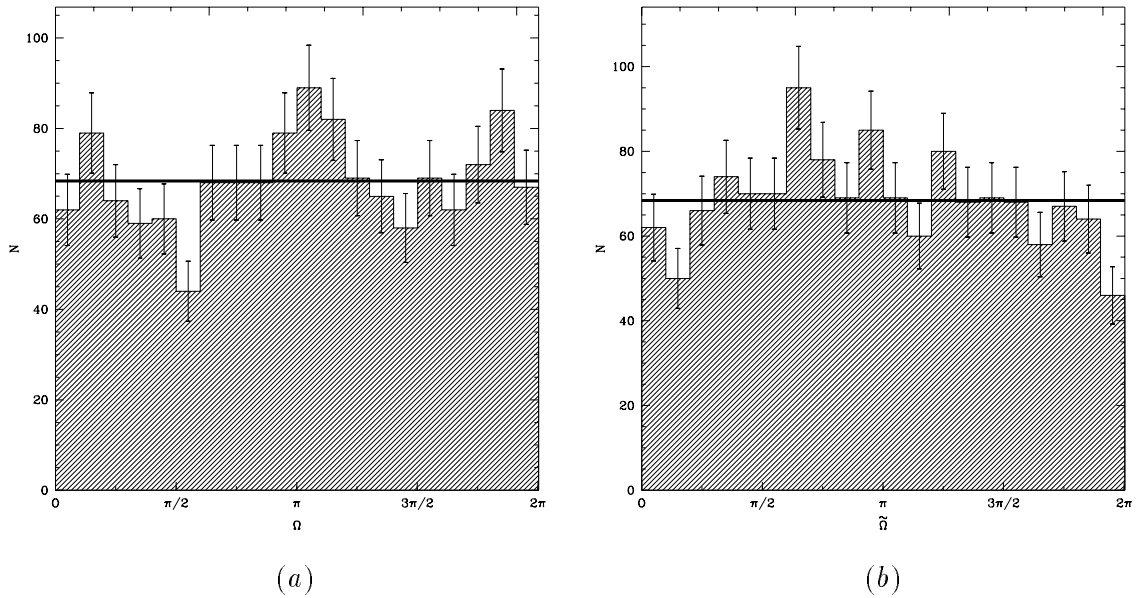


Figure 5.6: Distribution of the longitudes of the ascending nodes for the $V_1$ comets: $(a)$ at perihelion in the ecliptic frame, and $(b)$ at the previous aphelion in the Galactic frame.
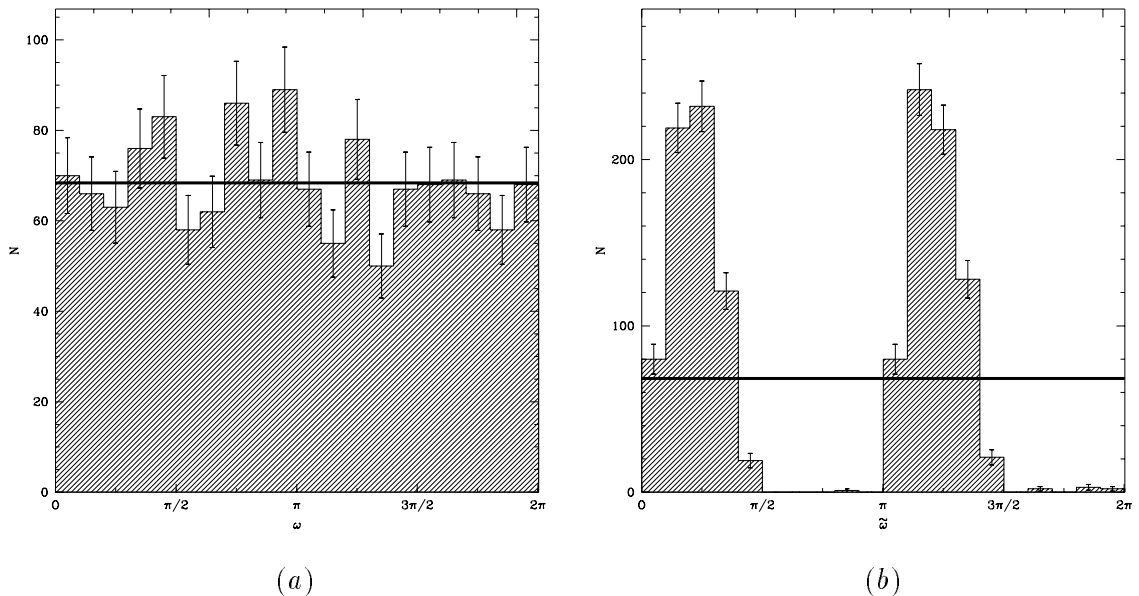
Figure 5.7: Distribution of the arguments of perihelion for the $V_1$ comets: $(a)$ at perihelion in the ecliptic frame, and $(b)$ at the previous aphelion in the Galactic frame.

be. The finite age of the Solar System provides no relief, as the dynamically oldest comets in our simulations are significantly less than 5 billion years old (Column 4 of Table 5.1). As it seems impossible to follow all comets to completion, it becomes necessary to arbitrarily terminate the simulations at some point, chosen here to be at their $5000^{th}$ orbit.

The longest-lived comets may provide clues to particularly stable regions in our Solar System, in terms of survival for large number of perihelion passages rather than for long times. The perihelion distances and semimajor axes of these comets on their $5000^{th}$ orbit are indicated in Figure 5.9. These comets tend to be on small orbits, with semimajor axes less than 1000 AU, and there is an excess (39/57, 68%) of prograde comets, unexpected due to the shorter diffusion times of prograde comets (§ 3.10.2). These comets' periods are typically much longer than the planets', and only a few comets are near mean motion resonance.

## 5.2  Dynamically evolved long-period comets

Given a set of $V_1$ comets, the next logical step is to evolve them forward in time. The set of all apparitions made by the LP comets throughout their evolution consitutes the dynamically evolved LP comets.

$(a)$                                                          $(b)$
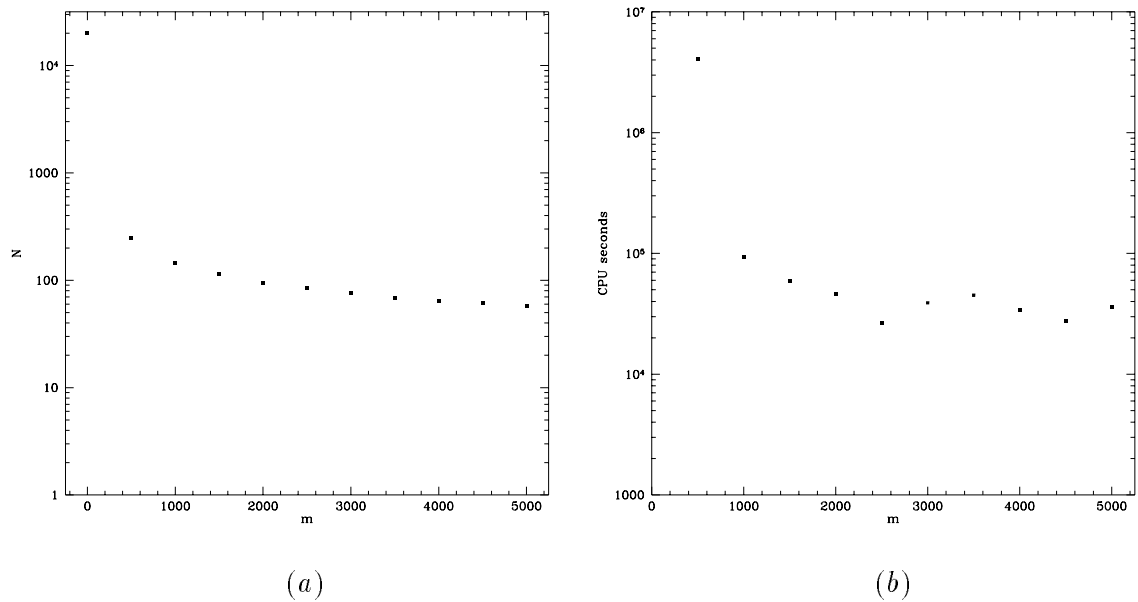
Figure 5.8: Number of $(a)$ long-period comets remaining in the Solar System , and $(b)$ CPU seconds required to simulate all surviving comets for the previous 500 orbits, both plotted as a function of age $m$ measured in perihelion passages since their to initial apparition.
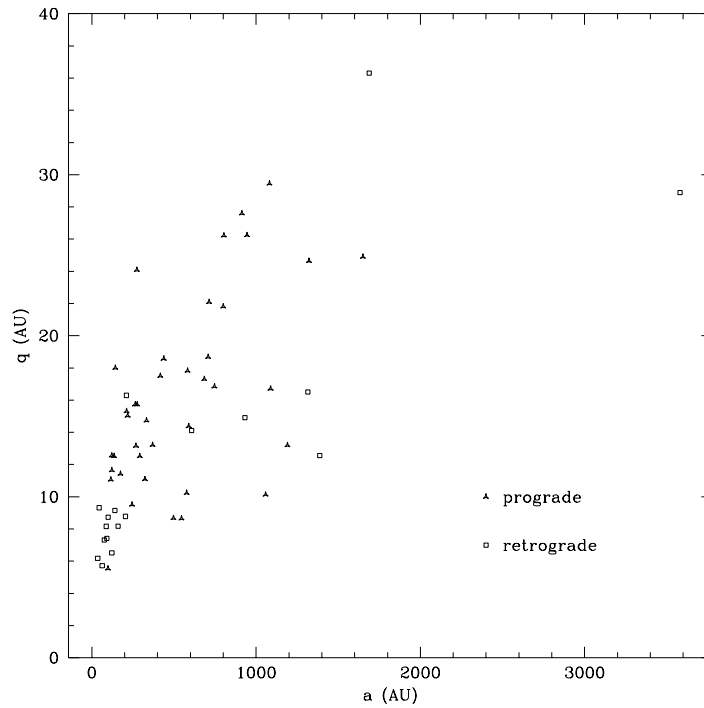


Figure 5.9: Perihelion distance $q$ versus semimajor axis $a$ for the 57 comets which survived 5000 orbits after their initialisation within the Oort cloud.

### 5.2.1 Element distribution parameters

It is useful to define a few simple parameters which describe the distributions of various orbital elements.

- The ratio $\Psi_1$ of the number of comets in the spike ($a > 10^4$ AU) to the total number of long-period comets was introduced in § 3.10.1.

- The inverse semimajor axis range available to LP comets runs from zero (unbound) to 0.029 AU$^{-1}$ (short-period). Let the ratio of the number of comets in the inner half of this range (0.0145 to 0.029 AU$^{-1}$) to the total number be $\Psi_2$, providing a measure of the "tail" of the energy distribution.

- Let the ratio of prograde comets to the total number be $\Psi_3$.

For each of these parameters, the ratio of the theoretical value $\Psi_n$ to the observed (indicated by a prime) value $\Psi'_n$ will be called $\Xi_n$. The following values of $\Psi'$ are adopted to be used for the determination of $\Xi$:

$$\Psi'_1 = 81/246 = 0.329 \pm 0.042,$$
$$\Psi'_2 = 18/246 = 0.073 \pm 0.018,$$
$$\Psi'_3 = 127/246 = 0.516 \pm 0.056.$$

These numbers are based on those comets in Marsden and Williams catalogue with perihelion distances less than 3 AU. The error estimates are based on Poisson noise.

### 5.2.2 Evolved long-period comets

The simulation that evolves the $V_1$ comets throughout their lifetimes, but which does not include any perturbers except for the giant planets and the tide will be called the **standard case**. The distribution of end-states for this case is shown in Table 5.3. The VISIBLE end-state is disabled, as it is in all further simulations described in this chapter, and all comets are evolved until destroyed or lost. The mean comet lifetime is 45.3 orbits per comet, a factor of two less than for a simple diffusion process (§ 3.1.2) but significantly less than required to solve the fading problem (§ 3.10.1). The standard case has $\Xi_1 = 0.086$, $\Xi_2 = 3.93$ and $\Xi_3 = 0.59$, and fails to match the observations. The maximum allowed number

| End-state | Ejection | Large $q$ | Short pd. | Total |
|---|---|---|---|---|
| Number | 1223 | 109 | 36 | 1368 |
| Fraction | 0.894 | 0.080 | 0.026 | 1.000 |
| Minimum $t_x$ | 0.296 | 2.61 | 0.014 | 0.014 |
| Median $t_x$ | 1.33 | 4.62 | 0.67 | 1.40 |
| Maximum $t_x$ | 31.7 | 71.0 | 7.94 | 71.0 |
| Minimum $m_x$ | 1 | 1 | 13 | 1 |
| Median $m_x$ | 1 | 2 | 330 | 1 |
| Maximum $m_x$ | 5832 | 2158 | 4277 | 5832 |

Table 5.3: The distribution of end-states of the $V_1$ comets, simulated from initial apparition until all are either lost or destroyed. The minimum, median and maximum lifetimes $t_x$ of these comets are measured from their first apparition. Of the 61 864 subsequent perihelion passages, 45% (28 004) are made by the 12 comets which survive for 1000 or more orbits after their first apparition. No comets escape, suffer collisions with the planets or Sun, or survive for the age of the Solar System.

of orbital periods before the EXCEEDED TIME LIMIT end-state (§ 4.3) is invoked is 10 000 orbits for the standard case simulations, but no comets reach this end-state.

The planets are the dominant perturbers of dynamically older comets, and ejection is the most common end-state: 89% of $V_1$ comets meet this fate. The details of close encounters between comets and the giant planets after initial visibility are detailed in Table 5.4. Perhaps most surprising is the high frequency of multiple encounters with a giant planet by a single comet. This does not indicate a capture by the planet but typically arises when a very distant encounter — often near the comet's perihelion and which leaves the comet's orbit relatively undisturbed — is followed by one or more subsequent encounters, in many cases resulting in the ultimate ejection of the comet.

About 8% (109/1368) of comets move back out to large perihelion distances. Most of these remain members of the Oort cloud: the median $1/a$ of these comets is $4 \times 10^{-5}$ AU$^{-1}$ ($a = 25\,000$ AU). Only 38 have $a < 10\,000$ AU, with the smallest orbit having a semimajor axis of about 1000 AU.

Poissonian, $\sqrt{N}$ error-bars are no longer appropriate for histograms of the number distributions, as the individual apparitions are no longer uncorrelated: one comet may contribute hundreds or thousands of perihelion passages. The appropriate error bars in this case are bootstrap estimators, and subsequent figures show the one standard deviation uncertainties estimated by this method (Efron 1982; Press et al. 1992).

| Planet | Sun | Jupiter | Saturn | Uranus | Neptune | Total |
|---|---|---|---|---|---|---|
| Number of comets | 7 | 28 | 12 | 2 | 3 | 52 |
| Number of encounters | 16 | 43 | 16 | 4 | 3 | 82 |
| Encounters/comet | 2.3 | 1.5 | 1.3 | 2.0 | 1.0 | 1.6 |
| Collisions | 0 | 0 | 0 | 0 | 0 | 0 |
| Captures | — | 0 | 0 | 0 | 0 | 0 |
| Min. distance ($R_I$) | — | 0.018 | 0.086 | 0.17 | 0.16 | 0.018 |
| Min. distance ($R_p$) | 1.61 | 12.5 | 77.9 | 335 | 553 | 12.5 |
| Outer satellite ($R_p$) | — | 326 | 216 | 23 | 222 | — |

Table 5.4: Planetary close encounter data for the dynamically evolved long-period comets. The distance to each planet's outermost satellite is given in the last row.

**Perihelion distance**

The perihelion distribution of the dynamically evolved visible comets is shown in Figure 5.10. The structure visible is partly due to the strongly correlated contributions of very long lived comets: of the 61 864 visible perihelion passages, over 45% (28 004) are made by the 12 comets which survive for 1000 or more orbits after their first apparition. Comparison with the observed distribution (Figure 2.5) reveals some superficial similarities, but the strong observational selection in favour of objects near the Sun or the Earth makes drawing conclusions difficult.

Let the total number of comets with perihelia inside $q$ be $N$. Then a linear least-squares fit to the simulated distribution yields $dN/dq$ roughly proportional to $1 + q$ for $q < 3$ AU, similar to Everhart's (1967b) earlier estimate of the intrinsic perihelion distribution. However, the simulations could arguably be consistent with any number of slowly varying functions of perihelion over $0 < q < 3$ AU, possibly including $dN/dq \propto q^{1/2}$, as proposed by Kresák and Pittich (1978). The estimates of the intrinsic perihelion distribution of LP comets published by Everhart and by Kresák and Pittich are indicated on Figure 5.10 by the solid and dashed curves.

**Orbital energy**

The original energy distribution of the visible comets is shown in Figure 5.11 at two different magnifications, for all 61 864 perihelion passages and for all 52 303 visible passages. The fraction $\Psi_1$ of comets in the spike obtained from these simulations is $1473/52303 = 0.028$, all perihelion passages with 3 AU of the Sun being deemed observed. Thus the simulations produce 35 visible LP comets for each comet in the spike, whereas the observed sample has
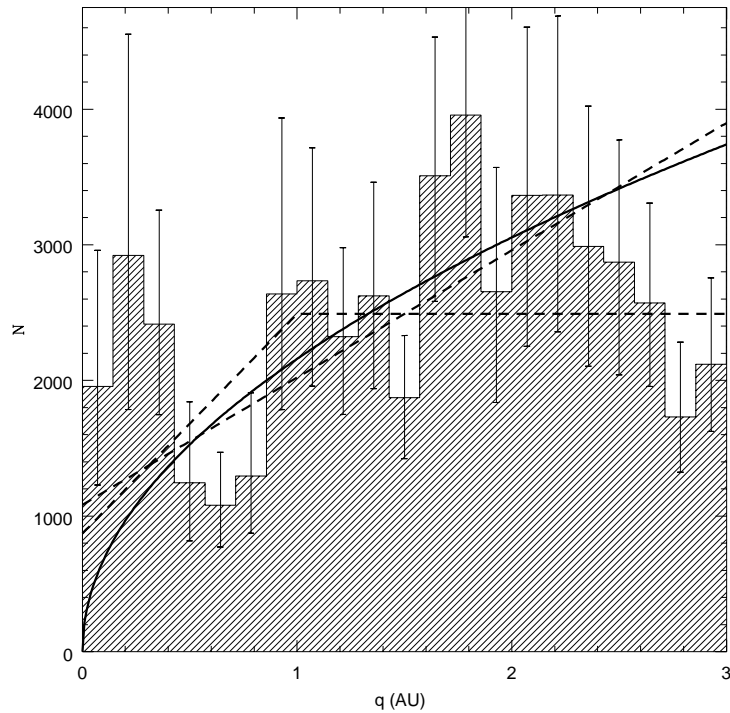
Figure 5.10: Distribution of perihelion distances $q$ for the dynamically evolved LP comet population. Error bars are bootstrap-based one $\sigma$ estimates. The curves are Everhart's (1967b, dashed lines) and Kresák and Pittich's (1982, solid line) estimates of the intrinsic perihelion distribution.

them in only a 3 to 1 ratio (Figure 2.3).

This disagreement is at the heart of the fading problem: how can the loss of 95% of the dynamically older long-period comets be explained? This question will be addressed in the upcoming sections of this chapter.

These simulations allow us to estimate the contamination of the spike by dynamically older comets. There are 1368 $V_1$ comets, of which 1340 have $a > 10^4$ AU, but a total of 1475 apparitions are made by comets with $a > 10^4$ AU. Thus roughly 7% of comets in the spike are not dynamically new, and 2% of comets coming from the Oort cloud do not make their first appearance within the spike. However, these numbers ignore the possibility of significant reductions in the brightness of LP comets over time, and are thus only upper limits (§ 5.5).
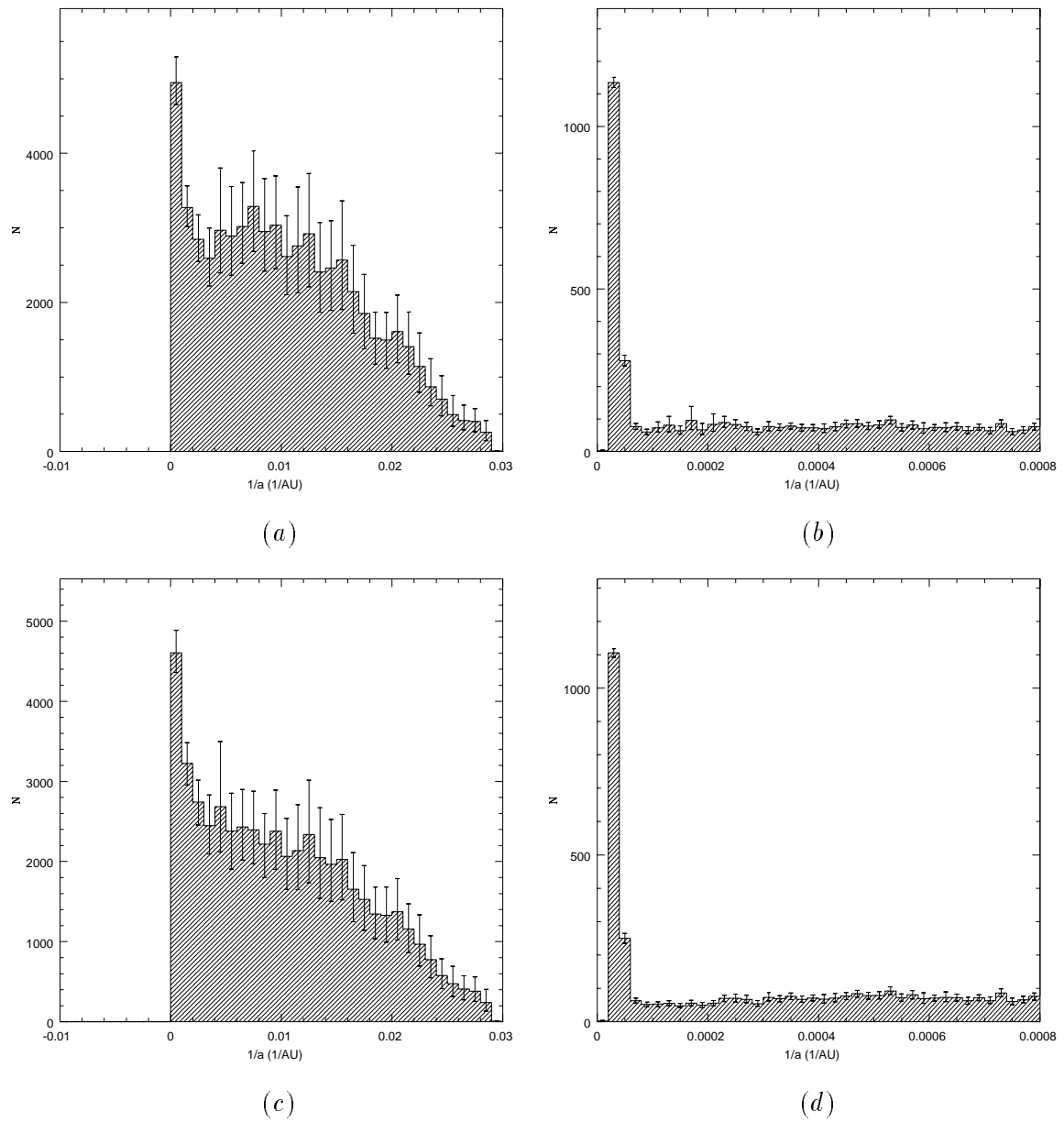
Figure 5.11: Distribution of original orbital energies for the dynamically evolved comets: $(a, b)$ for all perihelion passages and $(c, d)$ for those perihelion passages which are visible $(q < 3$ AU$)$.

**Angular elements**

The inclination distributions, in the ecliptic and Galactic frames, are shown in Figure 5.12. There is a noticeable excess of comets in ecliptic retrograde orbits: the fraction on prograde orbits is $15875/52303 \approx 0.3$. This is inconsistent with observations as Marsden's comets have a ratio near a half (Figure 2.7a). The simulated Galactic inclinations are consistent with a flat distribution, as expected from theory, but whether or not the observed distribution (Figure 2.7b) is flat is less clear.



$(a)$                                          $(b)$
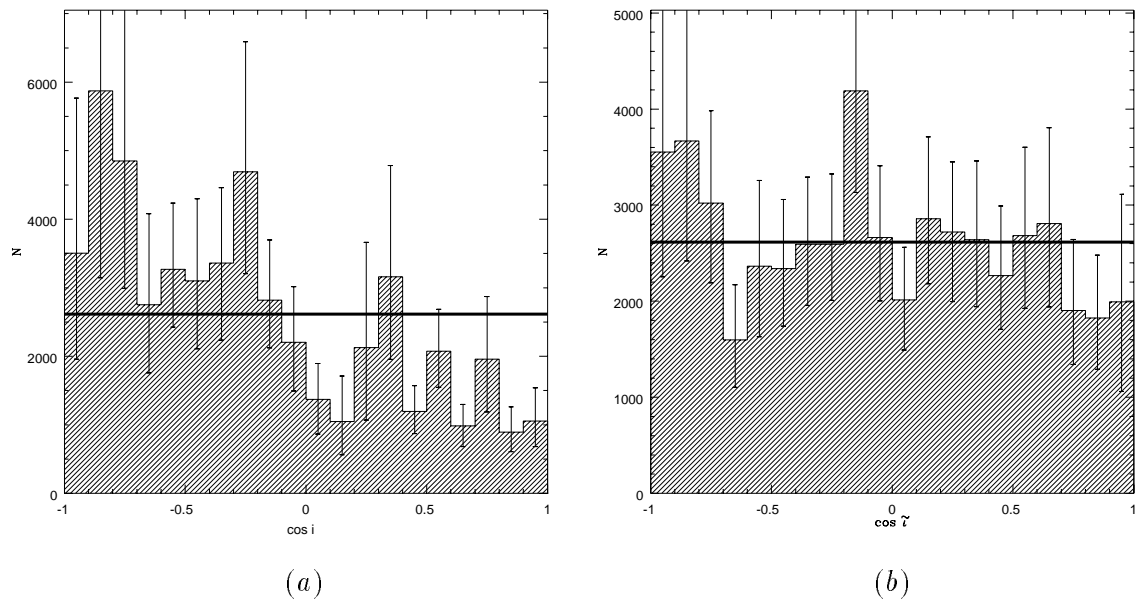
Figure 5.12: Distribution of the cosine of the inclination for the visible LP comets, $(a)$ taken at perihelion in the ecliptic frame, and $(b)$ at the previous aphelion in the Galactic frame.

Figure 5.13 shows the distribution of the longitude of the ascending node, and Figure 5.14, that of the argument of perihelion. The planets, the dominant perturbers, are not expected to produce strong signatures in these angular elements, and our results seem moderately consistent with this expectation. There are a few peaks in the figures, particularly in $\tilde{\Omega}$ and $\tilde{\omega}$, which may be statistically significant. These bumps are the result of several ($\sim 10$) long-lived comets clustered together in the phase space in question, but whether this is chance or a systematic effect is unclear.

The standard model provides only a poor fit to the observed distributions, in particular as regards the orbital energies and inclinations. Assuming that our simulations correctly portray the intended physics, the next question is: how do our simulations differ from
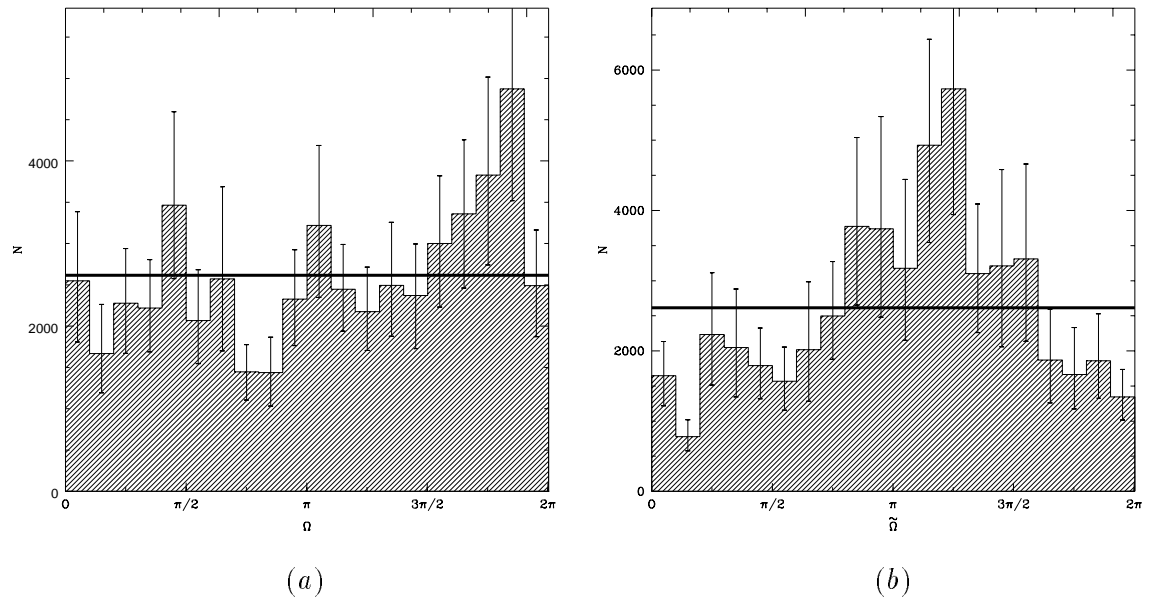
Figure 5.13: Distribution of the longitude of the ascending node of the visible LP comets, (a) taken at perihelion in the ecliptic frame, and (b) at the previous aphelion in the Galactic frame.
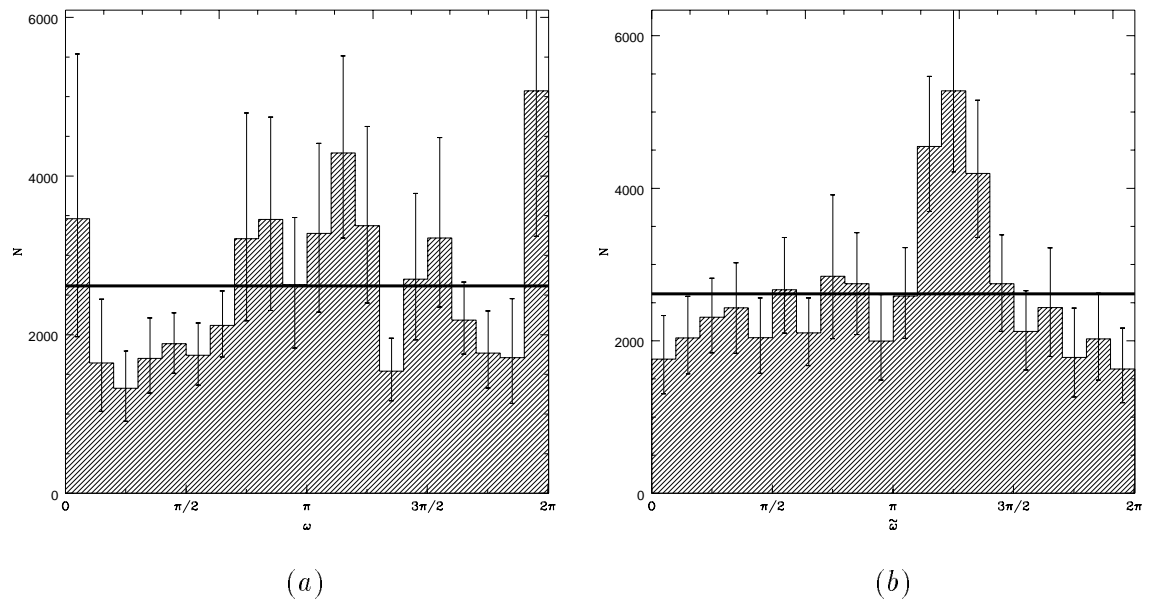


Figure 5.14: Distribution of the argument of perihelion of the visible LP comets, (a) taken at perihelion in the ecliptic frame, and (b) at the previous aphelion in the Galactic frame.

reality? Before going on to examine this question, we will consider the implications of these simulations regarding the population of the Oort cloud.

### 5.2.3   The current Oort cloud population

The flux into the entrance surface (Equations C.8a,b) can be integrated over all semimajor axes (or all $L$) in order to relate the constant $g_0$ to the total number of simulated comets $N_0$

$$t_s \int_{a_-}^{a_+} \Phi_E(a, q_E)\, da = t_s \int_{L_-}^{L_+} \Phi_E(L, J_E)\, dL = N_0. \tag{5.3}$$

where $t_s$ is the length of real time represented by our simulation. Equation 5.3 can easily be integrated numerically to yield $N_0 = 1.21 \times 10^{-10} g_0 t_s$ for the usual values of the parameters in question. For the 125 495 comets in our Oort cloud simulation (§ 5.1), this implies $g_0 = 1.04 \times 10^{15}\, t_s^{-1}$ yr. The value of $t_s$ depends on $N_0$ and the total number of comets in the Oort cloud.

Before calculating the value of $t_s$, consider first the total number of Oort cloud comets. As the Oort cloud is assumed to be in a steady-state, $r$ can be replaced in Equation 4.19 by its time average $\langle r \rangle \propto a$. Then the total number $N_{total}$ of comets in the Oort can be obtained through

$$\begin{aligned}
N_{total} &= \int_{a_-}^{a_+} n_0 a^\alpha 4\pi a^2 da = \int_0^{2\pi} df \int_0^{2\pi} d\tilde{\Omega} \int_0^{2\pi} d\tilde{\omega} \int_{L_-}^{L_+} dL \int_0^{L} dJ \int_{-J}^{J} g_0 L^{2\alpha+3}\, dJ_{\tilde{z}}, && \text{(5.4a)} \\
&= 4\pi^2 g_0 (a_-^{-1/2} - a_+^{-1/2}) && \text{(5.4b)} \\
&\approx 2.3 \times 10^{14} \left( \frac{t_s}{1\text{ year}} \right)^{-1}. && \text{(5.4c)}
\end{aligned}$$

where $\alpha = -3.5$ has been assumed, and from which the numerical value for the density coefficient can also be obtained

$$n_0 = \frac{\pi}{2} g_0 = 1.63 \times 10^{15} \left( \frac{t_s}{1\text{ year}} \right)^{-1}. \tag{5.5}$$

If one knows the number $N_{vo}$ of long-period comets crossing within 3 AU per unit time in our Solar System, the value of $t_s$ and hence the total number of comets in the Oort cloud can be estimated from Equation 5.4c. If the number of simulated comets which enter the visibility cylinder is $N_{vt}$ (1368 for our simulations), then $t_s \approx N_{vt}/N_{vo}$. The time-scale

over which Marsden and Williams (1993) catalogue is complete, if any, is unclear, but rough estimates of comet fluxes can be made. Everhart (1967b) estimated that 8000 comets passed within 4 AU of the Sun within a 127 year period, implying roughly 60 yr$^{-1}$ . Kresák and Pittich (1978) deduced 25 yr$^{-1}$ within Jupiter's orbit. Taking 10 yr$^{-1}$ within 3 AU as an estimate and assuming one in three of these is dynamically new (Festou et al. 1993b) yields

$$t_s \approx \frac{3 \cdot 1368}{10 \text{ yr}^{-1}} \approx 410 \text{ yr.} \tag{5.6}$$

This value implies an Oort cloud population of roughly $5 \times 10^{11}$ comets between 10 000 and 50 000 AU (Equation 5.4c). However, this method becomes an increasingly poor probe of the Oort cloud's population as distances become large and the visible flux falls to zero (Figure 5.3).

### 5.2.4 The original Oort cloud population

About 20% of Oort cloud comets crossing the entrance surface are removed from the cloud (§ 5.1). The flux of comets across the entrance surface is proportional to the total number of comets in the cloud (Equations 5.3 and 5.4a), thus both decay exponentially with time, ignoring other loss mechanisms. Roughly 20 000 comets are removed during the 400 years corresponding to these simulations, implying that approximately $3 \times 10^{11}$ objects have been lost since the Solar System's formation. As these figures ignore other loss mechanisms, particularly stripping by passing stars, they likely to be much too low. Nevertheless, it seems likely that the Oort cloud originally had at least twice its current population.

### 5.2.5 Discovery probability function

The previous simulations assumed that all comets passing within 3 AU of the Sun would be detected by astronomers; however, the strong bias in the observed distribution towards comets near either the Sun or the Earth (Figure 2.5) indicates that this is unlikely to be true.

Everhart (1967a) examined the LP comets which became part of the observed sample and concluded that comets which have the same **excess magnitude** $S_0$ have equal *a priori* chances of being discovered. The excess magnitude is defined by

$$S_0 = \int_0^\tau (H_{an} - H) \, \Theta(H_{an} - H) \, dt, \tag{5.7}$$

where $\tau$ is the comet's period, $H$ is its visual magnitude at the Earth (Equation 1.8), $H_{an}$ is some lower limiting magnitude, and $\Theta(x)$ is a step function which is unity where $x > 0$ and zero where $x \leq 0$. Comets with large values of $S_0$ are bright and visible for a relatively long time, and thus more likely to be observed.

Everhart found that the discovery probability $p_d$ increases roughly linearly with $S_0$. Here a form for $p_d(S_0)$ of

$$p_d(S_0) = \begin{cases} S_0/80 \text{ mag-weeks} & \text{if } S_0 < 80 \text{ magnitude-weeks} \\ 1 & \text{if } S_0 \geq 80 \text{ magnitude-weeks} \end{cases} \tag{5.8}$$

will be adopted. The excess magnitude depends sensitively on the position of the Earth, but for simplicity the Earth will be taken to be at its "average" position *i.e.* at the Sun, for these calculations. In this case, Equation 1.8 becomes

$$H \sim H_0 + (5 + 2.5n) \log_{10} r, \tag{5.9}$$

recalling that $r$ must be measured in AU. The values of $n$, $H_0$ and $H_{an}$ are taken to be 4, 7 and 13 respectively (Everhart 1967a,b). These values imply that the excess magnitude becomes non-zero at $q \lesssim 2.5$ AU.

Given the previous assumptions, the excess magnitude is simply a function of $q$. The trajectories of LP comets near the Sun approximate parabolas, and thus $r \approx 2q/(1 + \cos f)$ will be adopted. The excess magnitude is then

$$S_0 \approx \int_0^\tau [H_{an} - H_0 - (5 + 2.5n) \log_{10} r] \, \Theta(H_{an} - H) \, dt, \tag{5.10}$$

$$\approx \frac{12q^{3/2}}{(2GM_\odot)^{1/2}} \int_{-f_{an}}^{f_{an}} \frac{2 - 5 \log_{10}[2q/(1 + \cos f)]}{(1 + \cos f)^2} df, \tag{5.11}$$

where $f_{an}$ is the true anomaly at which the comet's visual magnitude exceeds the limit $H_{an}$, given by

$$f_{an} = \left| \cos^{-1} \left( 2q \, 10^{\frac{H_0 - H_{an}}{5 + 2.5n}} - 1 \right) \right| \approx |\cos^{-1} (0.8q - 1)|. \tag{5.12}$$

A plot of $S_0$ versus $q$ appears in Figure 5.15. The excess magnitude is 80 magnitude-weeks at $q \approx 1.5$ AU, and drops to zero at $q \approx 2.5$ AU, with a roughly linear relationship
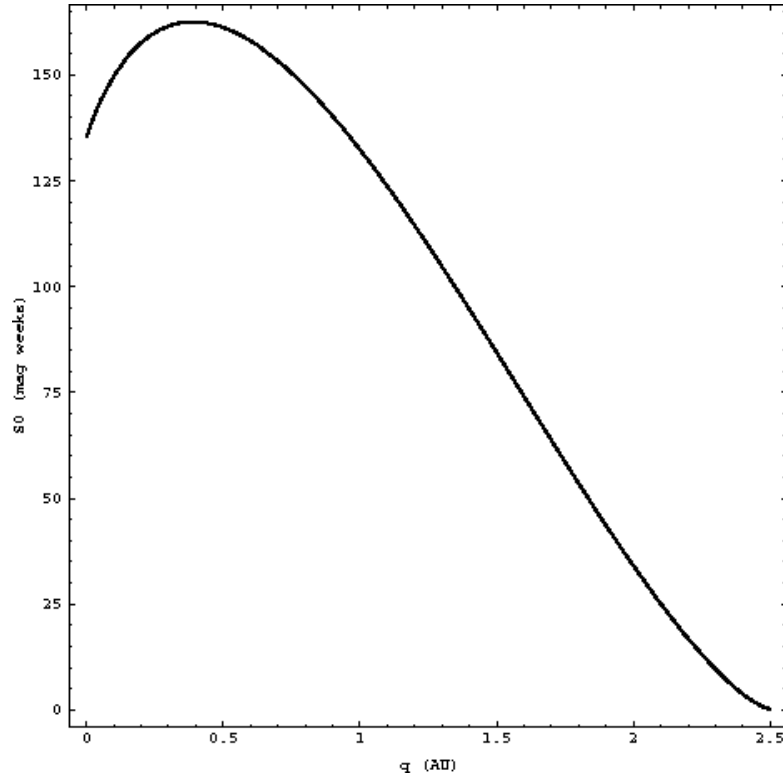
Figure 5.15: The simplified excess magnitude $S_0$ versus perihelion distance $q$, as expressed in Equation 5.11.

between these two points. As an approximation, the discovery probability is taken to be

$$p_d(q) = \begin{cases} 0 & \text{if } q > 2.5 \text{ AU}, \\ 2.5 - (q/1 \text{ AU}) & \text{if } 1.5 \leq q \leq 2.5 \text{ AU} \\ 1 & \text{if } q < 1.5 \text{ AU} \end{cases} \qquad (5.13)$$

The application of this discovery probability to our simulations is shown in Figure 5.16. This addition changes the agreement with observations very little, as the other orbital elements are only weakly correlated with perihelion. In some simulations where this is not the case, the comet discovery probability proves to be important, but it does little to improve the standard model.

## 5.2.6   Short-period comets

Before going on to consider other possible dynamical effects, let's consider first those short-period comets which originate at the Oort cloud. During the standard simulations, only 68 Oort cloud comets eventually become short-period comets, 36 of them after having made
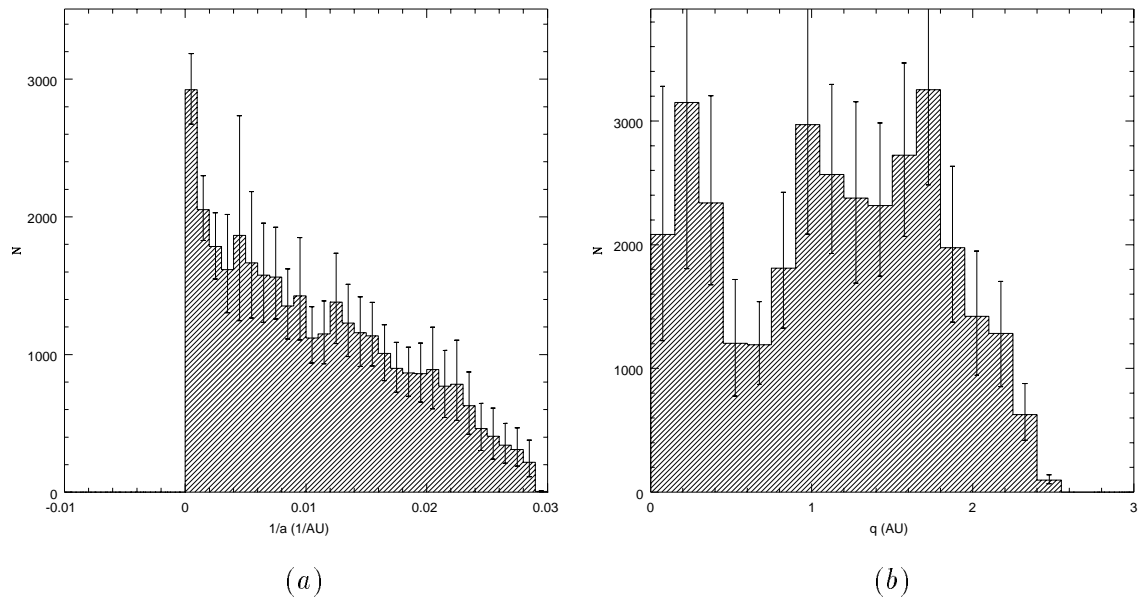
Figure 5.16: Distribution of (a) original orbital energies $1/a$ and (b) perihelion distances $q$ for the visible long-period comets, subject to the discovery probability function given by Equation 5.13.

one or more apparitions as LP comets. Only 34 of these have perihelia less than 3 AU *i.e.* are visible, on their first perihelion passage as SP comets.

The aphelion directions of all 68 of these SP comets are shown in Figure 5.17. Though small numbers make the data relatively noisy, there may be some concentration of comets in the ecliptic plane.

The distributions of inverse semimajor axis, perihelion distance and inclination are shown in Figure 5.18. None of the SP comets arrive directly from the Oort cloud. The one with the largest orbit at the previous aphelion has a semimajor axis of only 1850 AU, and was on its sixth orbit since crossing the entrance surface. The perihelion distribution tends to increase towards the Sun, but the error bars are too large to draw any firm conclusions from this trend. There is a distinct concentration of orbits near zero inclination, as expected from studies of captures of comets by Jupiter from spherical sources (Everhart 1972), but much less than that of short-period comets in our Solar System (Figure 2.1). The prograde fraction is $44/68 \approx 0.65$.

In § 5.2.3, the standard case simulations are found to correspond to approximately 400 years of real time (Equation 5.6). The standard model thus implies that $68/400 \approx 0.17$ short-period comets per year arrive (indirectly) from the Oort cloud, though this number
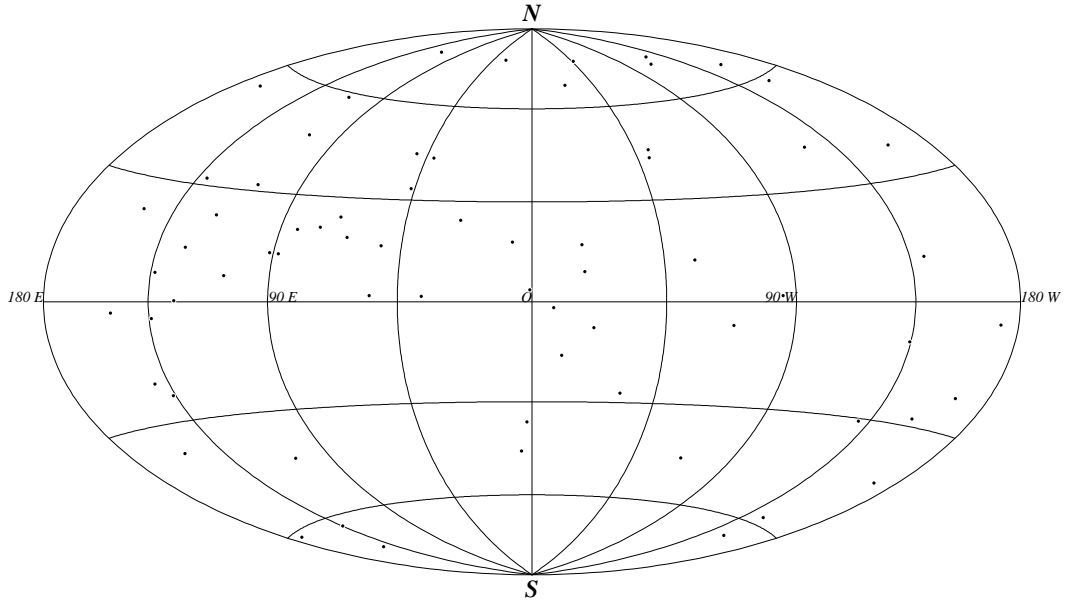
Figure 5.17: Short-period comet aphelion directions (standard case) on an ecliptic equal-area map. Aphelion directions are measured on the aphelion previous to their first perihelion passage as a short-period comet.

is really an upper limit as fading has not yet been considered. As an average of five new SP comets are discovered each year (Festou et al. 1993a), one deduces that the Oort cloud must contribute less than 3% of the population of SP comets, and another source for these comets is required. Our results thus are consistent with the the primary source of SP comets being the Kuiper belt.

### 5.2.7 Planetary encounter rates

The length of time represented by these simulations will be shown to be roughly 400 yr (§ 5.2.3), and from this the rate of close encounters between the LP comets and the giant planets can be calculated. A total of 253 encounters by 88 objects were recorded for Jupiter, 333 by 157 for Saturn, 111 by 73 for Uranus and 96 by 70 for Neptune. These numbers translate to total rates of 0.6, 0.8, 0.3 and 0.2 comets per year passing through the spheres of influence (Equation 4.5) of Jupiter through Neptune respectively.

If these numbers are naively taken to represent a uniform flux $\mathcal{F}$ across the sphere of influence, the rate $n$ of impacts between LP comets and the giant planets can be deduced to be

$$n = \mathcal{F} \left( \frac{M_p}{M_\odot} \right)^{-4/5} \left( \frac{R_p}{r_p} \right)^2, \tag{5.14}$$
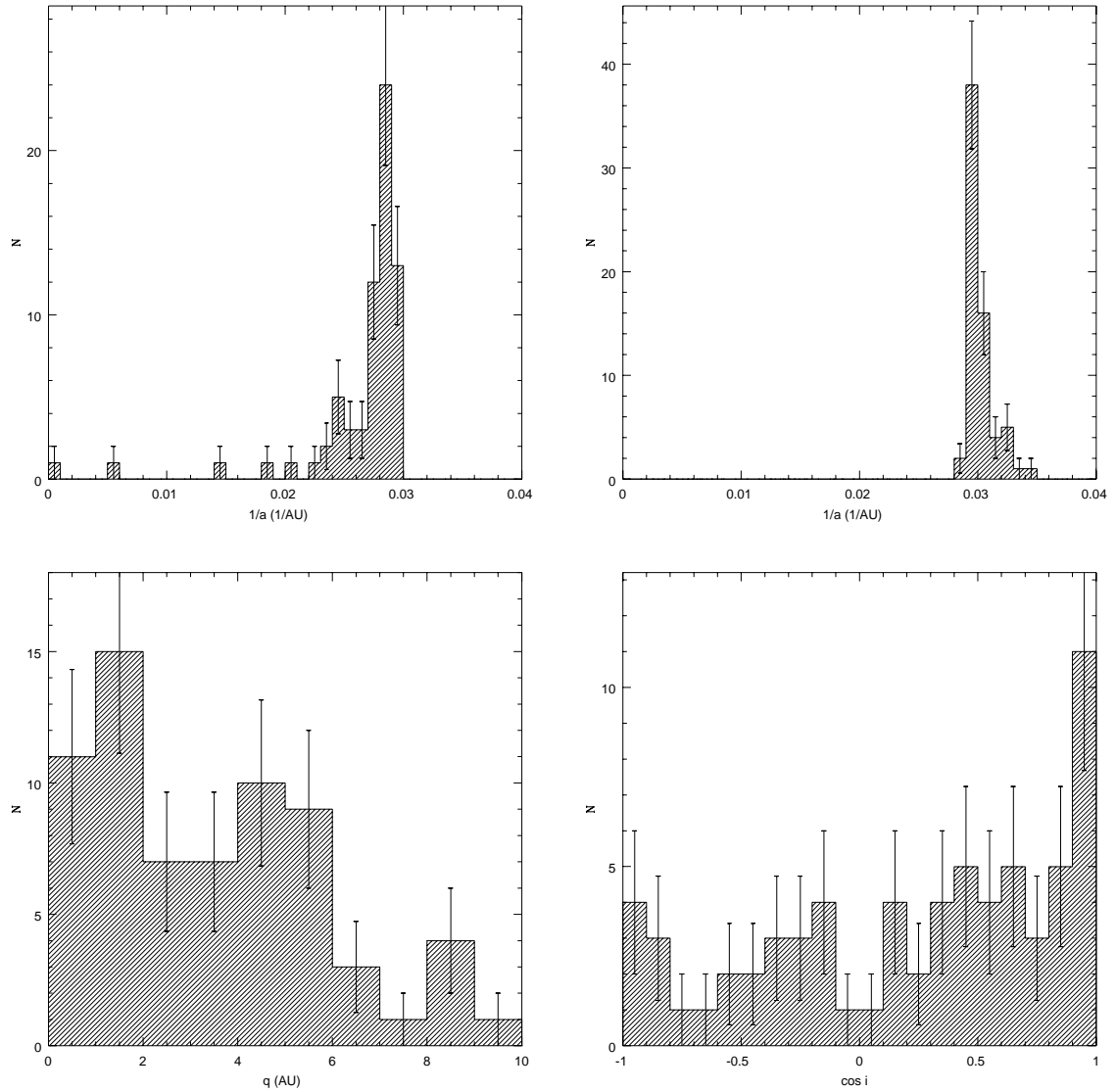
Figure 5.18: The distribution of the inverse semimajor axis $1/a$, perihelion distance $q$ and cosine of the inclination $i$ for the short-period comets produced in the standard model. The distribution of $1/a$ on the left is measured at the aphelion previous to, and the other distributions measured at the initial perihelion passage as a SP comet, for the standard case.

where $r_p$ and $R_p$ are the planets' orbital and physical radii, and $M_p$, their mass. The resulting collision rates are $2 \times 10^{-6}$, $10^{-6}$, $7 \times 10^{-8}$, $2 \times 10^{-8}$ per year for Jupiter through Neptune respectively. It should be noted that Comet Shoemaker-Levy 9, which collided with Jupiter in July of 1994, was not a LP comet when captured by that giant planet but rather a SP Jupiter-family comet (Benner and McKinnon 1995).

## 5.3 Non-gravitational forces

In the previous simulations, only the Galactic tide and giant planets were included. The expected effects of outgassing forces on the dynamics of comets were detailed in § 3.3. Non-gravitational forces are specified by two parameters (§ 3.3). The radial component $A_1$ is always positive, as the outgassing force always accelerates the comet away from the Sun. The tangential component $A_2$ is generally less than $A_1$ ($|A_2| = 0.1|A_1|$ will typically be adopted here), and may be of either sign depending on the comet's rotation.

### 5.3.1 Two simple cases

Consider two simple cases, each with non-gravitational forces $A_1 = 10^{-8}$ AU day$^{-2}$, and $|A_2| = 0.1A_1$. In the first case, $A_2$ will be taken to be positive, and in the second, negative. These choices imply a constant rotation vector for the nucleus, which is unlikely, but test the cases in which the NG forces are maximally efficient.

In the first case, $A_1 = 10^{-8}$ AU day$^{-2}$ and $A_2 = +10^{-9}$ AU day$^{-2}$. The distributions of orbital elements produced are shown in Figure 5.19, and are characterised by the parameters $\Xi_1 = 0.13, \Xi_2 = 2.85$ and $\Xi_3 = 0.68$. The orbital energy and perihelion distance are expected to decrease secularly under the NG forces (Equations 3.35a and 3.35b). Thus the NG forces act to unbind comets, both by reducing $1/a$ and by drawing the comets' perihelia inwards to where the NG forces are more effective. This results in an increase in $\Xi_1$ to 0.13 from 0.09 in the standard case, insufficient to produce a match with observations.

There is only a 3% increase in the number of comets ejected over the standard case, but there is a significant reduction in comet lifetimes, to a mean of 36.1 from 47.7 orbits. This is due to a decrease in the lifetime of ejected comets to 22.2 orbits from 29.7. The perihelion distribution (Figure 5.19) shows a strong erosion of the comet population at small perihelion distances. This indicates that even modest non-gravitational forces likely play a

$(a)$                                            $(b)$
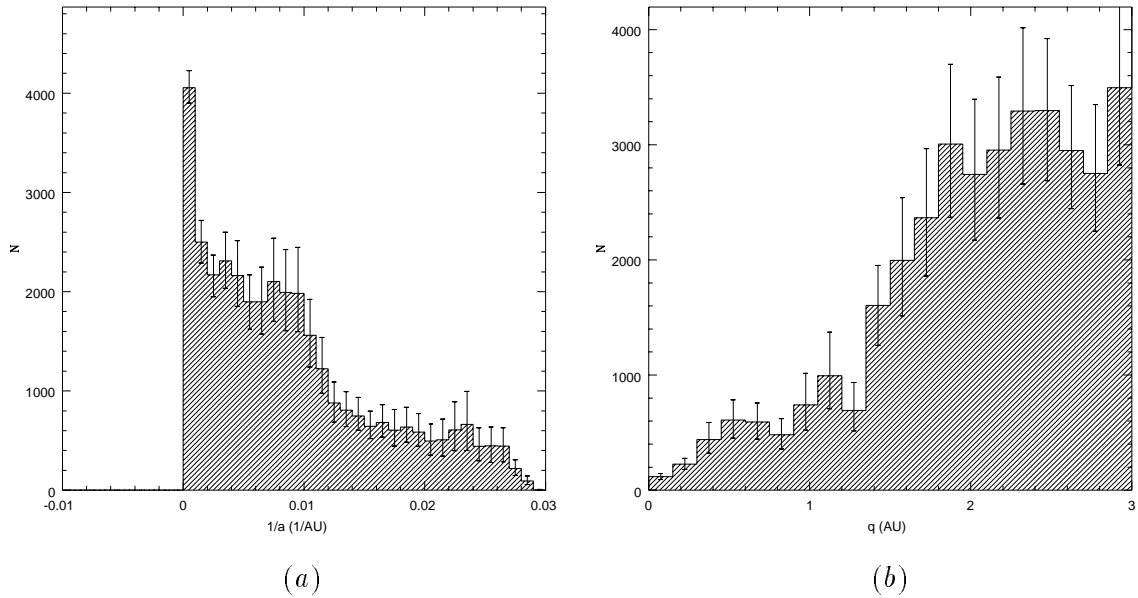
Figure 5.19: Distribution of the $(a)$ original inverse semimajor axis $1/a$, and $(b)$ the perihelion distance $q$ for the visible LP comets under non-gravitational forces characterised by $A_1 = 10^{-8}$ AU day$^{-2}$ and $A_2 = 10^{-9}$ AU day$^{-2}$.

significant role in shaping the perihelion distribution of the LP comets.

The second case, with $A_1 = 10^{-8}$ AU day$^{-2}$, $A_2 = -10^{-9}$ AU day$^{-2}$ is identical to the previous one, except for $A_2$ being of the opposite sign. In this case, the NG forces act to increase the perihelion distance and $1/a$ of comets (Equations 3.35a and 3.35b), tending to circularise their orbits. The increase in $1/a$ causes comets to evolve into more tightly bound, and hence long-lived orbits (average lifetime: 51.0 orbits). There is also an increase in short-period comet production: 102 versus 68 in the standard case. The distribution parameters are $\Xi_1 = 0.08$, $\Xi_2 = 5.07$ and $\Xi_3 = 0.77$, which show no improvement over the standard case.

The perihelion distribution shows little or no erosion near the Sun, as there is no preferential unbinding of comets with small $q$. The distribution does not increase noticeably towards larger perihelion, despite the secular increase in $q$, presumably because the rate of increase of perihelion is quite small.

## 5.3.2   More realistic non-gravitational forces

Neither of the two simple cases presented above match the observed distributions particularly well. But realistically, Oort cloud comet nuclei are likely to have randomly oriented
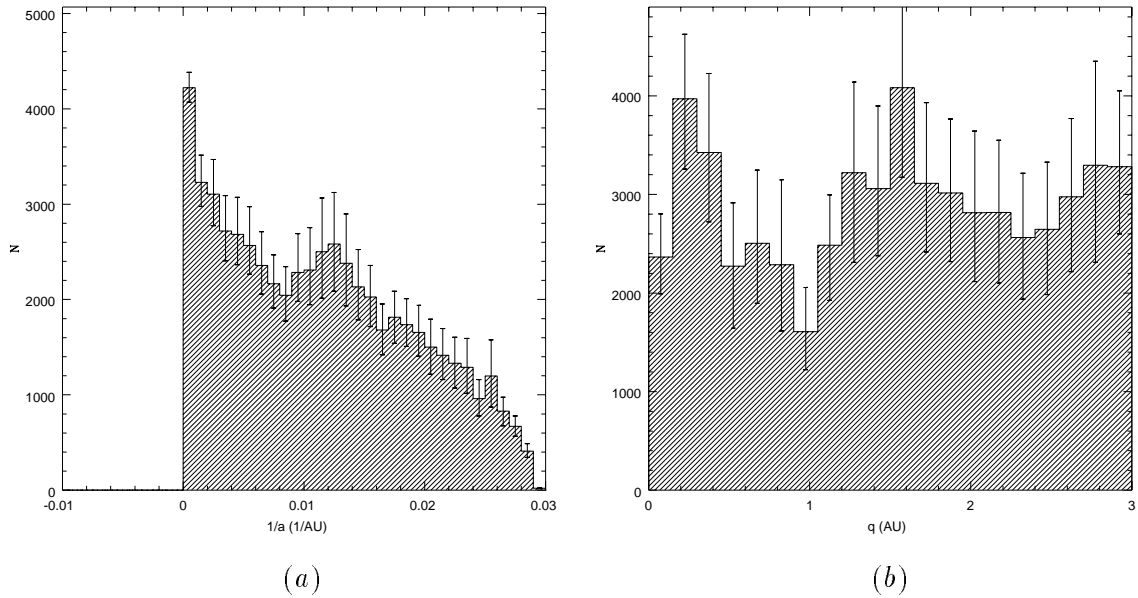
Figure 5.20: Distribution of the $(a)$ original inverse semimajor axis $1/a$, and $(b)$ the perihelion distance $q$ for the LP comets, under non-gravitational forces characterised by $A_1 = 10^{-8}$ AU day$^{-2}$ and $A_2 = -10^{-9}$ AU day$^{-2}$.

axes of rotation, with a corresponding random value of $A_2$. While a complete investigation of the available parameter space is beyond this project, the inadequacy of NG forces to resolve the fading problem completely can be demonstrated with only a few sample simulations.

It will be assumed that the value of $A_1$ is always ten times that of $|A_2|$. Two distributions of the sign of $A_2$ will be considered:

1. Half the comets have positive values of $A_2$, half negative, and the sign of $A_2$ is constant throughout a comet's lifetime. This corresponds to the axis of rotation of the nucleus remaining essentially unchanged throughout the comet's dynamical lifetime.

2. The sign of $A_2$ is randomised after each perihelion passage, with a 50% chance of being either positive or negative. This corresponds to a rapid changing of the axis of rotation due to precession of the nucleus.

Eight different simulations were performed: four values of $A_2$ are examined from $10^{-9}$ to $10^{-5}$ AU day$^{-2}$, in factor of ten increments, and each is run for both distributions of $A_2$ discussed above. The sets containing the weakest NG forces $i.e.$ $A_2 = 10^{-9}$ and $10^{-8}$ AU$^{-1}$, are reasonably consistent with the NG forces calculated for known LP comets (Marsden et al. 1973). The two largest values for $A_2$ are probably unrealistic: in the

strongest case, the $\Delta(1/a)$ due to NG forces over one orbit exceeds that due to the planets by a factor of 100. Nonetheless, these experiments provide useful test cases.

There are a number of biases introduced into the simulations when very strong NG forces are introduced. Firstly, NG forces may become non-negligible for comets with $q > 3$ AU, which is not accounted for in our simulations. Secondly, though some NG perturbations average to zero over a full orbit, their effects over fractions of an orbit may become dynamically important for very large NG forces *e.g.* Equation 3.37a.

Figure 5.21 illustrates the results of the simulations including the more realistic NG forces, and Table 5.5 lists some associated quantities. It is found that increasing the NG forces does decrease the number of dynamically older LP comets in the system, (*i.e.* increasing $\Xi_1$, decreasing $\Xi_2$), but also erodes the population of comets at small perihelion distances. Note that even excessive NG forces cannot bring the distribution of inverse semi-major axes into line with observations and result in an extreme depletion of comets with small perihelia, in contradiction with observations (Figure 2.5). The failure of the NG forces can be summarised as follows:

- Perturbations due to radial NG forces average to zero over a full orbit and thus have no long-term effect on LP comet evolution, assuming outgassing is symmetrical about perihelion.

- Positive values of the tangential acceleration $A_2$ reduce the tail of the population, resulting in an increase in $\Xi_1$ towards unity and improving the match with observations, but erode the population at small perihelia, an effect which is not seen in the observed sample.

- Negative values of $A_2$ preserve a reasonable perihelion distribution, but increase the number of comets in the tail of the energy distribution, thus reducing $\Xi_1$ and degrading the match of the $1/a$ distribution.

Though one might be able to concoct a mixture of NG forces which will result in a better match with the observations, non-gravitational forces seem unable to decisively resolve the fading problem.
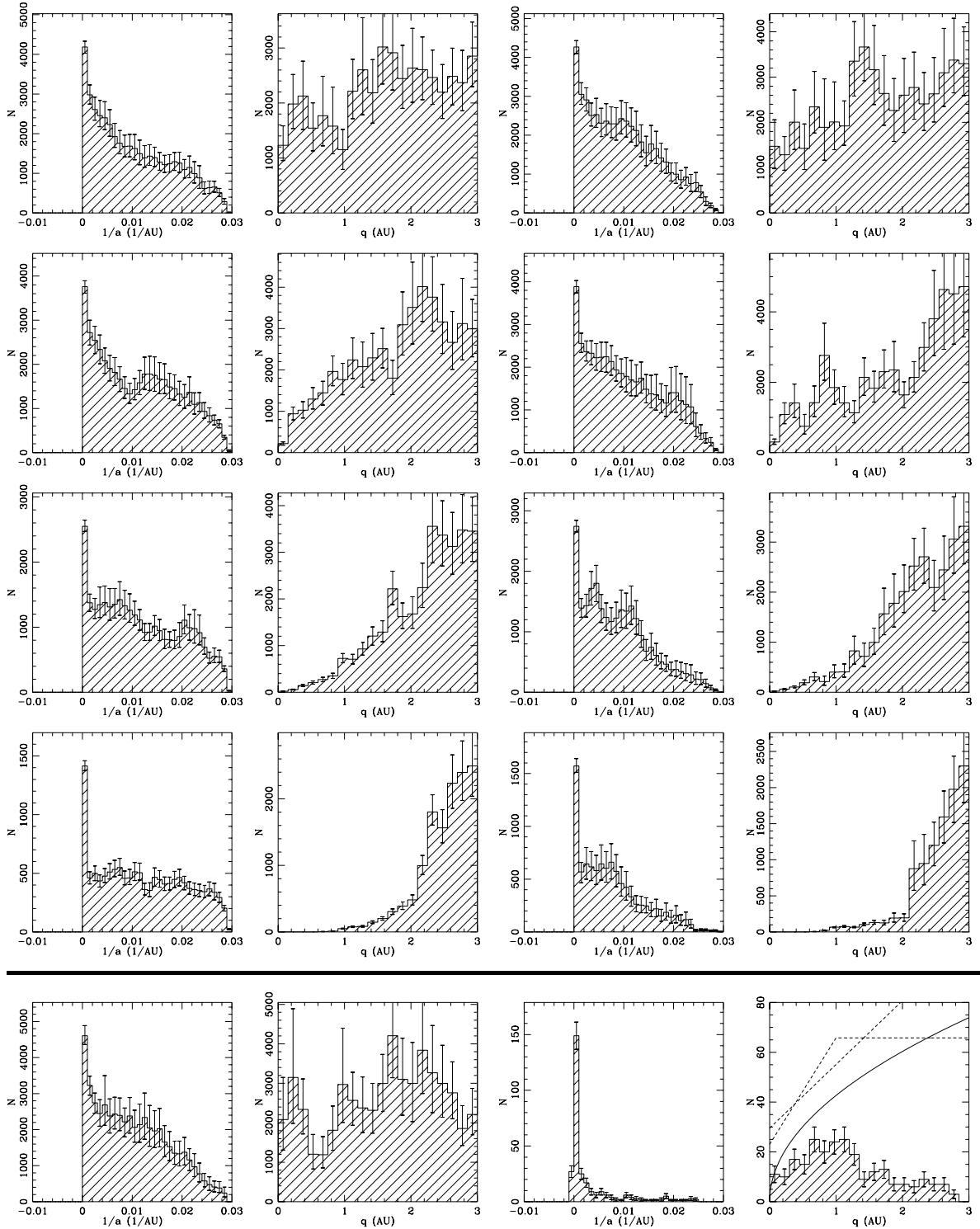
Figure 5.21: Distributions of the inverse semimajor axis $1/a$ and perihelion distance $q$ for the visible LP comets. On the left: constant values for $A_2$, half positive, half negative. On the right: the sign of $A_2$ is randomised for each perihelion passage. The values of $|A_2|$ used are, from the top down, $10^{-9}$, $10^{-8}$, $10^{-7}$ and $10^{-6}$ AU day$^{-2}$, with $A_1 = 10|A_2|$. The bottom section is for comparison, and includes the standard case (left side) and the observations (right side). The observed perihelion distribution includes curves indicating the estimated intrinsic distribution (§ 5.2.2).
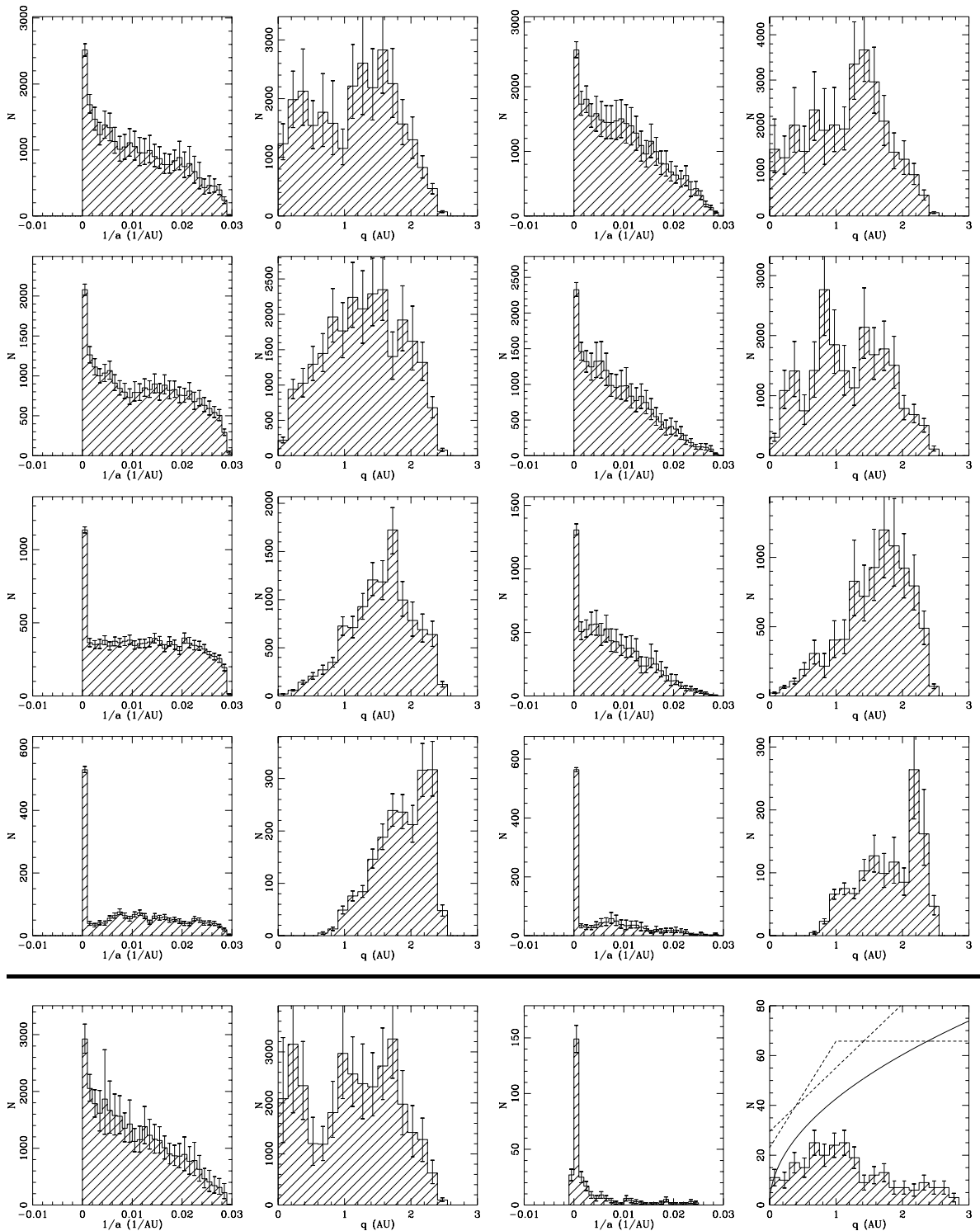
Figure 5.22: Distributions of the inverse semimajor axis $1/a$ and perihelion distances $q$ for the LP comets, when a discovery probability (Equation 5.13) is applied. The simulations are otherwise identical to those in Figure 5.21.

| $A_1$ | $A_2$ | Total | Spike | Tail | Prograde | $\Xi_1$ | $\Xi_2$ | $\Xi_3$ | $\bar{m}$ |
|---|---|---|---|---|---|---|---|---|---|
| 0.0 | 0.0 | 52303 | 1473 | 15004 | 15875 | 0.09 | 3.93 | 0.59 | 45.4 |
| 1.0 | 0.1 | 35370 | 1457 | 7368 | 12381 | 0.13 | 2.85 | 0.68 | 36.1 |
| 1.0 | $-0.1$ | 57819 | 1462 | 19364 | 21110 | 0.03 | 4.59 | 0.71 | 51.0 |
| 1.0 | $\pm 0.1^a$ | 44383 | 1461 | 13705 | 19021 | 0.10 | 4.23 | 0.83 | 38.4 |
| 10 | $\pm 1^a$ | 45899 | 1425 | 16628 | 18504 | 0.09 | 4.96 | 0.78 | 42.5 |
| 100 | $\pm 10^a$ | 30660 | 1341 | 11296 | 11012 | 0.13 | 5.05 | 0.70 | 33.1 |
| 1000 | $\pm 100^a$ | 13248 | 995 | 5432 | 5872 | 0.23 | 5.62 | 0.86 | 14.4 |
| 1.0 | $\pm 0.1^b$ | 49642 | 1450 | 13203 | 16387 | 0.09 | 3.64 | 0.64 | 46.7 |
| 10 | $\pm 1^b$ | 45202 | 1448 | 13631 | 17311 | 0.10 | 4.13 | 0.74 | 41.4 |
| 100 | $\pm 10^b$ | 25774 | 1364 | 4969 | 11452 | 0.16 | 2.64 | 0.86 | 27.7 |
| 1000 | $\pm 100^b$ | 9878 | 1035 | 1536 | 5042 | 0.32 | 2.13 | 0.99 | 13.2 |

Table 5.5: The parameters of the visible LP comet orbits under different non-gravitational forces. "Total" is the total number of apparitions *i.e.* $q < 3$ AU, "Spike" is the number of these with original semimajor axes greater than $10^4$ AU, and "Prograde" the number with ecliptic inclinations less than $90°$. The lifetime in orbits $\bar{m}$ includes all perihelion passages, regardless of $q$, after the initial apparition. The superscript $^a$ indicates that half the sample have positive $A_2$, half negative; $^b$ indicates $A_2$ has a random sign assigned for each perihelion passage.

| $A_1$ | $A_2$ | Total | Spike | Tail | Prograde | $\Xi_1$ | $\Xi_2$ | $\Xi_3$ | Undisc. |
|---|---|---|---|---|---|---|---|---|---|
| 0.0 | 0.0 | 33365 | 957 | 10008 | 10140 | 0.09 | 4.11 | 0.59 | 0.36 |
| 1.0 | 0.1 | 15010 | 941 | 2247 | 5422 | 0.19 | 2.05 | 0.70 | 0.57 |
| 1.0 | $-0.1$ | 38126 | 945 | 14121 | 15132 | 0.08 | 5.07 | 0.77 | 0.34 |
| 1.0 | $\pm 0.1^a$ | 27617 | 944 | 9256 | 11223 | 0.10 | 4.59 | 0.79 | 0.38 |
| 10 | $\pm 1^a$ | 24606 | 908 | 9946 | 11281 | 0.11 | 5.54 | 0.89 | 0.46 |
| 100 | $\pm 10^a$ | 10789 | 843 | 4659 | 4326 | 0.24 | 5.92 | 0.78 | 0.65 |
| 1000 | $\pm 100^a$ | 1943 | 508 | 668 | 821 | 0.80 | 4.71 | 0.82 | 0.85 |
| 1.0 | $\pm 0.1^b$ | 30469 | 934 | 8193 | 11407 | 0.09 | 3.68 | 0.73 | 0.38 |
| 10 | $\pm 1^b$ | 21310 | 931 | 4316 | 10438 | 0.13 | 2.77 | 0.95 | 0.53 |
| 100 | $\pm 10^b$ | 8859 | 860 | 1551 | 4215 | 0.30 | 2.40 | 0.92 | 0.66 |
| 1000 | $\pm 100^b$ | 1252 | 545 | 175 | 669 | 1.32 | 1.91 | 1.03 | 0.87 |

Table 5.6: The parameters of the LP comets, for the same conditions as in Table 5.5, but with the inclusion of the discovery probability as given by Equation 5.13. The rightmost column lists the fraction of comets with $q < 3$ AU that go undiscovered under this probability function.

### 5.3.3 Discovery probability function

The application of a discovery probability to these simulations is shown in Figure 5.22: the non-gravitational forces are identical to those in Figure 5.21, but apparitions are given a weight proportional to their discovery probability (Equation 5.13).

The addition of the discovery probability to the simulations improves the match with the observations to some degree: $\Xi_1$, $\Xi_2$ and $\Xi_3$ all tend towards unity as one moves down

Table 5.6. However, unrealistically strong NG forces are still required to match the inverse semimajor axis distribution, and result in an unacceptable perihelion distribution. Thus it seems that NG forces are unable to solve the fading problem, though they likely contribute to the shaping of both the $1/a$ and $q$ distributions.

## 5.4  Other scenarios

The fading problem refers to the discrepancy between theory and observations in the number of comets with semimajor axes between a hundred and a few thousand AU (see Figure 5.9). Thus, the presence of a (possibly unsuspected) mechanism which preferentially removes such comets could explain the discrepancy. Such a removal mechanism might arise from structures with size scales comparable to those of the orbits which they are to affect most strongly. Some real and hypothetical structures with hundred AU size scales include:

1. The heliopause, where the solar wind meets the interstellar medium,

2. A massive circumsolar disk, perhaps related to the 10 to 100 kilometer sized objects that have been discovered in the Kuiper belt beyond Neptune (Jewitt and Luu 1993; Cochran et al. 1995).

3. A massive solar companion object at 100 to 1000 AU.

The existence of the heliopause is well established (*e.g.* Kurth et al. 1984; Linsky and Wood 1995); however, it will be shown that its dynamical influence is small and no simulations were performed to examine its effects on LP comets (§ 5.4.3).

The two other hypotheses are more controversial. Though little if any evidence supports the existence of undiscovered disks or planetary objects in our Solar System, they cannot yet be excluded, and long-period comets may prove to be the most sensitive tools we have for constraining their properties. For this reason, these two scenarios will be examined here.

In order to reduce the computational cost of these investigations, the $V_1$ comets are used as a starting point *i.e.* the effect of the disk or companion is ignored previous to the comet's first visible apparition. More precisely, $V_1$ comets are restarted at the aphelion previous to their initial apparition, in order to correctly calculate any perturbations occurring on the inbound leg immediately preceding their first apparition. Though the addition of the perturbations due to a disk or companion only after comets become visible is unrealistic,

it provides a first look at whether or not these features act in the right direction to resolve the fading problem.

### 5.4.1  Massive circumsolar disk

A circumsolar disk is represented by means of a Miyamoto-Nagai potential (Equation 3.52) centred on the Solar System's centre of mass. The disk looks like a point mass at distances $r_{cm}$ from the centre of mass which are large compared with the disk's characteristic radius $a_d$, thus it might be expected to influence the dynamical lifetimes of comets with $a \lesssim a_d$ most strongly.

Comets coming in from the Oort cloud, falling through the disk's potential, are subject to an "apparent" decrease in their original inverse semimajor axis. This offset, $2 \times 10^{-4}$ AU$^{-1}$ for a $0.01 M_\odot$ disk with radius 100 AU and less for larger or less massive disks (Equation 5.2) is omitted from the figures to follow. The original inverse semi-major axes are measured at aphelion, as discussed in § 5.0.1.

Three disk masses were examined, 10, 1 and 0.1 Jupiter masses. The results are displayed in Figures 5.23 and 5.24, with a discovery probability given by Equation 5.13 used in the latter. In § 3.6, it was noted that disk masses above one Jupiter mass violate various dynamical and observational constraints and that the upper limits might be even lower; thus our chosen disks include some of unrealistically high mass. Two disk shapes were investigated, both with axis ratios of $a_d/b_d = 10$. The first had a characteristic size $a_d = 100$ AU corresponding to a Kuiper belt-like disk, the second had $a_d = 1000$ AU, similar in size to the $\beta$ Pictoris disk.

The evolution of comets with perihelia outside the planetary system is more complicated in the presence of a disk. Of most concern here is the validity of the PERIHELION TOO LARGE end-state (§ 4.3). This end-state assumes that comets with perihelia at 40 AU and with $\sin 2\tilde{\omega} > 0$ are unlikely to become visible (§ 4.3). This assumption is only correct if the torque is dominated by the Galactic tide, and this may not be the case when a disk is present. However, to keep the simulation times reasonable it was necessary to retain the PERIHELION TOO LARGE end-state's threshold at 40 AU. The *a posteriori* justification is that, in simulations which include disks, this end-state is similarly populated (in fact ordinarily a bit underpopulated) relative to the standard case (Table 5.7), indicating that this shortcut is not grossly affecting the simulation results.

The threshold for the EXCEEDED TIME LIMIT end-state (§ 4.3) was again set at 10 000 orbits. Only one comet reached this state, in the simulation with the largest and most massive disk. It was on a high-inclination, large perihelion orbit ($a = 220$ AU, $q = 59$ AU, $i = 93°$). Upon re-examination, it was found to be ejected 1095 orbits later, after contributing 11 visible perihelion passages. These apparitions are included in all the relevant figures.

The disk applies a torque to the comets, resulting in a change in perihelion distance. As with the Galactic tide, the disk torque can produce an oscillatory motion of the cometary perihelion, the frequency of which increases with increasing disk mass. This effect ordinarily results in an increase in the comet's average lifetime, as the risk of ejection is much reduced when the comet's perihelion is outside Saturn's orbit, but also significantly reduces the number of apparitions comets make in a given number of perihelion passages.

The net effect of the disks is shown in Figure 5.23. The perihelion distribution of visible comets is not strongly affected, remaining more or less flat. The disk does decrease the perihelion distance of some comets sufficiently to collide with the Sun. The number of such incidents is noted in Table 5.8.

The values of the $\Xi$ parameters for this model are also listed in Table 5.8. The values of $\Xi_1$ are far smaller than unity even for the most massive disks, and it is clear from Figure 5.23 that the simulated $1/a$ distributions remain much broader than the observations, though with some improvement as disk mass is increased.

| $M_d$ | $a_d$ | $b_d$ | Number | Oort | Min. $1/a$ | Med. $1/a$ | Max. $1/a$ |
|---|---|---|---|---|---|---|---|
| 0 | — | — | 109 | 71 | $2.1 \times 10^{-5}$ | $3.2 \times 10^{-5}$ | $9.0 \times 10^{-4}$ |
| 0.1 | 100 | 10 | 100 | 66 | $1.9 \times 10^{-5}$ | $4.2 \times 10^{-5}$ | $3.1 \times 10^{-3}$ |
| 0.1 | 1000 | 100 | 104 | 67 | $2.0 \times 10^{-5}$ | $4.6 \times 10^{-5}$ | $1.0 \times 10^{-3}$ |
| 1 | 100 | 10 | 105 | 64 | $1.5 \times 10^{-5}$ | $4.0 \times 10^{-5}$ | $1.4 \times 10^{-2}$ |
| 1 | 1000 | 100 | 87 | 65 | $1.5 \times 10^{-5}$ | $4.1 \times 10^{-5}$ | $2.3 \times 10^{-3}$ |
| 10 | 100 | 10 | 109 | 52 | $1.8 \times 10^{-5}$ | $4.4 \times 10^{-5}$ | $1.5 \times 10^{-2}$ |
| 10 | 1000 | 100 | 255 | 59 | $1.4 \times 10^{-5}$ | $3.0 \times 10^{-5}$ | $3.9 \times 10^{-3}$ |

Table 5.7: Characteristics of the inverse semimajor axis distributions for the PERIHELION TOO LARGE end-state, when the Solar System contains a massive circumsolar disk. "Number" is the number of comets which entered this end-state and "Oort" the number with semimajor axes greater than 10 000 AU. Units of $1/a$ are AU$^{-1}$. The standard case (no disk) is indicated on the first line, and all simulations start from the set of 1368 $V_1$ comets. $M_d$, $a_d$ and $b_d$ are the parameters of the disk, measured in Jupiter masses and AU (Equation 3.52).
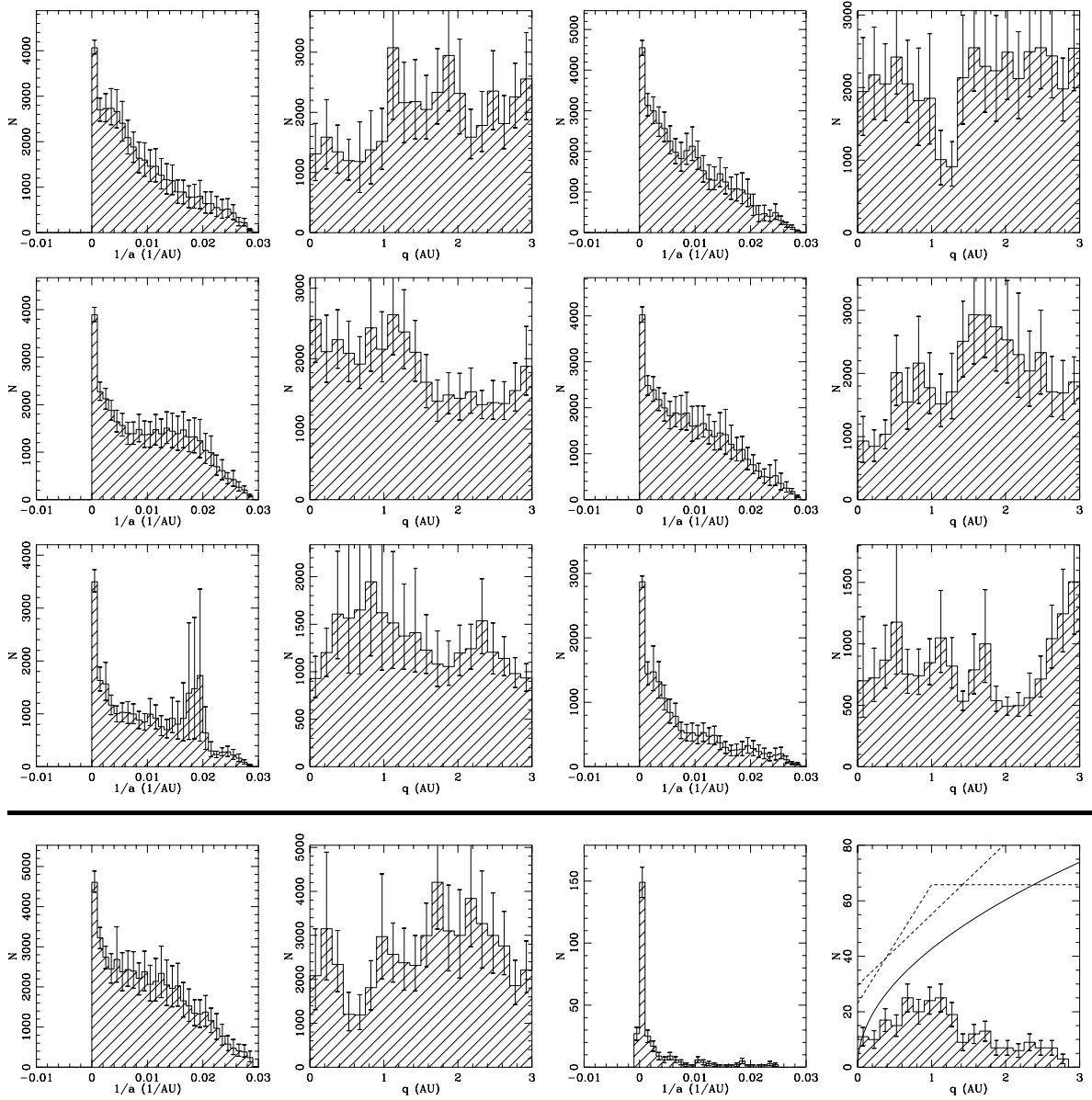
Figure 5.23: Distribution of the inverse semimajor axis $1/a$ and perihelion distance $q$ for the visible LP comets when the Solar System contains a massive circumsolar disk. All simulations have disk axis ratios $a_d/b_d = 10$. The simulations on the left have characteristic disk widths $a_d = 100$ AU, those on the right $a_d = 1000$ AU. The disk masses increase from the top down, with values of 0.1, 1 and 10 Jupiter masses. The bottom line of graphs is for comparison, and includes the standard case (left side) and the observations (right side). The lower rightmost graph includes Everhart's and Kresák's estimates of the intrinsic perihelion distribution (§ 2.3.2), shown as the dashed and solid curves respectively.
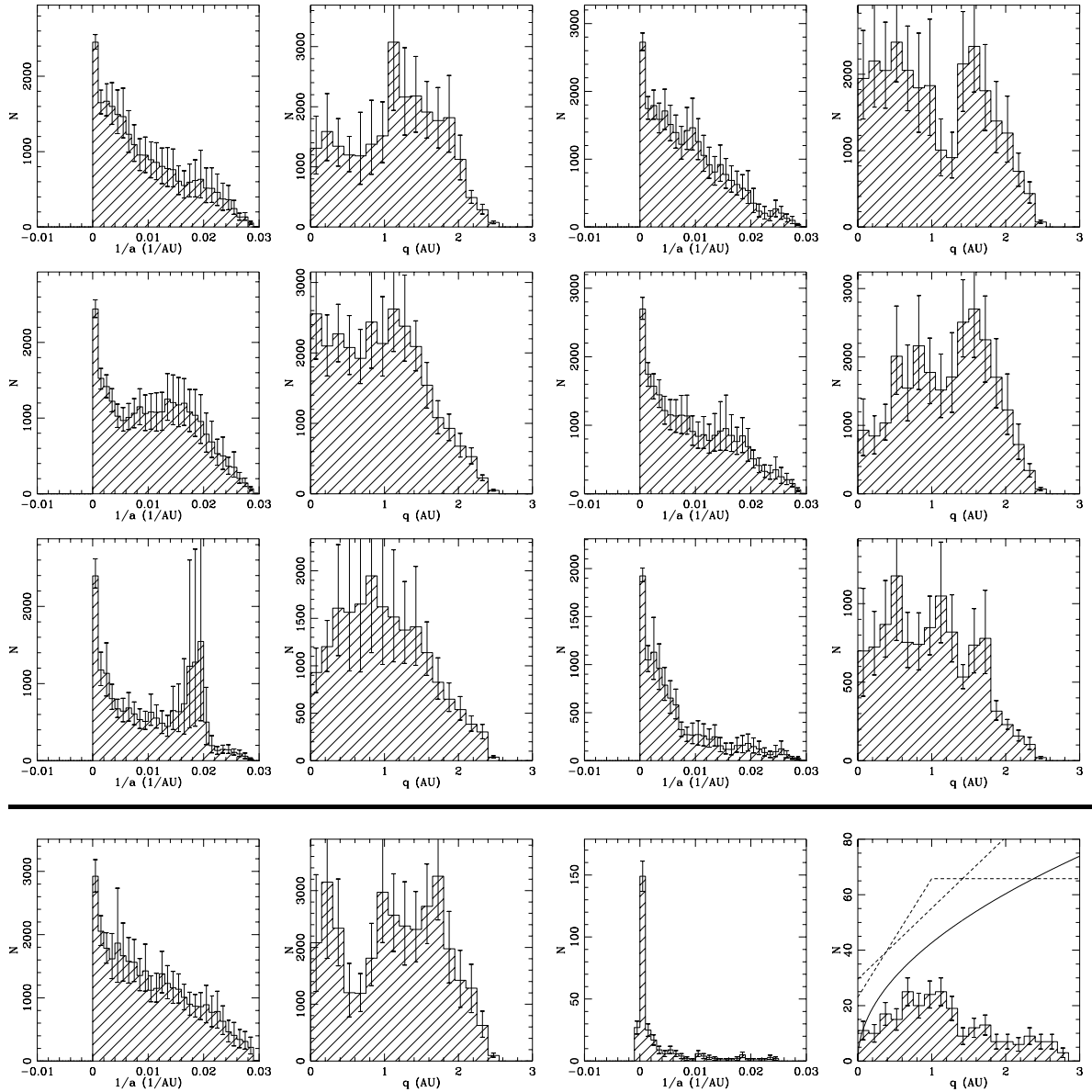
Figure 5.24: Distributions of the inverse semimajor axis $1/a$ and perihelion distance $q$ for the visible LP comets when the Solar System contains a massive circumsolar disk and the discovery probability function is given by Equation 5.13. The disk characteristics are the same as in Figure 5.23.

| $M_d$ | $a_d$ | $b_d$ | Total | Spike | Tail | Prograde | $\Xi_1$ | $\Xi_2$ | $\Xi_3$ | $\bar{m}$ | $R_\odot$ |
|---|---|---|---|---|---|---|---|---|---|---|---|
| 0.1 | 100 | 10 | 38947 | 1486 | 8382 | 15178 | 0.12 | 2.95 | 0.75 | 60.4 | 0 |
| 0.1 | 1000 | 100 | 42106 | 1496 | 9122 | 16957 | 0.11 | 2.97 | 0.78 | 33.7 | 1 |
| 1 | 100 | 10 | 37676 | 1459 | 12027 | 11888 | 0.12 | 4.37 | 0.61 | 60.8 | 2 |
| 1 | 1000 | 100 | 39138 | 1458 | 9944 | 16141 | 0.11 | 3.48 | 0.80 | 44.7 | 1 |
| 10 | 100 | 10 | 26445 | 1416 | 8881 | 6813 | 0.16 | 4.60 | 0.50 | 62.6 | 5 |
| 10 | 1000 | 100 | 16636 | 1324 | 3020 | 7555 | 0.24 | 2.49 | 0.88 | 66.9 | 3 |
| $0.1^d$ | 100 | 10 | 24535 | 968 | 6086 | 8589 | 0.12 | 3.40 | 0.68 | 60.4 | 0 |
| $0.1^d$ | 1000 | 100 | 26335 | 969 | 5261 | 11950 | 0.11 | 2.74 | 0.88 | 33.7 | 1 |
| $1^d$ | 100 | 10 | 27655 | 947 | 9514 | 8712 | 0.10 | 4.71 | 0.61 | 60.8 | 2 |
| $1^d$ | 1000 | 100 | 25200 | 947 | 7070 | 9881 | 0.11 | 3.84 | 0.76 | 44.7 | 1 |
| $10^d$ | 100 | 10 | 18769 | 939 | 7104 | 4103 | 0.15 | 5.18 | 0.42 | 62.6 | 5 |
| $10^d$ | 1000 | 100 | 10600 | 910 | 1541 | 4650 | 0.26 | 1.99 | 0.85 | 66.9 | 3 |

Table 5.8: Parameters of the distributions of the visible long-period comets when the Solar System contains a circumsolar disk. The units of $M_d$ are Jupiter masses, those of $a_d$ and $b_d$, AU. The rightmost column indicates the number of comets which collided with the Sun. The superscript $^d$ indicates that the discovery probability from Equation 5.13 has been applied. The definitions of the other columns are the same as in Table 5.5.

| $M_d$ | 0.1 $M_{Jup}$ | | 1 $M_{Jup}$ | | 10 $M_{Jup}$ | |
|---|---|---|---|---|---|---|
| $a_d$ | 100 AU | 1000 AU | 100 AU | 1000 AU | 100 AU | 1000 AU |
| Number of objects | 40 | 39 | 66 | 43 | 50 | 41 |
| Number of encounters | 51 | 76 | 111 | 88 | 82 | 65 |
| Encounters/object | 1.3 | 1.9 | 1.7 | 2.0 | 1.6 | 1.6 |
| Collisions | 0 | 1 | 2 | 1 | 5 | 3 |
| Captures | 0 | 0 | 0 | 0 | 0 | 0 |

Table 5.9: Planetary close encounter data for the dynamically evolved long-period comets under a massive disk. All collisions listed are with the Sun; however, close encounters with the Sun are not included in this table.

Increasing the disk mass also tends to improve $\Xi_2$ and $\Xi_3$ for the 1000 AU disk, though it acts in the opposite direction for the smaller disk. There is no set of disk parameters that comes close to producing a match with observations. More massive disks might be able to do better, but these would violate even more strongly the mass constraints on such an object (§ 3.6). Thus, it seems unlikely that the fading problem is the result of a massive circumsolar disk.

### 5.4.2  Massive solar companion

A massive, unseen companion to the Sun such as a Planet X or Nemesis object can be modelled as a fifth planet. For simplicity, only circular orbits lying in the ecliptic plane are considered. The companion was added to the simulations at the aphelion immediately

preceding the comets' first visible apparition, as was done for the disk (§ 5.4).

Companions of 0.1, 1 and 10 Jupiter masses were simulated, on orbits with radii of 100 and 1000 AU. The orbital periods of these objects are 1000 and 31 600 years respectively. The companion masses used are based on Figure 5 in Tremaine (1990), and chosen so that the companion would not violate, or violate only weakly, the constraints on its mass arising from considerations of the properties of Oort cloud comets and the planets. Note that, as in the previous section, the original semimajor axes of the comets are measured at aphelion, and thus do not include the energy offset caused by their fall through the companion's gravitational potential (Equation 5.2).

Nine comets reached the EXCEEDED TIME LIMIT end-state, here set at 10 000 orbits, many more than in the standard case where it was not reached at all. Of these nine, five survived for another 10 000 orbits without becoming visible; these will be neglected. The other four do eventually become visible, contributing a total of 335 apparitions, which are included in the following figures.

The simulation results are presented in Figure 5.25, and in Figure 5.26 with the addition of a discovery probability (Equation 5.13). The perihelion distribution takes on a variety of forms, from those concentrated at smaller ($< 1$ AU) distances to those concentrated further out. There is no clear trend with mass or companion orbit size. The large error bars seen on some of the histogram bars indicate a noisy distribution *i.e.* one where a few individual comets contribute a significant fraction of the total number of apparitions. In particular, the perihelion distribution for the 1000 AU–10 Jupiter mass disk shows a sharp spike in the smallest bin, but with an error bar roughly two-thirds its height. This is due to a single comet becoming "trapped" for a long time in high-inclination orbit, and does not seem to be indicative of a real clustering of objects in that vicinity.

The $\Xi$ parameters for this model are listed in Table 5.10. As the companion mass is increased, the fraction of prograde to retrograde comets improves, especially in the case of the larger companion orbit. The companion also reduces the height of the tail of the $1/a$ distribution, $\Xi_1$ increasing slightly with disk mass but remaining below unity. The number of dynamically oldest comets remains high without any clear trend with increasing mass. Overall, the presence of a companion produces little improvement in the match with observations, thus we conclude that the fading problem is unlikely to arise due to such a companion object, at least of the type examined here.
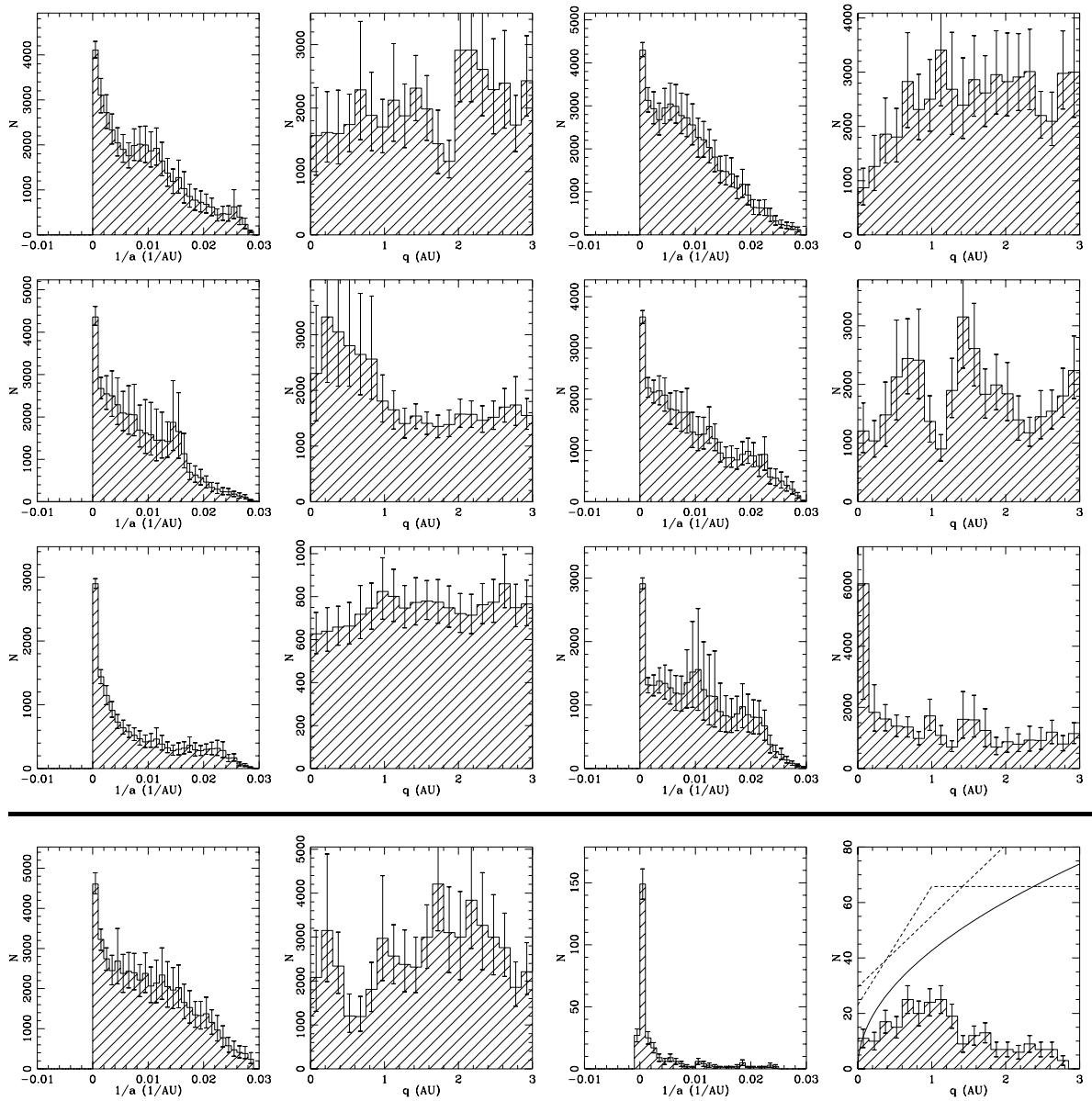
Figure 5.25: Distribution of the inverse semimajor axis $1/a$ and perihelion distance $q$ for the visible LP comets when the Solar System contains a massive solar companion. The simulations on the left have companion semimajor axes $a_X = 100$ AU, those on the right $a_X = 1000$ AU. The companion masses increase from the top down, with values of 0.1, 1 and 10 Jupiter masses. The bottom line of graphs is for comparison, and includes the standard case (left side) and the observations (right side). The lower rightmost graph includes Everhart's and Kresák's estimates of the intrinsic perihelion distribution (§ 2.3.2), shown as the dashed and solid curves respectively.
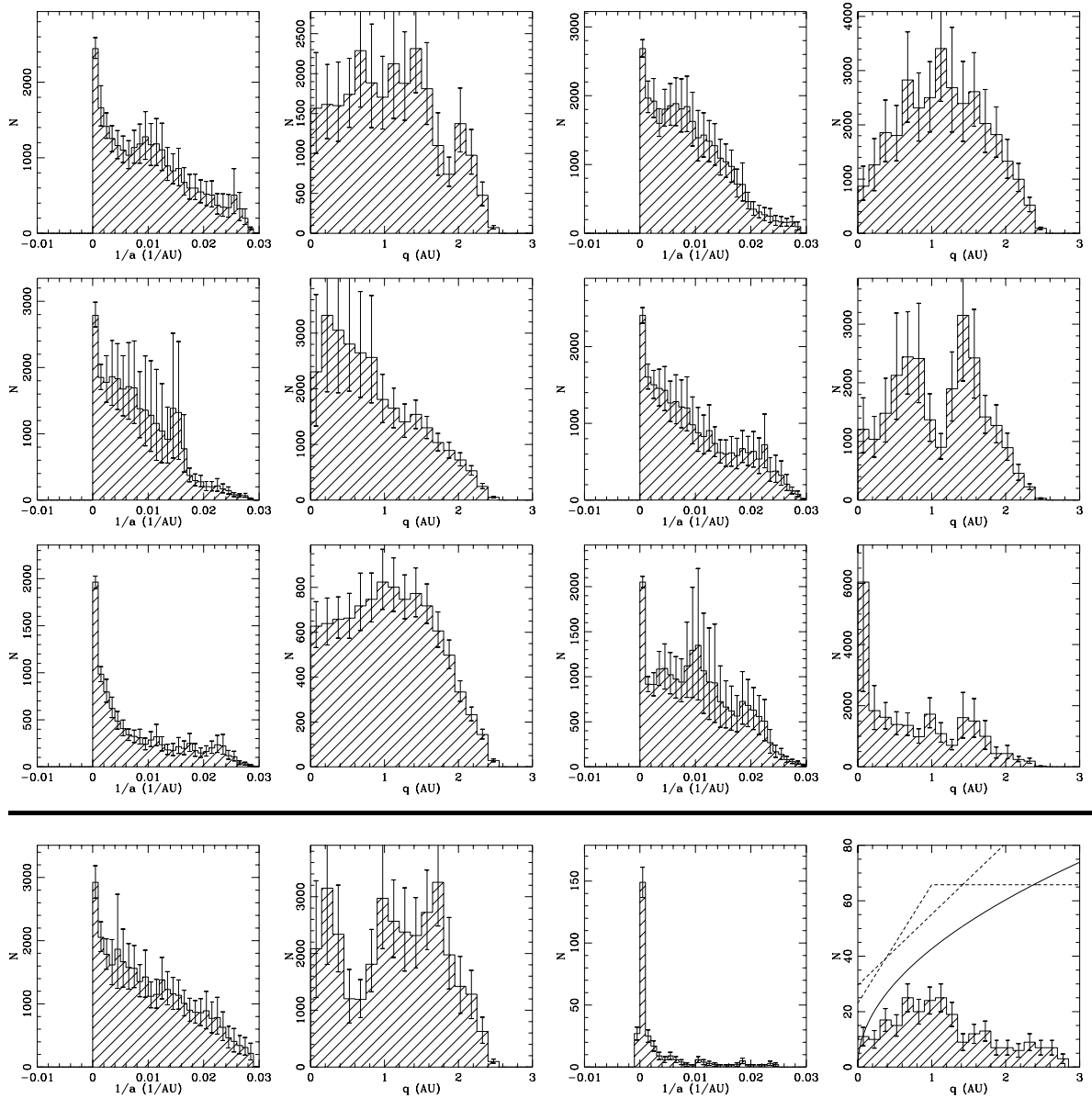
Figure 5.26: Distribution of the inverse semimajor axis $1/a$ and perihelion distance $q$ for the visible LP comets when the Solar System contains a massive solar companion and the discovery probability function is of the form of Equation 5.13. Conditions are otherwise identical to those in Figure 5.25.

| $M_X$ | $a_X$ | Total | Spike | Tail | Prograde | $\Xi_1$ | $\Xi_2$ | $\Xi_3$ | $\bar{m}$ | $R_\odot$ |
|---|---|---|---|---|---|---|---|---|---|---|
| 0.1 | 100 | 40662 | 1451 | 9111 | 14074 | 0.11 | 3.07 | 0.67 | 43.1 | 1 |
| 0.1 | 1000 | 49420 | 1490 | 10057 | 13550 | 0.09 | 2.79 | 0.53 | 44.4 | 1 |
| 1 | 100 | 38397 | 1473 | 7465 | 9379 | 0.12 | 2.66 | 0.47 | 85.4 | 4 |
| 1 | 1000 | 35940 | 1438 | 9338 | 13544 | 0.12 | 3.56 | 0.73 | 68.1 | 1 |
| 10 | 100 | 14877 | 1379 | 3365 | 5846 | 0.28 | 3.10 | 0.76 | 66.0 | 4 |
| 10 | 1000 | 28600 | 1400 | 8183 | 15489 | 0.15 | 3.92 | 1.05 | 146.3 | 2 |
| $0.1^d$ | 100 | 25300 | 944 | 6762 | 8893 | 0.11 | 3.66 | 0.68 | 43.1 | 1 |
| $0.1^d$ | 1000 | 31376 | 975 | 6206 | 8623 | 0.09 | 2.71 | 0.53 | 44.4 | 1 |
| $1^d$ | 100 | 27918 | 963 | 4764 | 6047 | 0.10 | 2.34 | 0.42 | 85.4 | 4 |
| $1^d$ | 1000 | 24740 | 943 | 6713 | 8281 | 0.12 | 3.72 | 0.65 | 68.1 | 1 |
| $10^d$ | 100 | 9749 | 928 | 2197 | 4059 | 0.29 | 3.09 | 0.81 | 66.0 | 4 |
| $10^d$ | 1000 | 22177 | 1030 | 6052 | 12649 | 0.14 | 3.74 | 1.11 | 146.3 | 2 |

Table 5.10: Parameters of the visible long-period comets when the Solar System contains a massive solar companion. The companion's mass $M_X$ is in Jupiter masses, the size of its orbit $a_X$ in AU. The rightmost column indicates the number of comets which collided with the Sun. The superscript $^d$ indicates that the discovery probability (Equation 5.13) has been applied. The other columns are the same as in Table 5.5.

| $M_X$ | 0.1 $M_{Jup}$ | | 1 $M_{Jup}$ | | 10 $M_{Jup}$ | |
|---|---|---|---|---|---|---|
| $a_X$ | 100 AU | 1000 AU | 100 AU | 1000 AU | 100 AU | 1000 AU |
| Number of objects | 52 | 38 | 55 | 39 | 38 | 49 |
| Number of encounters | 88 | 64 | 127 | 64 | 80 | 109 |
| Encounters/object | 1.7 | 1.7 | 2.3 | 1.6 | 2.1 | 2.2 |
| Collisions | 1 | 1 | 4 | 1 | 4 | 2 |
| Captures | 0 | 0 | 0 | 0 | 0 | 0 |

Table 5.11: Planetary close encounter data for simulations including a solar companion. Close encounters with the Sun and the companion are excluded. All collisions occurred with the Sun.

### 5.4.3   Heliopause

The outflowing solar wind encounters the interstellar medium at the heliopause. Shocks form both inside and outside this interface as the low-density, high-velocity solar wind meets the higher density but slower moving ISM. These shocks heat the gas to temperatures of up to 100 000 K throughout a shell roughly 25 AU thick. This shell is located approximately 100 AU from the Sun in the upstream direction (Hall et al. 1993). Both the radio and ultraviolet signatures of these shocks have been detected (Kurth et al. 1984; Linsky and Wood 1995), and the heliopause's existence is well-established.

If the shocks associated with the heliopause produced conditions which significantly eroded comet nuclei, they could significantly reduce the lifetime of LP comets. However, a

first glance seems to indicate that there is neither enough mass nor energy in these structures to do so. The density at the boundary is not expected to exceed that of the ISM, and the gas velocity is not expected to exceed that of the solar wind (Steinolfson et al. 1994; Baranov and Zaitsev 1995); thus the plasma density remains low, and the conditions of drag do not appreciably differ from those discussed in § 3.7.2.

The gas temperature at the heliopause is roughly $10^5$ K, exceeding that of the interstellar medium by roughly two orders of magnitude. An upper limit to the amount of heat $E_h$ deposited in the nucleus through direct contact with this hot medium can be set by assuming complete transfer to the comet of all the kinetic energy in any molecule coming striking the nucleus. Then $E_h$ is just the energy flux due to gas thermal motions multiplied by the time the comet is in the heated region,

$$
\begin{aligned}
E_h &= 4\pi R_c^2 v_g n k T \frac{w_h}{v}, & \text{(5.15a)} \\
&\approx 4\pi R_c^2 n w_h (kT)^{3/2} \left(\frac{r_h}{GM_\odot m_g}\right)^{1/2}, & \text{(5.15b)} \\
&\approx 5 \times 10^8 \left(\frac{R_c}{1 \text{ km}}\right)^2 \left(\frac{n}{1 \text{ cm}^{-3}}\right) \left(\frac{w_h}{25 \text{ AU}}\right) \left(\frac{r_h}{50 \text{ AU}}\right)^{1/2} \left(\frac{T}{10^5 \text{ K}}\right)^{3/2} \text{ J}, & \text{(5.15c)}
\end{aligned}
$$

where $R_c$ is the comet's radius, $n$ is the gas number density, $m_g$ is the gas molecular mass, here assumed to be protons, $T$ is the gas temperature, $v_g \approx \sqrt{2kT/m_g}$ is the gas thermal velocity, $w_h$ is the width of the heated zone, $r_h$ is its distance from the Sun, and $v$ is the comet's velocity there. The latent heat of sublimation $\mathcal{L}$ for $H_2O$ is about 50 kJ mol$^{-1}$ (Keller 1990), and the deposition of $E_h$ thus results in the release of a mass $M$ of gas such that

$$
\begin{aligned}
M &= \frac{E_h N_A m_{H_2 0}}{\mathcal{L}}, & \text{(5.16a)} \\
&\approx 200 \left(\frac{E_h}{5 \times 10^8 \text{ J}}\right) \left(\frac{\mathcal{L}}{50 \text{ kJ mol}^{-1}}\right)^{-1} \text{ kg}, & \text{(5.16b)}
\end{aligned}
$$

where $N_A$ is Avogadro's number. The loss of this small amount of material is unlikely to significantly affect the nucleus.

Other possibilities remain: the shocked gas emits UV photons which might deposit significant energy in the nucleus; however the photon energy density is unlikely to exceed the thermal energy density by the several orders of magnitude required. More speculative possibilities include thermal and/or acoustic shocks to the nucleus during its passage through

this region. However, it seems most likely that the heliopause has little or no effect on the evolution of long-period comets.

## 5.5  Fading

In the previous sections, a number of dynamical mechanisms were explored with a view to resolving the fading problem. However, none of them are capable of bringing the simulations into agreement with observations. These mechanisms share a common defect: the tail of the simulated inverse semimajor axis distribution is overpopulated relative to that of the observed distribution. Since the comets diffuse in $1/a$ after leaving the Oort cloud (§ 3.1.2), the overpopulation of the tail appears to be a result of longer comet lifetimes in the simulations than in reality. Thus one is led to consider **fading** *i.e.* the physical degradation of the nucleus either into an increasingly faint object through loss of volatiles, or through its breakup into less easily detectable pieces.

Our interest here lies not in attempting to model in detail the physical processes by which comet nuclei fade over time, but rather in determining the mathematical relationship between a comet's brightness and its age, the **fading function**. The distributions of all the orbital elements, ecliptic and Galactic, are available to help with this construction. However, only the $1/a$, $i$, $\tilde{\imath}$ and $\tilde{\omega}$ distributions display significant changes over the first several apparitions; the others change more slowly or not at all.

The ecliptic and Galactic inclination are closely related, but the relationship of $i$ to the planets, the dominant perturbers of visible long-period comets, is clearer and thus only the ecliptic inclination will be used here to constrain the fading function. Though our assumption that the Galactic tide is the dominant injector of comets (§ 3.9) is correct, the contribution of passing stars is likely to heavily contaminate the observed distribution of these elements. Thus, $\tilde{\omega}$ is likely to be of little usefulness in the determination of the fading function. The inverse semimajor axis and the ecliptic inclination will serve as our primary fading benchmarks, through the values of $\Xi_1$, $\Xi_2$ and $\Xi_3$ (§ 5.2.1).

As it seems likely that non-gravitational forces play a role in determining the orbital distribution of evolved LP comets, their contribution, along with that of the discovery probability function, will be investigated. The set of NG parameters chosen as typical for our purposes has the following characteristics:  $A_1 = 10^{-7}$ AU day$^{-2}$, $A_2 = \pm 10^{-8}$ AU day$^{-2}$,

$A_3 = 0$, with a random sign for $A_2$ at each perihelion passage. Simulations containing these NG forces will be referred to as the **standard NG** case, and were investigated earlier (§ 5.3.2).

### 5.5.1 Determining the fading function directly

The most direct approach to the construction of the fading function would be to break down the simulated data set into individual distributions, one for each perihelion passage *i.e.* $\{V_1, V_2, V_3, \ldots, V_i, \ldots\}$, and then use a fitting procedure to determine the fractional amount $\alpha_i$ of each distribution required such that the union of them matches the observed distributions, subject to the restriction that $\alpha_{i+1} \leq \alpha_i$. Unfortunately, this problem is poorly conditioned. The inclination and inverse semimajor axis distributions change only slowly after the first few apparitions, creating a degeneracy *i.e.* $V_n \approx V_{n+1}$ when $n \gg 1$. The only feature reliably extracted via the direct approach is the need for a fairly rapid fading ($\sim 50\%$) over the first few orbits. The numerical complications associated with the direct approach lead us instead to experiment with a few simple fading laws with clear physical bases.

### 5.5.2 One parameter fading functions

Consider a number of simple, one-parameter fading functions. In each case a weight function $\phi$, ranging between one (no fading) and zero (completely faded), is applied to each apparition. This weight function represents the probability that any given apparition will be observed. Let $m$ be the number of perihelion passages and $m'$ be the number of apparitions since a comet's first apparition, inclusive, and let $t$ be the time in Myr since the first apparition. The fading functions examined here are:

**A) Constant lifetime** Each comet is assigned a fixed lifetime, measured either in

      1. apparitions $m_v$; $\phi(m' \leq m_v) = 1$, otherwise $\phi = 0$,

      2. perihelion passages $m_x$; $\phi(m \leq m_x) = 1$, otherwise $\phi = 0$,

      3. time $t_x$; $\phi(t \leq t_x) = 1$, otherwise $\phi = 0$.

**B) Constant fading probability** Comets are assigned a fixed probability $\lambda$ of fading, measured either

1. per apparition; $\phi = (1 - \lambda)^{m'-1}$,

2. per perihelion passage; $\phi = (1 - \lambda)^{m-1}$,

3. per million years; $\phi = e^{-t/t_x}$.

Note that there is no fading previous to the first visible perihelion passage. For time-based fading, the equivalent exponential decay has be used, where the decay time $t_x = -1/\ln \lambda$.

**C) Power law** The fraction of comets remaining goes like a power law based on either

1. number of apparitions; $\phi = (m')^{-\kappa}$,

2. perihelion passages; $\phi = m^{-\kappa}$,

where $\kappa$ is constant and greater than zero. Note that this implies that the comets' lifetimes $m_x$ are distributed such that $m_x \propto d\phi/dm \propto m^{-\kappa-1}$. If lifetime is proportional to comet mass, as might be expected if each apparition releases an approximately equal amount of volatiles, then the comet mass $M$ has a differential number distribution such that

$$dN \propto M^{-\kappa-1} \, dM. \tag{5.17}$$

To determine the effects of each of these fading functions, the three quantities $\Xi_i$ are plotted as a function of the associated parameter. If all three are unity for a particular value of the parameter, then the fading function provides a good match to our observed sample, at least in terms of $1/a$ and $i$.

### Fading by orbit number

The fading laws based on apparition and orbit number will be considered together as they produce very similar results, shown in Figures 5.27 to 5.32.

The first two of these figures display the $\Xi$ parameters assuming long-period comets have constant lifetimes (models A1 and A2). The spike/total ratio $\Xi_1$ matches observations at $m$ or $m' \approx 10$, but the tail/total ratio $\Xi_2$ is too low at that point. Given a longer lifetime, the number in the tail increases, matching the observed tail at $m \approx 100$, but $\Xi_1$ is now too low. The prograde/total ratio $\Xi_3$ is typically near but below unity. The match with observations (Figure 5.33) is poor.
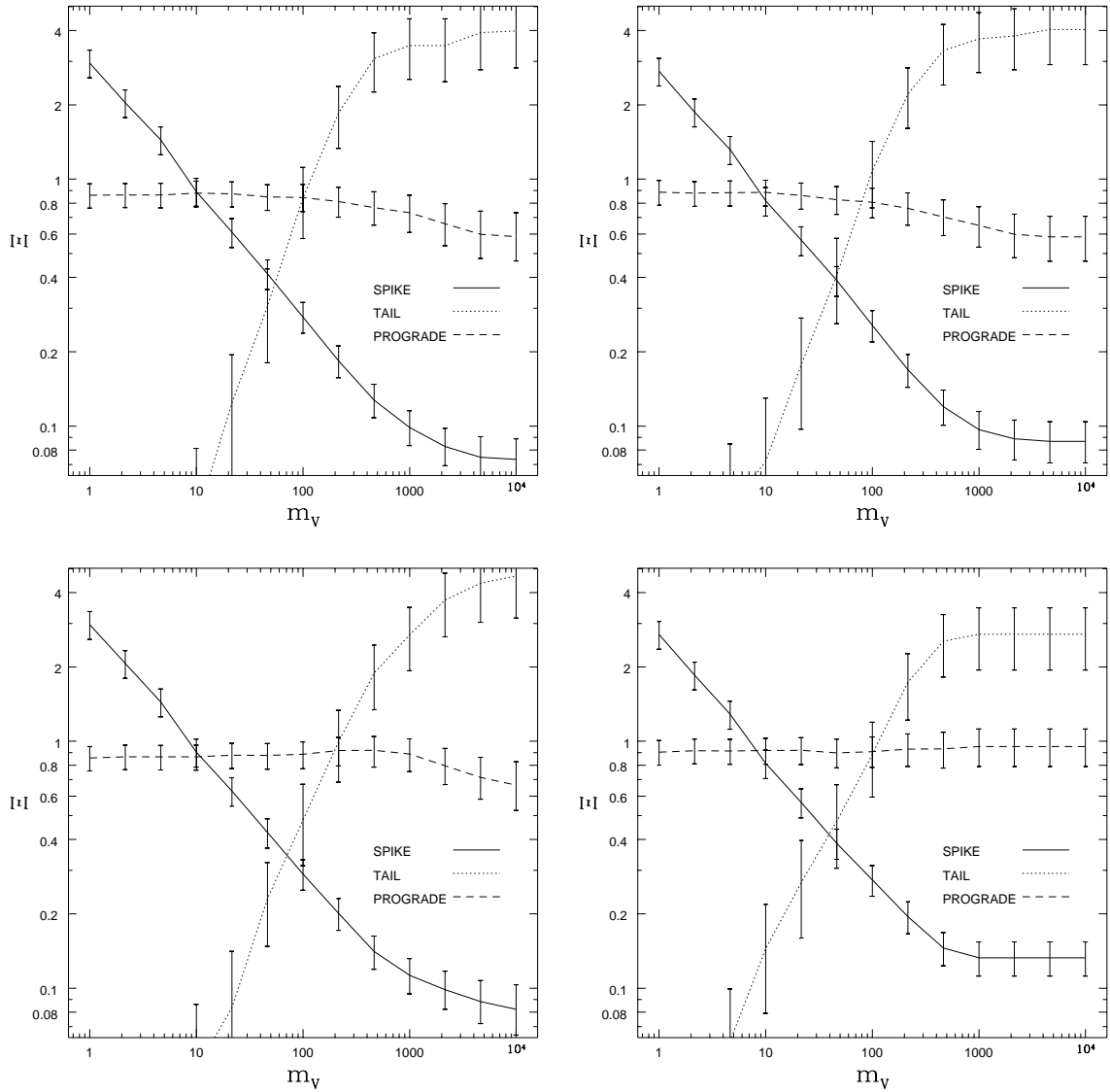
Figure 5.27: The values of $\Xi_i$ given a fixed lifetime $m_v$ in apparitions (model A1). The graphs on the right include a discovery probability, those on the left do not. The upper two graphs are based on the standard case, the lower two on the standard NG case.
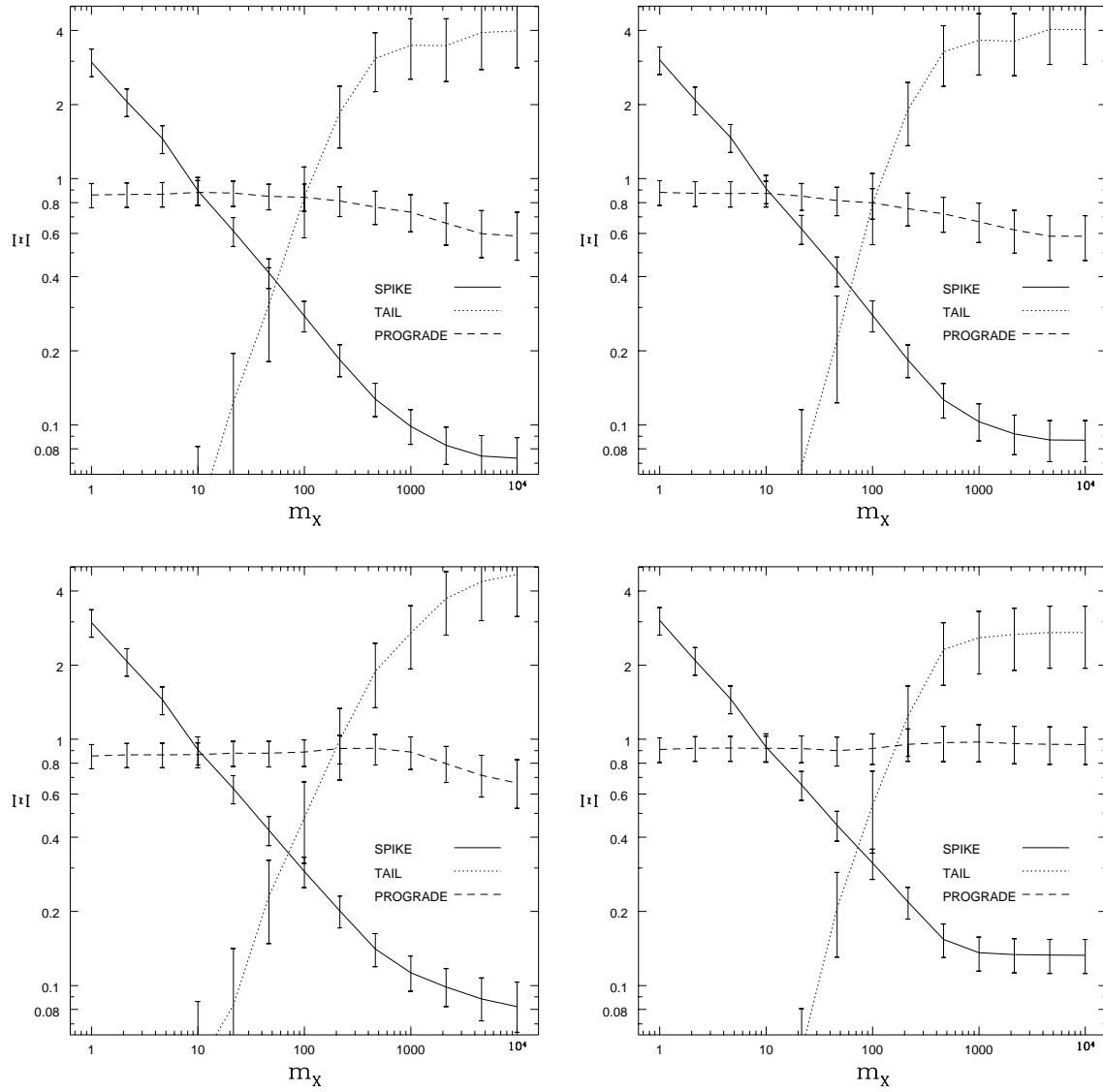
Figure 5.28: The values of $\Xi_i$ given a fixed lifetime $m_x$ in perihelion passages (model A2). The graphs on the right include a discovery probability, those on the left do not. The upper two graphs are based on the standard case, the lower two on the standard NG case.
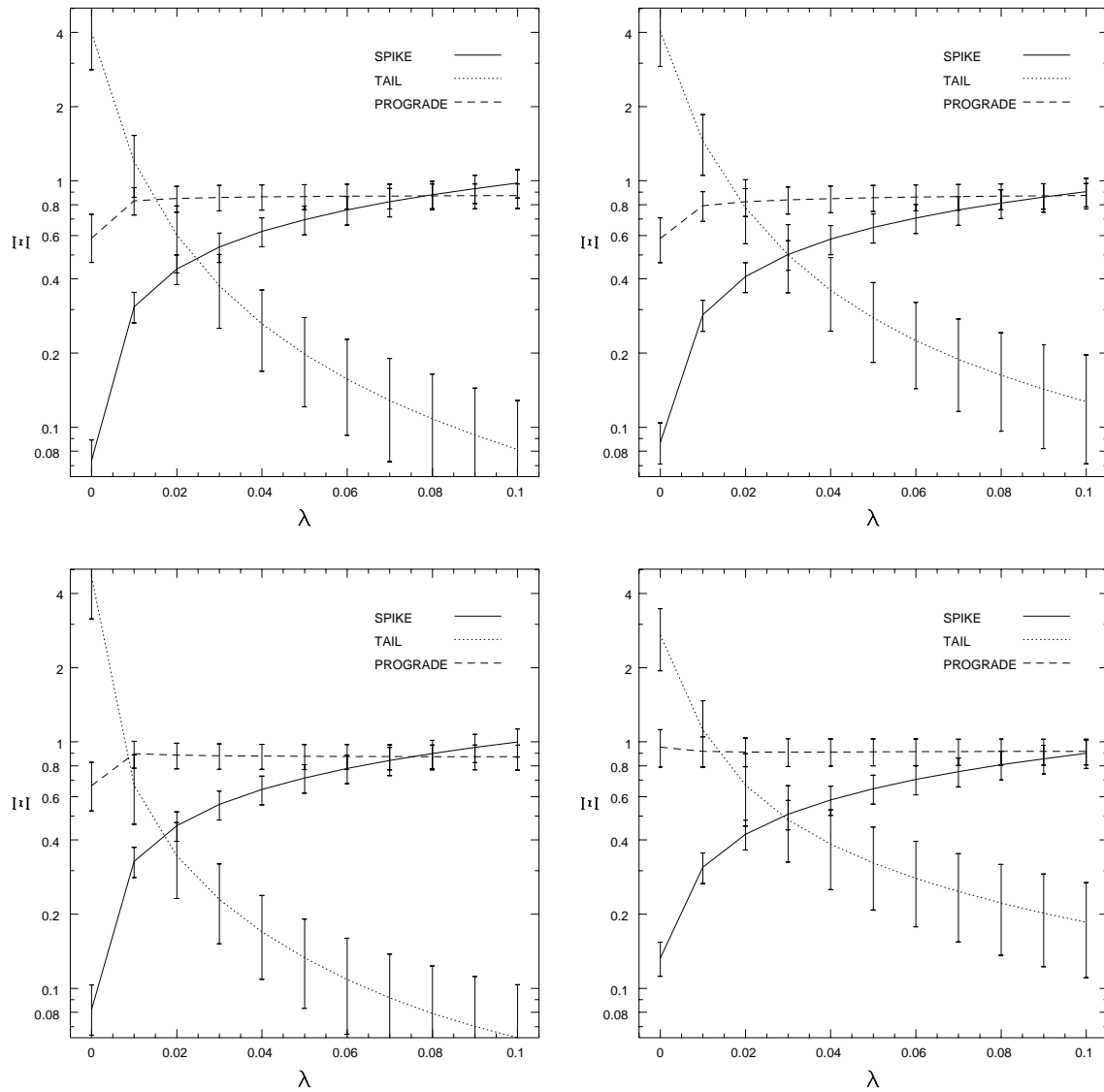
Figure 5.29: The values of $\Xi_i$ given a fixed fading probability $\lambda$ per apparition (model B1). The graphs on the right include a discovery probability, those on the left do not. The upper two graphs are based on the standard case, the lower two on the standard NG case.
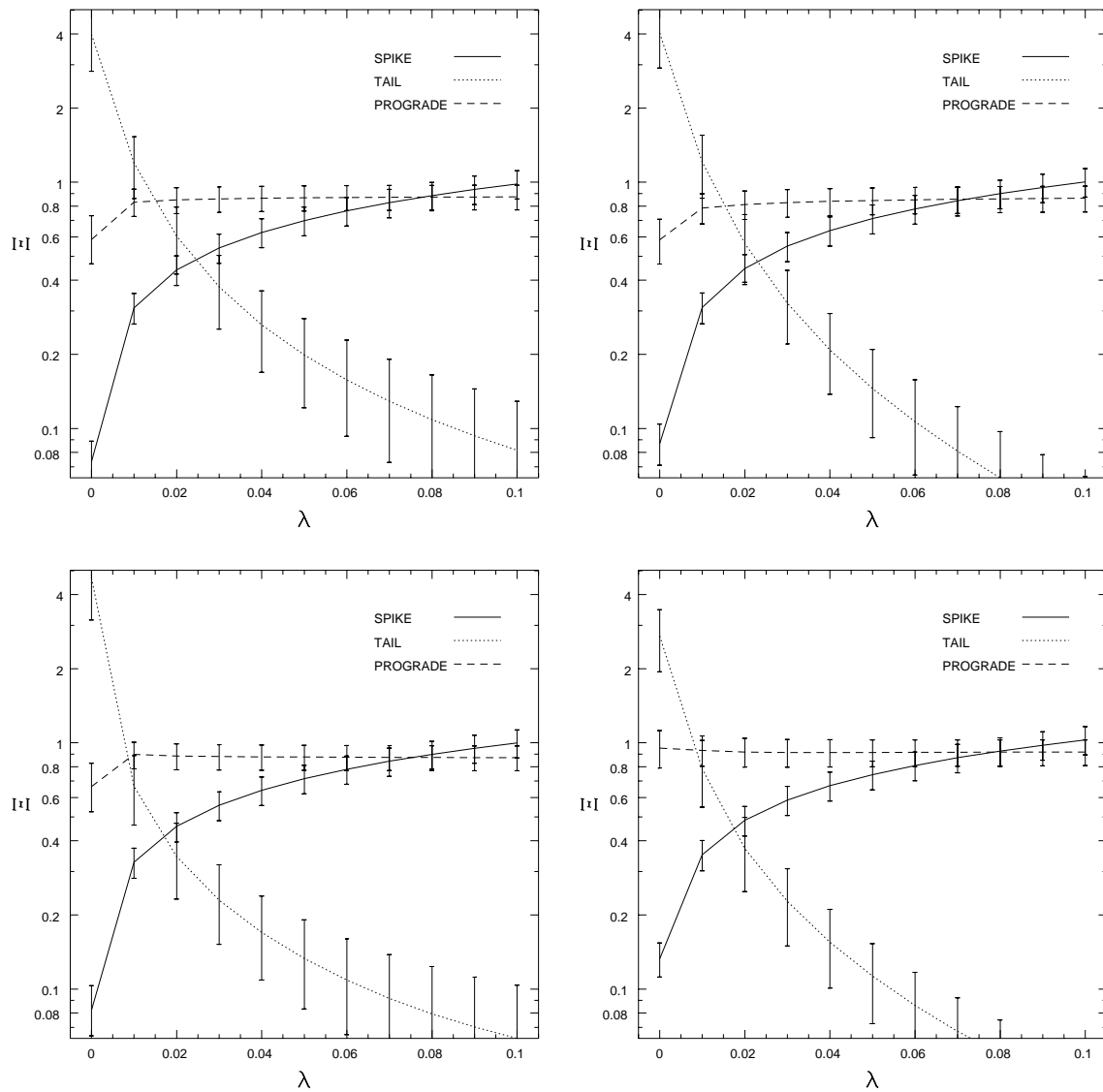
Figure 5.30: The values of $\Xi_i$ given a fixed fading probability $\lambda$ per perihelion passage (model B2). The graphs on the right include a discovery probability, those on the left do not. The upper two graphs are based on the standard case, the lower two on the standard NG case.
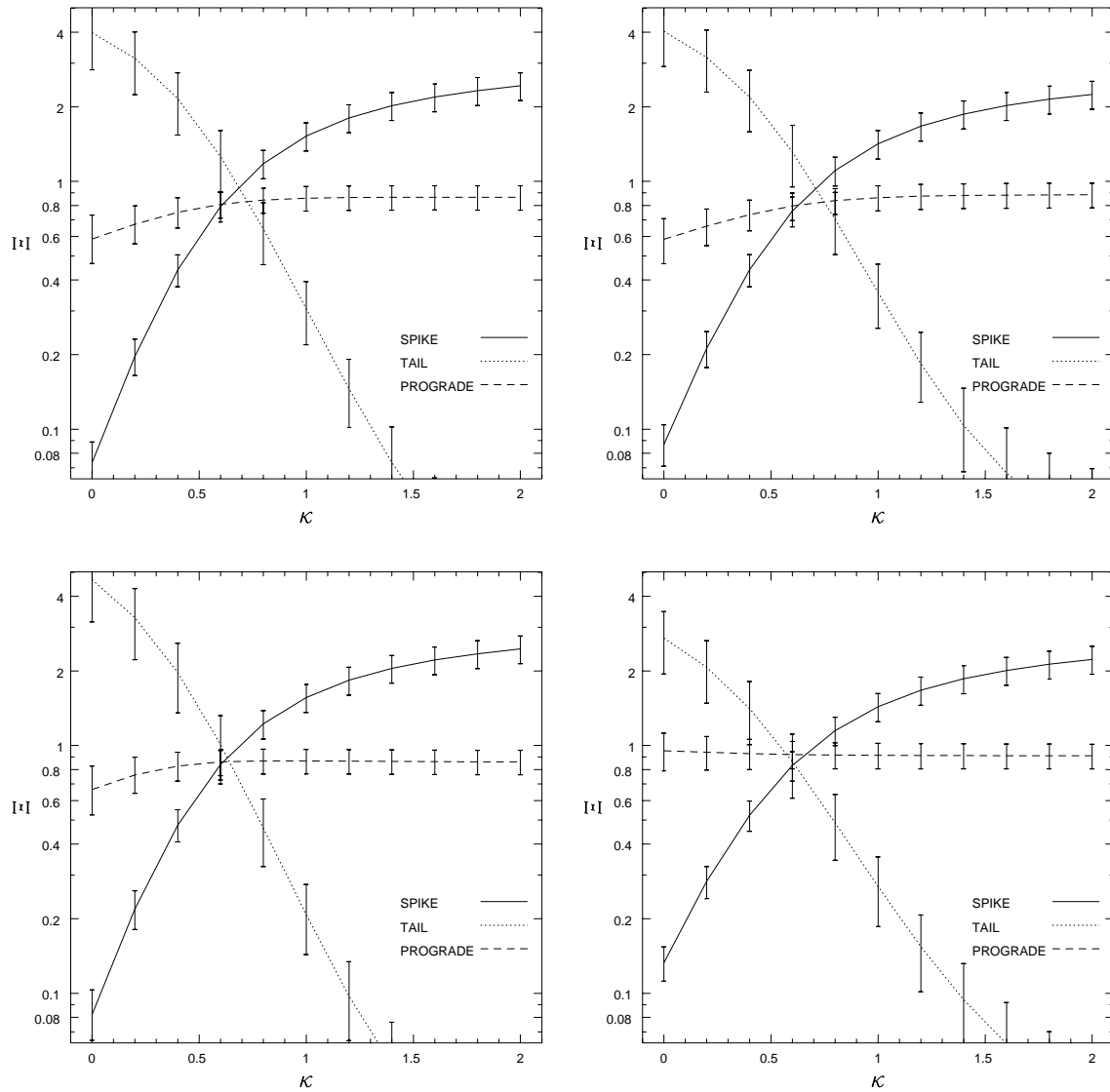
Figure 5.31: The values of $\Xi_i$ given a power law lifetime based on apparition number and with exponent $-\kappa$ (model C1). The graphs on the right include a discovery probability, those on the left do not. The upper two graphs are based on the standard case, the lower two on the standard NG case.
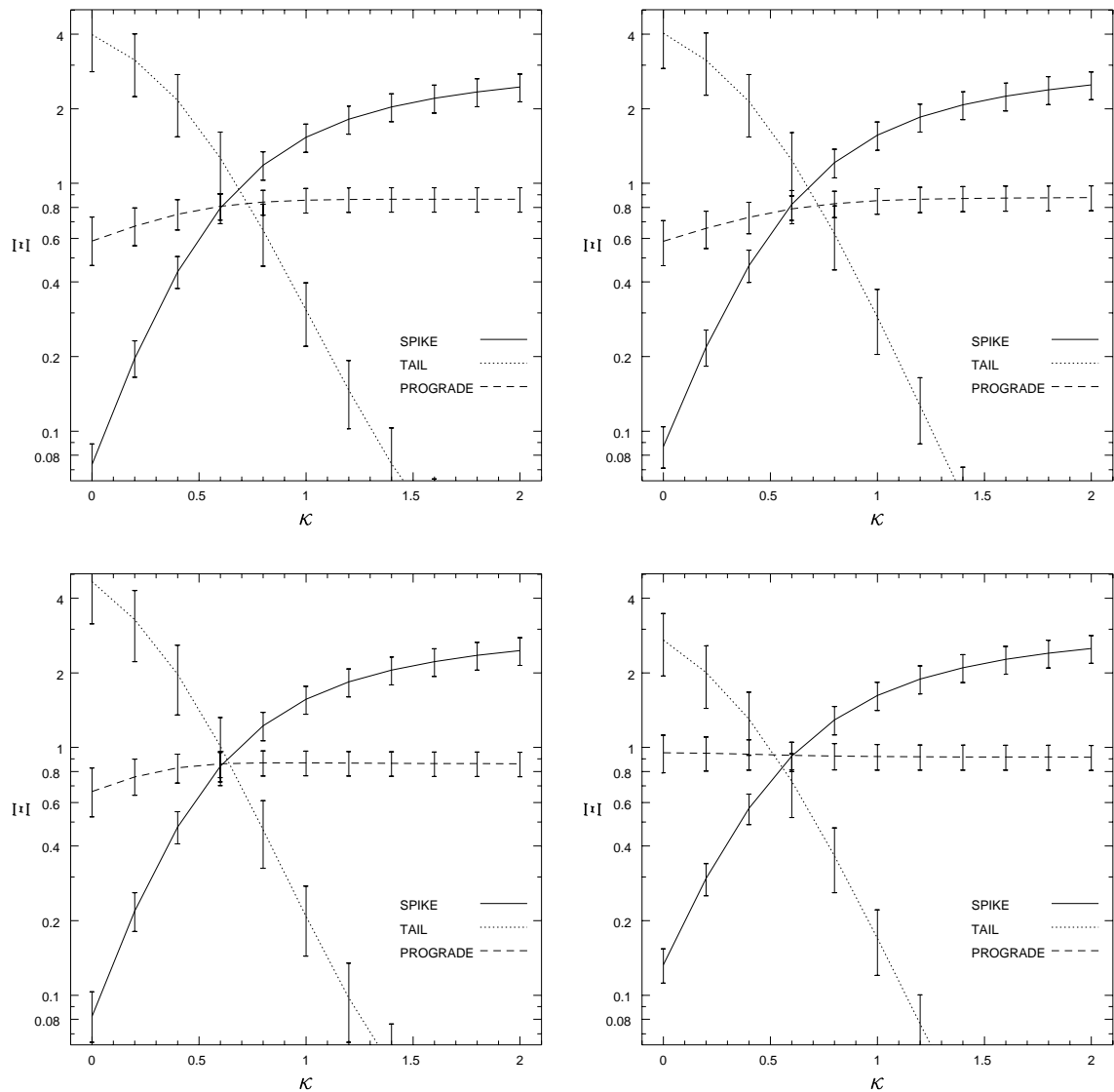
Figure 5.32: The values of $\Xi_i$ given a power law lifetime based on orbit number, and with exponent $-\kappa$ (model C2). The graphs on the right include a discovery probability, those on the left do not. The upper two graphs are based on the standard case, the lower two on the standard NG case.
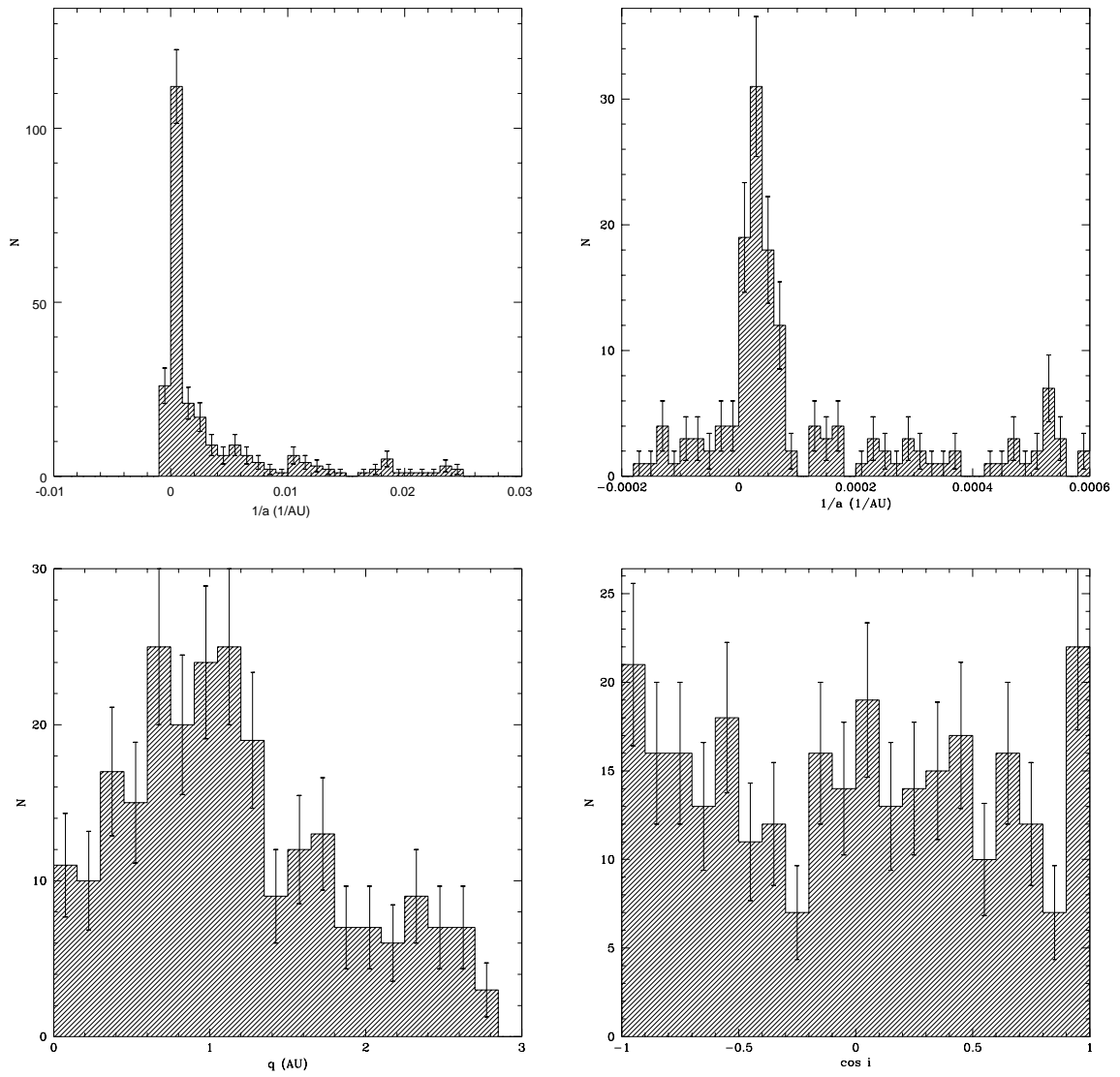
Figure 5.33: The distribution of the inverse semimajor axis $1/a$, perihelion distance $q$ and cosine of the inclination $i$ for the observed comets (Marsden and Williams 1993).
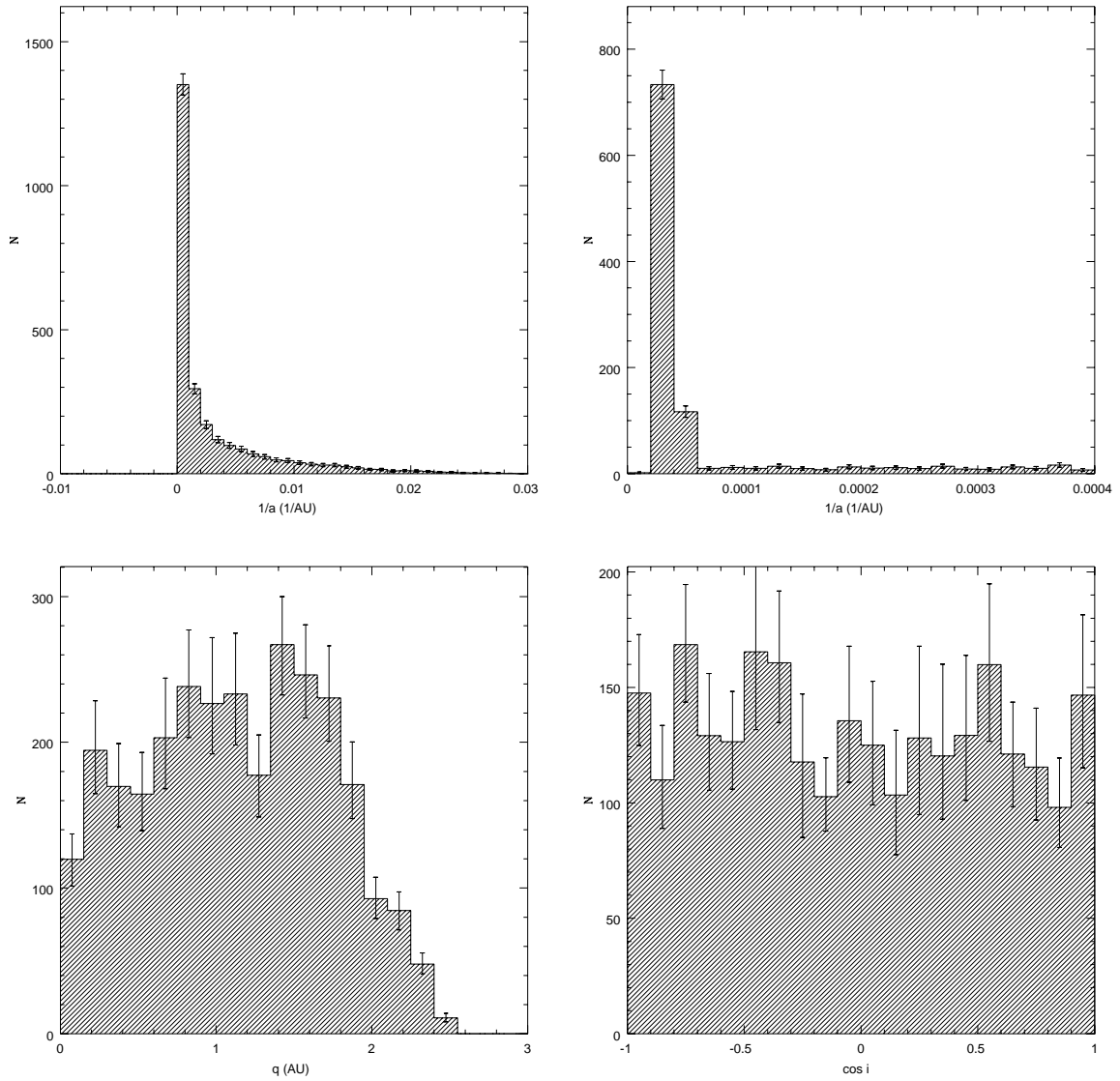
Figure 5.34: The distribution of the inverse semimajor axis $1/a$, perihelion distance $q$ and cosine of the inclination $i$ given a power law fading function with $\kappa = 0.6$ (model C1). These simulations include standard NG forces and the discovery probability given by Equation 5.13.

Figures 5.29 and 5.30 display the behaviour of the parameters $\Xi_i$ given a fixed fading probability $\lambda$ (models B1 and B2). This fading law does not allow for a simultaneous matching of the requirements on both the spike and tail, and must be considered unlikely.

In Figures 5.31 and 5.32, the effects of a power-law lifetime are shown (models C1 and C2). Though the match is not perfect (note in particular that the prograde fraction $\Xi_3$ remains too low for all $\kappa$ explored), it is better than in the previous two cases. A value of $\kappa$ of $0.6\pm0.1$ seems to provide the best match. The distributions of orbital elements under this fading law are shown in Figure 5.34. For comparison, the observed distributions are shown in Figure 5.33. The C models can provide a reasonable match with observations: a prograde to retrograde ratio is near unity, and a perihelion distribution decreasing somewhat towards the Sun.

If the C models represent reality correctly, then some information about the LP comets' mass distribution may be extracted. If comets give up approximately the same amount of mass per apparition and mass is proportional to lifetime, then the differential mass distribution of the LP comets goes roughly like $M^{-1.6}$ (Equation 5.17). The actual mass distribution of LP comet nuclei is difficult to obtain owing to the obscuring effects of the coma, but is estimated at $M^{-2.5}$ for the brightest LP comets, and at $M^{-1.7}$ for the fainter ones (Weissman 1983). Measurements of the sizes of main-belt asteroids imply differential mass distributions proportional to $M^{-2}$ at large ($\gtrsim 100$ km) diameters (Hughes and Harris 1994). There is also evidence for shallower slopes ($M^{-1.35}$) at smaller sizes, but these measurements still only include diameters greater than 20 km (Cellino et al. 1991). Thus it seems that a $\kappa \approx 0.6 \pm 0.1$ fading law is not inconsistent with our knowledge of the size distributions of small objects in the Solar System.

**Fading based on time since first apparition**

A cometary lifetime $t_x$ measured in physical time since first apparition seems *a priori* less likely than one based on the number of apparitions. Such a lifetime might be expected if the first apparition removes a protective layer, possibly of insulating refractory material, from the nucleus and thus "starts the clock" on some kind of time-based decay process.

A constant lifetime $t_x$ (model A3, Figure 5.35) provides a remarkably good match with observations, if $t_x \sim 10^5$ yr. This scenario works because one hundred thousand years provides enough time for the relatively few comets captured directly into tight orbits ($a \lesssim$

100 AU) to fill out the tail, while not providing enough time for those on larger ($a \sim$ 1000 AU) orbits to return as frequently and fill out the middle part of the $1/a$ distribution. Even $\Xi_3$, typically too low when the fading function is based on orbit number, here reaches unity near the lifetime in question. The orbital element distributions for this case are shown in Figure 5.37. Neither the perihelion nor inclination distributions match observations very well.

The time-based exponential decay law (model B3), shown in Figure 5.36, provides only fairly poor matches when NG forces are excluded, but is improved by their inclusion. The orbital elements distributions for the case $t_x = 0.09$ Myr is shown in Figure 5.38. The inclination distribution shows an excess of prograde comets, and the perihelion distribution is concentrated towards smaller values of $q$. This fading law provides a fair but far from ideal match.

### Bailey's fading law

One other fading law, proposed by Bailey (1984), will be considered here, though it has no free parameters. Bailey derived a fading function by using an analytical treatment to calculate the expected $1/a$ distribution. The resulting fading law has a per-revolution probability $p_d$ of a comet fading completely and permanently given by

$$p_d \approx 0.3[1 + (250/a)^2]^{-3/2} \tag{5.18}$$

where $a$ is measured in AU. Note that this fading law depends solely on the size of the orbit. Though not derived from physical principles, the mechanism proposed *a posteriori* to explain this fading law is "thermal shock": comets with large aphelia have lower temperatures $T$ as they approach perihelion than those with shorter periods. The thermal diffusivity of the nucleus is proportional to its thermal conductivity (which goes like $T^{-1}$) and inversely proportional to the specific heat (which goes like $T^3$), and thus is a strongly decreasing function of temperature. The resulting deeper and more rapid heating is proposed to disrupt the nucleus, possibly by mechanisms similar to those which produce cometary outbursts and splittings (§ 3.10.1).

The results of the application of this fading function to the simulations are listed in Table 5.12. The best match is provided when standard NG forces are included but not a discovery probability; however, the perihelion distribution shows a sharp spike at $q \approx 3$ AU
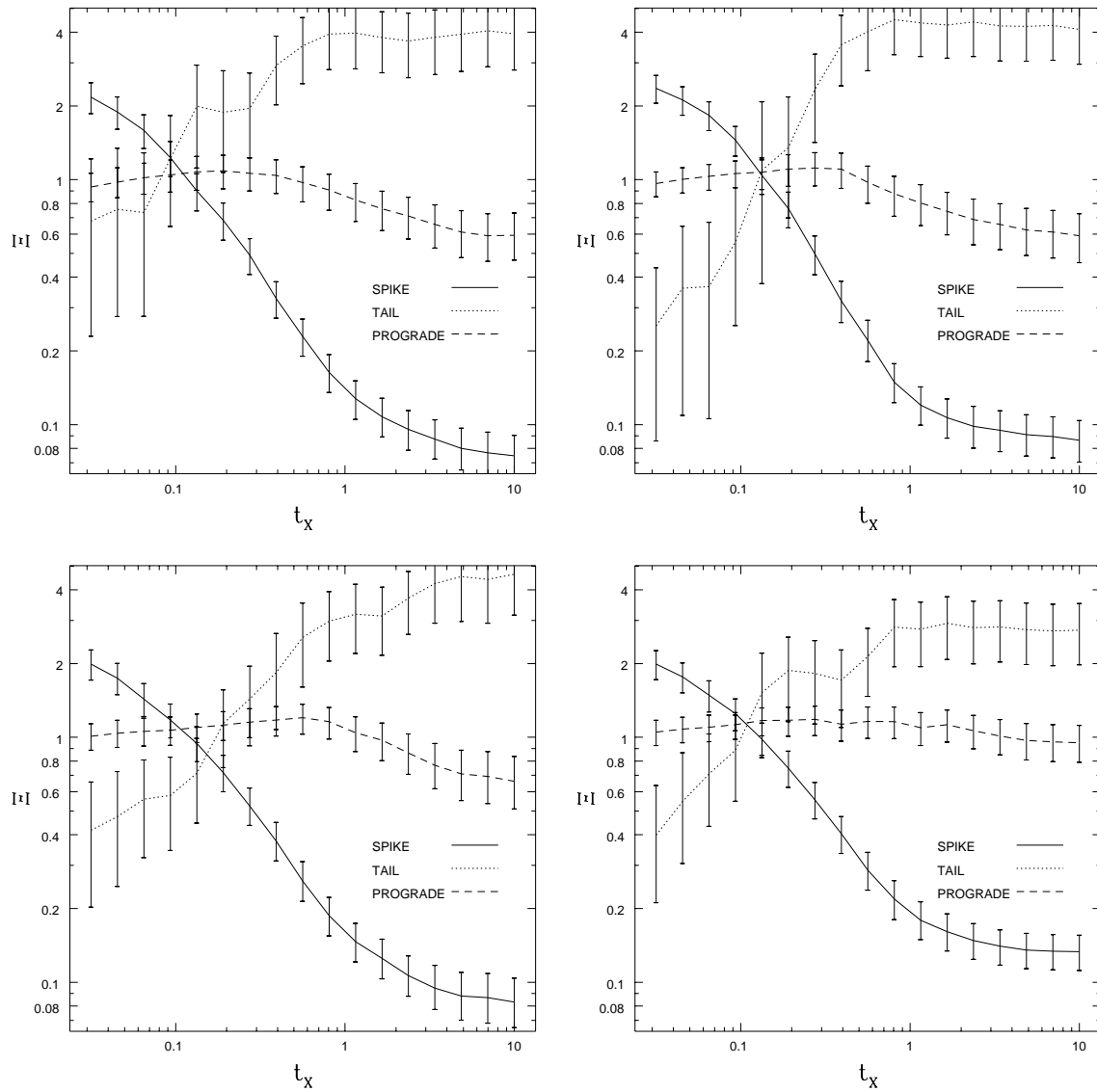
Figure 5.35: The values of $\Xi_i$ given a constant lifetime $t_x$ in physical time (model A3). The graphs on the right include a discovery probability, those on the left do not. The upper two graphs are based on the standard case, the lower two on the standard NG case.
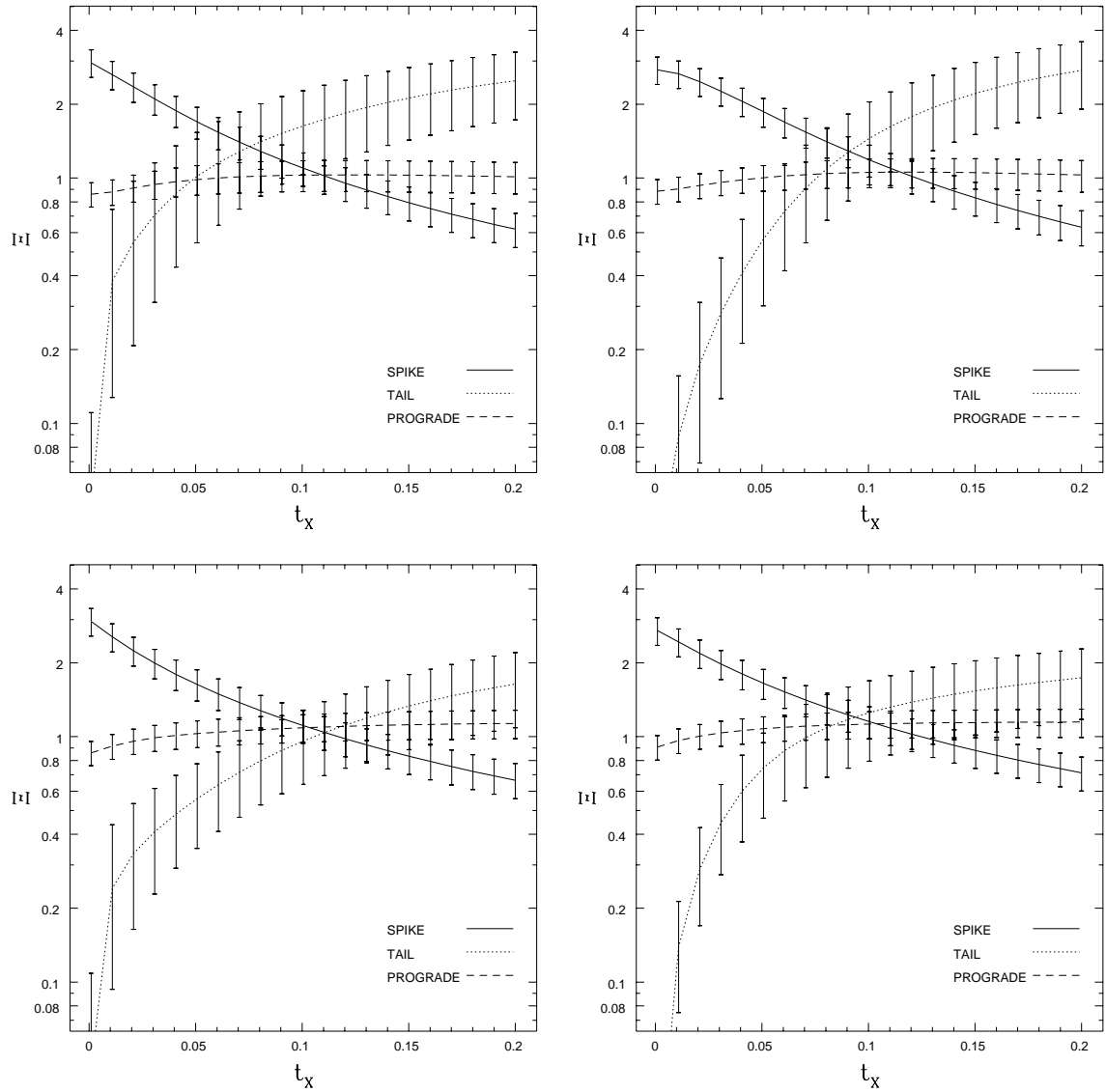
Figure 5.36: The values of $\Xi_i$ given an exponential decay with decay constant $t_x$ Myr (model B3). The graphs on the right include a discovery probability, those on the left do not. The upper two graphs are based on the standard case, the lower two on the standard NG case.
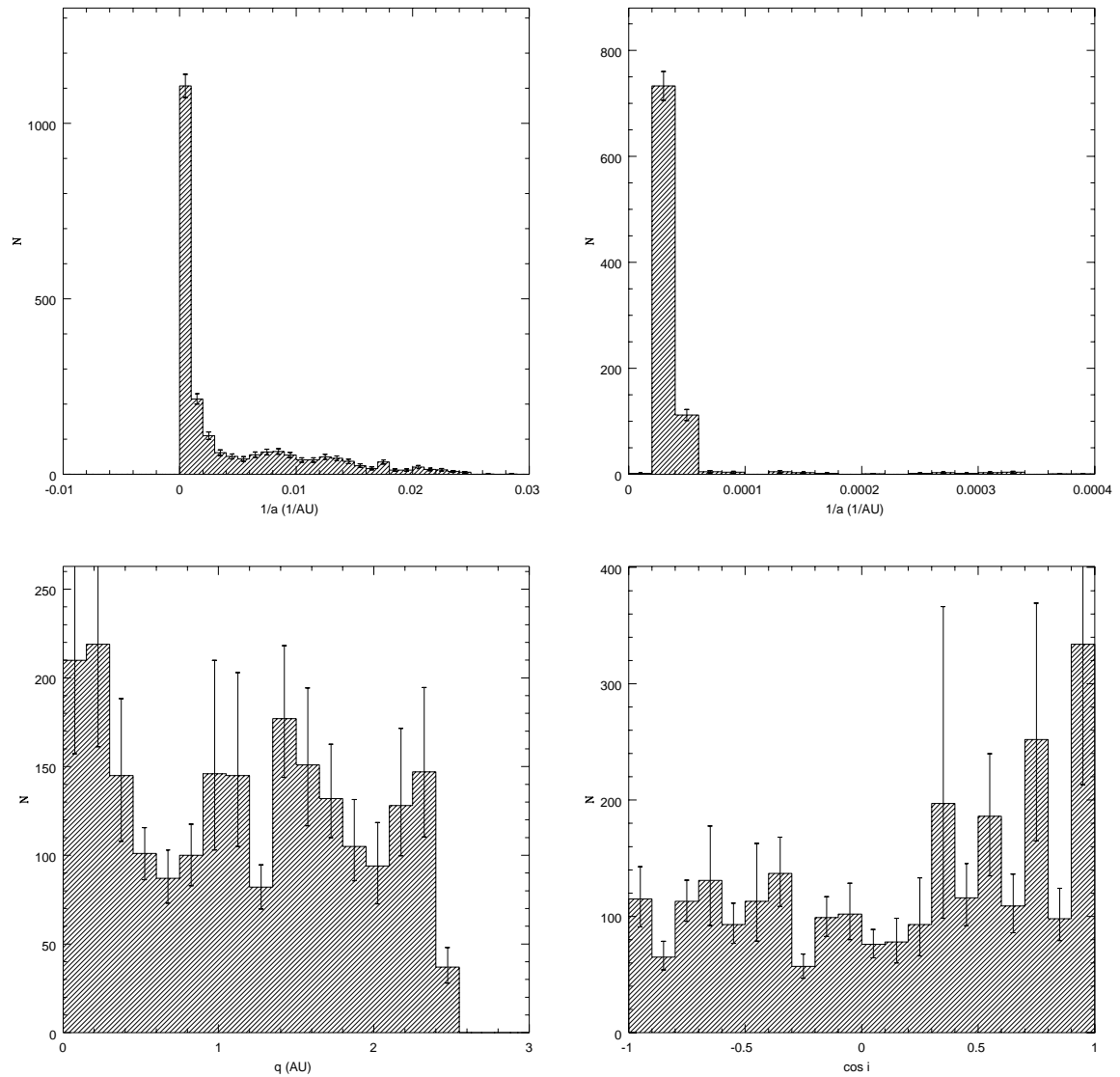
Figure 5.37: The distribution of the inverse semimajor axis $1/a$, perihelion distance $q$ and inclination $i$ given a fixed lifetime $t_x = 10^5$ yr (model A3). Simulation includes standard NG forces and a discovery probability.
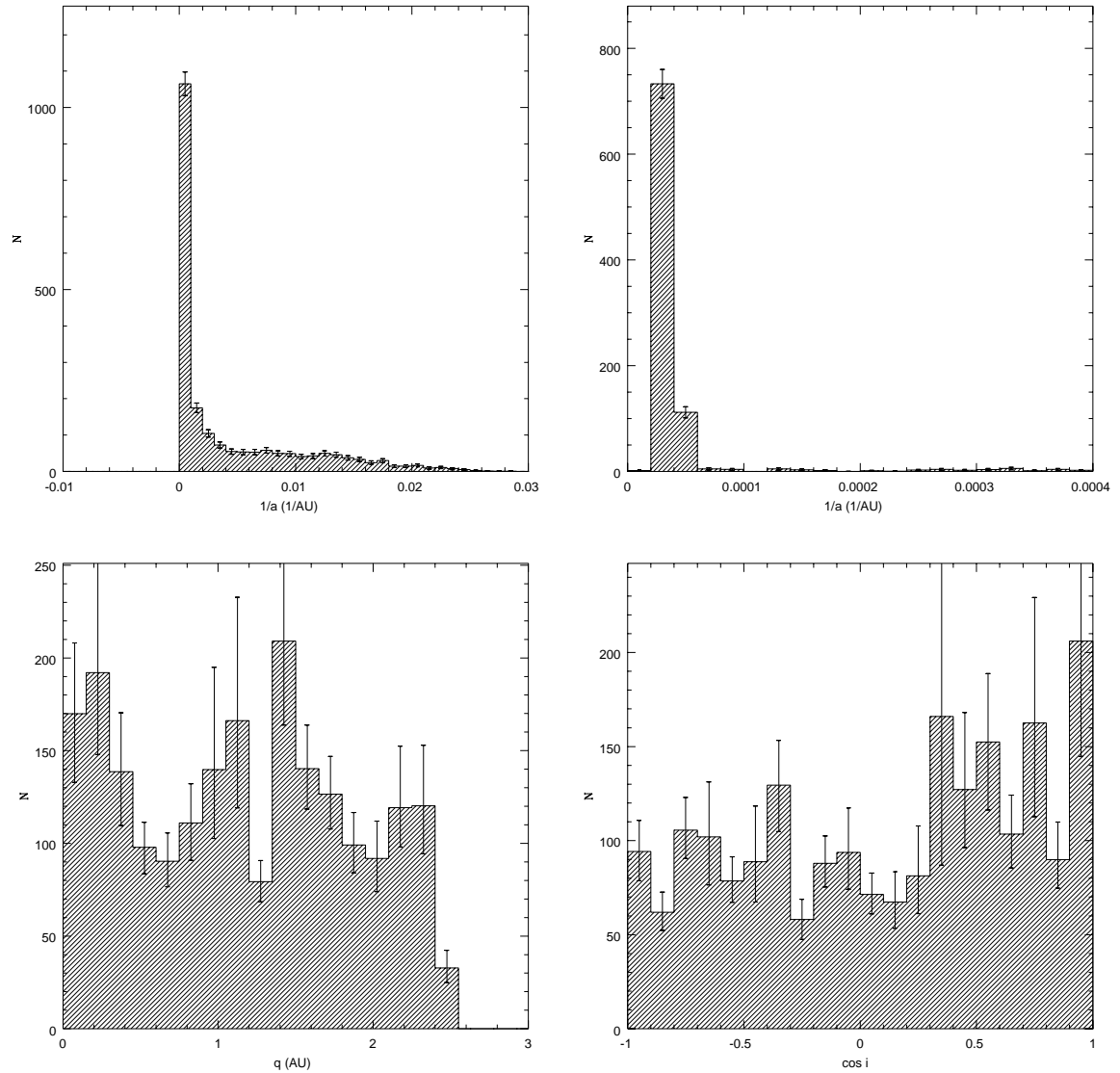
Figure 5.38: The distribution of the inverse semimajor axis $1/a$, perihelion distance $q$ and inclination $i$ given a exponential decay constant $t_x = 0.09$ Myr (model B3). Simulation includes standard NG forces and a discovery probability.

| NG forces? | Discovery? | $\Xi_1$ | $\Xi_2$ | $\Xi_3$ |
|:---:|:---:|:---:|:---:|:---:|
| No | No | $1.04 \pm 0.17$ | $1.92 \pm 0.72$ | $1.00 \pm 0.14$ |
| No | Yes | $1.05 \pm 0.15$ | $1.76 \pm 0.65$ | $0.95 \pm 0.13$ |
| Yes | No | $1.09 \pm 0.16$ | $0.99 \pm 0.45$ | $1.06 \pm 0.13$ |
| Yes | Yes | $0.94 \pm 0.14$ | $1.51 \pm 0.57$ | $1.04 \pm 0.14$ |

Table 5.12: Parameters $\Xi_i$ under Bailey's (1984) fading function, for cases which may include NG forces and a discovery probability.

which is not present in the observations or the expected intrinsic distribution. The case which includes both NG forces and a discovery probability is barely consistent (within the error bars) with the observations, but provides a more reasonable perihelion distribution. The orbital element distributions for this case are shown in Figure 5.39. The match with observations (Figure 5.33) is good except for the perihelion distribution, which increases near the Sun. There is also a small excess of comets on retrograde orbits. Bailey's fading law provides a good, but not ideal match with observations.

**Summary**

The best overall match by the one-parameter fading laws considered is provided by the power law model based on apparition or perihelion passage number (models C1 and C2), which alone provide a good match to the perihelion distribution (Figure 5.34). Fair matches are provided by a time-based exponential decay (B3) with decay constant $t_x \approx 0.09$ Myr, a constant lifetime $t_x = 0.1$ Myr (A3), and Bailey's fading law, whereas the other models produce only poor matches or can be ruled out entirely.

### 5.5.3   Two parameter fading functions

Though the available function space becomes increasingly large, a few two-parameter fading functions will be examined here. Fading laws based on orbit number will not be considered due to the similarity of the results for apparition number and orbit number.

**D) Two populations** Let the Oort cloud consist of two populations of comets, distinguished by their internal strength. The first and more fragile set of objects have a finite lifetime while the other objects, comprising a fraction $f_2$ of the total, are unaffected by fading. The fragile population's lifetimes are either

   1. a fixed number of apparitions $m_v$; $\phi(m' \leq m_v) = 1$, otherwise $\phi = f_2$,
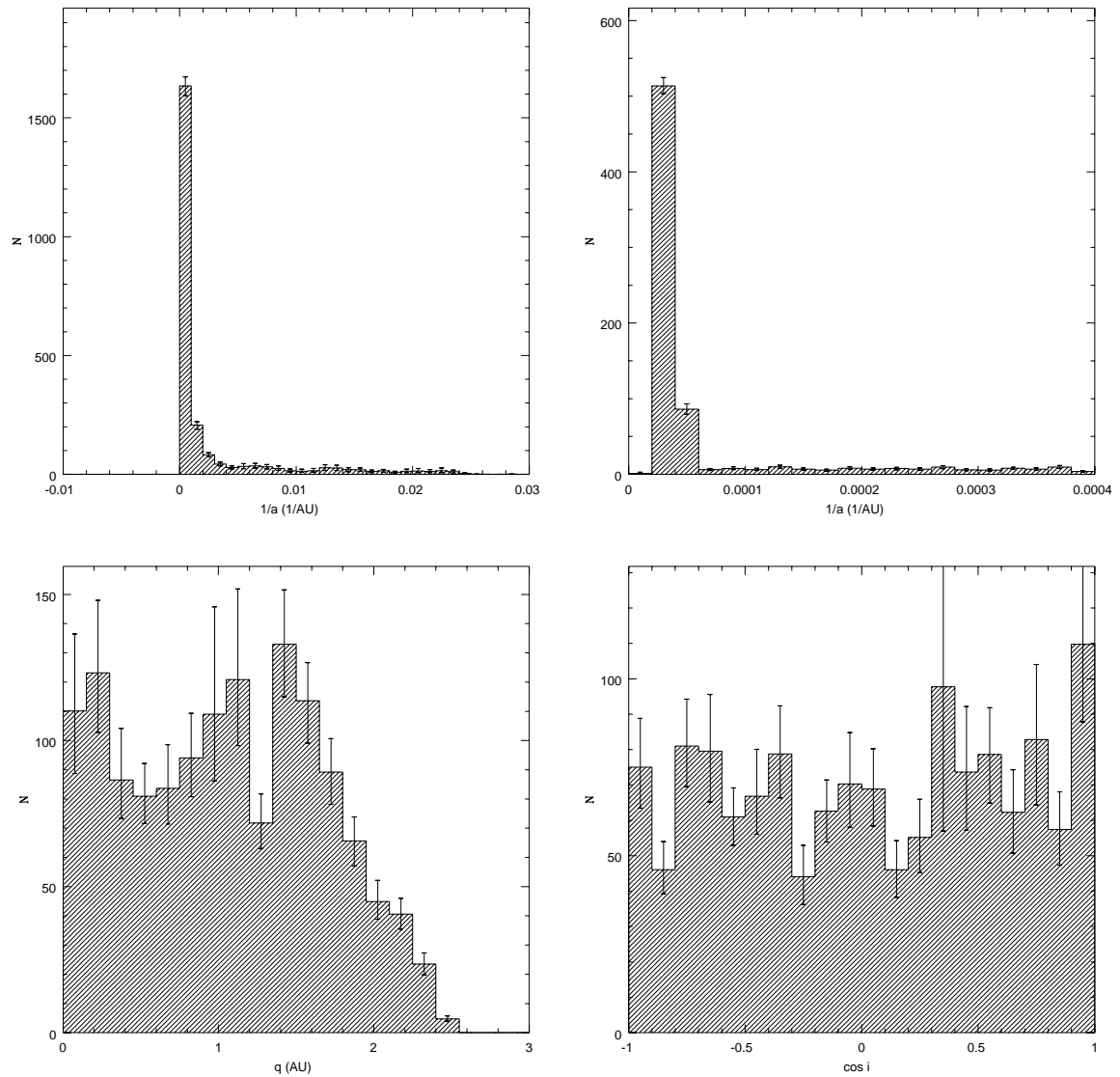
Figure 5.39: The distribution of the inverse semimajor axis $1/a$, perihelion distance $q$ and inclination $i$ given Bailey's fading law. Simulations include NG forces and a discovery probability.

2. a fixed time $t_x$ from first apparition; $\phi(t \leq t_x) = 1$, otherwise $\phi = f_2$.

Such a fading law might be appropriate if the Oort cloud contains both relatively weak "snowy" nuclei and stronger "icy" nuclei.

**E) Fixed fading probability plus survivors** In this case, one portion of the LP comets population has a fixed fading probability $\lambda$ while some fraction $f_2$ survive indefinitely. The fading functions are based either on

1. apparition number $m'$; $\phi = (1 - f_2)\lambda^{m'-1} + f_2$,

2. time $t$ since first apparition; $\phi = (1 - f_2)e^{t/t_x} + f_2$.

This is a more sophisticated treatment of the two population model.

**F) Power law variant** The fading function is a variant of the one-parameter power law, and is based either on

1. apparition number $m'$; $\phi = [(m' + \beta)/(1 + \beta)]^{-\kappa}$,

2. time $t$ in Myr since first apparition; $\phi = [(t + \beta)/\beta]^{-\kappa}$,

where $\kappa$ and $\beta$ are positive constants. Note that $\phi$ is constructed so as to be unity at $t = 0$ or $m' = 1$.

**Fading based on apparition number**

The results of model D1 are shown in Figure 5.40. The fit is generally worse than the one-parameter case (A1) shown by the heavy line, because the prograde fraction $\Xi_3$ is lower when some fraction of comets are allowed to live indefinitely. The best match among the families of curves with both NG forces and a discovery probability occurs near $m_v = 6$ orbits, for a survival fraction of roughly 0.04. This case corresponds to roughly 96% of Oort cloud comets being fragile with lifetimes against disruption or fading of approximately six orbits, while the remaining 4% are longer-lived, perhaps more similar in nature to the fading-resistant SP comets. The orbital element distributions for this scenario are in Figure 5.43, and match observations (Figure 5.33) well. Weissman (1978) also found that a two-population Monte Carlo model, in which a large fraction (85%) of LP comets had significant fading probabilities while the reminder survived indefinitely, matched the observations best. Note that the observed splitting probability for dynamically new Oort cloud comets of 0.1 per
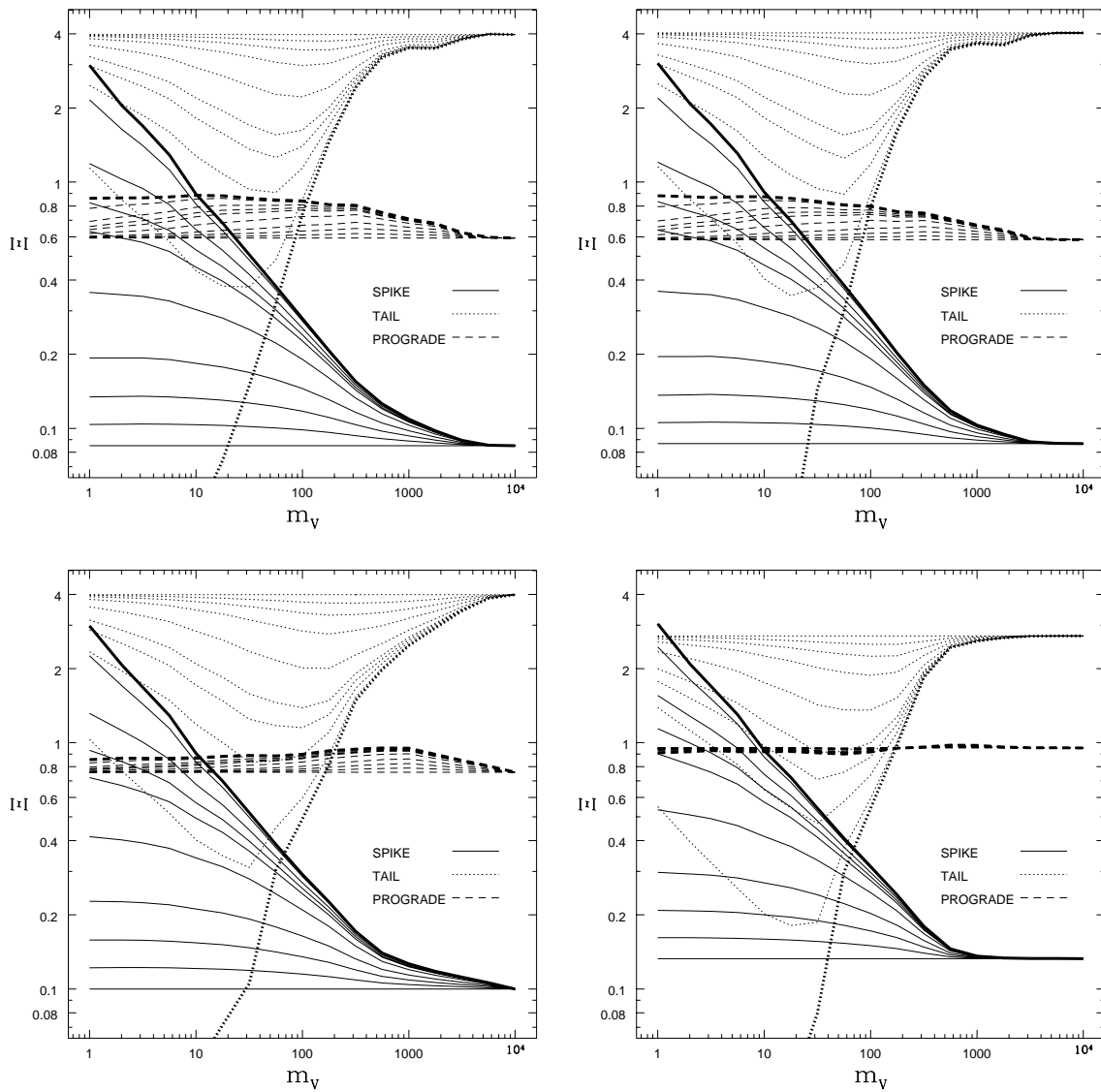
Figure 5.40: The values of $\Xi_i$ given a two-population model based on apparition number (model D1). The graphs on the right include a discovery probability, those on the left do not. The upper two graphs are based on the standard case, the lower two on the standard NG case. The fraction $f_2$ which survive past the lifetime $m_v$ are 0, 0.01, 0.04, 0.07, 0.1, 0.2, 0.4, 0.6, 0.8 and 1, beginning with the heavy line.
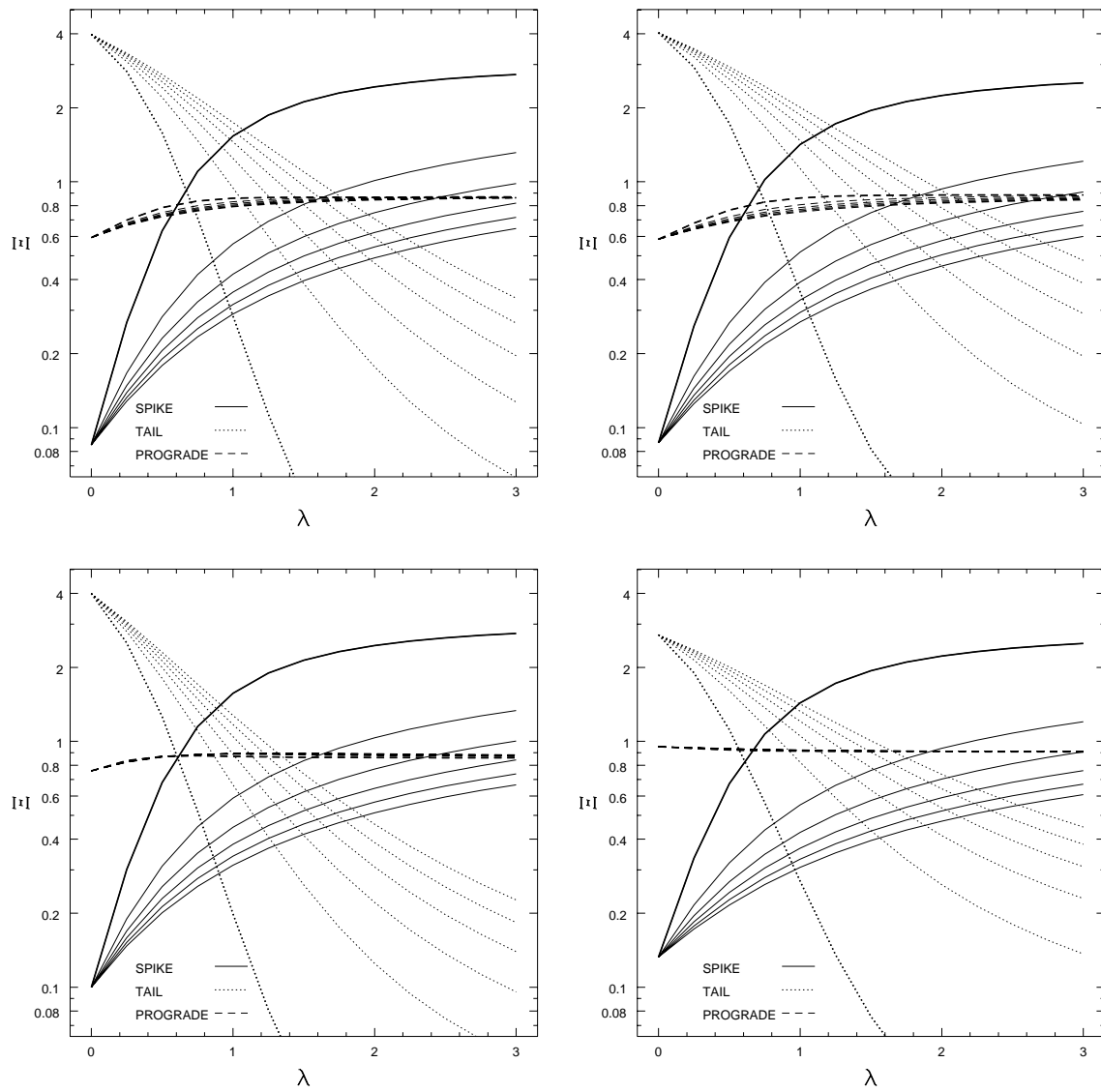
Figure 5.41: The values of $\Xi_i$ given a a fixed fading probability $\lambda$ per apparition together with a fraction $f_2$ of unfading survivors (model E1). The graphs on the right include a discovery probability, those on the left do not. The upper two graphs are based on the standard case, the lower two on the standard NG case. The values of $f_2$ are 0, 0.04, 0.08, 0.12, 0.16, 0.2, beginning with the heavy line.
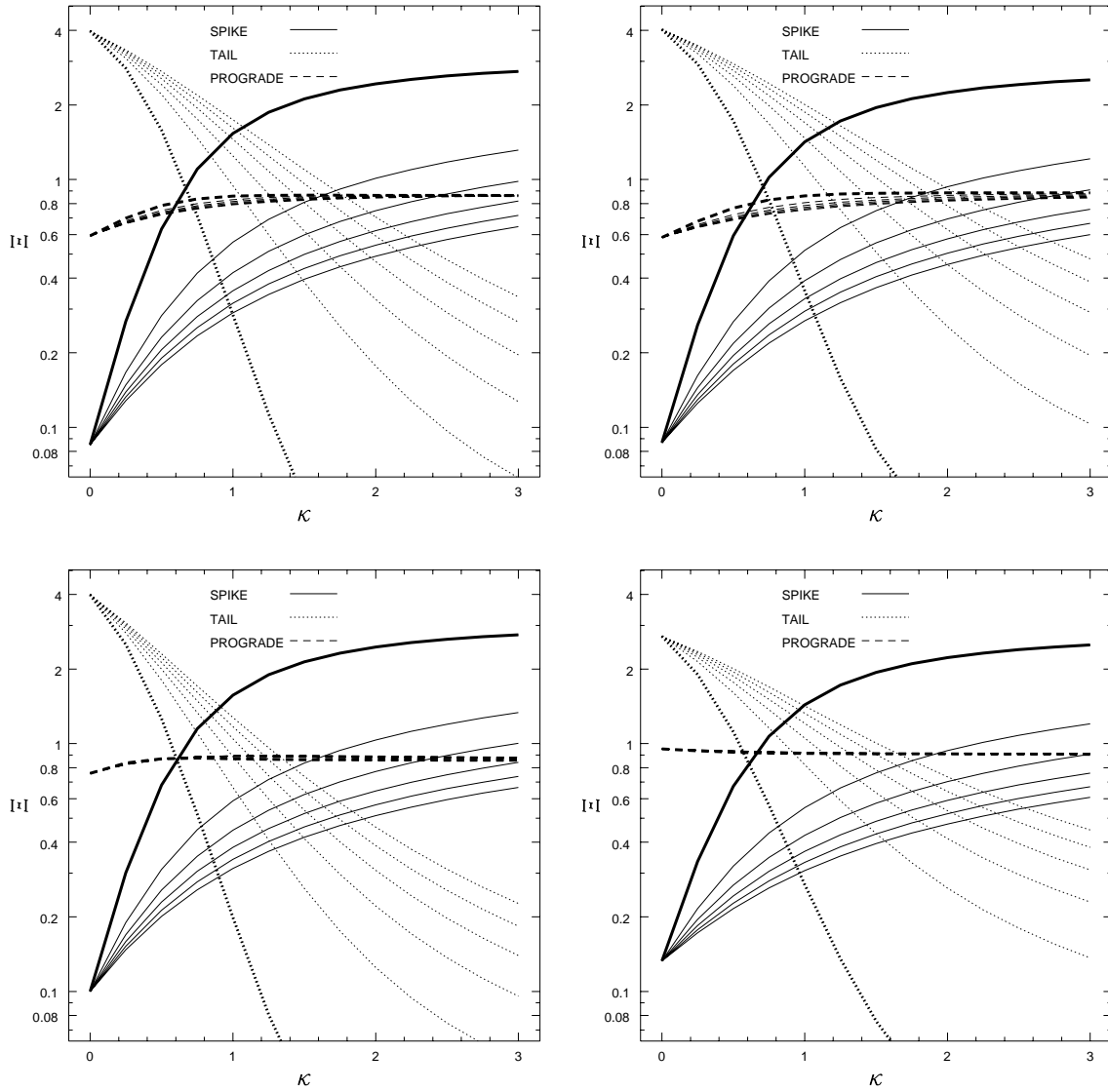
Figure 5.42: The values of $\Xi_i$ given a two-parameter power law lifetime based on apparition number (model F1). The graphs on the right include a discovery probability, those on the left do not. The upper two graphs are based on the standard case, the lower two on the standard NG case. The values of $\beta$ are 0, 10, 20, 30, 40 and 50, beginning with the heavy line.

orbit results in a half-life of seven orbits (Equation 3.62), suggesting splitting may be the source of fading if there is indeed a "fragile" population of Oort cloud comets.

The fading law involving a fixed fading probability for one segment of the population, and an indefinite lifetime against fading for the rest (model E1) produces results as shown in Figure 5.41. The match is usually no better than the no survivor case (B1), shown by the heavy line, and typically gets worse as the survival fraction $f_2$ increases.

The two-parameter power law (model F1), displayed in Figure 5.42, ordinarily does no better than its one-parameter counterpart. Though the prograde fraction $\Xi_3$ shows little variation, the intersection of the $\Xi_1$ and $\Xi_2$ curves is typically below the value of one required to match observations when $\beta > 0$. Though an eventual return to near unity as $\kappa \to \infty$ is not excluded by these figures, the extremely rapid fading required in such a case seems unlikely.

The two-parameter fading models based on apparition number typically do no better job of matching the observed distribution than one-parameter models, with the exception of model D1, which can provide a good match to observations when most comets have short ($\sim 6$ orbits) lifetimes, while a small fraction ($\sim 4\%$) live indefinitely.

**Fading based on time since first apparition**

When the two-population fading model is based on the time since first apparition (model D2, Figure 5.44), the fit is typically only slightly better than the corresponding one-parameter model. The normalised tail to total ratio $\Xi_2$ provides the most stringent restriction on the survival fraction. Only a small fraction, roughly 1%, of comets could survive indefinitely and still produce a match, as long as the remaining comets have a lifetime against fading $t_x \approx 10^5$ yr. The distributions of orbital elements for this case are displayed in Figure 5.47. The perihelion distance and inclination distributions are very similar to those of the one-parameter (A3) model (Figure 5.37), and match the observations only poorly.

The case of exponential decay with time plus a small fraction of non-fading comets produces the results displayed in Figure 5.45 (model E2). Only a very small fraction ($\lesssim 2\%$) can survive in either of the four cases if a match is to be obtained, and the best match appears to remain with the case of no survivors (model B3).

Figure 5.46 displays the effects of model F2. The intersection of $\Xi_1$ and $\Xi_2$ occurs above unity for all curves in the families plotted, approaching it more closely as $\kappa$ increases. The
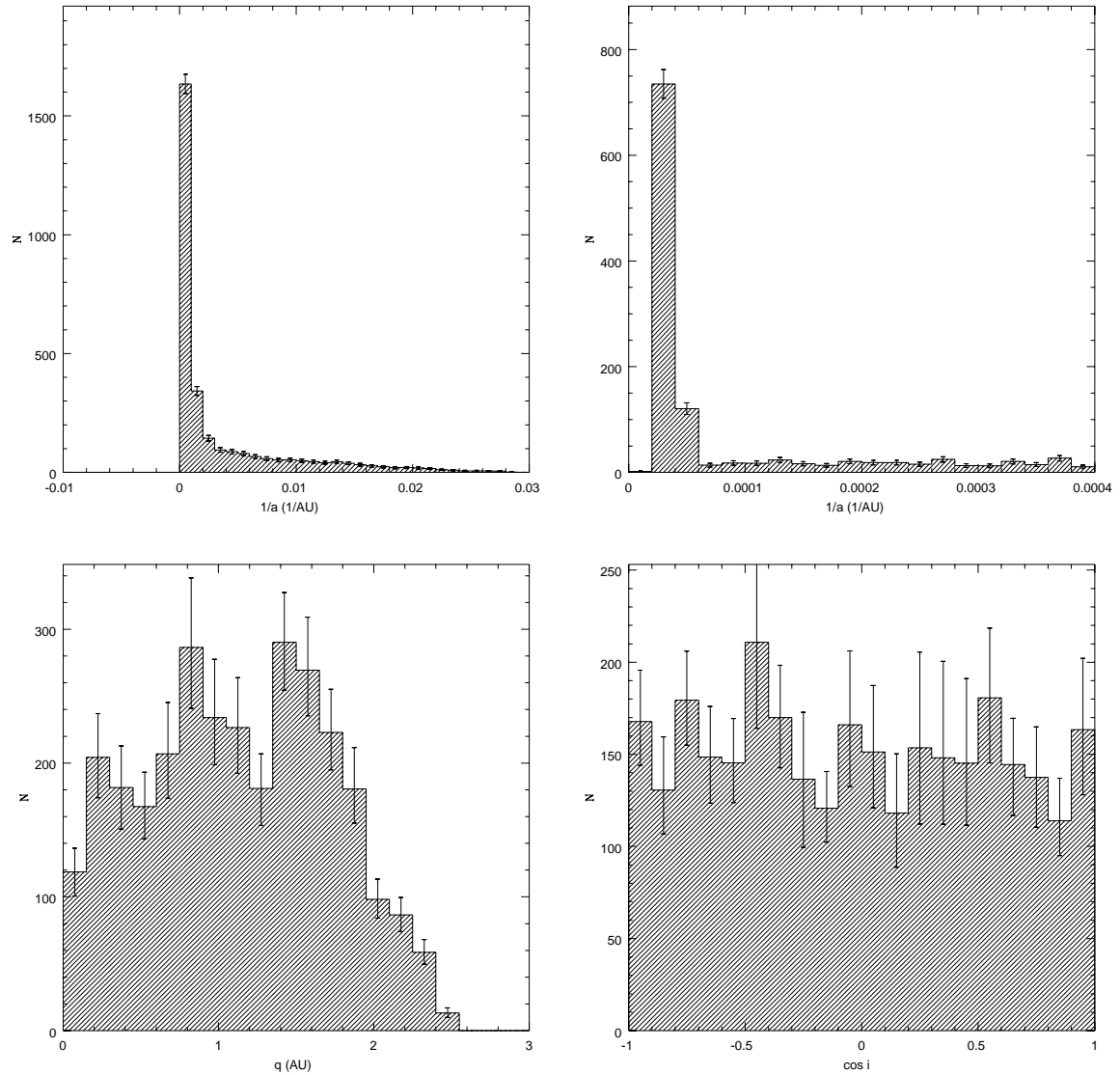
Figure 5.43: The distribution of the inverse semimajor axis $1/a$, perihelion distance $q$ and inclination $i$ given a two population model (D1) with $m_v = 6$ apparitions and a survival fraction $f_2$ of 0.04. Simulations include NG forces and the discovery probability.
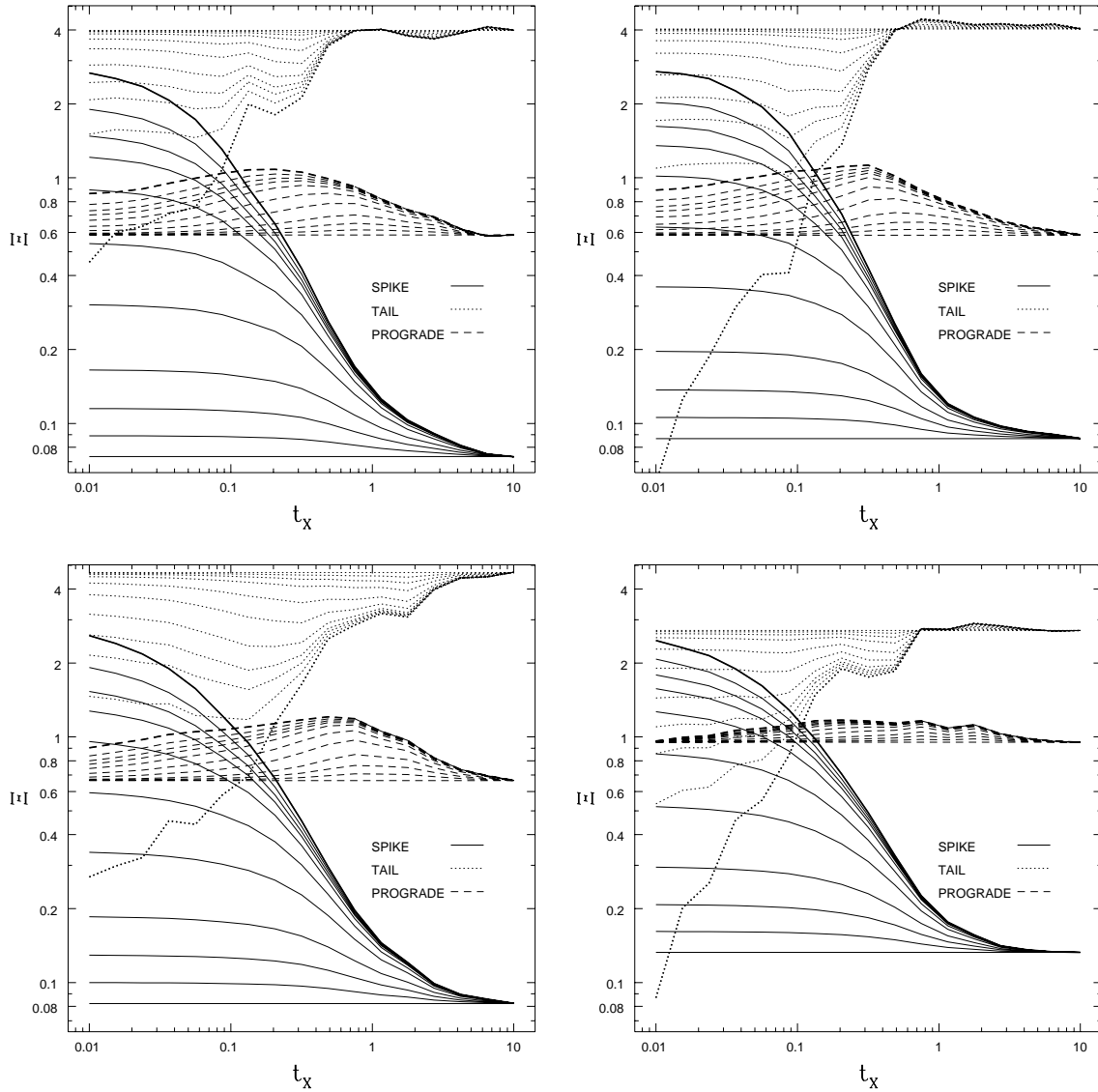
Figure 5.44: The values of $\Xi_i$ given a two population model where a fraction $f_2$ survive indefinitely and the remainder have a lifetime $t_x$ based on time since first apparition (model D2). The graphs on the right include a discovery probability, those on the left do not. The upper two graphs are based on the standard case, the lower two on the standard NG case. The values of $f_2$ are 0, 0.01, 0.02, 0.03, 0.05, 0.1, 0.2, 0.4, 0.6, 0.8 and 1, beginning with the heavy line.
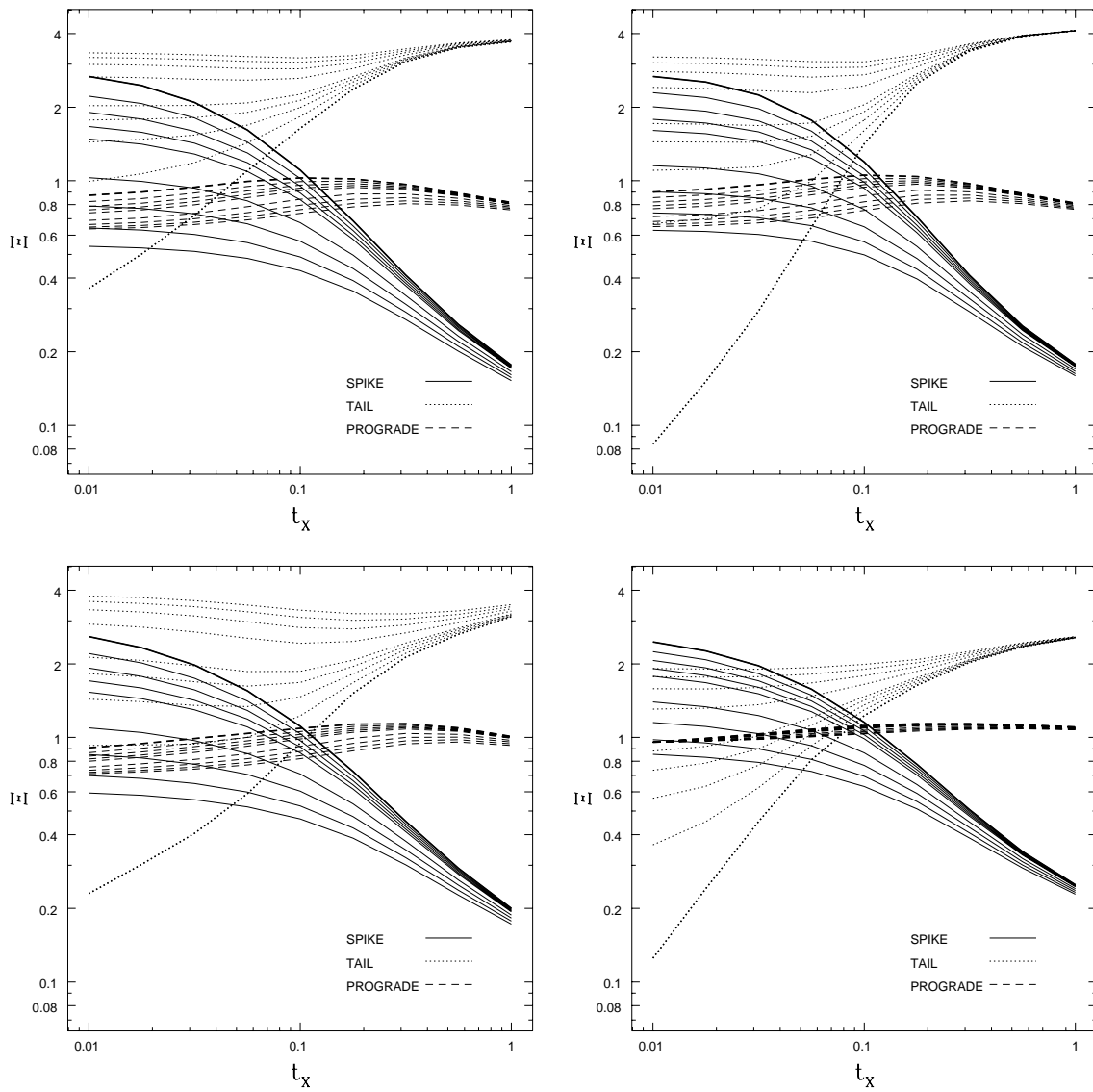
Figure 5.45: The values of $\Xi_i$ given an exponential decay plus survivors fading model with a decay time $t_x$ based on time since first apparition (model E2). The graphs on the right include a discovery probability, those on the left do not. The upper two graphs are based on the standard case, the lower two on the standard NG case. The survivor fractions are 0, 0.005, 0.01, 0.015, 0.02, 0.04, 0.06, 0.08 and 0.1, beginning with the heavy line.
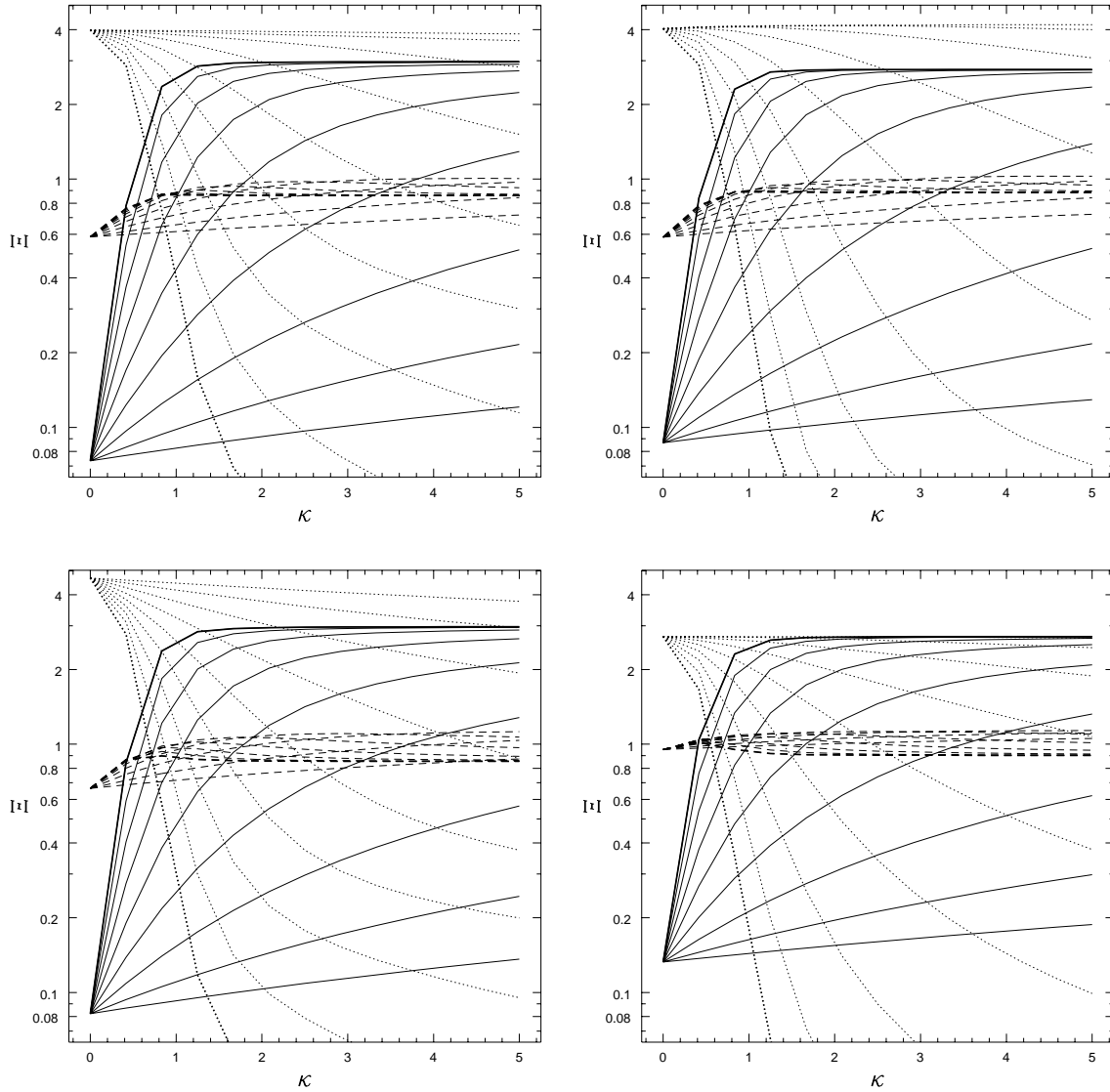
Figure 5.46: The values of $\Xi_i$ given a two parameter power law with exponent $-\kappa$, and based on time since first apparition (model F2). The graphs on the right include a discovery probability, those on the left do not. The upper two graphs are based on the standard case, the lower two on the standard NG case. The $\beta$ parameter runs from 1000 Myr to 0.1 Myr, in steps of 1/2 in the base-10 logarithm, beginning with the heavy line (solid line: $\Xi_1$, dotted: $\Xi_2$, dashed: $\Xi_3$).
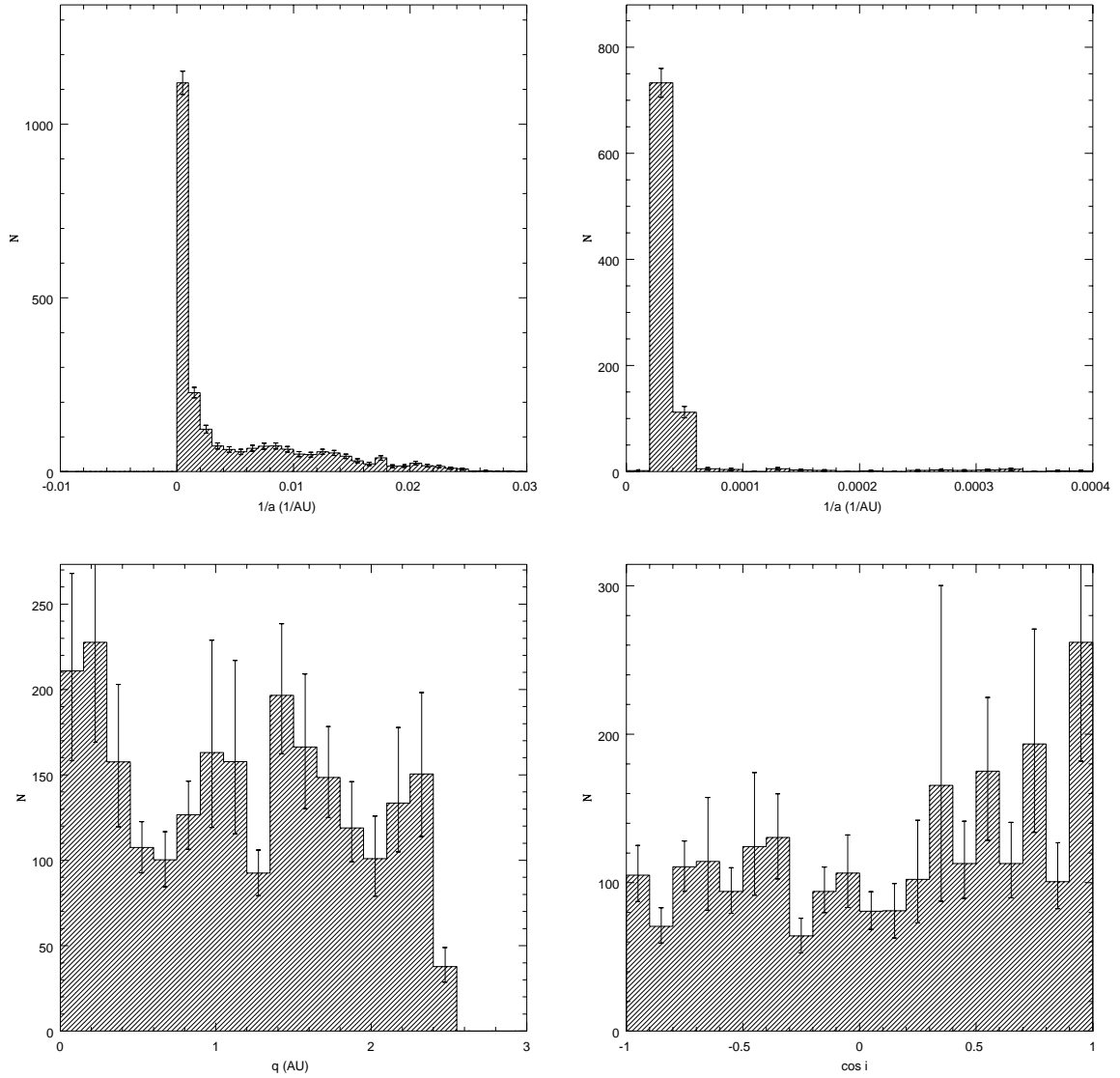
Figure 5.47: The distribution of the inverse semimajor axis $1/a$, perihelion distance $q$ and inclination $i$ given a two population model with $t_x = 10^5$ yr and a survival fraction of 0.01 (model D2). Simulations include NG forces and the discovery probability.

value of $\Xi_3$ also remains close to unity, particularly in the case which includes NG forces and a discovery probability. Thus, the best matches are provided as $\kappa \to \infty$, but the increasing steepness of this fading law makes it an unlikely candidate.

### 5.5.4   Summary

The two-parameter fading laws examined here typically do only slightly better than the one-parameter laws at matching the observed distributions, if at all. The best one-parameter fading functions, based on the values of the $\Xi_i$ parameters and an examination of the orbital elements distributions, are C1 and C2 (power law based on apparition/orbit number, $\kappa \approx 0.6$). The best match among the two-parameter families is obtained from model D1 (two populations, 96% of comets live only 6 orbits, the remainder indefinitely). In particular, C1, C2 and D1 can provide good matches to the perihelion distributions, particularly in regards to the decrease in numbers observed at $q$ close to the Sun.

# Chapter 6

# Conclusions

The dynamical evolution of long-period comets has been simulated from its beginning in the Oort cloud to its end with the comets' loss or destruction. A numerical integration algorithm was used to follow each comet's trajectory individually, under the influence of the giant planets and the dominant component of the Galactic tide, though the effects of passing stars were ignored. Additional simulations studied the effects of outgassing reaction forces, a hypothetical circumsolar disk or solar companion and the disruption or fading of the nucleus. Solar wind and radiation pressure, the heliopause, molecular clouds and drag were also examined but proved to be either negligible or inapplicable. Various conclusions can be drawn from this research:

The concentration of aphelion directions of the observed long-period comets at mid-Galactic latitudes (Figure 2.11b) is due to the action of the Galactic tide, and is not simply an artifact of statistical noise. It may be possible to use the observed distribution of the Galactic argument of perihelion $\tilde{\omega}$ to estimate the relative comet injection rates of the tide and passing stars, as injection due to the tide should be restricted to the range $\sin 2\tilde{\omega} > 0$ while that due to stars will be uniform over $\tilde{\omega}$. However, the observed sample of dynamically new long-period comets is too small to disentangle these components as yet.

The current Oort cloud contains roughly $5 \times 10^{11}$ objects orbiting between 10 000 and 50 000 AU from the Sun (§ 5.2.3), assuming the Oort cloud is in a near steady-state, with a number density proportional to $r^{-3.5}$, and that the flux of dynamically new long-period comets through a sphere of radius 3 AU around the Sun is currently 10 yr$^{-1}$. As many as $3 \times 10^{11}$ Oort comets may have entered the loss cylinder since the Solar System's formation,

indicating that the original Oort cloud had over $10^{12}$ members, and probably more.

All but a small fraction of comets in the Oort spike are making their first apparition. In the absence of fading, roughly 7% of observed comets with $1/a < 10^{-4}$ AU$^{-1}$ have made one or more previous apparitions; similarly, 2% of comets originating in the Oort cloud do not make their first visible perihelion passage within the spike, but on more tightly bound orbits (§ 5.2.2). As these numbers ignore the effects of fading, they provide only upper limits and the actual fractions are likely to be much lower.

The Oort cloud provides only a small fraction of the short-period comets, up to 3% if fading is ignored. Thus another source or sources must be providing the bulk of the short-period comets.

Long-period comets pass through each giant planet's sphere of influence at a rate of approximately one every few years (§ 5.2.7). Collision rates may be as high as once per million years for Jupiter and Saturn, dropping to roughly once per few hundred million years for Uranus and Neptune.

The purely dynamical lifetimes of simulated long-period comets are too long to reproduce the observed distributions of these comets, with discrepancies in particular in the original inverse semimajor axis and inclination distributions. Thus the "fading problem" is not simply a result of incomplete theoretical treatments, but represents a real gap in our understanding of the evolution of long-period comets, and possibly in our knowledge of the inventory of the Solar System.

The observed prograde fraction $\Psi_3$ of long-period comets is near 0.5, as is that of the dynamically new ($V_1$) comets simulated here. However, $\Psi_3$ is expected to decrease as the comet population ages due to preferential ejection of prograde comets by the giant planets; in the standard model, $\Psi_3$ is 0.3 (§ 5.2.2). The prograde fraction thus provides a measure of the age of the long-period comet population. The observed value of near 0.5 implies that long-period comet lifetimes are much shorter than their dynamical lifetimes, and indicates that a fast-acting fading mechanism of some kind is at work.

Non-gravitational forces play a significant role in shaping the distributions of the long-period comet orbital elements, in particular by shortening their lifetimes against ejection and by sculpting the distribution at small perihelia. NG forces reduce the dynamical lifetimes of comets but are too small by roughly two orders of magnitude to resolve the fading the problem of themselves.

The fading problem probably does not reflect the presence of a massive circumsolar disk or solar companion object, at least as far as can be determined from the somewhat simplified treatment given these features here. Low mass disks and companions are unable to produce orbital element distributions which match observations, while at higher masses, these features prevent the filling of the loss cylinder (§ 5.0.1).

No clear explanation for the existence of the observed visible comets on hyperbolic original orbits is provided by this research. The excess velocities are small, corresponding to roughly $-10^{-4}$ AU$^{-1}$ in inverse semimajor axis, but are larger than those produced by the Galactic tide ($\sim -10^{-6}$ AU$^{-1}$, Equation 5.1) or non-gravitational forces ($\sim -10^{-5}$ AU$^{-1}$, Equation 3.36a) over a single comet orbit. A circumsolar disk or solar companion might produce a change $\Delta(1/a)$ of this magnitude, but would strongly influence the Oort cloud and prevent the filling of the loss cylinder (§ 5.0.1). Other effects, such as rapid variations in outgassing or asymmetrical outgassing about perihelion might produce hyperbolic comets, but such effects were not examined here.

The observed distributions of orbital elements can be matched by the addition of fading to the simulations, though of a fairly restricted form: a large fraction of comets must fade fairly quickly ($\lesssim 10$ orbits) while a smaller fraction must survive much longer times ($\gtrsim 1000$ orbits). The fact that the cratering rate is near that expected from the current known populations of comets and asteroids (§ 3.10.1) implies that fading results in the complete disruption of the comet nucleus. This hypothesis is supported by the lack of observed sharp decreases in the brightnesses of long-period comets as they pass perihelion, decreases which might be expect if fading were due to a rapid loss of volatiles which left the comets inert but intact (§ 3.8).

A one-parameter power law fading function (model C1 and C2) with exponent $\kappa \approx 0.6$ provides a good match between our simulations and observations. This fading law might be expected if each apparition results in the loss of approximately equal amounts of volatiles, and the differential mass distribution of dynamically new long-period comets $N(M)dM \propto M^{-1.6}dM$ (§ 5.5.2).

A two-population fading model (D1) in which approximately 95% of comets survive for roughly six orbits and the remainder indefinitely also provides good agreement with observations, and could be explained by a division of the Oort cloud population into objects with low and high internal cohesiveness. Such a fading model would be roughly consistent with

the observed splitting probabilities of dynamically new long-period comets, approximately 0.1 per orbit (Equation 3.62).

The fading problem remains partly unresolved. Though it seems likely to be associated with the disruption of the nucleus rather than a dynamical effect, the exact nature of this decay process remains unclear. The fading process is likely to be sensitive to the each comet's particular properties and to the pattern of thermal and other stresses to which they are subject, and thus very difficult to predict. Future progress will likely require improved observational data rather than more sophisticated theoretical treatments; in particular more information on the physical characteristics of comet nuclei, as well as greater observational coverage of their orbits, is needed.

# Appendix A

# Celestial Mechanics

## A.1 Orbital elements

The six standard elements of a two-body orbit are: semimajor axis $a$, eccentricity $e$, inclination $i$, longitude of the ascending node $\Omega$, argument of perihelion $\omega$, and true anomaly $f$ (*e.g.* Roy 1978). The reader is assumed to be familiar with these elements, but a brief sketch of the angular orbital elements is presented in Figure A.1.

The elements are usually measured in the heliocentric reference frame, but can also be taken in the barycentric frame, in which case the centre of mass is the origin about which the elements are computed instead of the Sun. The notation used here for the heliocentric and barycentric elements is the same, with the context indicating which is being used.

## A.2 Galactic elements

The angular orbital elements as measured in the Galactic frame are also of interest here (§ 3.2.1). In this case, the Sun is at the origin, but the "vernal equinox" is directed instead towards the Galactic centre, and the "ecliptic pole" is directed towards the Galactic pole. The Galactic angular elements are denoted by a tilde *i.e.* $\tilde{i}$, $\tilde{\Omega}$ and $\tilde{\omega}$. The Galactic argument of perihelion $\tilde{\omega}$ should not be confused with the commonly-used symbol for the longitude of perihelion, $\varpi = \Omega + \omega$, as the longitude of perihelion will not be used here.
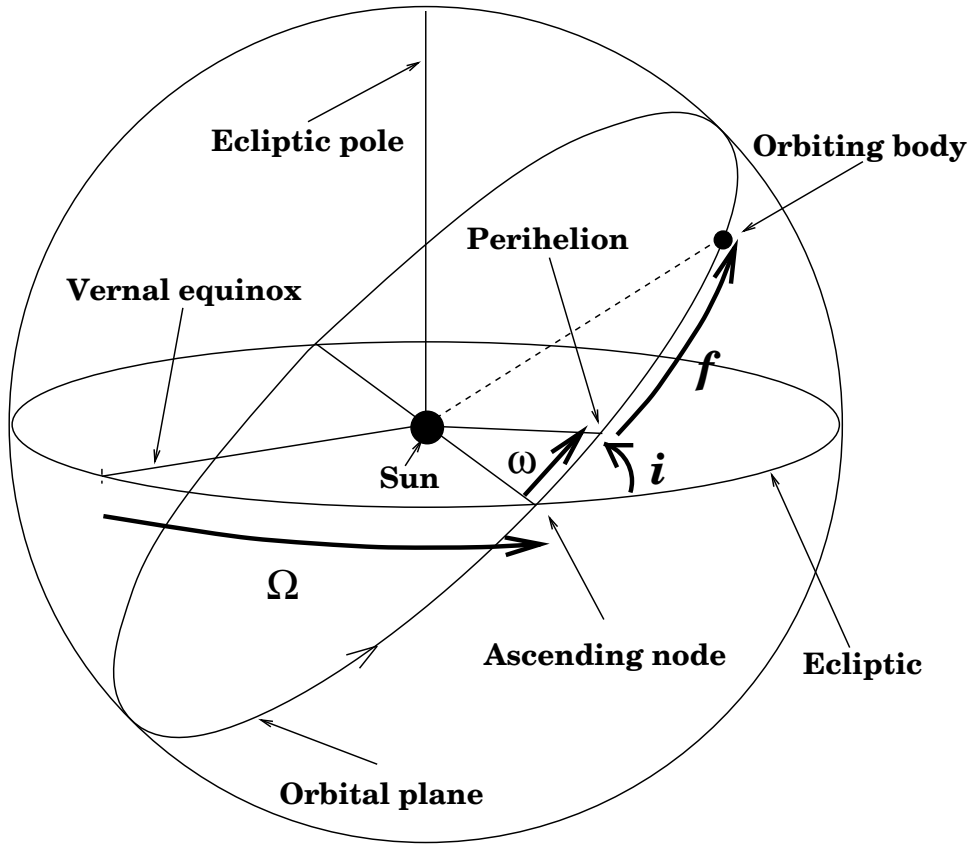
Figure A.1: The inclination $i$, longitude of the ascending node $\Omega$, argument of perihelion $\omega$ and true anomaly $f$ in the ecliptic frame. Adapted from Roy (1978).

## A.3 Kepler's third law

The orbital period $\tau$ of a comet can easily be related to its semimajor axis $a$ through Kepler's third law:

$$\tau = 2\pi \left( \frac{a^3}{GM_\odot} \right)^{1/2}, \tag{1.1}$$

where $G$ is the gravitational constant, $M_\odot$ is the mass of the Sun, and the mass of the orbiting body has been assumed to be negligible. In the case where $a$ is measured in AU, $M_\odot$ in solar masses and $\tau$ in years, this expression reduces to

$$\tau = a^{3/2}. \tag{1.2}$$

## A.4  Radius in the orbit

The distance $r$ of the orbiting body from the origin is given

$$r = \frac{a(1 - e^2)}{1 + e \cos f}. \tag{A.17}$$

The true anomaly $f$ can be determined from the time $t$ since perihelion passage by solving the transcendental **Kepler's equation**, but this equation will not be required for these discussions.

## A.5  Two-body energy

The energy per unit mass $E$ of a particle on a bound orbit in a two-body system is simply $-GM/2a$, where $M$ is the total mass of the system and $a$ is the semimajor axis measured in the barycentric or centre of mass frame. For a massless (test) particle orbiting the Sun, $M = M_\odot$, and the barycentric and heliocentric frame coincide. In this case, the inverse semimajor axis $1/a$ provides an unambiguous measure of the test particle's energy.

## A.6  Energy in multi-body systems

If potentials other than that of the Sun are present, the semimajor axis $a$ of a test particle's orbit may vary due to the perturbing presence of these other fields. In the presence of massive planets, the Solar System's heliocentric and barycentric frames no longer coincide, owing to the accelerations imparted to the Sun by the planets. Nevertheless, a useful "snapshot" of a test particle's energy is provided by the osculating value of $1/a$. The osculating elements are those which would be measured if the particle were travelling with its instantaneous position and velocity in a simple two-body system rather than a perturbed one. For our purposes, if is convenient to measure $1/a$ in the barycentric frame: though its accuracy as a measure of energy is degraded while the comets travel within the planetary system, the barycentric $1/a$ reduces to the correct two-body value as the particle moves towards infinity. For this reason the inverse semimajor axis of comets will be measured at aphelion here.

## A.7 Gauss' equations

If a particle orbiting the Sun is subject to a small perturbing force $\vec{F}_{pert}$, Gauss's planetary equations can be used to deduce the resulting change in its orbital elements. A "small" perturbing force is taken here to mean that the fractional change in any orbital element is small over a single orbit.

Let the perturbing force be written as

$$\vec{F}_{pert} = F_1 \hat{e}_1 + F_2 \hat{e}_2 + F_3 \hat{e}_3, \tag{A.18}$$

where the three orthogonal unit vectors are: radial $\hat{e}_1$ (positive outward from the Sun), transverse $\hat{e}_2$ (in the orbital plane, positive along the direction 90° ahead of the Sun-comet line), and normal $\hat{e}_3$ (perpendicular to the orbital plane, parallel to $\hat{e}_1 \times \hat{e}_2$). Then, in terms of these components, Gauss's planetary equations are

$$\frac{da}{dt} = \left[ \frac{4a^3}{GM_\odot(1 - e^2)} \right]^{1/2} \left[ F_1 e \sin f + F_2(1 + e \cos f) \right], \tag{A.19a}$$

$$\frac{de}{dt} = \left[ \frac{a(1 - e^2)}{GM_\odot} \right]^{1/2} \left[ F_1 \sin f + F_2 \left( \cos u + \cos f \right) \right], \tag{A.19b}$$

$$\frac{di}{dt} = \frac{F_3 r \cos(\omega + f)}{[GM_\odot a(1 - e^2)]^{1/2}}, \tag{A.19c}$$

$$\frac{d\Omega}{dt} = \frac{F_3 r \sin(\omega + f)}{[GM_\odot a(1 - e^2)]^{1/2} \sin i}, \tag{A.19d}$$

$$\frac{d\omega}{dt} = \left[ \frac{a(1 - e^2)}{e^2 GM_\odot} \right]^{1/2} \left[ -F_1 \cos f + F_2 \left( \frac{2 + e \cos f}{1 + e \cos f} \right) \sin f \right] - \frac{d\Omega}{dt} \cos i, \tag{A.19e}$$

$$\frac{d\epsilon}{dt} = \frac{e^2}{1 + (1 - e^2)^{1/2}} \left( \frac{d\Omega}{dt} + \frac{d\omega}{dt} \right) + 2 \frac{d\Omega}{dt} (1 - e^2)^{1/2} \sin^2 \frac{i}{2} - \frac{2 F_1 r}{(GM_\odot a)^{1/2}}, \tag{A.19f}$$

where $u$ is the eccentric anomaly, such that $\cos u = (a - r)/ae$, and $\epsilon$ is the mean longitude at $t = 0$, *i.e.* the mean longitude $\ell$ is

$$\ell = \int_0^t \frac{d\mu}{dt} dt + \epsilon, \tag{A.20}$$

where $d\mu/dt$, the rate of change of the mean anomaly $\mu$, is just the mean Keplerian angular velocity $d\mu/dt = 2\pi/\tau$.

The median eccentricity of Marsden's (1993) comet catalogue is 0.66; for the 289 long-period comets with computed original orbits, the median $e$ is 0.9999. Thus, it is convenient

to consider Gauss's equations under the approximation $e \approx 1$, or equivalently, $q/a \ll 1$:

$$\frac{da}{dt} \approx \left(\frac{2a^4}{GM_\odot q}\right)^{1/2} [\, F_1 \sin f + F_2(1 + \cos f)\,], \tag{A.21a}$$

$$\frac{de}{dt} \approx \left(\frac{2q}{GM_\odot}\right)^{1/2} [\, F_1 \sin f + F_2\,(\cos E + \cos f)\,], \tag{A.21b}$$

$$\frac{di}{dt} \approx \left(\frac{2q}{GM_\odot}\right)^{1/2} F_3 \frac{\cos(\omega + f)}{1 + \cos f}, \tag{A.21c}$$

$$\frac{d\Omega}{dt} \approx \left(\frac{2q}{GM_\odot}\right)^{1/2} F_3 \frac{\sin(\omega + f)}{(1 + \cos f)\sin i}, \tag{A.21d}$$

$$\frac{d\omega}{dt} \approx \left(\frac{2q}{GM_\odot}\right)^{1/2} \left[-F_1 \cos f + F_2 \left(\frac{2 + \cos f}{1 + \cos f}\right) \sin f\right] - \frac{d\Omega}{dt} \cos i, \tag{A.21e}$$

$$\frac{d\epsilon}{dt} \approx \frac{d\omega}{dt} + \left[1 + 2\left(\frac{2q}{a}\right)^{1/2} \sin^2 \frac{i}{2}\right] \frac{d\Omega}{dt} - \frac{4qF_1}{(GM_\odot a)^{1/2}(1 + \cos f)}, \tag{A.21f}$$

These equations will prove useful in determining the effects of outgassing and other perturbations on comets.

# Appendix B

# Error tolerances

The error tolerance $\zeta$ is converted to an error limit for each individual regularised coordinate through a combination of **relative** and **absolute** terms: the first is dependent on the comet's instantaneous orbit; the second is not.

Because the unperturbed regularised equations are those of a simple harmonic oscillator (§ 4.1.2), the error limits for the position and velocity coordinates are taken simply to be $\zeta$ times their instantaneous amplitudes. For the energy $h$ and time $t$, the relative term is based on the instantaneous values of $h$ and and the period $\tau$ respectively.

The absolute term is required to avoid excessively stringent error limits on coordinates that happen to have near-zero amplitudes. The absolute terms are based on an arbitrary Sun-centred reference orbit, usually taken to have $a_0 = 10^4$ AU, with corresponding regularised energy $h_0$. The error limit equations are shown in Equations B.1a,b,c and d below, with the relative term first, the absolute term second. The error tolerance for $t$ has no absolute term as comets with small orbits are terminated in our simulations before their period becomes too small.

$$
\begin{aligned}
\mathcal{E}_{u_j} &= \zeta \left( \frac{2}{h} u_j'^{\,2} + u_j^2 \right)^{1/2} + \zeta a_0^{1/2} & j = 1, 2, 3, 4; && \text{(B.1a)} \\
\mathcal{E}_{u_j'} &= \zeta \left( \frac{h}{2} u_j^2 + u_j'^{\,2} \right)^{1/2} + \zeta \left( \frac{h_0 \, a_0}{2} \right)^{1/2} & j = 1, 2, 3, 4; && \text{(B.1b)} \\
\mathcal{E}_h &= \zeta \, h + \zeta \, h_0, &&& \text{(B.1c)} \\
\mathcal{E}_t &= \zeta \, \tau. &&& \text{(B.1d)}
\end{aligned}
$$

# Appendix C

# The Flux of Long-Period Comets

## C.1  The flux across the entrance surface

The orbit-averaged inwards flux $\Phi_E$ per unit time due to the Galactic tide across any surface of constant angular momentum $J = J_E$ per unit $L$ is the integral of Equation 4.24 over the all other canonical coordinates,

$$\Phi_E(L, J_E)\, dL = \frac{dL}{\tau} \int\limits_0^{2\pi} df \int\limits_0^{2\pi} d\tilde{\Omega} \int\limits_0^{2\pi} d\tilde{\omega} \int\limits_{-J_E}^{J_E} dJ_{\tilde{z}} \int\limits_{J_E}^{J_E - \dot{J}\tau} g(L, J, J_{\tilde{z}}, \tilde{\Omega}, \tilde{\omega}, f)\Theta(\dot{J})\, dJ, \quad \text{(C.1)}$$

where $\Theta(\dot{J})$ is a step function, unity when $\dot{J} < 0$ and zero otherwise, which removes the outwards flux from the integral. Using the independence of the orbit-averaged $\dot{J}$ on $f$ and $\tilde{\Omega}$, (Equation 3.28b) and assuming the phase space density is of the form $g = g_0 L^{2\alpha+3}$ (Equation 4.23), we easily integrate over $f$ and $\tilde{\Omega}$ to get

$$\Phi(L, J_E)\, dL = \frac{4\pi^2 g_0 L^{2\alpha+3} dL}{\tau} \int\limits_0^{2\pi} d\tilde{\omega} \int\limits_{-J_E}^{J_E} dJ_{\tilde{z}} \int\limits_{J_E}^{J_E - \dot{J}\tau} \Theta(\dot{J})\, dJ. \qquad \text{(C.2)}$$

Integrating this equation with respect to $J$ simply yields

$$\Phi(L, J_E)\, dL = -4\pi^2 g_0 L^{2\alpha+3} dL \int\limits_0^{2\pi} d\tilde{\omega} \int\limits_{-J_E}^{J_E} \dot{J}\Theta(\dot{J})\, dJ_{\tilde{z}}. \qquad \text{(C.3)}$$

The expression for $\dot{J}$ is given by Equation 3.28b. Upon substitution, Equation C.3 becomes

$$\Phi(L, J_E) dL = -4\pi^2 g_0 L^{2\alpha+3} dL \int\limits_0^{2\pi} d\tilde{\omega} \int\limits_{-J_E}^{J_E} -\frac{5\pi\rho_0}{GM_\odot^2} \frac{L^2}{J_E^2}(J_E^2 - J_{\tilde{z}}^2)(L^2 - J_E^2) \sin 2\tilde{\omega}\, \Theta(\dot{J})\, dJ_{\tilde{z}} \text{(C.4a)}$$

$$= \frac{20\pi^3 g_0 \rho_0}{GM_\odot^2} \frac{L^{2\alpha+5}}{J_E^2} (L^2 - J_E^2) dL \int_0^{2\pi} \sin 2\tilde{\omega} \, \Theta(-\sin 2\tilde{\omega}) \, d\tilde{\omega} \int_{-J_E}^{J_E} (J_E^2 - J_{\tilde{z}}^2) \, dJ_{\tilde{z}}, \quad \text{(C.4b)}$$

where the dependence of the sign of $\dot{J}$ on $\sin 2\tilde{\omega}$ has been explicitly acknowledged. The integrals over $\tilde{\omega}$ and $J_{\tilde{z}}$ are easily done, yielding

$$\Phi(L, J_E) dL = \frac{160\pi^3 g_0 \rho_0}{3GM_\odot^2} L^{2\alpha+5} J_E (L^2 - J_E^2) dL. \quad \text{(C.5)}$$

The total flux across the entrance cylinder per unit $L$ is the integral of Equation C.5 over the entrance cylinder, which is given by Equation 4.14, and which is here expressed in our chosen canonical coordinates as

$$J_E(L) = \begin{cases} J_{E-} & \text{where } L_- \leq L \leq L_= \\ \mathcal{Z} k L^7 & \text{where } L_= \leq L \leq L_+ \end{cases} \quad \text{(C.6)}$$

where $L_-$ and $L_+$ are the minimum and maximum values of $L$ in the Oort cloud, corresponding to the minimum and maximum semimajor axes $a_-$ and $a_+$, $k = 10\pi^2 \rho_0 / G^3 M_\odot^4$ (Equation 4.7), and $L_=$ is the point at which $J_{E-} = \mathcal{Z} k L^7$ i.e. $L_= = (J_{E-}/\mathcal{Z} k)^{1/7}$ (Equation 4.9a).

Equation C.5 must be integrated along the path in $L$–$J$ space corresponding to the entrance cylinder, and may require an extra factor measuring the arclength along this path. However, the flux is always parallel to $\vec{J}$ and so is reduced by a factor of the cosine of the angle between $\vec{J}$ and the normal to the entrance cylinder. It easy to conclude that these contributions cancel out, and deduce that

$$\Phi_E^i(L, J_E) dL = \frac{160\pi^3 g_0 \rho_0}{3GM_\odot^2} L^{2\alpha+5} J_{E-} (L^2 - J_{E-}^2) dL, \quad \text{(C.7a)}$$

$$\Phi_E^o(L, J_E) dL = \frac{160\pi^3 g_0 \rho_0 k \mathcal{Z}}{3GM_\odot^2} L^{2\alpha+14} (1 - \mathcal{Z}^2 k^2 L^{12}) dL \quad \text{(C.7b)}$$

where the superscripts $i$ and $o$ indicate the inner and outer regions of the entrance surface respectively. This flux can be expressed in terms of the semimajor axis $a = L^2/GM_\odot$ by using the expression $dL = \sqrt{GM_\odot/4a} \, da$,

$$\Phi_E^i(a, q_E) da = \frac{80\sqrt{2}\pi^3}{3} g_0 \rho_0 G^{\alpha+7/2} M_\odot^{\alpha+5/2} q_{E-}^{1/2} a^{\alpha+2} (a - 2q_{E-}) da, \quad \text{(C.8a)}$$

$$\Phi_E^o(a, q_E) da = \frac{800\pi^5}{3} g_0 \rho_0^2 \mathcal{Z} G^{\alpha+7/2} M_\odot^{\alpha+3/2} a^{\alpha+13/2} \left(1 - \frac{100\pi^4 \rho_0^2 \mathcal{Z}^2}{M_\odot^2} a^6\right) da, \quad \text{(C.8b)}$$
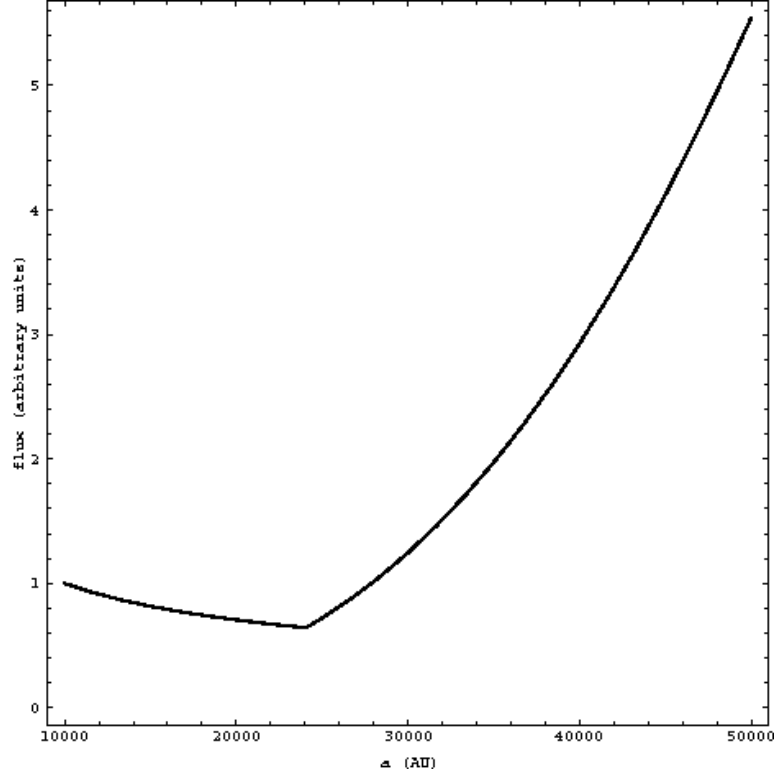
Figure C.1: The flux $\Phi_E$ of long-period comets into the entrance cylinder as a function of semimajor axis $a$.

where the approximation $J_{E-}^2 \approx 2GM_\odot q_{E-}$ has been made in the inner region. The flux is plotted in Figure C.1, assuming values of $\rho_0 = 0.15$ $M_\odot$ $pc^{-3}$, $\mathcal{Z} = 3$, $q_{E-} = 60$ AU, $\alpha = -3.5$, and with $g_0$ normalised so that $\Phi_E = 1$ at $a_-$. This function is the basis for the probability function used to compute comet initial elements (Equation 4.28f).

## C.2  The flux into the visibility cylinder

The flux expected into the visibility cylinder can be deduced from the flux into the entrance cylinder under the assumption that the tide remains the dominant perturber until the comet reaches the visibility cylinder: this is true in the outer Oort cloud where the loss cylinder is filled.

Consider Figure C.2, which shows a cross-section of the entrance and visibility cylinders in $J_{\tilde{z}}$–$J_{\tilde{x}\tilde{y}}$ space, where $J_{\tilde{x}\tilde{y}} = \sqrt{J_{\tilde{x}}^2 + J_{\tilde{y}}^2}$ such that $J^2 = J_{\tilde{z}}^2 + J_{\tilde{x}\tilde{y}}^2$. The angular momenta $J_v$ and $J_E$ are those at which the comet's perihelion is within the visibility cylinder and the entrance surface respectively.
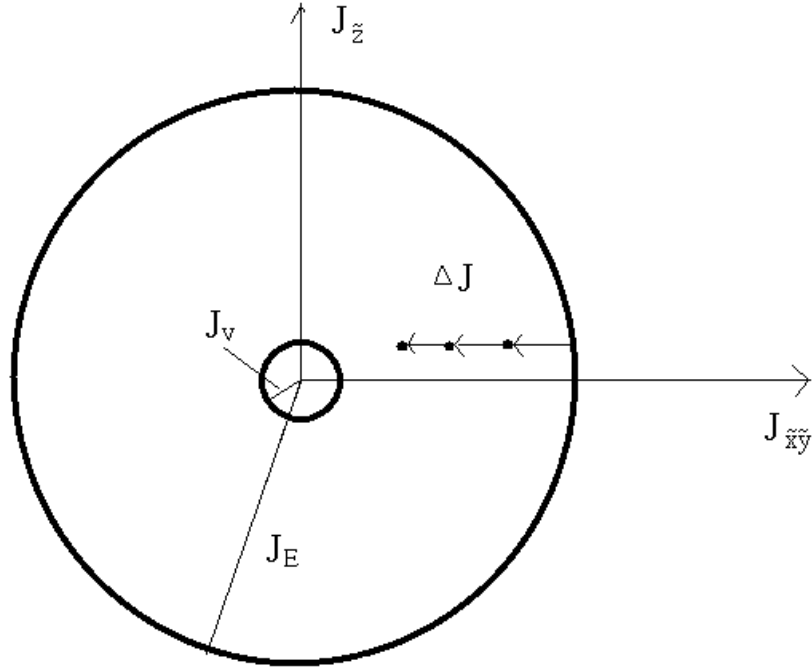
Figure C.2: Diagram of the entrance cylinder.

Since $J_{\tilde{z}}$ is conserved under the tide but $J_{\tilde{x}\tilde{y}}$ is not (§ 3.2.1), the evolution of an LP comet is a horizontal trajectory in Figure C.2. The sequence of dots moving inwards from the right side of the entrance cylinder represents the angular momentum values of a particular comet at a series of perihelion passages. The flux into the visibility cylinder is just the fraction of perihelion passages made within the entrance surface to that made within the visibility cylinder.

The step size $\Delta J$ is not generally constant from orbit to orbit, thus the flux into the visibility cylinder is reduced by a factor $\dot{J}_{\tilde{x}\tilde{y}}(J_v)/\dot{J}_{\tilde{x}\tilde{y}}(J_E)$ over that into the entrance surface. Since $J_{\tilde{z}}$ must be small if the comet is to enter the visibility cylinder, it is easy to show that $\dot{J}_{\tilde{x}\tilde{y}}(J_v)/\dot{J}_{\tilde{x}\tilde{y}}(J_E) \approx \dot{J}(J_v)/\dot{J}(J_E)$. The flux into the visibility cylinder is also reduced by a factor of $J_v/J_E$ due to the smaller cross-section of the visibility cylinder.

The visible flux is also reduced by the possibility that a comet passing through the visibility cylinder will do so in less than one orbit. If $\Delta J \gtrsim J_v$, the comet's angular momentum could move through and out the other side of the visibility cylinder between perihelion passages, and the comet would thus fail to become visible. Ignoring the dependence of this

phenomenon on $J_{\tilde{z}}$, the fraction of comets becoming visible is just the area of the visibility cylinder divided by the rectangle $2J_v\Delta J$, where $\Delta J = \dot{J}(J_v)\tau$. Assumed that $J_v \ll J_E$, certainly true for Oort cloud comets, the probability of a comet passing within $J_v$ becoming visible is $\pi J_v^2/2J_v\dot{J}(J_v)\tau$.

Combining these three factors, one finds that the flux into the visibility cylinder $\Phi_v$ is

$$\Phi_v \quad = \quad \frac{\dot{J}(J_v)}{\dot{J}(J_E)}\frac{J_v}{J_E}\frac{\pi J_v^2}{2J_v\dot{J}(J_v)}\Phi_E, \tag{C.9a}$$

$$= \quad \frac{\pi J_v^2}{2J_E\dot{J}(J_E)\tau}. \tag{C.9b}$$

Considering only the region where the loss cylinder is full ($a \gtrsim 25\,000$ AU), the expressions $J_E = \mathcal{Z}kL^7$ (Equation C.6), $\dot{J}_E\tau = e_E^2kL^7$ (Equation 3.30), and $J_v^2 = 2GM_\odot q_v$ can be used express Equation C.9b as

$$\Phi_v^o \approx \frac{\pi J_v^2}{2e_E^2k^2\mathcal{Z}L^{14}}\Phi_E = \frac{q_vM_\odot^2}{100\pi^3e_E^2\rho_0^2\mathcal{Z}a^7}\Phi_E. \tag{C.10}$$

where the superscript $^o$ indicates the flux in the region $a \geq a_=$. Using the expression $e_E^2 = (L^2 - J_E^2)/L^2$, the flux can be reduced to

$$\Phi_v^o(a, q_v)da \approx \frac{8\pi^2}{3}g_0q_v(GM_\odot)^{\alpha+7/2}a^{\alpha-1/2}\,da. \tag{C.11}$$

Note that this expression does not depend on the characteristics of the entrance surface, as would be hoped. It is also independent of $\rho_0$, removing the possibility of measuring the local matter density directly from the flux of visible comets.

For an Oort cloud with $\alpha = -3.5$, the flux into the visible cylinder from the outer cloud will fall as $a^{-4}$. This decrease is due in part to the increasing likelihood of a comet "jumping over" the visibility cylinder between perihelion passages as $\Delta J$ becomes large. The flux into the visibility cylinder is plotted in Figure 5.3, along with a plot of the distribution of the original inverse semimajor axes of the $V_1$ comets.

# Bibliography:

A'Hearn, M. F. and Festou, M. C. 1990. The neutral coma. In *Physics and Chemistry of Comets*, W. F. Huebner (ed.), pages 69–112. New York: Springer-Verlag.

A'Hearn, M. F. 1988. Observations of cometary nuclei. *Ann. Rev. Earth Planet. Sci.* 16:273–293.

Antonov, V. A. and Latyshev, I. N. 1972. Determination of the form of the Oort cometary cloud as the Hill surface in the galactic field. In *The Motion, Evolution of Orbits, and Origin of Comets*, G. A. Chebotarev, E. I. Kazimirchak-Polonskaya, and B. G. Marsden (eds.), pages 341–345. IAU Symposium no. 45.

Antrack, D., Biermann, L., and Lüst, R. 1964. Some statistical properties of comets with plasma tails. *Ann. Rev. Astron. Astrophys.* 2:327–340.

Backman, D. E., Dasgupta, A., and Stencel, R. E. 1995. Model of a Kuiper belt small grain population and resulting far infrared emission. *Astrophys. J. Lett.* 450:35–38.

Backman, D. E. 1995. private communication.

Bahcall, J. N. and Soneira, R. M. 1980. The universe at faint magnitudes. I. Models for the Galaxy and predicted star counts. *Astrophys. J. Suppl.* 44:73–110.

Bahcall, J. N., Flynn, C., and Gould, A. 1992. Local dark matter density from a carefully selected sample. *Astrophys. J.* 389:234–250.

Bahcall, J. N. 1984. The distribution of stars perpendicular to a galactic disk. *Astrophys. J.* 276:156–168.

Bailey, M. E. 1983. The structure and evolution of the Solar System comet cloud. *Mon. Not. Roy. Astron. Soc.* 204:603–633.

Bailey, M. E. 1984. The steady-state $1/a$ distribution and the problem of cometary fading. *Mon. Not. Roy. Astron. Soc.* 211:347–368.

Bailey, M. E. 1986. The mean energy transfer rate to comets in the Oort cloud and implications for cometary origins. *Mon. Not. Roy. Astron. Soc.* 218:1–30.

Bailey, M. E. 1987. The formation of comets in wind-driven shells around protostars. *Icarus* 69:70–82.

Baranov, V. B. and Zaitsev, N. A. 1995. On the problem of the solar wind interaction with a magnetized interstellar plasma. *Astron. Astrophys.* 304:631–637.

Baranov, V. B. 1986. The interface between the heliosphere and the local interstellar

medium. In *UV Space Astronomy — Physical Processes in the Local Interstellar Medium*, C. Gry and W. Wamsteker (eds.), pages 5–12. Toronto: Pergamon Press.

Benner, L. A. M. and McKinnon, W. B. 1995. On the orbital evolution and origin of Comet Shoemaker-Levy 9. *Icarus* 118:155–168.

Biermann, L. 1978. Dense interstellar clouds and comets. In *Astronomical Papers Dedicated to Bengt Strömgren*, A. Reiz and T. Anderson (eds.), pages 327–336. Copenhagen: Copenhagen Observatory Press.

Binney, J. and Tremaine, S. 1987. *Galactic Dynamics*. Princeton: Princeton University Press.

Brandt, J. C. 1968. The physics of comet tails. *Ann. Rev. Astron. Astrophys.* 6:267–286.

Burden, R. L. and Faires, J. D. 1989. *Numerical Analysis*. Boston: PWS-Kent, $4^{th}$ edition.

Carusi, A. and Valsecchi, G. B. 1992. Dynamics of comets. In *Chaos, Resonance and Collective Dynamical Phenomena in the Solar System*, S. Ferraz-Mello (ed.), pages 255–268. IAU Symposium no. 152.

Cellino, A., Zappala, V., and Farinella, P. 1991. The size distribution of main-belt asteroid from IRAS. *Mon. Not. Roy. Astron. Soc.* 253:561–574.

Chirikov, B. V. and Vecheslavov, V. V. 1986. Chaotic dynamics of comet Halley. *Russian Institute for Nuclear Physics preprint* 86-184.

Clube, S. V. M. and Napier, W. M. 1984. Comet capture from molecular clouds: a dynamical constraint on star and planet formation. *Mon. Not. Roy. Astron. Soc.* 208:575–588.

Cochran, A. L., Levison, H. F., Stern, S. A., and Duncan, M. J. 1995. The discovery of Halley-sized Kuiper belt objects using the Hubble Space Telescope. *Astrophys. J.* 455:342–346.

Delsemme, A. H. and Miller, D. C. 1971. Physico-chemical phenomena in comets. III. The continuum of comet Burnham (1960 II). *Plan. Space Sci.* 19:1229–1257.

Delsemme, A. H. 1982. Chemical composition of cometary nuclei. In *Comets*, L. L. Wilkening (ed.), pages 85–130. Tucson: University of Arizona Press.

Drapatz, S. and Zinnecker, H. 1984. The size and mass distribution of galactic molecular clouds. *Mon. Not. Roy. Astron. Soc.* 210:11–14.

Duncan, M., Quinn, T., and Tremaine, S. 1987. The formation and extent of the Solar System comet cloud. *Astron. J.* 94:1330–1338.

Dvorak, R. and Kribbel, J. 1990. Dynamics of Halley-like comets for 1 million years. *Astron. Astrophys.* 227:264–270.

Eberhardt, P., Dolder, U., Schulte, W., Krankowsky, D., Lämmerzahl, P., Hoffman, J. H., Hodges, R. R., Berthelier, J. J., and Illiano, J. M. 1986. The D/H ratio in water from Halley. In *Exploration of Halley's Comet*, B. Battrick et al. (eds.), Vol. I. ESA SP-250.

Efron, B. 1982. *The Jackknife, the Bootstrap and Other Resampling Plans.* Philadelphia: Society for Industrial and Applied Mathematics.

Everhart, E. 1967a. Comet discoveries and observational selection. *Astron. J.* 72:716–726.

Everhart, E. 1967b. Intrinsic distributions of cometary perihelia and magnitudes. *Astron. J.* 72:1002–1011.

Everhart, E. 1968. Change in total energy of comets passing through the Solar System. *Astron. J.* 73:1039–1052.

Everhart, E. 1972. The origin of short-period comets. *Astrophys. Lett.* 10:131–135.

Everhart, E. 1976. The evolution of comet orbits. In *The Study of Comets*, B. Donn, M. Mumma, W. Jackson, M. A'Hearn, and R. Harrington (eds.), Vol. I, pages 445–464. IAU Colloquium no. 25.

Everhart, E. 1979. The shortage of long-period comets in elliptical orbits. In *Dynamics of the Solar System*, R. L. Duncombe (ed.), pages 273–275. IAU Symposium no. 81.

Fernández, J. A. and Ip, W. H. 1983. Dynamical origin of the short-period comets. In *Asteroids, Comets and Meteors*, C. I. Lagerkvist and H. Rickman (eds.), pages 387–390. Uppsala, Sweden: Uppsala University Press.

Fernández, J. A. and Ip, W. H. 1991. Statistical and evolutionary aspects of cometary orbits. In *Comets in the Post-Halley Era*, R. L. Kluwer (ed.), pages 487–535. IAU Colloquium no. 116.

Fernández, J. A. 1980. Evolution of comet orbits under the perturbing influence of the giant planets and nearby stars. *Icarus* 42:406–421.

Fernández, J. A. 1981. New and evolved comets in the Solar System. *Astron. Astrophys.* 96:26–35.

Fernández, J. A. 1985. The formation and dynamical survival of the comet cloud. In *Dynamics of Comets: Their Origin and Evolution*, A. Carusi and G. B. Valsecchi (eds.), pages 45–70. IAU Colloquium no. 83.

Festou, M. C., Rickman, H., and West, R. M. 1993a. Comets. *Ann. Rev. Astron. Astrophys.*

4:363–447.

Festou, M. C., Rickman, H., and West, R. M. 1993b. Comets. *Ann. Rev. Astron. Astrophys.* 5:37–163.

Festou, M. C. 1986. The derivation of OH gas production rates from visual magnitudes of comets. In *Asteroids, Comets and Meteors*, C. I. Lagerkvist, B. A. Lindblad, H. Lundstedt, and H. Rickman (eds.), Vol. II, pages 299–303. Uppsala: Uppsala University Press.

Foukal, P. 1990. *Solar Astrophysics.* Toronto: John Wiley & Sons.

Froeschlé, C. and Rickman, H. 1988. Monte Carlo modelling of cometary dynamics. *Celest. Mech.* 43:265–284.

Galeev, A. A., Griov, B. E., Gombosi, T., Gringauz, K. I., Klimov, S. I., Oberz, P., Remisov, A. P., Reidler, W., Sagdeev, R. S., Savin, S. P., Sokolov, A. Y., Shapiro, V. D., Shevchenko, V. I., Szego, K., Verigin, M. I., and Yeroshenko, Y. G. 1986. The position and structure of the Comet Halley bow shock: Vega–1 and Vega–2 measurements. *Geophys. Res. Lett.* 13:841–844.

Groth, E. J., Kristian, J. A., Lynds, R., O'Neil, E. J., Balsano, R., and Rhodes, J. 1994. A survey with the HST. *Bull. Amer. Astron. Soc.* 185:1403.

Grün, E. and Jessberger, E. K. 1990. Dust. In *Physics and Chemistry of Comets*, W. F. Huebner (ed.), pages 113–176. New York: Springer-Verlag.

Hall, D. T., Shemansky, D. E., Judge, D. L., Gangopadhyay, P., and Gruntman, M. A. 1993. Heliospheric hydrogen beyond 15 AU: evidence for a terminal shock. *J. Geophys. Res.* 98:15185–15192.

Heggie, D. C. 1975. Binary evolution in stellar encounters. *Mon. Not. Roy. Astron. Soc.* 173:729–787.

Heisler, J. and Tremaine, S. 1986. The influence of the galactic tidal field on the Oort comet cloud. *Icarus* 65:13–26.

Heisler, J., Tremaine, S., and Alcock, C. 1987. The frequency and intensity of comet showers from the Oort cloud. *Icarus* 70:269–288.

Heisler, J. 1990. Monte Carlo simulations of the Oort comet cloud. *Icarus* 88:104–121.

Hills, J. G. 1980. Comet showers and the steady-state infall of comets from the Oort cloud. *Astron. J.* 86:1730–1740.

Hills, J. G. 1981. Comet showers and the steady-state infall of comets from the Oort cloud. *Astron. J.* 86:1733–1740.

Hills, J. G. 1982. The formation of comets by radiation pressure in the outer protosun. *Astron. J.* 87:906–910.

Hogg, D. W., Quinlan, G. D., and Tremaine, S. 1991. Dynamical limits on dark mass in the outer Solar System. *Astron. J.* 101:2274–2286.

Hopkins, J. 1980. *Glossary of Astronomy and Astrophysics.* Chicago: University of Chicago Press, $2^{nd}$ edition.

Hughes, D. W. and Harris, N. W. 1994. The distribution of asteroid sizes and its significance. *Plan. Space Sci.* 42:291–295.

Hughes, D. W. 1975. Cometary outbursts: a brief survey. *Quart. J. Roy. Astron. Soc.* 16:410–427.

Jackson, W. M. 1976. Laboratory observations of the photochemistry of parent molecules: a review. In *The Study of Comets*, B. Donn, M. Mumma, W. Jackson, M. A'Hearn, and R. Harrington (eds.), Vol. I, pages 679–702. IAU Colloquium no. 25.

Jewitt, D. C. and Luu, J. X. 1993. Discovery of the candidate Kuiper belt object 1992 QB1. *Nature* 362:730–731.

Jewitt, D. C. and Luu, J. X. 1995. The Solar System beyond Neptune. *Astron. J.* 109:1867–1876.

Joss, P. C. 1973. On the origin of short-period comets. *Astron. Astrophys.* 25:271–273.

Kannan, D. 1979. *An Introduction to Stochastic Processes.* New York: North Holland.

Keller, H. U. 1990. The nucleus. In *Physics and Chemistry of Comets*, W. F. Huebner (ed.), pages 13–68. New York: Springer-Verlag.

Kendall, D. G. 1961. Some problems in the theory of comets, I and II. In *Proc. Fourth Berkeley Symposium on Mathematical Statistics and Probability*, J. Neyman (ed.), pages 99–147.

Kerr, F. J. and Lynden-Bell, D. 1986. Review of galactic constants. *Mon. Not. Roy. Astron. Soc.* 221:1023–1038.

Krankowsky, D., Lämmerzahl, P., Herrwerth, I., Woweries, J., Eberhardt, P., Dolder, U., Herrmann, U., Schulte, W., Berthelier, J. J., Illiano, J. M, Hodges, R. R., and Hoffmann, J. H. 1986. *In situ* gas and ion measurements at Comet Halley. *Nature* 321:326–329.

Kresák, Ľ. and Pittich, E. M. 1978. The intrinsic number density of active long-period comets in the inner Solar System. *Bull. Astron. Inst. Czech.* 29:299–309.

Kresák, Ľ. 1974. The aging and the brightness decrease of comets. *Bull. Astron. Inst.*

*Czech.* 25:87–112.

Kresák, Ľ. 1977. Asteroid vs. comet discrimination from orbital data. In *Comets, Asteroids, Meteorites: Interrelation, Evolution and Origin*, A. H. Delsemme (ed.), pages 313–321. Toledo, Ohio: University of Toledo Press. IAU Colloquium no. 39.

Kresák, Ľ. 1982. Comet discoveries, statistics and observational selection. In *Comets*, L. L. Wilkening (ed.), pages 56–82. Tucson: University of Arizona Press.

Kresák, Ľ. 1985. The aging and lifetimes of comets. In *Dynamics of Comets: Their Origin and Evolution*, A. Carusi and G. B. Valsecchi (eds.), pages 279–302. IAU Colloquium no. 83.

Kuijken, K. and Gilmore, G. 1989. The mass distribution in the galactic disc III. the local volume mass density. *Mon. Not. Roy. Astron. Soc.* 239:651–664.

Kuijken, K. 1991. Further limits on disklike dark matter from K dwarf kinematics. *Astrophys. J.* 372:125–131.

Kuiper, G. P. 1951. On the origin of the Solar System. In *Astrophysics*, J. A. Hynek (ed.), pages 357–427. New York: McGraw-Hill.

Kurth, W. S., Gurnett, D. A., Scarf, F. L., and Poynter, R. L. 1984. Detection of a radio emission at 3 kHz in the outer heliosphere. *Nature* 312:27–31.

Lang, K. R. 1992. *Astrophysical Data: Planets and Stars*. New York: Springer-Verlag.

Levison, H. F. and Duncan, M. J. 1994. The long-term dynamical behavior of short-period comets. *Icarus* 108:18–36.

Lindal, G. F. 1992. The atmosphere of Neptune - an analysis of radio occultation data acquired with Voyager 2. *Astron. J.* 103:967–982.

Linsky, J. L. and Wood, B. 1995. First measurement of the hydrogen wall around the heliosphere and the interstellar medium toward $\alpha$ Centauri. *Bull. Amer. Astron. Soc.* 27:1347.

Lüst, R. 1984. The distribution of the aphelion directions of long-period comets. *Astron. Astrophys.* 140:94–100.

Lyttleton, R. A. 1974. The non-existence of the Oort cometary shell. *Astrophys. Space Sci.* 31:385–401.

Manara, A. and Valsecchi, G. B. 1991. Dynamics of comets in the outer planetary region. I. a numerical experiment. *Astron. Astrophys.* 249:269–276.

Marsden, B. G. and Williams, G. V. 1993. *Catalogue of Cometary Orbits*. Cambridge,

Massachusetts: IAU Central Bureau for Astronomical Telegrams – Minor Planet Center, $8^{th}$ edition.

Marsden, B. G. and Williams, G. V. 1994. *Catalogue of Orbits of Unnumbered Minor Planets.* Cambridge, Massachusetts: IAU Central Bureau for Astronomical Telegrams – Minor Planet Center, $5^{th}$ edition.

Marsden, B. G., Sekanina, Z., and Yeomans, D. K. 1973. Comets and non-gravitational forces. V. *Astron. J.* 78:211–225.

Marsden, B. G. 1976. Nongravitational forces on comets. In *The Study of Comets*, B. Donn, M. Mumma, W. Jackson, M. A'Hearn, and R. Harrington (eds.), Vol. I, pages 465–489. IAU Colloquium no. 25.

Marsden, B. G. 1977. Orbital data on the existence of Oort's cloud of comets. In *Comets, Asteroids, Meteorites: Interrelation, Evolution and Origin*, A. H. Delsemme (ed.), pages 79–86. Toledo, Ohio: University of Toledo Press. IAU Colloquium no. 39.

Matese, J. J. and Whitman, P. G. 1989. The galactic disk tidal field and the nonrandom distribution of observed Oort cloud comets. *Icarus* 82:389–401.

Matese, J. J., Whitman, P. G., Innanen, K. A., and Valtonen, M. J. 1995. Periodic modulation of the Oort cloud comet flux by the adiabatically changing galactic tide. *Icarus* 116:255–268.

Meech, K. J. and Belton, M. J. S. 1990. The atmosphere of *2060* Chiron. *Astron. J.* 100:1323–1338.

Mendis, D. A. 1988. A post-encounter view of comets. *Ann. Rev. Astron. Astrophys.* 26:11–49.

Mihalas, D. and Binney, J. 1981. *Galactic Astronomy.* New York: W. H. Freeman and Co.

Miller, R. H. 1964. Irreversibility in small stellar dynamical systems. *Astrophys. J.* 140:250–256.

Minor Planet Circulars 23803-23804. 1994. Minor Planet Center, Smithsonian Astrophysical Observatory, Cambridge.

Morris, D. E. and Muller, R. A. 1986. Tidal gravitational forces: the infall of "new" comets and comet showers. *Icarus* 65:1–12.

Morrison, D. 1992. The Spaceguard Survey: Report of the NASA International Near–Earth Object Detection Workshop. Technical Report TM-107979, NASA.

Newhall, X. X., Standish, E. M., and Williams, J. G. 1983. DE 102: a numerically

integrated ephemeris of the Moon and planets spanning forty-four centuries. *Astron. Astrophys.* 125:150–167.

Noyes, R. W. and Avrett, E. H. 1987. The solar chromosphere. In *Spectroscopy of Astrophysical Plasmas*, A. Dalgarno and D. Layzer (eds.), pages 125–164. Cambridge: Cambridge University Press.

Oja, H. 1975. Perihelion distribution of near-parabolic comets. *Astron. Astrophys.* 43:317–319.

Oort, J. H. 1950. The structure of the cloud of comets surrounding the Solar System, and a hypothesis concerning its origin. *Bull. Astron. Inst. Netherlands* XI(408):91–110.

Opïk, E. J. 1973. Comets and the formation of planets. *Astrophys. Space Sci.* 21:307–398.

Paresce, F. and Burrows, C. 1987. Broad-band imaging of the Beta Pictoris circumstellar disk. *Astrophys. J. Lett.* 319:23–25.

Petrosky, T. Y. 1986. Chaos and cometary clouds in the Solar System. *Phys. Lett. A* 117:328.

Pittich, E. M. 1971. Space distribution of the splitting and outbursts of comets. *Bull. Astron. Inst. Czech.* 22:143–153.

Press, W. H., Flannery, B. P., Teukolsky, S. A., and Vetterling, W. T. 1986. *Numerical Recipes in C: The Art of Scientific Computing*. Cambridge: Cambridge University Press, $1^{st}$ edition.

Press, W. H., Teukolsky, S. A., Vetterling, W. T., and Flannery, B. P. 1992. *Numerical Recipes in C: The Art of Scientific Computing*. Cambridge: Cambridge University Press, $2^{nd}$ edition.

Quinn, T., Tremaine, S., and Duncan, M. 1990. Planetary perturbations and the origin of short-period comets. *Astrophys. J.* 355:667–679.

Rickman, H. 1986. Masses and densities of comets Halley and Kopff. In *The Comet Nucleus Sample Return Mission Workshop Proceedings*, pages 195–205. ESA SP-249.

Roettger, E. E., Feldman, P. D., A'Hearn, M. F., and Festou, M. C. 1990. Comparison of water production rates from UV spectroscopy and visual magnitudes of some recent comets. *Icarus* 86:100–114.

Roy, A. E. 1978. *Orbital Motion*. Bristol: Adam Hilger Ltd.

Safronov, V. S. 1972. Ejection of bodies from the Solar System in the course of the accumulation of the giant planets and the formation of the cometary cloud. In *The*

*Motion, Evolution of Orbits, and Origin of Comets*, G. A. Chebotarev, E. I. Kazimirchak-Polonskaya, and B. G. Marsden (eds.), pages 329–334. IAU Symposium no. 45.

Sagdeev, R. Z. and Zaslavsky, G. M. 1987. Stochasticity in the Kepler problem and a model of possible dynamics of comets in the Oort cloud. *Il Nuovo Cimento* 97B(2):119–130.

Saito, T. 1990. Interactions between the plasma tail of comet Halley and the solar wind magnetic field. In *Comet Halley: Investigations, Results, Interpretations*, J. W. Mason (ed.), Vol. I, pages 101–127. Toronto: Ellis Horwood.

Sekanina, Z. 1964. Perihelion asymmetry of photometric curves of comets. *Bull. Astron. Inst. Czech.* 15:8–20.

Sekanina, Z. 1969. Secular variations in the absolute brightness of short-period comets. *Bull. Astron. Inst. Czech.* 15:1–7.

Shoemaker, E. M. 1983. Asteroid and comet bombardment of the earth. *Ann. Rev. Earth Planet. Sci.* 11:461–494.

Smith, B. A. and Terrile, R. J. 1984. A circumstellar disk around $\beta$ Pictoris. *Science* 226:1421–1424.

Smith, B. A. and Terrile, R. J. 1987. The Beta Pictoris disk: recent optical observations. *Bull. Amer. Astron. Soc.* 19:829.

Smoluchowski, R. 1986. Brightness curves and porosity of cometary nuclei. In *Asteroids, Comets and Meteors*, C. I. Lagerkvist, B. A. Lindblad, H. Lundstedt, and H. Rickman (eds.), Vol. II, pages 305–315. Uppsala: Uppsala University Press.

Spinrad, H. 1987. Comets and their composition. *Ann. Rev. Astron. Astrophys.* 25:231–269.

Spitzer, L. 1978. *Physical Processes in the Interstellar Medium.* Toronto: J. Wiley and Sons.

Steinolfson, R. S., Pizzo, V. J., and Holzer, T. 1994. Gasdynamic models of the solar wind/interstellar medium interaction. *Geophys. Res. Lett.* 21:245–248.

Stiefel, E. L. and Scheifele, G. 1971. *Linear and Regular Celestial Mechanics.* New York: Springer-Verlag.

Streeter, V. L. and Wylie, E. B. 1985. *Fluid Mechanics.* New York: McGraw-Hill, $8^{th}$ edition.

Torbett, M. V. 1986. Injection of Oort cloud comets to the inner Solar System by galactic tidal fields. *Mon. Not. Roy. Astron. Soc.* 223:885–895.

Tremaine, S. 1990. Dark matter in the Solar System. In *Baryonic Dark Matter*, D. Lynden-

Bell and G. Gilmore (eds.), pages 37–65. Netherlands: Kluwer Academic Publishers.

Tremaine, S. 1993. The distribution of comets around stars. In *Planets around Pulsars*, J. A. Phillips, S. E. Thorsett, and S. R. Kulkarni (eds.), Vol. 36 of *Astron. Soc. Pac. Conference Series*, pages 335–344. San Francisco: Astronomical Society of the Pacific.

Tyror, J. G. 1957. The distribution of the directions of perihelia of long-period comets. *Mon. Not. Roy. Astron. Soc.* 117:370–379.

U.S. Naval Observatory. 1992. *Astronomical Almanac for the Year 1992*. Washington: U.S. Naval Observatory.

van Flandern, T. C. 1978. A former asteroidal planet as the origin of comets. *Icarus* 36:51–74.

van Woerkom, A. J. J. 1948. On the origin of comets. *Bull. Astron. Inst. Netherlands* X(399):445–472.

R. C. Weast, D. R. Lide, M. J. Astle, and W. H. Beyer (eds.). 1989. *CRC Handbook of Chemistry and Physics*. Boca Raton: CRC Press, $70^{th}$ edition.

Weissman, P. R. 1978. *Physical and Dynamical Evolution of Long-Period Comets*. PhD thesis, University of California, Los Angeles.

Weissman, P. R. 1979. Physical and dynamical evolution of long-period comets. In *Dynamics of the Solar System*, R. L. Duncombe (ed.), pages 277–282. IAU Symposium no. 81.

Weissman, P. R. 1980. Physical loss of long-period comets. *Astron. Astrophys.* 85:191–196.

Weissman, P. R. 1983. The mass of the Oort cloud. *Astron. Astrophys.* 118:90–94.

Weissman, P. R. 1985. Dynamical evolution of the Oort cloud. In *Dynamics of Comets: Their Origin and Evolution*, A. Carusi and G. B. Valsecchi (eds.), pages 87–96. IAU Colloquium no. 83.

Weissman, P. R. 1991. Dynamical history of the Oort cloud. In *Comets in the Post-Halley Era*, R. L. Newburn et al. (eds.), Vol. I, pages 463–486. IAU Colloquium no. 116.

Whipple, F. L. and Huebner, W. F. 1976. Physical processes in comets. *Ann. Rev. Astron. Astrophys.* 14:143–172.

Whipple, F. L. 1950. A comet model. I. the acceleration of comet Encke. *Astrophys. J.* 111:375–394.

Whipple, F. L. 1972. The origin of comets. In *The Motion, Evolution of Orbits, and Origin of Comets*, G. A. Chebotarev, E. I. Kazimirchak-Polonskaya, and B. G. Marsden (eds.),

pages 401–408. IAU Symposium no. 45.

Whipple, F. L. 1977. The reality of comet groups and pairs. *Icarus* 30:736–746.

Whipple, F. L. 1978. Cometary brightness variation and nucleus structure. *The Moon and the Planets* 18:343–359.

Wilhelm, K. 1987. Rotation and precession of comet Halley. *Nature* 327:27–30.

Yabushita, S. and Hasegawa, I. 1978. A note on the possible origin of comets in an interstellar gas cloud. *Mon. Not. Roy. Astron. Soc.* 185:549–553.

Yabushita, S. 1979. A statistical study of the evolution of the orbits of long-period comets. *Mon. Not. Roy. Astron. Soc.* 187:445–462.